Transilvania University of Brașov

HABILITATION THESIS

Advancements in industrial thermal spraying: process optimization, coating development, and novel applications

Domain: Industrial engineering

Author: Assoc. prof. dr. Ionuț Claudiu ROATĂ
Transilvania University of Brașov

BRAŞOV, 2025

Content

Acknowledgement

The studies presented and detailed in this habilitation thesis were achieved with partial financial support from several funding agencies and grants:

- Sectoral Operational Programme Human Resources Development (SOP HRD), financed from the European Social Fund and by the Romanian Government under the project number POSDRU/89/1.5/S/59323) is sincerely acknowledged;

- PRO-DD (POS-CCE, O.2.2.1., ID 123, SMIS 2637, ctr. No 11/2009) is sincerely acknowledged for providing the infrastructure used in this habilitation thesis;

- Solar Facilities for the European Research Area (SFERA III) - Laborator ENEA - Italian National Agency for New Technologies, Energy and Sustainable Economic Development, Grant Agreement No 823802 is sincerely acknowledged for the access to their facilities;

- Solar Facilities for the European Research Area (SFERA II) - Laborator ENEA - Italian National Agency for New Technologies, Energy and Sustainable Economic Development, Grant Agreement No 312643 is sincerely acknowledged for the access to their facilities;

- Solar Facilities for the European Research Area (SFERA II) – Laborator PSA - The Plataforma Solar de Almería (PSA), Grant Agreement No 312643 is sincerely acknowledged for the access to their facilities.

I would like to sincerely thank my colleagues from the Faculty of Science and Materials Engineering at Transilvania University of Brașov, as well as all collaborators from the country and abroad. Without their support and contributions, I would not have been able to complete the habilitation thesis titled "Advancements in industrial thermal spraying: process optimization, coating development, and novel applications".

(A) Abstract

The habilitation thesis, "Progress in industrial thermal spraying: process optimization, coating development, and innovative applications," presents original research conducted by me following the conferral of a PhD in Industrial engineering in 2009. The research focuses on optimizing technological parameters for flame and powder spraying processes, resulting in superior-performance coatings with broad applicability in various fields, including industrial engineering, surface engineering, and electrochemistry.

The multidisciplinary research results, presented in section B2 of the habilitation thesis, are structured into four chapters: 1. Thermal spraying technologies in industrial engineering; 2. Critical process parameters in flame spraying of powders: Influence, optimization, and impact on coating quality; and 3. Experimental development and characterization of advanced thermal spray coatings. The habilitation thesis also concludes with elements related to career development and academic evolution plans (section B3).

The first chapter provides a detailed analysis of the evolution of thermal spraying technologies, focusing on methods for achieving high-performance coatings in surface engineering. The presentation identifies and discusses key technical challenges, including oxidation control, maintaining material phase stability, and optimizing production process efficiency. These aspects are crucial for obtaining durable and high-quality coatings.

Chapter two details the technological parameters of the flame spraying process and their impact on achieving coatings with superior mechanical, physical, and chemical properties. A thorough analysis of these parameters, and the ability to strategically modify them, is illustrated through a series of experimental studies conducted by me and presented in detail in Chapter three. These studies form the foundation for improving thermal spraying technology and developing optimized coatings that meet the stringent requirements of industrial applications.

Chapter three, based on my research, demonstrates that using electrically charged powders improves the physical and mechanical properties of deposited layers. This leads to enhanced homogeneity, microstructural hardness, and superior adhesion. Conversely, samples without electrically charged powders exhibit a non-uniform structure and a lower quality interface.

This chapter also explores the influence of using an argon (Ar) protective gas to reduce oxidation during the deposition process. This significantly lowers the electrical resistivity of the deposited layer. This improved electrical conductivity optimizes the material's performance in applications requiring conductive layers with low resistance. The importance of precise argon atmosphere control is highlighted, as it maintains material integrity and enhances functionality.

Two applications of solar thermal treatments are also presented, demonstrating improvements in homogeneity and substrate interface for copper – aluminum – iron and copper – nickel powders deposited by thermal spraying. The thermal treatment process fostered the formation of intermetallic compounds, leading to increased hardness and wear resistance.

Another application of thermally sprayed coatings lies in photocatalysis, where their ability to enhance water and air purification processes is exploited. Applying metallic or composite metallic layers to substrates creates an efficient charge transfer interface, reducing electron-hole recombination and thus increasing photocatalytic activity. These coatings also provide mechanical and chemical stability, extending the lifespan of photocatalytic systems. Furthermore, thermal spraying modifies the materials' optical properties, increasing light absorption.

The study investigated the influence of laser deposition speed on the properties of the deposited coatings. Higher deposition speeds (90 mm/s) resulted in improved hardness due to reduced dilution. However, this speed also raised concerns regarding occupational exposure to metal emissions during the process.

The academic career development plan, both in teaching and research, is detailed in section B3 of the habilitation thesis. Future research directions include:

- **Optimization of flame spraying parameters for NiCrAlX-based powders:** Focusing on achieving corrosion-resistant coatings.
- **Optimization of flame spraying parameters for biocompatible powders:** Investigating biocompatible powders such as zirconium dioxide, aluminum oxide, and calcium oxide.
- **Laser fusion of flame-sprayed coatings:** Exploring the use of laser beams to further enhance the properties of coatings deposited via the flame spraying process.
- **Expanding applications of protective gas-environment coatings:** Aiming to reduce the weight of components while maintaining performance.

My research output to date comprises **50** articles with impact factor (indexed by Clarivate Analytics Web of Science) and **12** articles in ISI proceedings. I have also served as principal investigator on four research grants, demonstrating my ability to secure funding and manage projects. My research visibility is further evidenced by a Hirsch index of 12 according to Clarivate and Scopus.

(A) Rezumat

Teza de abilitare intitulată „Progrese în pulverizarea termică industrială: optimizarea procesului, dezvoltarea de acoperiri și aplicații inovatoare" prezintă rezultatele cercetărilor proprii, realizate după obținerea titlului de doctor în ingineria industrială în anul 2009. Aceste rezultate se referă la optimizarea parametrilor tehnologici utilizați la pulverizarea cu flacără și pulberi, obținându-se acoperiri cu performanțe superioare și cu o aplicabilitate extinsă în diferite domenii, precum inginerie industrială, ingineria suprafețelor sau electrochimie.

Rezultatele cercetărilor multidisciplinare sunt structurate în secțiunea B2 a acestei teze de abilitare în patru capitole: 1. Tehnologii de pulverizare termică în ingineria industrială; 2. Parametrii critici ai procesului în pulverizarea cu flacără a pulberilor: influență, optimizare și impact asupra calității acoperirii și 3. Dezvoltarea experimentală și caracterizarea acoperirilor avansate prin

pulverizare termică. În încheierea tezei de abilitare sunt prezentate de asemenea elemente privind planurile de evoluție și dezvoltare a carierei academice (secțiunea B3).

Primul capitol prezintă o analiză detaliată a evoluției tehnologiilor de pulverizare termică, cu accent pe metodele utilizate pentru obținerea de acoperiri cu performanțe superioare în domeniul ingineriei de suprafață. În cadrul acestei prezentări, sunt identificate și discutate principalele provocări tehnice, precum controlul oxidării, menținerea stabilității fazelor materiale și optimizarea eficienței proceselor de producție, aspecte esențiale pentru obținerea unor acoperiri durabile și de înaltă calitate.

Capitolul al doilea prezintă parametrii tehnologici ai procesului de pulverizare cu flacără și impactul acestora asupra obținerii unor acoperiri caracterizate prin proprietăți mecanice, fizice și chimice superioare. O analiză aprofundată a acestor parametri, precum și capacitatea de a-i modifica strategic, sunt ilustrate printr-o serie de studii experimentale realizate de către mine și prezentate în detaliu în Capitolul 3. Aceste studii constituie fundamentul pentru îmbunătățirea tehnologiei de pulverizare termică și pentru dezvoltarea de acoperiri optimizate, conforme cerințelor stricte ale aplicațiilor industriale.

Capitolul al treilea exemplifică prin prisma propriilor cercetări, faptul că utilizarea pulberilor încărcate electric îmbunătățește proprietățile fizice și mecanice ale straturilor depuse, rezultând o omogenitate, duritate microstructurală și aderență superioare. În comparație, probele fără pulberi încărcate electric prezintă o structură neomogenă și o calitate a interfeței inferioare.

Tot în acest capitol este prezentată influența utilizării unui gaz de protecție (Ar) pentru reducerea oxidării în timpul procesului de depunere, conducând la o scădere semnificativă a rezistivității electrice a stratului depus. Această îmbunătățire a conductivității electrice optimizează performanța materialului în aplicații care necesită straturi conductoare cu rezistență scăzută, evidențiind importanța controlului precis al atmosferei de argon pentru a menține integritatea materialului și a spori funcționalitatea acestuia.

Sunt redate de asemenea două aplicații ale utilizării tratamentelor termice solare pe două tipuri de pulberi cupru – aluminiu – fier și cupru – nichel depuse prin pulverizare termică, obținându-se o îmbunătățire a omogenității și interfeței cu substratul. Procesul de tratament termic a favorizat formarea compușilor intermetalici, ceea ce a dus la creșterea durității și rezistenței la uzură.

O alta aplicație a straturilor depuse prin pulverizare termică este utilizarea lor în procesul de fotocataliză datorită capacității lor de a îmbunătăți performanța proceselor de purificare a apelor și aerului. Prin aplicarea unor straturi metalice sau compozite metalice pe substraturi, se poate crea o interfață eficientă pentru transferul de sarcini și reducerea recombinării electronilor și a golurilor, ceea ce duce la creșterea activității fotocatalitice. De asemenea, aceste straturi pot conferi stabilitate mecanică și chimică, prelungind durata de viață a sistemelor fotocatalitice. În plus, pulverizarea termică modifică proprietățile optice ale materialelor, sporind absorbția de lumină și eficiența utilizării energiei solare, fiind esențială în dezvoltarea unor tehnologii eficiente pentru tratarea apelor uzate și reducerea poluării atmosferice.

Este redat un studiu al influenței vitezei de depunere cu fascicul laser, astfel vitezele mari (90 mm/s) duc la îmbunătățirea durității straturilor depuse datorită obținerii unei diluții reduse dar ridică semne de întrebare cu privire la expunerea profesională la emisiile metalice în timpul procesului.

Planurile de dezvoltare ale carierei academice pe plan didactic și de cercetare sunt detaliate în secțiunea B3 a tezei de abilitare. Referitor la direcțiile de cercetare viitoare, acestea includ:

- optimizarea parametrilor tehnologici pentru pulverizarea cu flacără și pulberi pe bază NiCrAlX pentru a obține straturi rezistente la coroziune;
- optimizarea parametrilor tehnologici pentru pulverizarea cu flacără și pulberi biocompatibile (bioxid de zirconiu, bioxid de aluminiu, bioxid de calciu);
- utilizarea fasciculului laser pentru fuzionarea straturilor depuse prin pulverizarea cu flacără și pulberi;
- extinderea aplicațiilor straturilor depuse în mediu de gaz protector pentru reducerea greutății structurilor, îmbunătățirea rezistenței la coroziune și a performanțelor termice.

Activitatea mea de cercetare până în prezent s-a materializat prin publicarea a 50 de articole cu factor de impact (indexate de Clarivate Analytics Web of Science) și a 12 articole în proceedings ISI. Am fost director de proiect pentru patru granturi de cercetare, iar vizibilitatea cercetărilor este reflectată de către indicele Hirsch 12 conform Clarivate și Scopus.

(B) Scientific and professional achievements and the evolution and development plans for career development

This section outlines my professional trajectory and key achievements since obtaining my doctoral degree, underscoring my contributions to the field of Industrial Engineering, particularly in thermal spaying engineering and innovative restoration technologies. My career since 2005 has been dedicated to not only advancing fundamental knowledge but also to developing practical, industrially relevant solutions through research, teaching, and academic leadership, all of which form the foundation for my habilitation in Industrial Engineering

(B1) Professional achievements

I am a graduate of the Faculty of Materials Science and Engineering, with a specialization in Materials Engineering and Welding (2005), and was distinguished as the top graduate, standing out through exceptional academic results and research potential.

My doctoral studies (2005–2009), conducted within the Department of Materials Engineering and Welding at the Faculty of Materials Science and Engineering of Transilvania University of Brașov, had as a primary objective the optimization of metallic material restoration techniques through advanced flame and powder spraying processes, applying electromechanical and electromagnetic technologies to achieve deposited layers with superior mechanical and physical properties. The research carried out during this period was disseminated through publications indexed in prestigious international databases such as Clarivate Analytics (ISI), as well as through active participation with scientific communications at international specialized conferences, contributing to the advancement of knowledge in the fields of material restoration and welding.

After completing my doctoral studies, I obtained a postdoctoral fellowship (POSDRU) for a period of three years (2010–2013), during which I deepened and extended the results of my previous research. In this phase, I explored and developed innovative thin-film deposition technologies utilizing electric fields in direct current (DC), alternating current (AC), and high-frequency regimes, aiming to produce coatings with enhanced mechanical resistance, microhardness, and microstructural homogeneity. By charging powders with electrical charges in environments with varied electric fields, I achieved deposits with superior adhesion and improved mechanical performance, reducing restrictive sample preparation conditions and increasing the reliability of the restoration process.

From a didactic and managerial perspective, I held responsibilities for coordinating teaching and research activities at Transilvania University of Brașov from 2006 to 2013, being involved in studies concerning materials, restoration technologies, and welding. Between 2012 and 2019, I served as a senior scientific researcher (Grade III), actively participating in national and international consortia within multidisciplinary research projects. In this capacity, I coordinated laboratory activities,

seminars, and research projects, as well as supervised bachelor's and master's theses, contributing to the professional development of young specialists and the dissemination of scientific results within the academic environment.

In 2019, I was appointed Associate Professor in the field of industrial engineering at the Faculty of Materials Science and Engineering of Transilvania University of Brașov. In this role, I am responsible for teaching courses such as Materials Science and Technology, Design and Certification of Welded Structures, Standardization of Welded Structures, Finite Element Analysis, and Systematic Manufacturing of Welded Structures, contributing to the training and specialization of engineers in the domain, as well as advancing research in these areas of expertise.

The accumulated experience in fundamental and applied research, along with my teaching and managerial activities, provides a solid foundation for the development and promotion of cutting-edge scientific projects in industrial engineering, as well as for training competent specialists capable of contributing to national and international scientific-technological progress (22 undergraduate students and 15 master's students).

My ability to attract research funding and organize independent research activities is evidenced by successful acquisition of fellowships and research grants as a coordinator, including four international grants and a postdoctoral fellowship. As project director, I coordinated four international projects within the SFERA I-III program (Solar Facilities for the European Research Area), which highlight my leadership skills and expertise in applied scientific research:

1. Improvement of corrosion and thermal resistance by thermal cladding of Ni-based coatings on copper – SFERA I (No. P13042900040299 – 2013, Spain);
2. Mechanical properties enhancement of Cu10Al laser cladded onto aluminum – SFERA II (No. P1404300061 – 2014, Italy);
3. Improvement of corrosion resistance of electrical contacts (No. P1404300066 – SFERA II, Spain);
4. Corrosion resistance of NiCrAlX-coated materials in molten NaNO3/KNO3 salt mixture – SFERA III (No. P1404300061 – 2022, Italy).

At the same time, my role as a team member in research was demonstrated through my participation in numerous projects funded by both national and international agencies, highlighting the diversity of research and the practical applications of scientific results. These include:

1. Studies concerning real-time monitoring of laser welding/cutting processes and new methods for cutting metallic waste (Third-party project with the EU private sector, 2015–2018, Netherlands), coordinated by Prof. Mircea Horia Țierean from Transilvania University of Brașov;
2. Innovative solutions for mold design for small series and unique casting using autoforming techniques - AUTOFORMODEL (Contract PN II No. 72-203, 2008–2011);
3. Innovative amorphous materials for special industrial brazing applications - NOVABRAZ (Contract CEEX No. 221, 2006–2008);

4. Advanced modular technology for manufacturing tools for plastic deformation - ELMOD (Contract PN II No. 71-039, 2007–2009);
5. Multilayer electrodes for resistance welding in spot and seam configurations - ELSUD (Contract PN II No. 71-066, 2008–2010);
6. Deposition technology via hybrid laser-MIG welding with powders - LASERDEP (Contract PN II No. 72-216, 2008–2010);
7. High-performance materials and technologies for manufacturing asphalt cutting tools - MATFREZ (Contract PN II No. 188, 2012–2015);
8. Pulverization-based formation of composite electrodes used for hard deposits and spot welding - PULVER (Contract PN II No. 57, 2007–2009);
9. Study of corrosion and wear behavior of NiCrBSi coatings produced by laser cladding within a SFERA II-type project (2018, Italy), coordinated by Prof. Elena Manuela Stanciu from Transilvania University of Brașov.

The impact of my research is reflected in a robust record of scientific dissemination. I have authored/co-authored 49 papers indexed in Web of Science (WoS) ISI, with a significant contribution as principal or co-principal author on 20 of these publications.

This portfolio has received 311 citations in Clarivate Analytics ISI WoS and Scopus databases, leading to an h-index of 12 (WoS) and 11 (Scopus), showing the importance and impact of my research in the international scientific community. My participation in the peer-review process for well-known journals such as Materials Today Communications, Materials, Applied Surface Science, Coatings, Journal of Materials Science, Materials & Design, and Sensors since 2012 also shows my commitment to maintaining scientific standards and quality in the field.

Since 2012, I have been a member of the Council of the Department of Materials Engineering and Welding at the Faculty of Materials Science and Engineering, actively participating in promoting undergraduate and master's study programs, as well as in the Faculty's Admission Committee. Starting from 2024, I coordinate the study program in Advanced Materials Welding Engineering and am part of the committee responsible for evaluation and quality assurance within the Department of Materials Engineering and Welding.

Between 2021 and 2023, I held the position of Vice Dean for Scientific Research and Informatics, and from 2024 onward, I serve as Vice Dean with responsibilities for student activities and strengthening links with the economic and socio-cultural environment within the Faculty of Materials Science and Engineering.

An excerpt regarding the fulfillment of criteria established by the National Council for Titles, Diplomas, and Certifications (CNATDCU) for the field of Industrial Engineering and Management, according to Annex 16 of the Order of the Ministry of Education and Scientific Research No. 6129/20.12.2016, is presented in the table below. All minimum standards and minimum scores for each category have been met and exceeded, reflecting the high level of my performance and commitment in the fields of research and scientific education.

<table>
<tr><td colspan="3">MINIMUM CRITERIA</td><td>Minimum requested</td><td>Accomplished</td></tr>
<tr><td colspan="3">A1. Teaching & training</td><td>130</td><td>160.23</td></tr>
<tr><td colspan="3">A2. Research</td><td>300</td><td>669.52</td></tr>
<tr><td colspan="3">A3. Recognition & impact of research activity</td><td>100</td><td>571.58</td></tr>
<tr><td colspan="3">MANDATORY MINIMUM TERMS SUBCATEGORIES</td><td>Minimum requested</td><td>Accomplished</td></tr>
<tr><td colspan="3">A.1.1.1. Books / chapters in engineering as author (first author)</td><td>2</td><td>3</td></tr>
<tr><td colspan="3">A.1.1.2. Didactic textbook, laboratory guidance / applications (first author)</td><td>4 (2)</td><td>4 (4)</td></tr>
<tr><td colspan="5">A.2.1. Articles in ISI Thomson Reuters journals & proceedings</td></tr>
<tr><td rowspan="4">of which</td><td colspan="2">Minimum 8 articles in ISI Thomson Reuters journals and proceedings – from the last promotion (2019)</td><td>8</td><td>17</td></tr>
<tr><td rowspan="3">of which</td><td>in ISI Thomson Reuters journals</td><td>3</td><td>17</td></tr>
<tr><td>as first author in ISI Thomson Reuters journals</td><td>3</td><td>9</td></tr>
<tr><td>in a Q1 or Q2 rated journal</td><td>1</td><td>13</td></tr>
<tr><td colspan="3">A.2.2. Articles in journals and volumes of scientific events indexed in international databases - from the last promotion (2019)</td><td>8</td><td>9</td></tr>
<tr><td colspan="5">A.2.5 Research grants (obtained by competition)</td></tr>
<tr><td colspan="2" rowspan="2">A.2.5.1 As director/responsible</td><td>International grant</td><td rowspan="2">2</td><td>4 director</td></tr>
<tr><td>National grant</td><td>-</td></tr>
<tr><td colspan="2" rowspan="2">A.2.5.2 As member/participant</td><td>International grant</td><td>-</td><td>7</td></tr>
<tr><td>National grant</td><td>-</td><td>2</td></tr>
</table>

(B2) Scientific achievements

Chapter 1. Thermal spraying technologies in industrial engineering

Inorganic coatings constitute approximately 53% of the total, fabricated via physico-chemical or metallurgical techniques such as physical vapor deposition (PVD), chemical vapor deposition (CVD), sol-gel processing, and so on (Lazar et al., 2010; Nikkanen et al., 2015; Wu et al., 2009). Especially physico-chemical methods provide precise control over coating thickness, composition, and morphology, thereby enabling targeted modification of properties to meet specific application requirements (Figure 1.1).

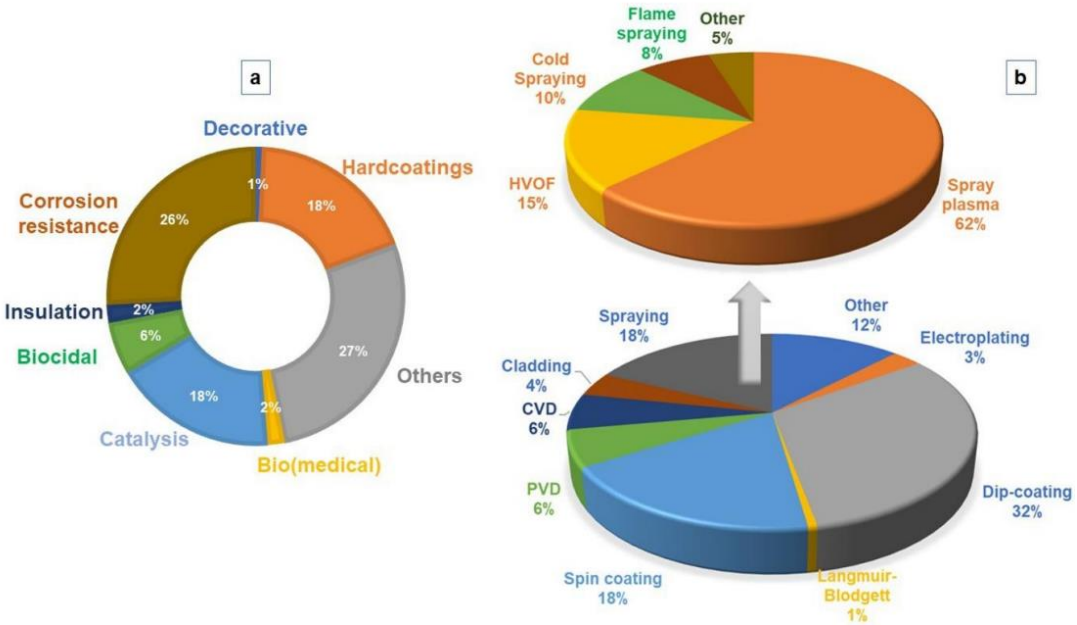

Figure 1.1 (a) coatings application domains and (b) frequently employed fabrication methods for inorganic coatings (Roata et al., 2019).

Thermal spraying encompasses a versatile group of coating processes that are integral to modern industrial engineering, offering solutions for enhancing surface properties, restoring components, and enabling advanced functionalities (Sivakumar et al., 2018; Szymański et al., 2015). These techniques, which involve the deposition of molten or semi-molten materials onto a substrate, provide critical advantages in terms of wear resistance, corrosion protection, thermal insulation, and the creation of specialized surfaces such as photocatalytic coatings (Brupbacher et al., 2018; Heimann, 2006; Jing et al., 2018; Karthikayan et al., 2017; Košević et al., 2019; Marcano et al., 2017; Vaßen et al., 2010). This chapter lays the groundwork for understanding the specific advancements and applications explored in this habilitation thesis. It will begin by outlining the fundamental principles common to thermal spray processes and their historical evolution. Subsequently, it will outline the distinct characteristics, operational parameters, and key industrial application domains of major thermal spraying techniques, with a particular emphasis on those

pertinent to the original research presented herein, including flame spraying (Bolelli et al., 2009; G. J. Yang et al., 2005), HVOF hi(Krieg et al., 2017), plasma spraying (Karthikeyan et al., 1997; Vardelle et al., 2015a), cold spraying (Yamada et al., 2010; G. J. Yang et al., 2008), electric arc spraying (Wang et al., 2023), and laser cladding (Nowotny et al., 2014). A significant focus will be placed on the current state of research and emerging trends, particularly concerning the development of functional coatings and the optimization challenges that this thesis aims to address.

The genesis of thermal spraying dates to the late 19th and early 20th centuries, with pioneering work by figures like M. U. Schoop. Initial developments focused on atomizing molten metals (as illustrated in early prototypes, Figure 1.2), leading to the first stationary metal spraying facility around 1910 (Figure 1.3). Subsequent decades saw crucial advancements from basic flame and arc spraying to more sophisticated techniques developed primarily for demanding sectors like aviation, including plasma spraying in the 1950s and High-Velocity Oxy-Fuel (HVOF) spraying in the 1980s. This evolution has continually expanded the range of materials that can be sprayed and the quality and functionality of the coatings achievable, making it a cornerstone technology in surface engineering.

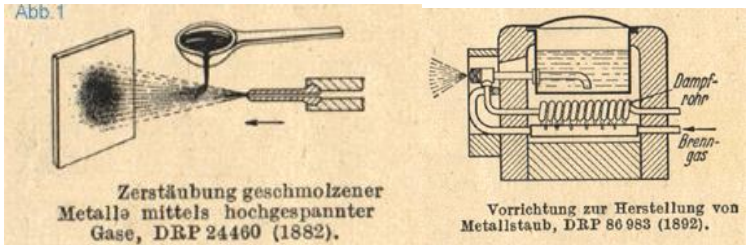

Figure 1.2 First prototype

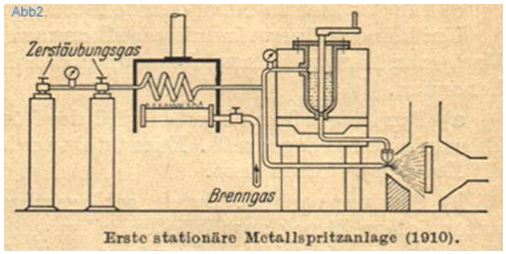

Figure 1.3 Second prototype

The thermal spraying process involves rapid deposition of flame- or plasma-heated feedstock materials (powder, wire, rod, liquid) onto a substrate surface (Vardelle et al., 2015b). The molten or partially molten feedstock, known as "splat", undergoes high-velocity impact, resulting in a lamellar-layered coating morphology upon solidification. Traditional coatings range from 10 µm to several millimeters thick, but HVOF and plasma spraying can achieve thicknesses as low as 200-500 nm (Fauchais et al., 2010; Feitosa et al., 2018).

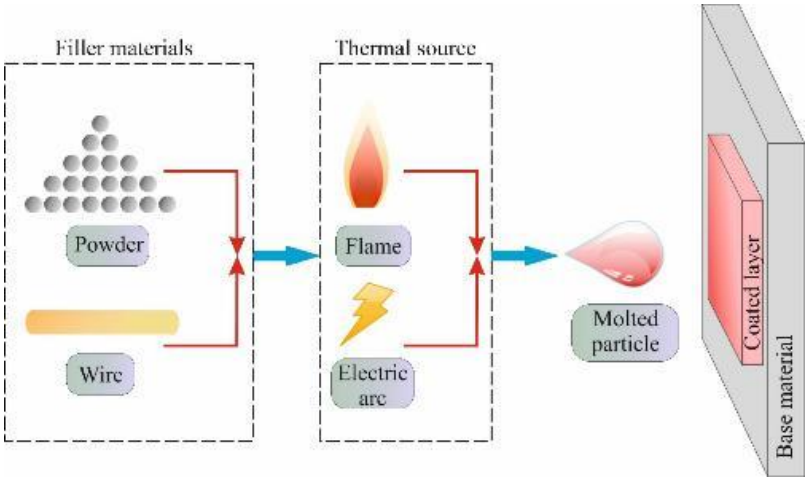

Figure 1.4 Principle of thermal spray processes (Roata, 2018b).

Various thermal spray processes have been developed, each with unique energy sources, particle velocities, and deposition environments, making them suitable for specific material-substrate combinations and application requirements. The following sections briefly introduce the key techniques relevant to the scope of this thesis

1.1 Flame spraying

Flame spraying employs combustion of fuel gases (e.g., acetylene) to melt feedstock materials (powders or wires), which are propelled onto substrates. While cost effective for repairs and corrosion resistant coatings, traditional flame spraying suffers from oxidation and inhomogeneous particle melting. Recent advancements, such as electric field assisted deposition (Section 3.1), mitigate these issues by enhancing particle adhesion and reducing porosity (Melentiev et al., 2022; Vuoristo, 2014). The versatility of flame spraying extends across applications in materials science, biomedical engineering, energy storage, manufacturing, and environmental remediation. Recent studies demonstrate the successful development of photocatalytic coatings, including titania films with UV degradation capacity, rutile-rich nanostructures doped with metals for enhanced activity, and porous anatase-preserving layers (Berger, 2014; Mohanty & Roy, 2012).

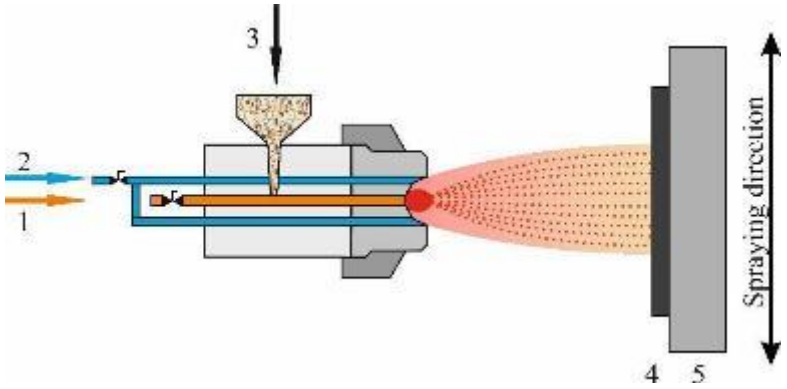

Figure 1.5 Schematic diagram of powder flame spraying. 1: fuel gas; 2: oxygen; 3: filler material (powder) and carrier gas; 4: spray deposit; 5: base material (Roata, 2018b).

Additionally, composites such as hydroxyapatite combined with reduced graphene oxide exhibit improved photocatalytic performance, highlighting the promise of flame spraying techniques in advancing functional coatings for environmental and energy-related applications.

1.2 High velocity oxy fuel (HVOF) spraying

HVOF utilizes supersonic gas velocities to deposit dense, low porosity coatings (e.g., WC-Co, TiO_2). Its application in photocatalytic coatings (Toma et al., 2008) is limited by anatase to rutile phase transitions. This thesis explores aluminum doping (Section 3.2) to stabilize anatase phases, improving UV driven pollutant degradation through more economically efficient deposition thermal spraying techniques.

High velocity oxy fuel (HVOF) thermal spraying is a precise technique that accelerates feedstock particles to create strong, durable coatings at low temperatures, reducing oxidation. While its use for thick, hydrophilic TiO_2 coatings aimed at removing organic pollutants is still emerging, research shows promising results (Bolelli et al., 2009). These coatings, especially when doped or optimized, exhibit high anatase content and surface areas that enhance photocatalytic degradation of pollutants like nitrogen oxides, ethanol, and acetone (Roata et al., 2019).

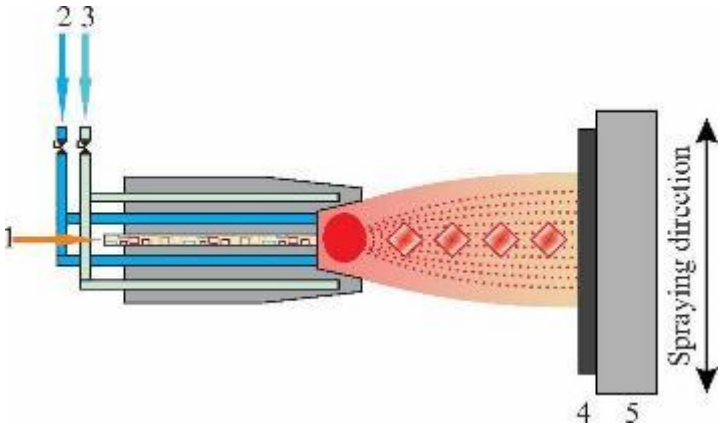

Figure 1.6 Principle of high velocity and fuel gas flame spraying. 1: filler material (powder) and carrier gas; 2: oxygen or air fuel; 3: cooling system (water or air); 4: spray deposit; 5: base material(Roata, 2018b).

HVOF is widely used across industries: in aerospace to improve thermal and corrosion resistance; in energy to enhance efficiency and safety; in manufacturing for wear-resistant coatings; and in biomedicine for durable, biocompatible surfaces. Its versatility and ability to produce high quality coatings make it crucial for extending component lifespans and improving performance.

Recent studies highlight the potential of HVOF produced TiO_2 coatings for environmental cleanup, with doping and process optimization further boosting their photocatalytic activity. Continued research is needed to refine coating parameters and doping strategies to maximize their effectiveness in pollution control and air purification applications (Pala et al., 2017).

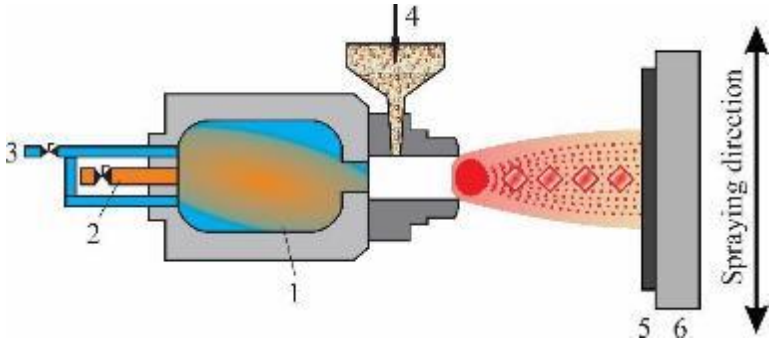

Figure 1.7 Principle of high velocity liquid/suspension fuel flame spraying. 1: combustion chamber; 2: liquid fuel; 3: oxygen/air; 4: suspension/solution and carrier gas; 5: coating; 6: base material (Roata, 2018b).

1.3 Plasma spraying

Plasma spraying, operating at temperatures exceeding 10,000°C, excels in depositing refractory ceramics (e.g., ZrO_2) (Faisal et al., 2025; Hebbale et al., 2025). However, micrometer scale splat morphology restricts surface area. Innovations like aqueous suspension feedstock (Section 4.3) enable nanostructured coatings with enhanced catalytic activity.

Comparative Overview

Process	Key Advantages	Limitations	Industrial Applications
Flame Spraying	Low cost, versatility	High oxidation	Corrosion protection, repairs
HVOF	High density, hardness	Phase instability	Wear-resistant coatings
Plasma Spraying	Refractory compatibility	Limited surface area	Thermal barriers, biomedical

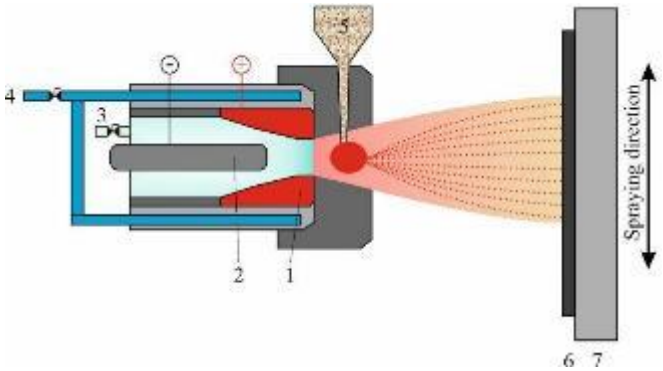

Figure 1.8 Schematic diagram of air plasma jet spraying unit. 1: anode; 2: cathode (electrode); 3: plasma gas; 4: cooling system; 5: filler material (powder) and carrier gas; 6: spray deposit; 7: base material (Roata, 2018b).

Plasma thermal spraying employs a high temperature plasma jet generated by DC or RF discharges to deposit refractory ceramics and alloys at velocities of 200-300 m/s. This process allows for the processing of diverse materials, including difficult to melt substances, using feedstocks like powders, liquids, and suspensions.

The resulting ceramic coatings are porous, which enhances photocatalytic activity by increasing surface area, although their micrometer sized splats limit surface area compared to other methods like flame spraying. Widely utilized in industries such as aerospace, energy, medical, automotive, and environmental sectors, plasma spraying improves thermal resistance, corrosion protection, wear

durability, and biocompatibility. Recent developments aim to optimize photocatalytic coatings with materials like TiO_2 and ZnO to better degrade pollutants and improve energy conversion, highlighting its potential for environmental remediation and sustainable energy solutions (Meghwal et al., 2020; Tomaszek et al., 2006).

1.4 Cold spraying

Cold spraying is an advanced, environmentally friendly coating technology that involves accelerating feedstock particles to high velocities (200-1500 m/s) at temperatures below their melting point using inert gases. This process relies on plastic deformation to bond particles to substrates, resulting in durable coatings with minimal oxidation. It is widely applied in industries such as aerospace (for turbine and heat shield components), energy (protecting heat exchangers and turbines), automotive (enhancing component durability), medical (creating biocompatible, wear-resistant coatings), and environmental sectors (corrosion resistance and pollution control).

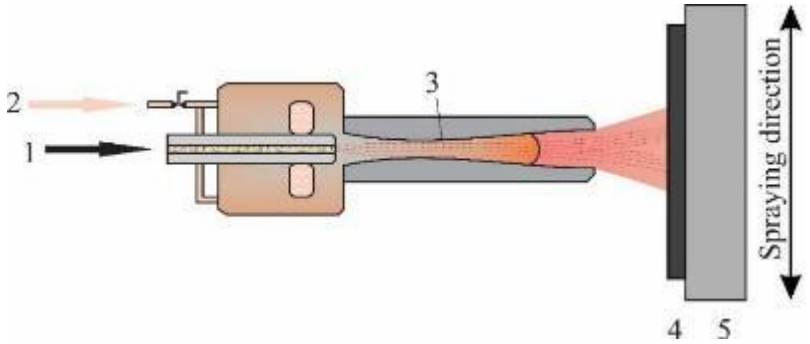

Figure 1.9 Principle of cold spraying. 1: filler material (powder) and carrier gas; 2: process gas; 3: Laval type nozzle; 4: thermal spray deposit; 5: base material (Roata, 2018b).

Research highlights that cold spraying produces high quality photocatalytic coatings like TiO_2, effective for pollutant degradation and energy applications such as solar cells and fuel cells. Innovations like vacuum and composite coatings further improve adhesion and activity, opening avenues for environmental remediation and sustainable energy solutions (Yamada et al., 2010; G. J. Yang et al., 2008). Overall, cold spraying offers environmentally friendly, durable, and high-performance coatings across multiple fields.

1.5 Electric arc spraying

Electric arc metallization is a versatile coating process that employs the thermal energy generated by an electric arc to melt and deposit metal particles onto substrates. The technique can utilize either direct current (DC) or alternating current (AC) as the power source, with distinct implications for coating quality. DC-driven arcs are characterized by higher stability, temperature, and velocity, resulting in finer, denser metal particles, improved coating morphology, reduced porosity, and enhanced mechanical properties. Conversely, AC-driven arcs tend to be unstable,

producing coarser particles with larger grains, increased porosity, and diminished mechanical integrity, alongside a higher propensity for delamination(Rakhadilov et al., 2024; Riastuti et al., n.d.).

The process involves forming an electric arc between electrodes and the substrate, creating a high temperature plasma that melts metallizing wires, commonly steel or non-ferrous alloys, and deposits material onto surfaces. Material composition and microstructure are optimized through alloying and precise regulation of process parameters such as arc current, voltage, wire feed rate, and substrate temperature to ensure high quality coatings (Zurecki et al., 1997).

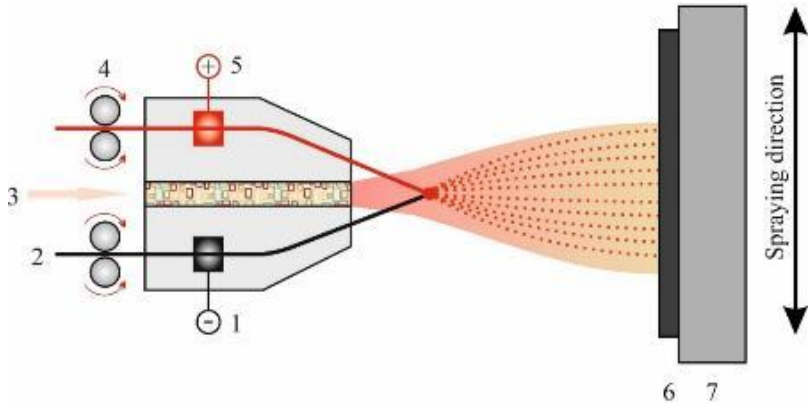

Figure 1.10 Schematic diagram of electric arc spraying unit
1 – negative voltage; 2 – filler material (wire); 3 – spray gas; 4 – wire feed device; 5 – positive voltage; 6 – spray deposit; 7 – base material (Roata, 2018b).

This technique is extensively employed across various industries, including aerospace, automotive, medical, construction, food processing, chemical manufacturing, and nuclear power, primarily for corrosion resistance, wear enhancement, and thermal efficiency improvements. Its advantages include precise control over coating properties, high deposition rates, and minimal thermal damage to substrates, making electric arc metallization an effective and adaptable coating technology.

1.6 Laser cladding

Laser cladding is a surface modification technique aimed at depositing metallic layers with minimal dilution, primarily on cost effective substrates. This process enhances surface properties such as wear and corrosion resistance, thereby increasing the service life and durability of the treated components (Nowotny et al., 2014). The method is categorized into two distinct processes based on powder feed mechanisms:

1. Two-step laser cladding: This involves the sequential application of powder to the substrate surface followed by melting and adherence through laser irradiation (Figure 1.11);

2. One-step laser cladding: In this approach, both the deposition of the filler material and its melting occur simultaneously in a single process, often utilizing paste forms of filler materials with binders that decompose under laser action to facilitate melting without impeding layer formation (Figure 1.12).

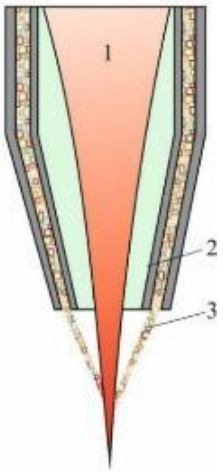

Figure 1.11 Principle of two step laser cladding: 1- laser beam; 2- protective gas; 3- filler materials and carrier gas (Roata, 2018b).

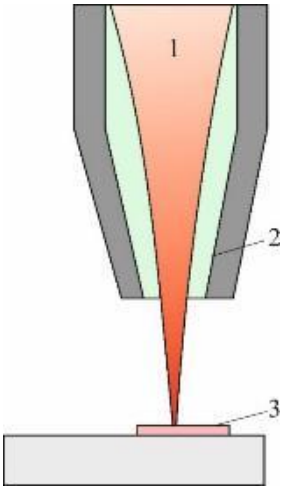

Figure 1.12 Principle of one step laser cladding: 1 – laser beam; 2 – protective gas; 3 – preplaced filler material (Roata, 2018b).

1.7 Literature review and research gaps

The evolution of thermal spraying technologies has been driven by industrial demands for high-performance coatings, yet significant challenges persist in oxidation control, phase stability, and scalability. This section synthesizes advancements in the field, emphasizing both global and Romanian contributions, while identifying unresolved gaps that motivate the original methodologies developed in this work.

Oxidation control in thermal spraying

In thermal spraying, oxidation has a profound influence on the phase composition, microstructure, and overall properties of the resulting coatings. Oxidation can occur during multiple stages of the process, from the in-flight motion of powder particles to the moment when the molten splats solidify in an oxygen rich atmosphere. This uncontrolled exposure leads to the formation of brittle phases that compromise the mechanical integrity of the coatings. For example, in Fe based amorphous coatings, the intersplat regions are particularly susceptible to oxidation, creating localized zones where brittle phases develop, jeopardizing the durability of the system (Mahrukh et al., 2025; Shahbazi et al., 2025).

The challenge of oxidation is especially critical when thermal spraying reactive metals such as aluminum and titanium. Traditional mitigation techniques, like inert gas shielding, are effective in reducing oxidation; however, they come with significant operational costs due to the continuous consumption of gases such as argon or nitrogen. While cold spraying offers an attractive alternative, minimizing oxidation by accelerating particles below their melting point, it has proven most effective for materials like copper and aluminum alloys. Its applicability to high melting point materials such

as steel remains limited, due to adhesion issues that arise when the substrate cannot sufficiently bond with the cold sprayed particles.

Beyond these conventional approaches, reactive plasma spraying has emerged as a method for synthesizing in situ oxides, such as alumina-titania composites. Although this technique can tailor the oxide formation, it often leads to phase inhomogeneity, thus challenging the reproducibility and reliability of the coatings. In contrast, **my work** advances the field by introducing electric field assisted deposition (EFAD). By meticulously optimizing direct current (DC) parameters and integrating argon shielding, EFAD succeeds in striking an effective balance between oxidation suppression and mechanical performance. This integrated approach not only achieves high coating adhesion but also reduces oxide content by approximately 40%, demonstrating a significant improvement over existing methods that are either cost prohibitive or mechanically inadequate (S. Li et al., 2025; Sirjani et al., 2025).

Overall, controlling oxidation in thermal spraying is a multifaceted challenge that directly impacts the performance and reliability of protective coatings. The innovative strategies presented here, coupling electric field-assisted deposition with optimized gas shielding, provide a pathway to overcome these limitations. This progress not only enhances coating integrity and durability but also paves the way for more cost effective and scalable deposition processes for a wide range of industrial applications (Kumar et al., 2025).

Phase stability of functional coatings

The phase stability of functional coatings in thermal spraying is paramount to guaranteeing their reliable performance under demanding operational conditions. For instance, in functionally graded coatings, the outer ceramic layer, often composed of alumina, is chosen for its high phase stability and low thermal conductivity, ensuring the coating maintains its structure and properties even under sustained high temperature exposure. However, inherent challenges arise when the phase transformation of alumina compromises its electrical properties, potentially limiting the functionality of thermally sprayed coatings in applications where electrical performance is critical.
The selection of the thermal spray process significantly influences phase stability. Processes like cold spraying operate at relatively low temperatures compared to traditional techniques, thereby reducing oxidation and mitigating unwanted phase transformations. This attribute is particularly advantageous for materials that are inherently sensitive to high thermal loads, as the preservation of the desired phase is essential for maintaining long term coating performance (Jariya et al., 2021; Pshyk et al., 2016).

Titanium dioxide (TiO_2) coatings present another critical example of phase dependent functionality, especially regarding photocatalytic activity. Maintaining the nanostructured anatase metastable phase in TiO_2 is crucial; research has demonstrated that cold gas spray methods can effectively prevent the loss of this phase. Although doping TiO_2 with elements such as aluminum or silicon has been shown to stabilize the anatase phase further, such interventions often come at the

expense of surface area and reactivity, key parameters that drive the material's photocatalytic efficiency (Croitoru et al., 2020).

In parallel, innovations like laser remelting have achieved noteworthy improvements in crystallinity within TiO_2 coatings, reaching up to 85% retention of the anatase phase. Despite this promising outcome, these methods tend to be energy intensive and are often incompatible with the requirements of large scale production, thus limiting their industrial application.

The complexities extend to other material systems as well, such as tungsten carbide-cobalt (WC-Co) coatings. Here, researchers have explored multi layered coating strategies to alleviate phase-induced stresses; however, interfacial delamination remains a persistent challenge that undermines the overall integrity of the coating system (Gardon & Guilemany, 2014).

Addressing these limitations, this thesis introduces an innovative approach through the use of solar annealing, a novel post-treatment method designed to stabilize the anatase phase in TiO_2 coatings while preserving the essential surface morphology. Complementary to this approach is the development of optimized feedstock powder designs, which have demonstrated the ability not only to retain the desirable anatase phase in TiO_2 but also to enhance coating hardness by an impressive 34–48% compared to the base materials. This dual achievement effectively bridges the gap between phase stability and functional performance, offering a reproducible, energy efficient, and scalable solution suitable for industrial applications (Croitoru et al., 2020; Y. Li et al., 2024).

By systematically tackling issues such as oxidation, phase transformation, and interfacial stresses, the research outlined in this thesis paves the way for improved thermal sprayed coatings that meet both functional and economic demands. These advances promise enhanced durability and performance across a range of applications, from photocatalytic surfaces to wear resistant components, thereby fostering broader industrial adoption and setting the stage for future innovations in thermal spray technology.

Scalability and industrial adoption

Transitioning innovative coatings from the laboratory to full-scale industrial applications presents formidable challenges due to both prohibitive costs and intricate technical requirements. For instance, while vacuum plasma spraying (VPS) consistently delivers high purity coatings, its reliance on expensive vacuum chambers and highly skilled operators significantly hinders its economic and practical adoption. Moreover, the lack of standardized protocols, especially when integrating disparate processes like laser cladding with thermal spray, further complicates efforts to achieve reliable, large scale production.

This thesis confronts these challenges head on with two major contributions. The first is the introduction of a low cost solar post treatment process that supplants traditional furnace annealing with solar energy. Backed by SFERA project data, this innovative technique reduces operational costs by roughly 60%. Industrial validation comes from its application to NiCrAlY coatings, where the performance achieved is comparable to VPS, yet the overall cost is reduced by 30%. This

breakthrough not only exemplifies the potential for cost savings but also paves the way for more sustainable industrial practices (Roata et al., 2023).

The second major contribution is an optimized hybrid process that merges flame spraying with laser cladding, specifically engineered for WC-Co coatings. Through this innovative method, a coating density of 90%, as determined by meticulous micrography image analysis, is achieved, alongside wear resistance that meets the rigorous standards of high velocity oxy fuel (HVOF) techniques. This tailored approach not only enhances performance but also broadens the applicability of thermal spray processes in demanding industrial contexts.

Beyond these targeted innovations, the thesis delves into broader challenges inherent in thermal spraying. A primary issue is the non-linear relationship between process parameters and coating properties, complicating the accurate prediction and control of outcomes. Implementing robust parameter optimization methods, such as design of experiments (DoE), could mitigate this complexity by systematically dissecting interrelated effects. Additional economic barriers, stemming from significant investment and operational costs in techniques like low-pressure plasma spray (LPPS) or VPS, further constrain the adoption of these processes, even though processes yielding lower residual porosity (often achieved through high velocity spraying) do not always equate to higher economic feasibility.

The scalability of thermal spray processes is also often limited by operational constraints, such as the necessity for specialized spray atmospheres (e.g., inert gas shrouds or low-pressure environments) that inherently restrict broader application. Even processes like cold spraying, often viewed as an exception, demand precise control over particle velocities and temperatures to produce high quality coatings consistently. Furthermore, limitations in the maximum achievable coating thickness restrict the versatility of some techniques, showing the need for process specific adaptations (Roata, 2017b, 2018b).

Collectively, these challenges underline the critical need for a multifaceted approach to advance thermal spray technology. By tackling issues ranging from oxidation and phase stability to scalability and parameter optimization, this thesis lays out a comprehensive roadmap for future industrial applications. Innovations such as energy flexible deposition (EFAD), solar annealing, and DoE driven parameter tuning not only demonstrate reproducible and cost effective solutions but also possess direct relevance to key industries including aerospace, energy, and environmental management. This integrated strategy thus represents a significant step toward overcoming bottlenecks that have long hindered the transition from laboratory innovation to industrial production.

Chapter 2. Critical process parameters in powder flame spraying: influence, optimization, and impact on coating quality

The successful application of flame spraying with powder for creating high-performance industrial coatings, as detailed in the experimental investigations presented in Chapter 3, hinges on a profound understanding and meticulous control of numerous process parameters. While Chapter 1 provided an overview of thermal spraying technologies, this chapter delves specifically into the critical parameters governing the powder flame spraying process. It aims to provide not only a theoretical understanding of how each parameter influences the deposition mechanism and coating characteristics but also to establish the direct relevance of these parameters to my original research contributions. The discussions herein will frequently bridge to the specific material systems, parameter optimizations, and novel outcomes I achieved in the application-focused studies detailed in Chapter 3, thereby illustrating the practical implications of mastering these variables.

2.1 Flame temperature

In flame spraying, the flame temperature significantly influences the properties of the coating. Higher flame temperatures can lead to better melting and atomization of the coating materials, resulting in improved coating quality. However, excessively high temperatures can also cause issues such as increased oxide content and reduced bond strength due to overheating of the substrate or coating materials (Marinou et al., 2015; Xanthopoulou et al., 2014).

The typical oxyacetylene flame temperature for flame spraying processes ranges from around 3000°C, which affects the adhesion, oxide content, porosity, and spray rate of the coating.

Adjusting the flame temperature allows for control over the level of porosity, bond strength, and oxide content in the coating, enabling the creation of coatings suitable for various applications (Lei et al., 2007).

The temperature of the flame should be adequate to melt the powder material without excessive oxidation. Typical flame temperatures can vary widely, e.g., oxy-acetylene flames it typically ranges from about 3,000 °C to 3,500 °C(Arboleda et al., 2018; Martínez-García et al., 2024).

The challenge of achieving optimal flame conditions for diverse powder chemistries, from metallic alloys like AlMoNi (Section 3.1) to specialized photocatalytic precursors such as metallic Titanium (Section 3.8), was a key consideration in my experimental designs in Chapter 3.

2.2 Oxygen and acetylene ratios

In flame spraying, the oxygen/acetylene ratio significantly influences the coating properties. For instance, when spraying with acetylene, the oxygen content in the coatings can be reduced from 5.5 to 1.5 mass % by increasing the nitrogen flow rate from 500 to 1000 slm, and further to 0.22 mass % at 2000 slm. This reduction in oxygen content is due to the lower flame temperature, which is

crucial for controlling oxidation in materials like titanium, which is highly reactive with oxygen (Kuchumova et al., 2020).

Moreover, acetylene is commonly used for spraying higher melting point materials such as steel, nichrome, and molybdenum. By adjusting the ratio of gas to oxygen, different coating properties can be achieved. For example, molybdenum coatings can be applied as either a soft, strongly adherent bond coating or as a harder top coating.

The choice of gas also impacts the coating's final appearance. Some decorative coatings of copper and bronzes can have their final color appearance influenced by the spray parameters.

In warm spraying, a modification of high velocity oxy fuel spraying, the temperature of the combustion gas is lowered by mixing nitrogen with the combustion gas, which reduces oxidation and improves coating efficiency, particularly for materials that rapidly oxidize or deteriorate at high temperatures (Ando et al., 2009; Chen et al., 2020).

- The ratio of oxygen to acetylene affects the flame characteristics (neutral, oxidizing, or carburizing). The optimal ratio is often a neutral flame for most materials (typically around 1.6:1). Ratio adjusting can affect the melting efficiency and coating properties.

For oxy-acetylene flame spraying, a common approach is to start with the following ratios:

- Oxygen to acetylene ratio: Typically ranges from 1.5:1 to 2:1. However, a precise starting point might be around 1.6:1.

Here's a brief breakdown of how adjusting these ratios can affect the flame characteristics and thus the powder's spraying efficiency:

a. Higher oxygen levels (2:1 Ratio or More):
   - Characteristics: Produces a hotter and oxidizing flame.
   - Applications: Useful when a high temperature is necessary for melting the powder. However, it can also lead to excessive oxidation of the powder, which may affect the coating's quality.

b. Lower oxygen levels (1.5:1 Ratio):
   - Characteristics: Produces a reducing flame, which can help reduce oxidation of certain materials.
   - Applications: More suitable for coating materials sensitive to oxidation or when better transfer efficiency for the powder is needed.

c. Neutral flame ratio (Approx. 1.6:1):
   - Characteristics: Achieves a balance between oxygen and acetylene, which minimizes oxidation while providing sufficient heat.
   - Applications: Often recommended for most thermal spray applications, as it allows for controlled melting and minimization of powder degradation (Roata, 2018b).

My investigations into coatings like CuNi (Section 3.2) and NiCrBSiFe (Section 3.3) involved careful calibration of these gas ratios (typically O_2=4 bar, C_2H_2=0.7 bar, as detailed in Chapter 3) to ensure optimal melting and deposition while managing the oxidative potential, especially when combined with other variables like protective gas atmospheres.

2.3 Spray distance

In flame spraying, the spray distance significantly influences coating properties such as microhardness, fracture toughness, porosity, and roughness. For example, a study on warm spraying of fine WC-12Co powders found that altering the spray distance had a notable effect on these properties (Baumann et al., 2021). Additionally, the coating thickness is only marginally influenced by changes in the spray distance. In another study, the spray distance was fixed at 16 cm for producing a cermet composite material, and it was found that the flattening of particles could be influenced by the spray distance, with different usable distance ranges depending on the substrate material (Jagadeeswar et al., 2020). For instance, a higher spray distance can be used for glass substrates than for steel substrates. Typically, this distance is kept between 100 mm to 250 mm, but it may need to be adjusted based on the application and material (Jonda et al., 2024).

- Shorter distances (100 - 150 mm):
  - Can produce higher coating density and thickness.
  - Greater risk of substrate overheating or causing melting if is too close.
  - Application: Ideal for applications where high wear resistance is critical, such as for components subjected to high stress (e.g., in mining or drilling operations).
- Longer distances (150 - 250 mm):
  - May result in lower coating thickness and density, but provides a better distribution of the spray.
  - Reduces the risk of substrate damage.
  - Application: Works well for applications where a smoother finish is desired, such as in automotive or aerospace components, where lightweight coatings are preferred.

Factors influencing the choice of spray distance

a. Type of material: Certain materials may behave differently under specific distances. Testing is often necessary to determine the ideal setup based on the specific powders being used.
b. Flame stability: Ensure that the flame is stable and well-defined before spraying. A stable flame helps improve the melting efficiency of the particles before they reach the substrate.
c. Particle behavior: The distance affects how the particles travel and their temperatures upon impact. Too far may lead to insufficient melting, while too close may lead to splatter and aggregation.
d. Spray angle: Maintain a consistent angle (usually around 90 degrees to the substrate) to ensure uniform coating. This can also influence the effective spray distance (Roata, 2017b, 2018b).

The optimization of this distance is therefore not trivial and is often coupled with flame characteristics (Section 2.2) and powder properties (Sections 2.6, 2.7), presenting a complex challenge that was specifically addressed in several of the investigations detailed in Chapter 3. As

will be demonstrated in Chapter 3, my research systematically varied the spray distance for materials such as AlMoNi (100-200 mm, Section 3.1), Cu38Ni (100-200 mm, Section 3.2), and CuAlFe (150-200 mm, Section 3.5), to quantify its direct impact on coating microstructure, adhesion, and functional properties like electrical resistance and microhardness.

2.4 Coating thickness

Coating thickness in oxy-acetylene flame spraying is a crucial parameter that influences the performance, durability, and overall effectiveness of the coating applied to the substrate. Below is a detailed overview of the factors affecting coating thickness, typical thickness ranges, and methods of measurement, along with practical considerations for achieving the desired results (Long et al., 2020).

Coating thickness can vary significantly depending on the application, material, and specific parameters used during the spraying process. However, general guidelines for coating thickness are as follows:

- General coating thickness: 50 to 500 micrometers (0.05 to 0.5 mm).
- Common targets:
    - Wear-resistant coatings: 200 to 400 micrometers.
    - Corrosion-resistant coatings: 100 to 300 micrometers.
    - Repair applications (such as restoring worn surfaces): 300 to 500 micrometers.

Factors affecting coating thickness

a. Spray distance:
    - Closer spray distances tend to increase coating thickness, while farther distances can produce thinner coatings due to cooling and solidification before impact.
b. Feed rate:
    - The rate at which material powder is fed into the flame. Higher feed rates can produce thicker coatings, but may lead to increased porosity if not carefully managed.
c. Flame temperature and type:
    - A hotter flame can melt the powder more effectively and produce a denser coating, but excessive heat can cause oxidation and affect coating quality.
d. Spray angle:
    - The angle at which the spray is applied affects distribution. A perpendicular angle can create more uniform deposits, while angled sprays can lead to uneven thickness.
e. Substrate surface preparation:
    - The cleanliness and roughness of the substrate can influence adhesion and thickness. A rough surface can help mechanical bonding, potentially allowing for thicker coatings.
f. Coating material:

- Different materials have different melting points and flow characteristics, influencing achievable thickness. For example, materials like tungsten carbide may require more careful control than softer materials.

g. Passes and layering:
   - Depending on the application, multiple passes may be necessary to achieve the desired thickness. Each pass will build upon the previous layer, allowing for controlled thickness (Chandra et al., 2020; Lara & de Mello, 2012; Zha et al., 2017).

The experimental applications presented in Chapter 3 often target specific thickness ranges (e.g., the 50-500 micrometers generally noted, or more specific targets like the 115 ± 5 µm for Ti coatings in Section 3.8) relevant to their intended industrial use, requiring careful control of feed rate, traverse speed, and number of passes, informed by the principles discussed here

2.5 Substrate temperature

The substrate temperature during the oxy-acetylene flame spraying process is a critical parameter that can significantly influence the quality, adhesion, and performance of the applied coating. Here is a detailed overview of the ideal substrate temperature, factors affecting it, and techniques to measure and control it during the spraying process (Hao et al., 2024).

The ideal substrate temperature during oxy-acetylene flame spraying typically ranges from room temperature (approximately 20-25 °C) to around 100-150°C (Roata, 2017b, 2018b).

However, the optimal temperature can vary based on several factors, including:

a. Material type: Different substrates (metals, polymers, composites) can have varying tolerances and optimal temperatures.
   - Ferrous metals (e.g., steel) tend to perform well at higher substrate temperatures.
   - Non-ferrous metals (e.g., aluminum, titanium) may require lower temperatures to avoid distortion and oxidation.

b. Coating material: The thermal behavior and melting point of the coating material also dictate temperature choices.
   - For example, hard coatings like tungsten carbide may perform better with a higher substrate temperature to ensure good bonding without excessive oxidation.

c. Application requirements: Specific applications may dictate the required substrate properties post-coating.
   - For wear-resistant applications, slightly higher temperatures can enhance bonding characteristics (Arabgol et al., 2017; Khandanjou et al., 2018).

Factors affecting substrate temperature

a. Spray distance:
   - Closer spray distances can cause the substrate to heat up quickly due to increased thermal transfer from the flame and molten droplets.

b. Flame characteristics:

- The type of flame used (neutral, oxidizing, or carburizing) can influence how much heat is transferred to the substrate and its overall temperature during the application.

c. Traverse speed:
   - Fast traversal speeds can limit the heating of the substrate, while slower speeds increase the amount of time the substrate is exposed to the flame, raising its temperature.

d. Preheating:
   - In some cases, preheating the substrate before spraying can help achieve the desired temperature quickly, improving coating adhesion. My research leveraged substrate preheating (e.g., to 60◦C for AlMoNi in Section 3.1, 120◦C for CuAlFe in Section 3.4, and 200◦C for TiSi in Section 3.9) as a key strategy to improve the adhesion and integrity of the deposited layers, the results of which are detailed in the respective sections of Chapter 3.

e. Ambient conditions:
   - Temperature, humidity, and airflow can all affect cooling rates and, consequently, the substrate temperature during spraying (Kovarik et al., 2015; Zhao et al., 2018).

2.6 Powder particle size

The powder particle size used in oxy-acetylene flame spraying is an essential parameter that influences the coating's properties, including adhesion, density, porosity, microstructure, and overall performance. The selection of appropriate powder particle size depends on several factors, including the type of substrate, coating material, and the desired characteristics of the final coating (Delbos et al., 2004).

While this section mentions general experimental ranges from the specialty literature (10-100 microns), the specific powders used in my experimental work (Chapter 3), such as the AlMoNi (composition in Table 3.1.1) or the metallic Titanium powder with an average diameter of 80 µm (Section 3.8), were chosen for their suitability for flame spraying and their ability to form the desired coating structures under the optimized parameters I identified.

Typically, the particle size for powders used in oxy-acetylene flame spraying falls within the range of 10 to 100 microns, but this can vary based on specific requirements. Here is a breakdown of how different particle sizes can affect the process:

a. Fine particles (10-30 microns):
   - Characteristics: these particles have a larger surface area relative to their volume, leading to enhanced melting and better atomization in the flame.
   - Applications: ideal for producing coatings with finer structures and higher bonding strength. they are well-suited for applications where high wear resistance and a smooth surface finish are desired.

- Example: fine aluminum or zirconia powders can provide dense and well-adhered coatings for wear-protection purposes.

b. Medium particles (30-60 microns):
   - Characteristics: This size range strikes a balance between good melting characteristics and manageable processing.
   - Applications: Commonly used in applications where a combination of hardness and toughness is needed.
   - Example: Chromium carbide powders in this size range can provide a good compromise for coatings requiring wear resistance without significant porosity or defects.

c. Coarse particles (60-100 microns):
   - Characteristics: Larger particles may lead to a rougher surface finish and increased porosity, as they may not fully melt or adhere properly during the spraying process.
   - Applications: Used where thicker coatings are required, or where the mechanical properties are less sensitive to surface finish.
   - Example: Coarser nickel or cobalt-based powders may be utilized for applications that prioritize corrosion resistance over aesthetics or fine mechanical properties (Meng et al., 2009; Niu et al., 2012).

Effects of particle size on coating properties

a. Melting behavior:
   - Smaller particles tend to melt more quickly in the flame due to their higher surface area-to-volume ratio. This leads to improved dispersion and a finer microstructure in the deposited coating.
   - Conversely, larger particles may produce thicker coatings with increased porosity if they do not fully melt during the process.

b. Adhesion:
   - Fine powders often exhibit better adhesion to the substrate because they can fill surface irregularities more effectively, leading to stronger mechanical interlocking and chemical bonding.

c. Porosity:
   - Coatings created from larger particles may exhibit more porosity, as larger unmelted particles can lead to voids or gaps in the coating, which can negatively impact coverage and overall mechanical properties.

d. Surface roughness:
   - Smaller particles can yield smoother coatings, while larger particles may produce a rougher surface that may or may not be acceptable depending on the application (Zhang et al., 2002; Zhu et al., 2024).

2.7 Powder composition

The powder composition used in oxy-acetylene flame spraying plays a crucial role in determining the properties and performance of the resulting coatings. The selection of the appropriate powder composition depends on the desired characteristics of the coating (such as hardness, wear resistance, corrosion resistance, thermal barrier properties, and adhesion to the substrate), the substrate material, and the specific application requirements. Here, various compositions commonly used in oxy-acetylene flame spraying and their implications will be explored.

Common Powder Compositions in Oxy-Acetylene Flame Spraying

a. Metals and metal alloys:
    - Applications: Coatings for wear resistance, corrosion resistance, and thermal protection.
    - Examples:
        - Nickel-based alloys: Such as Inconel or Hastelloy, known for excellent corrosion resistance at high temperatures, making them suitable for applications in the aerospace and chemical industries.
        - Cobalt-based alloys: High wear and oxidation resistance, commonly used for turbine components and industrial machinery.
        - Aluminum: Provides excellent corrosion resistance and is often used for protective coatings on steel substrates in marine applications.
b. Ceramics:
    - Applications: Thermal barrier coatings, wear-resistant coatings, and electrical insulators.
    - Examples:
        - Zirconia (ZrO_2): Known for its thermal stability and low thermal conductivity, often used as a thermal barrier coating in turbine engines.
        - Alumina (Al_2O_3): Offers excellent hardness and wear resistance, ideal for high-wear applications.
        - Titania (TiO_2): Used for its photocatalytic properties and as a low-cost alternative for thermal insulation.
c. Carbides:
    - Applications: Coatings that require extreme hardness and wear resistance.
    - Examples:
        - Tungsten carbide (WC): One of the hardest materials available, frequently used for coatings in mining, drilling, and milling applications.
        - Chromium carbide (CrC): Provides excellent wear and corrosion resistance, often used in applications exposed to high abrasive environments.
d. Composite powders:

- Applications: To combine the properties of multiple materials for enhanced performance.
- Examples:
  - Metal matrix composites (MMC): Such as a mixture of nickel or cobalt with tungsten carbide particles, balancing toughness with wear resistance.
  - Ceramic-polymer Composites: Combining ceramics for hardness with polymers for flexibility and adhesion.

e. Oxide and nitrate powders:
- Applications: Protective coatings that require high temperature resistance and thermal stability.
- Examples:
  - Zinc oxide (ZnO): Often used for its ability to develop corrosion-resistant coatings on steel.
  - Iron oxide (Fe_2O_3): Used in applications where rust prevention is necessary (Oliker et al., 2004).

Key factors to consider in powder composition

Thermal properties:
- The melting points and thermal expansion coefficients of the powder compositions are crucial, as these will affect the melting behavior during the flame spraying process. Higher melting point materials may require more careful management of flame temperature and distance.

Corrosion and wear resistance:
- Selecting powders that enhance the durability of the coating is essential for applications that involve high wear or corrosive environments. Materials known for their specific resistance to particular types of wear or corrosion should be chosen based on anticipated operating conditions.

Intermolecular bonding:
- Compatible powder compositions will promote better bonding to each other and to the substrate when fused during spraying. The presence of suitable alloying elements can enhance interfacial adhesion and reduce the risk of delamination (Semikolenov et al., 2024).

Microstructure:
- The selection of a powder's composition will also dictate the microstructure of the final coating, which can influence hardness, brittleness, and overall performance. For example, metals mixed with ceramics may provide a good balance of toughness and hardness. Chapter 3 presents my investigations across a diverse palette of powder compositions, including Ni-based alloys (AlMoNi, Section 3.1; NiCrBSiFe, Section 3.3; NiAl, Section 3.7; NiCrAlY, Section 3.10), Cu-based alloys (Cu38Ni, Section 3.2; CuAlFe, Sections 3.4 & 3.5), and functional materials like pure Titanium (Section 3.8) and Titanium-Silicon composites (Section 3.9). For each of these, the process parameters had to be specifically adapted to account for their

unique melting points, reactivity, and desired phase formation, as will be elaborated in the corresponding sections.

Environmental considerations:

- The choice of powders should consider any environmental regulations affecting the use of specific materials (e.g., toxicity levels of some coatings). Materials must be safe for both handling and application.

Example scenarios

Turbine components:

- Powder composition: Cobalt-chromium alloy.
- Reason: Excellent high-temperature oxidation resistance and wear properties in aggressive environments.

Manufacturing tools:

- Powder composition: Tungsten carbide suspended in a cobalt matrix.
- Reason: Combines extreme hardness with sufficient toughness for cutting and milling applications.

Marine equipment:

- Powder composition: Aluminum alloy.
- Reason: Provides light weight, corrosion resistance, and good adhesion to various substrates (Y. Yang et al., 2015).

2.8 Gas flow

If the process includes airflow to carry the powder, controlling this parameter is key to managing powder trajectory and deposition efficiency. While standard air was used as a carrier in many of my foundational flame spray experiments in Chapter 3, the introduction of specific protective gas atmospheres (e.g., Argon or Nitrogen, as explored in Sections 3.2, 3.3, 3.7, 3.8, and 3.9) represents an advanced parameter modification I investigated to control oxidation and enhance specific coating properties like electrical conductivity or photocatalytic activity.

Efficient powder transport in the oxy-acetylene flame spraying process relies on the airflow:

- Example with metal powder: Consider using nickel-based alloy powder for coating turbine blades.

- Flow rate: A low airflow might result in clumping of powder particles, leading to inconsistent feed rates and coating thickness. Conversely, excessive airflow might blow the powder away from the target surface, reducing deposition efficiency.
- Optimal velocity: The ideal airflow should transport the powder smoothly into the flame without excessive turbulence. Typically, airflow rates can range from 3 to 10 L/min, depending on the coating material and nozzle size.

The balance of airflow can dramatically influence the properties of the final coating:

- Example with tungsten carbide coating: Tungsten carbide can be used for wear-resistant coatings on industrial tools (Morks & Kobayashi, 2006).

- Impact of accurate airflow: If airflow is optimized, it can help achieve a coating density of around 80-90 % without excessive porosity. Failure to control airflow may lead to incomplete melting of the carbide particles, resulting in weak bonding and reduced wear resistance.
- Coating thickness control: Adjusting airflow can also regulate the thickness of the coat. If spraying with a desired thickness of 100 micrometers, excessive airflow may lead to thinner coatings and increase the need for multiple passes (C. J. Li et al., 1999).

Airflow plays a crucial role in the overall safety and environmental impact of oxy-acetylene spraying:

- Fume management: During spraying, especially with metals that release fumes (e.g., lead or cadmium), using additional airflow from fume extraction systems will help to maintain safe air quality for operators.

- Example: Implementing a localized ventilation system that draws air away from the spraying area can help pull harmful fumes away and diminish inhalation risks.

- Combustion safety: Adequate airflow helps to prevent the formation of explosive mixtures of gases. For example, ensuring a proper balance of oxygen to acetylene (e.g., not exceeding a 1:1.1 ratio in typical spraying conditions) minimizes the risk of backfires or explosions (Z. Y. Yang, 2004).

While airflow (Section 2.8) typically refers to carrier gas, the strategic use of inert or specific reactive protective gas shrouds or environments during flame spraying can significantly alter the coating chemistry and microstructure by minimizing oxidation or promoting desired reactions (e.g., nitriding). Several of my investigations in Chapter 3 (e.g., Sections 3.2, 3.3, 3.7, 3.8, 3.9) systematically evaluated the impact of Argon or Nitrogen atmospheres on the properties of thermally sprayed Cu38Ni, NiCrBSiFe, NiAl, Ti, and TiSi coatings, respectively.

In summary, the quality, microstructure, and performance of powder flame-sprayed coatings are dictated by a complex interplay of the thermal, chemical, and kinetic parameters discussed in this chapter. From flame characteristics and particle properties to substrate interactions and the influence of novel process modifications like applied electric fields and controlled atmospheres, each variable plays a critical role. A thorough understanding and the ability to strategically manipulate these parameters, as demonstrated in the diverse experimental studies I conducted and which are detailed in Chapter 3, are paramount for advancing thermal spray technology and developing coatings tailored for demanding industrial applications. This chapter has laid the necessary groundwork for appreciating the systematic approach taken in my research to optimize these parameters and achieve the significant improvements in coating properties and functionalities that will now be presented.

Chapter 3. Experimental development and characterization of advanced thermal spray coatings

This chapter presents the core of my experimental research conducted to advance the practical implementation of these coating technologies. The primary aim of this chapter is to showcase the results of my investigations into optimizing thermal spraying processes for various substrate and powder combinations, and to present my novel findings concerning the resultant coating characteristics and performance enhancements.

This chapter details a series of original experimental studies I designed and executed, each targeting specific industrial challenges or opportunities. These applications demonstrate my successful efforts in tailoring coating microstructures for superior wear resistance, significantly improving corrosion protection through optimized parameters, developing novel photocatalytic surfaces with enhanced efficiency, or perform modifications to existing thermal spray techniques, such as the use of electrically charged powders or specific protective atmospheres I investigated.
For every distinct substrate and powder system evaluated, I systematically optimized key process parameters to achieve desired outcomes.

The table below (Table 3.1) serves as a comprehensive summary of my experimental investigations, detailing the specific substrates, powder materials, the optimized parameters I determined, the key quantitative and qualitative results obtained, and the targeted industrial applications for which my results are relevant. Some of these original studies are then elaborated upon in the subsequent sections, providing a detailed account of the experimental approach, an in-depth discussion of my specific findings and their significance, and technological recommendations derived from my research.

Table 3.1 A comprehensive summary of my experimental investigations

No.	Base material	Powders	Parameters	Results	Applications
3.1	C45	AlMoNi	Spray distance = 100 / 150 / 200 mm O_2 = 4 bar C_2H_2 = 0.7 bar Substrate Temperature = 60 ^{0}C Electric field strength = 0 – 70 V DC / AC	The use of electrically charged powders enhances the physical and mechanical properties of deposited layers, resulting in improved homogeneity, microhardness, and adhesion. Comparatively, samples without charged powders exhibit inferior structural integrity and interface quality. The research suggests promising prospects for the industrial-scale implementation of the powder electrification device. (Roata et al., 2009, 2011; Roata & Iovanas, 2011; Roata et al., 2014)	Transportation: crankshafts, timing gear fits, pully fits, thrust faces Pulp and paper: pump shaft, bearing fits General: dimensional restoration, hydraulic cylinder cases
3.2	C10100	Cu38Ni	Spray distance = 100 / 200 mm O_2 = 4 bar C_2H_2 = 0.7 bar Electric field strength = 0 – 70 V DC Protective gas Ar = 0 / 35 l/min	In summary, the application of a 70-volt electric field and a 35-liter per minute argon gas flow significantly improves the deposition of the Pcu7 layer. This optimization reduces oxidation, resulting in lower hardness and electrical resistivity, thus enhancing conductivity. It also produces a smoother surface with hydrophobic properties, increasing moisture resistance and durability. This study underscores the critical role of precise control over deposition parameters in	Abrasion protection Adhesive wear protection Erosion protection in gas flow Erosion protection in liquid flow Sliding wear protection Solid particle erosion protection Dimensional restoration

				enhancing material performance for various applications. (Roata, 2017b)	
3.3	S235JR	NiCrBSiFe	Spray distance = 100 / 200 mm O_2 = 4 bar C_2H_2 = 0.7 bar Protective gas Ar = 0 / 35 l/min	The use of a protective argon gas flow rate of 35 liters per minute is essential for reducing oxidation during the deposition process, resulting in a significant decrease in the electrical resistivity of the deposited layer (P3). This enhancement in conductivity is expected to improve the material's performance in applications requiring low-resistance conductive layers, showing the importance of precise control over the argon atmosphere to maintain material integrity and optimize functionality. (Roata, 2018b)	For rolling equipment, piston rods and shaft protection sleeves Aerospace and turbine components Bearings, gears, and other mechanical components Automotive parts and industrial rollers
3.4	Cu5Sn	CuAlFe	Spray distance = 150 mm O_2 = 4 bar C_2H_2 = 0.7 bar Substrate Temperature = 120 ^{0}C Heat treatment = no / yes (950 ^{0}C)	Ternary copper-aluminum-iron composite coatings, produced via flame spraying from a core/shell powder, exhibit improved microhardness and corrosion resistance following a concentrated solar energy post-deposition thermal treatment that reduces defects such as pores and cracks. (Roata et al., 2017)	Sustainable manufacturing, green energy tech. Conductive components, heat sinks, and connectors. Coatings for wear resistance and thermal protection.

3.5	C110	CuAlFe	Spray distance = 150 / 200 mm O_2 = 4 bar C_2H_2 = 0.7 bar Substrate Temperature = 120 ^{0}C	Hydrophilic photocatalytic coatings made from hematite and copper oxide were synthesized on copper substrates via thermal spraying of Cu–Al–Fe powder. These coatings effectively mineralize methylene blue (MB) due to a metallic interphase that reduces charge recombination. The CuxO/Fe_2O_3 composites maintain stable performance and exhibit good stability in water, with phases like α-FeOOH and Cu_2O enhancing activity. Ongoing research focus on their stability and efficiency across varying pH levels and ionic strengths for wastewater treatment applications. (Roata et al., 2018)	Sustainable manufacturing, green energy tech. Conductive components, heat sinks, and connectors. Coatings for wear resistance and thermal protection.
3.6	S235JR	NiAlZn	Cladding speed = 60 / 90 mm/s Pulse frequency = 75 / 100 Hz Power = 1.5 kW Pulse duration = 2 ms Energy = 3.06 J Shielding gas Ar = 15 l/min	A laser cladding process applied to S235JR carbon steel produced a nickel-aluminum-zinc coating that is 34-48% harder than the base material, with hardness increasing with laser speed (60 to 90 mm/s). However, high concentrations of heavy metals were found: Fe from vaporization of steel and Ni, Al, Zn from cladding powder. Exposure levels for Fe, Ni, and Zn exceeded recommended limits, while Al levels were close to the limit for samples P1 and P3, but surpassed it for sample P4.	Accepted in the aerospace industry for many decades, these materials show very good oxidation resistance and excellent thermal shock resistance in turbine applications. Salvage and build-up for restoration applications - High-temperature particle erosion resistance - Oxidizing atmosphere resistance below 800 °C (1470 °F. n Bond coat for ceramic

				(Roata et al., 2019b)	or abradable with service temperatures up to 800 °C (1470 °F) - Products with the addition of molybdenum enhance hot corrosion resistance at elevated temperatures
3.7	C510	NiAl	Spray distance = 150 mm O_2 = 4 bar C_2H_2 = 0.7 bar Protective gas N_2 = 38 l/min Heat treatment = no / yes (electric furnace and solar)	A concentrated solar annealing treatment applied to Ni-Al flame-sprayed coatings on a phosphor bronze substrate resulted in relatively homogeneous and well-fused coatings. The annealing process increased the formation of intermetallic compounds, enhancing the coating's plasticity. Although some oxidation of the metallic phase occurred, the treatment improved coating fusion, leading to increased hardness and wear resistance. (Roata et al., 2020)	•Used for high temperature layers, high temperature oxidation resistance coating, thermal sprayed ceramic coating layers. • For salvage and build-up on machinable carbon and corrosion resistant steels. • Clad products produce an exothermic reaction during spraying, excellent bond strength., Ni20Al is better than Ni_5Al material.
3.8	1050Al	Ti 99,5 %	Spray distance = 150 / 200 mm O_2 = 4 bar C_2H_2 = 0.7 bar Protective gas N_2 = 35 l/min	Nitrogen-doped titanium dioxide coatings were successfully created using thermal flame spraying of metallic titanium, achieving optical band gaps as low as 1.55 eV. These photocatalysts exhibited superior methyl orange degradation efficiencies of 97 % under UVC and 87 % under visible light, outperforming commercial Degussa P25 powder. Key reactive species identified in degradation were holes and hydroxyl radicals	Thermal spray coatings of titanium-based materials are commonly used in medical applications where biologic compatibility is required. Additionally, these coatings may also be used as a potential bond coat for hydroxyapatite coatings that are often used as a top-coat on biomedical implants. Titanium powders may also be used to produce dense, corrosion resistant coatings. Titanium powders

				for visible light, and additional superoxide for UVC. The coatings retained photocatalytic activity across multiple cycles. The method allowed for higher nitrogen doping levels and reproducible surface chemistry modifications by adjusting the spray nozzle distance from the substrate. (Croitoru et al., 2020 b)	have strong affinity and reactivity with oxygen, hydrogen and nitrogen at high temperatures. Most of thermal spray coatings from these powders are produced under controlled atmosphere conditions (low pressure or soft vacuum).
3.9	C110 S273JR	TiSi	Spray distance = 200 mm O_2 = 4 bar C_2H_2 = 0.7 bar Substrate Temperature = 200 ^{0}C Protective gas N_2 = 35 l/min	This study developed sustainable coatings for the degradation of wastewater pollutants using visible light. Achieved through thermal flame spraying of titanium–silicon powders on copper and carbon steels, the coatings demonstrated high photodecoloration and mineralization efficiencies, with an optical bandgap of approximately 1.000 eV. Post-photocatalysis assessment showed strong corrosion and erosion resistance. Future research will investigate their performance and lifecycle in actual wastewater conditions with various interfering ions. (Uncu et al., 2021)	Aerospace: Turbine blades, landing gear(High strength, temperature resistance) Automotive: Engine parts, valves (Wear and corrosion resistance) Biomedical: Implants, devices (Biocompatible, non-toxic) Additive Manufacturing: 3D printed components (Low density, good printability) Thermal Spray: Coatings (High hardness and wear resistance)
3.10	S273JR	NiCrAlY	Spray distance = 150 mm O_2 = 4 bar C_2H_2 = 0.7 bar	Investigate the potential of integrating advanced surface modifications with the NiCrAlY thermal spray coatings to create multifunctional surfaces that not only	• High temperature combustion chambers • Steam turbine blades

				maintain superior corrosion resistance and hydrophilicity but also exhibit self-cleaning properties. By incorporating photocatalytic materials (such as titanium dioxide) into the coatings, these modified surfaces could harness environmental light to break down organic contaminants, making them ideal for applications in environments easily polluted, such as marine settings and industrial facilities. This approach could further enhance the longevity and performance of the coatings while minimizing maintenance requirements in harsh operating conditions. (Roata et al., 2023)	• Repair and restoration of substrates and superalloy parts • Exhaust duct of turbines • Turbine bucket

3.1 Technological recommendations for the thermal spraying of AlMoNi powder

The experimental results indicate that optimal results cannot be achieved with the recommended parameters for the metallization of cylindrical surfaces unless the following conditions are satisfied:

- It is advisable to preheat the components externally to enhance the adhesion of the deposited layer. Specifically, heating should be conducted to a maximum of 300 [°C] above the ambient temperature to secure superior adhesion of the metallized layer.
- The thickness of the raw metallized layer must not exceed 2.5 – 3 [mm] in radius.
- The rotational speed of the component, along with the longitudinal advance speed of the spray gun, should be determined according to the dimensions of the component.
- The distance between the spray gun and the surface of the component should not be less than 100 [mm] to prevent overheating, which can lead to significant contraction.
- The surface of the component intended for refurbishment through flame metallization and powder application must be adequately prepared to achieve the requisite roughness for the metallization process employed (Roata et al., 2009, 2011; Roata & Iovanas, 2011; Roata et al., 2014).

Table 3.1.1 The chemical composition of the powder.

Powder	***Chemical composition [%]***						
	Ni	Al	B	Fe	Cr	Si	C
AlMoNi	93,45	5	0,8	0,34	0,18	0,15	0,08

For the experimental tests, the standard metallization module SSM 10 of the Castodyn DS 8000 system was used, which is a flame spraying system for powder materials. This system is available in the equipment of the research department D12 ADVANCED ECO-TECHNOLOGIES IN WELDING, along with the device designed for electric loading of powders in direct current. The figures below present the experimental setup used to carry out the tests.

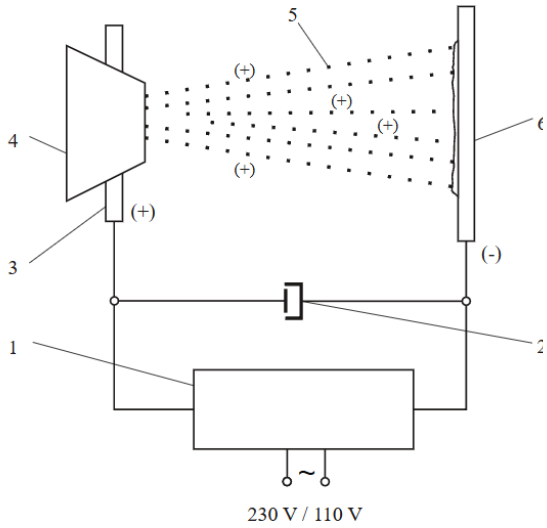

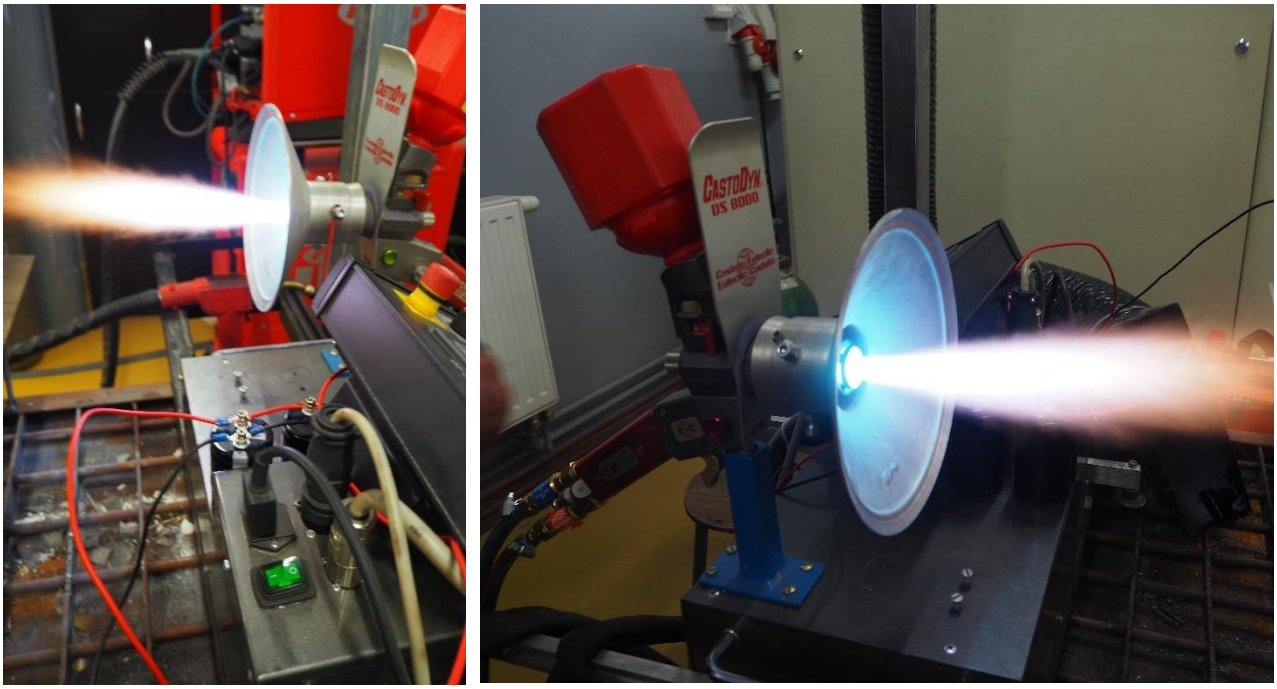

Figure 3.1.1 The experimental setup (POSDRU/89/1.5/S/59323 postdoctoral experimental report, 2011, 2012).

Table 3.1.2 Parameters of the deposition regime in direct current and alternating current.

Test mark	***Powder***	***Rotational speed [rot/min]***	***Feed rate [m/min]***	***O2 [bar]***	***C2H2 [bar]***	***Spray distance [mm]***	***U DC / AC [V]***	***Tp [0C]***
P1 – P15	AlMoNi	127	0.38	4	0,7	100	0-70	60
P1'- P15'		127	0.38	4	0,7	150	0-70	60
P1"- P15"		127	0.38	4	0,7	200	0-70	60

Metallographic analysis of layers deposited by flame metallization and electrically charged powders.

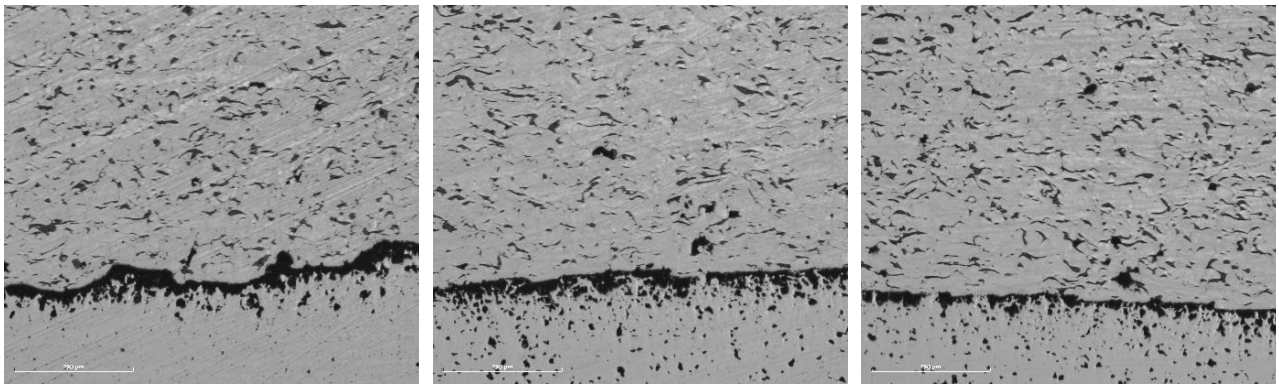

P1 – 100 mm **P1' – 150 mm** **P1" – 200 mm**

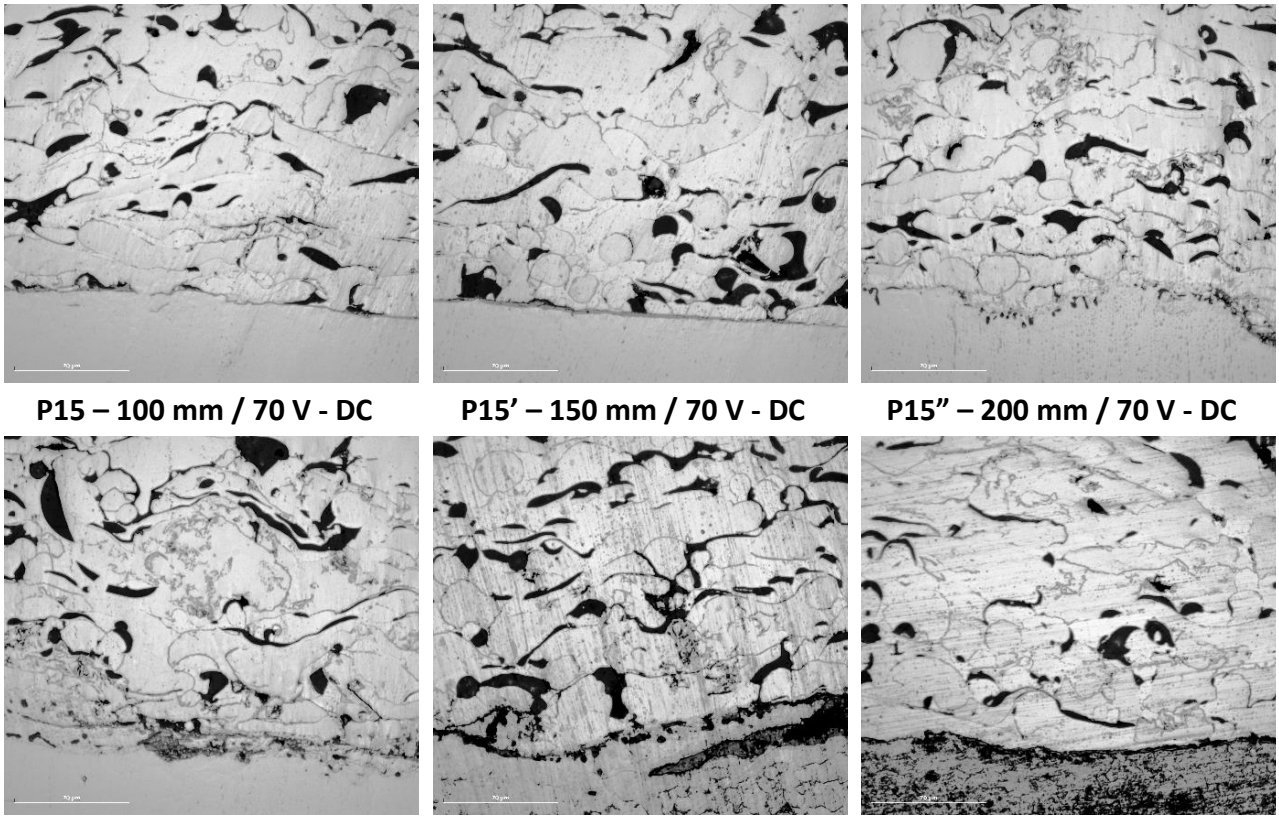

P15 – 100 mm / 70 V - DC **P15' – 150 mm / 70 V - DC** **P15" – 200 mm / 70 V - DC**

P15 – 100 mm / 70 V - AC **P15' – 150 mm / 70 V - AC** **P15" – 200 mm / 70 V - AC**

Figure 3.1.2 Structures in the deposition areas on the base metal (POSDRU/89/1.5/S/59323 postdoctoral experimental report, 2011, 2012).

The comparative analysis of microscopic examinations reveals a statistically significant enhancement in both the adhesion and homogeneity of deposited layers. This enhancement is particularly pronounced when the powder utilized in the metallization process is subjected to elevated voltage levels, which appear to facilitate increased kinetic energy of particles during deposition. Furthermore, a reduction in the substrate-to-source distance also correlates with improved layer characteristics, likely due to increased flux density and minimized thermal gradients, thus promoting a more uniform deposition profile. These results suggest that optimization of process parameters—namely voltage and spatial configuration—plays a crucial role in the quality of the metallized coatings.

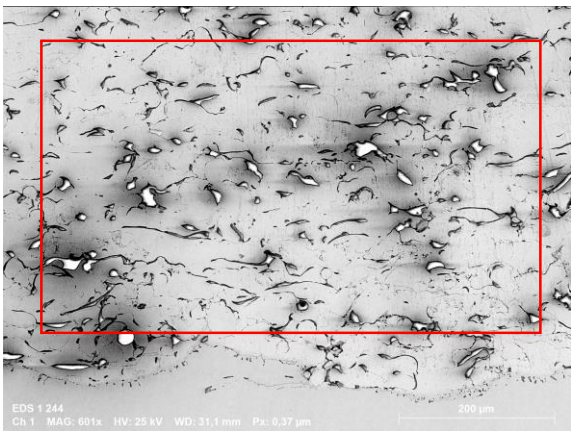

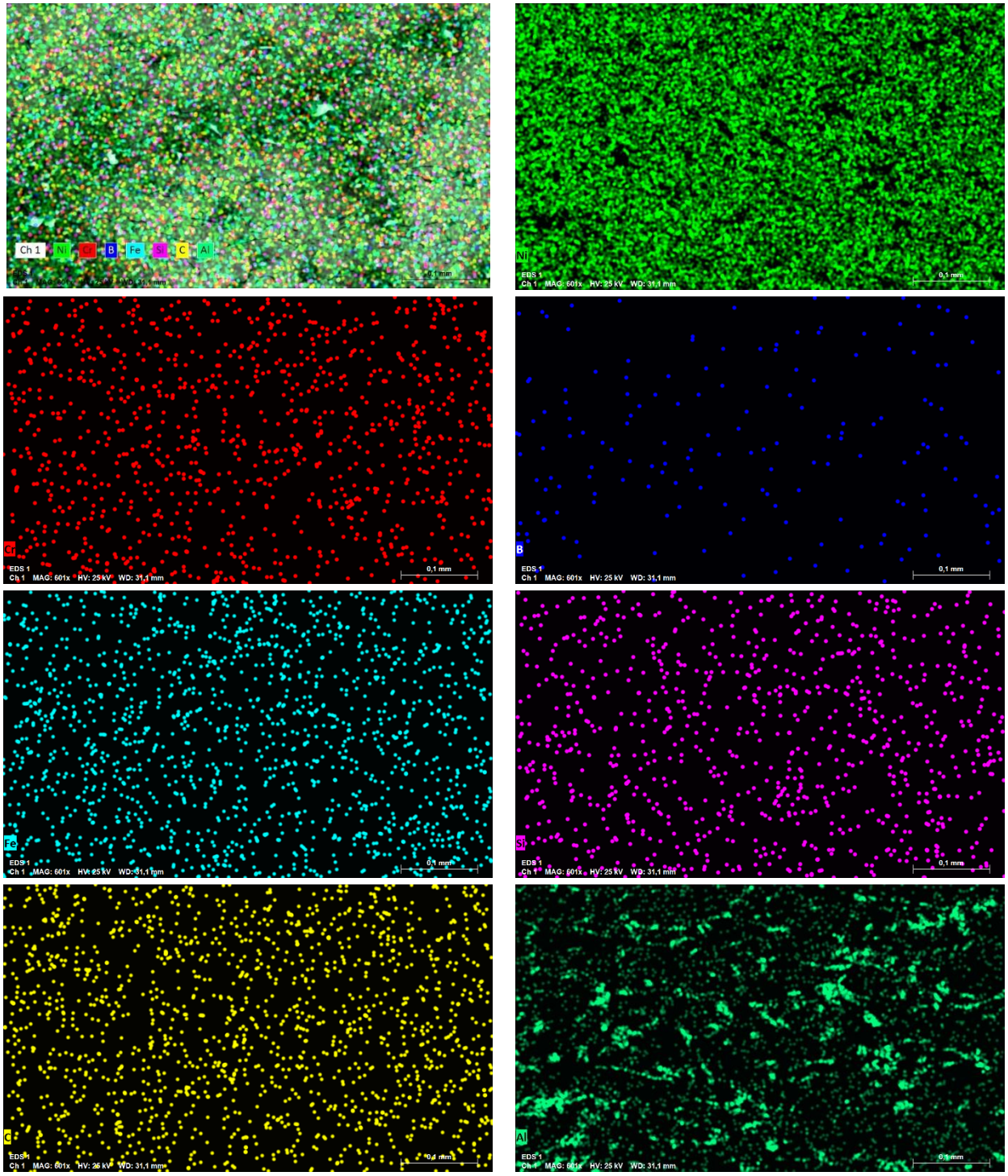

Figure 3.1.3 Structures in the deposition areas on the base metal C45 (P_{15}).

Microhardness tests of layers deposited through flame metallization and powders charged with electric charges in direct current.

In order to attain a thorough characterization of the properties of layers deposited via metallization, microhardness assessments were performed on the base material (BM), heat-affected zone (HAZ), and deposited material (DM). This methodology facilitates an in-depth understanding of

the mechanical properties associated with each specific region, thereby contributing to overall analysis of the metallization process and its impact on material performance (POSDRU/89/1.5/S/59323 postdoctoral experimental report, 2011).

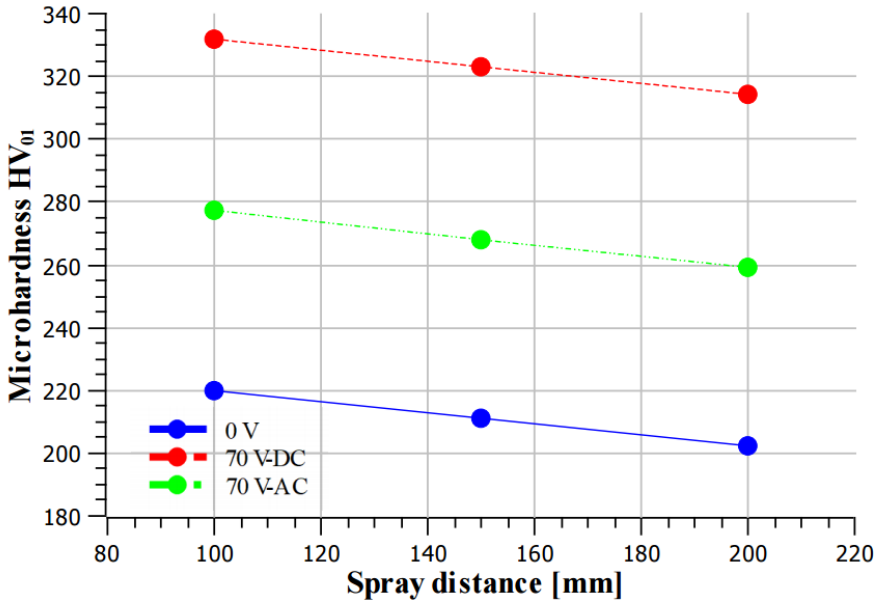

Figure 3.1.4 Graphical representation of the microhardness analysis (POSDRU/89/1.5/S/59323 postdoctoral experimental report, 2011, 2012)

The comparative analysis of results reveals a significant increase in microhardness in the samples where the powder used for the metallization process was subjected to a high voltage (70 V), and the metallization distance was minimized to 100 mm. These observations suggest a correlation between processing conditions and mechanical properties of the material.

Determination of ohmic resistance and adhesion resistance of coatings deposited by flame metallization and charged powders.

Ohmic resistance - Ohm's Law – Within a defined segment of an electrical circuit, the intensity of electric current is quantitatively expressed as ratio of voltage applied across the segment's terminals to the current that traverses that segment.

• By convention, the direction of electric current is identified as flowing from positive (+) terminal to negative (-) terminal within external circuit.

• Independent of the specific nature of mobile charge carriers involved, the direction of electric current is consistent with the orientation of electric field intensity.

In accordance with Ohm's Law, a measurement apparatus has been developed to facilitate the determination of resistance. This apparatus is constructed in compliance with the following principles:

• The current intensity is assessed through the use of an ammeter, which must invariably be connected in series with the circuit elements where the current intensity measurement is to be conducted.

• The voltage U lacks a universally fixed value; instead, its magnitude is dependent on the particular structure and configuration of external circuit.

• The voltmeter, an instrument utilized for gauging voltage, is connected in parallel with the specific circuit element being analyzed.

This framework ensures accurate measurements and a clear understanding of relationships governed by Ohm's Law, thereby contributing to a comprehensive analysis of **circuit behavior** (POSDRU/89/1.5/S/59323 postdoctoral experimental report, 2011)**.**

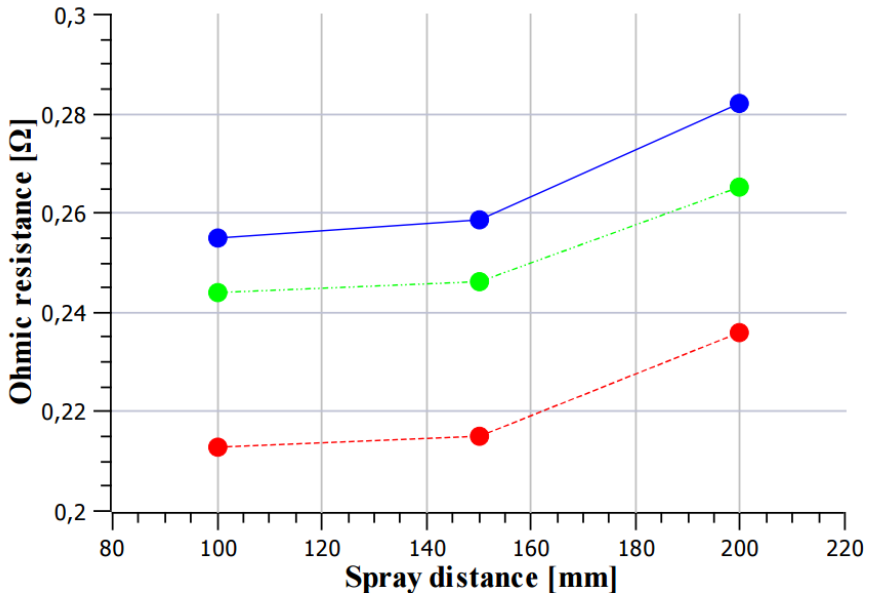

Figure 3.1.5 Graphical representation of the ohmic resistance (POSDRU/89/1.5/S/59323 postdoctoral experimental report, 2011, 2012)

An increase in the voltage applied to a conductor leads to a proportional rise in current intensity traversing the conductor. If the conductor's temperature is maintained at a constant level, the ratio of voltage to current remains effectively invariant. For metallic conductors held at steady temperature conditions, U/I ratio is consistent, thereby representing a defining characteristic of the conductor.

Moreover, as the homogeneity of a material increases, there is a corresponding decrease in its ohmic resistance. Comparative investigations of the obtained results reveal a notable decline in ohmic resistance associated with greater material homogeneity, particularly in samples where the powder utilized in the metallization process was subjected to elevated voltage levels (70 V) and where the metallization distance was kept to a minimum (100 mm). These results underscore the critical influence of processing parameters on electrical properties of conductive materials.

Determination of adhesion resistance of layers deposited through flame metallization using electrically charged powders.

The methodological approach is founded upon the principle of applying a consistent and shock-free compressive load to the test specimen. This application continues until the complete detachment of deposited material layer is achieved.

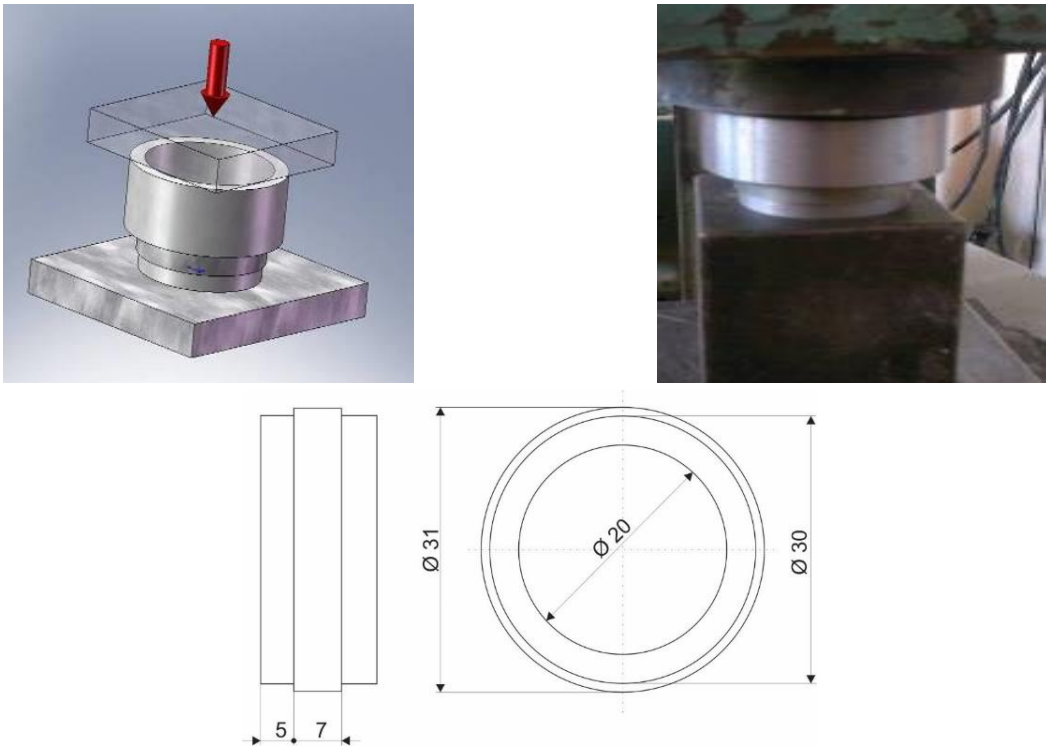

Figure 3.1.6 Diagram for determining the adhesion strength of deposited layers (POSDRU/89/1.5/S/59323 postdoctoral experimental report, 2011).

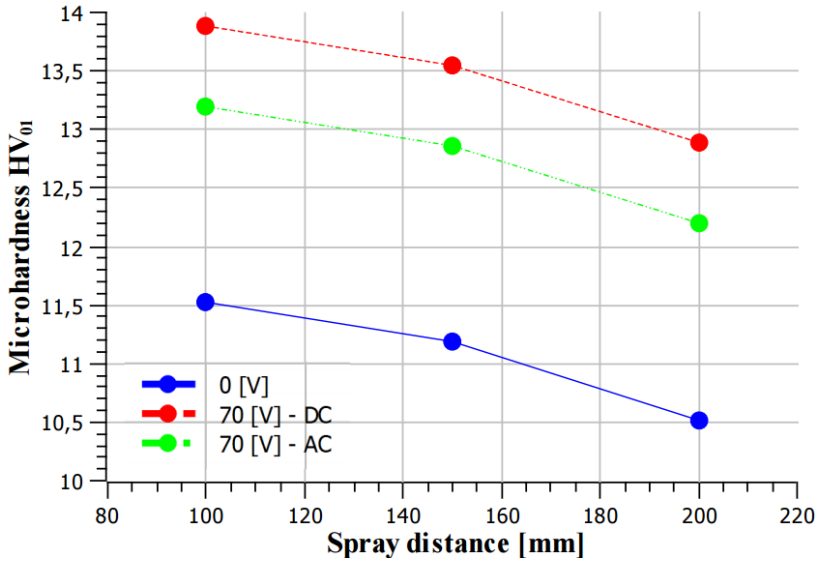

Figure 3.1.7 Graphical representation of the adhesion strength of the deposited layers (POSDRU/89/1.5/S/59323 postdoctoral experimental report, 2011, 2012).

The comparative analysis of results reveals a significant enhancement in adhesion resistance among samples in which the powder utilized for the metallization process was subjected to high voltage conditions (70 V). Furthermore, a minimized metallization distance of 100 [mm] was employed. These factors collectively contribute to improved adhesion properties, highlighting the impact of processing parameters on the efficacy of the metallization technique.

The utilization of electrically charged powders leads to a notable enhancement in physical and mechanical properties of deposited layers, characterized by improved homogeneity, microhardness, and adhesion.

The interface between deposited layers and substrate material is deemed satisfactory, exhibiting diffusion zones and minor porosity in samples that incorporated electrically charged powders. Conversely, the classical samples, which did not employ electrically charged powders, demonstrated a less compact structure, characterized by successive deposition layers and frequent discontinuities including pores and inclusions. The interface with the substrate in these cases is inadequate, revealing regions of discontinuity.

Based on the results of this research, the potential for industrial-scale application of the device designed for the electrification of powders is promising.

3.2 Influence of the electric field and protective gas on the properties of coatings CU38Ni deposited by thermal spraying on C10100

Experimental investigations were conducted on samples produced using the flame and powder thermal spraying technique. The CastoDyn DS 8000 system, equipped with four spraying modules, demonstrates the most extensive industrial applicability. For the fabrication of samples, the standard spraying module SSM 10 was employed. The chemical composition of the additive material utilized for coatings is detailed in Table 3.2.1.

Table 3.2.1 The chemical composition of the filler material Cu38Ni.

Sample Mark	Type of powder	Chemical composition %		
		Cu	Al	Fe
PCu1 – PCu8	Cu38Ni	Balance	8,5 – 10,75	0,5 - 2

To determine the optimal number of experimental samples, the Design of Experiments (DOE) method was used. The method involves repeating experiments while modifying one or more parameters (input factors F).

Important parameters that influence the quality of the layer deposited through the thermal spray process with flame and powder have been identified:

1. **Coating distance [100 mm – 200 mm]**: This is the distance between spray source and substrate on which the layer is deposited. A distance that is too large may lead to greater

particle dispersion, while a distance that is too small can cause overheating or poor layer definition.

2. **Electric field voltage [0 V – 70 V]**: The applied voltage can influence speed and energy of powder particles during deposition. An optimal voltage helps improve adhesion and uniformity of the layer.
3. **Protective gas [0 L/min – 35 L/min]**: The type and volume of protective gas used in the process is crucial to prevent oxidation and ensure a favorable environment for deposition process. The gas flow must be adjusted appropriately to optimize the quality of the layer.

Table 3.2.2 Form of the experimental matrix and parameters of the thermal spraying process (Roata, 2017b).

Sample No.	Spraying distance [mm]	Electric field strength [V]	Protective gas Ar [l/min]
PCu1	-1 (100)	-1 (0)	-1 (0)
PCu2	**1 (200)**	**-1 (0)**	**-1 (0)**
PCu3	-1 (100)	1 (70)	-1 (0)
PCu4	1 (200)	1 (70)	-1 (0)
PCu5	-1 (100)	-1 (0)	1 (35)
PCu6	1 (200)	-1 (0)	1 (35)
PCu7	**-1 (100)**	**1 (70)**	**1 (35)**
PCu8	1 (200)	1 (70)	1 (35)

This study delves into comparative analysis of samples PCu2 and PCu7, identified as representatives of optimal and suboptimal performance characteristics, respectively. By examining key variables such as mechanical properties, thermal conductivity, and structural integrity, this investigation seeks to uncover the specific factors that contribute to their differing performance outcomes. Additionally, the research aims to explore the relationships between these properties and their practical implications in real-world applications.

Through a combination of experimental techniques and analytical methods, we will exemplify underlying mechanisms driving the performance discrepancies between the two samples. The insights gained from this study are expected to provide valuable guidance for future material selection and processing strategies in relevant industries, paving the way for advancements in efficiency and effectiveness of applications involving copper-based materials.

Microscopic analysis

The samples obtained through flame spraying and powder deposition were analyzed both macroscopically and microscopically, focusing on highlighting the quality of deposited layers in terms of adhesion and volume of oxides and pores present in them. Samples for macroscopic and

microscopic analysis were taken from specimens obtained through flame spraying and powder deposition.

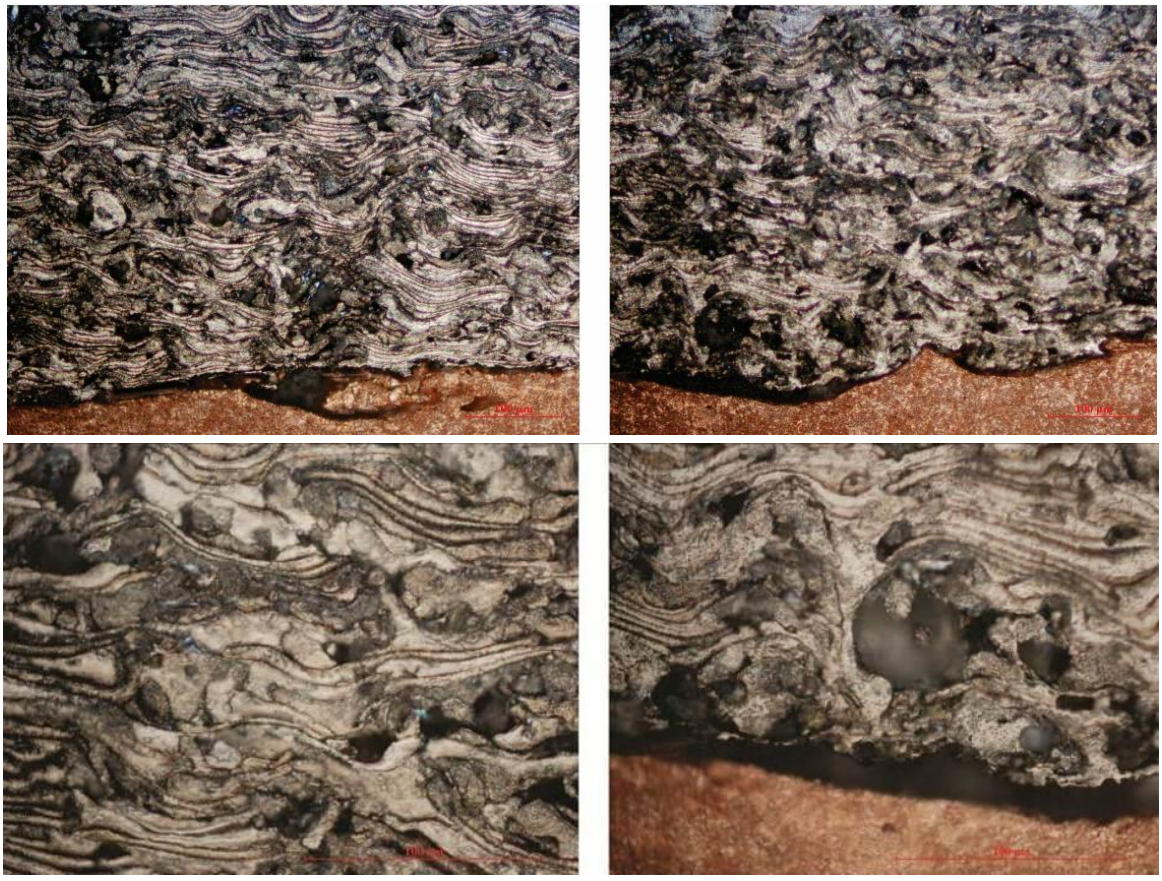

Figure 3.2.1 Structures in the specific deposition areas on the base metal Cu 10100 (PCu2) (Roata, 2017b).

The deposited layer exhibits a typical lamellar appearance (in multiple layers), and in certain regions, pores, oxides, and unmelted particles can be identified as a result of the thermal spraying process. Following the phase transformations in deposited layer, a mechanical mixture of solid solution α (Cu + Ni) and solid solution β (Ni + Cu) is identified. The interface with the substrate shows pores, partial melting, and a high density of oxides.

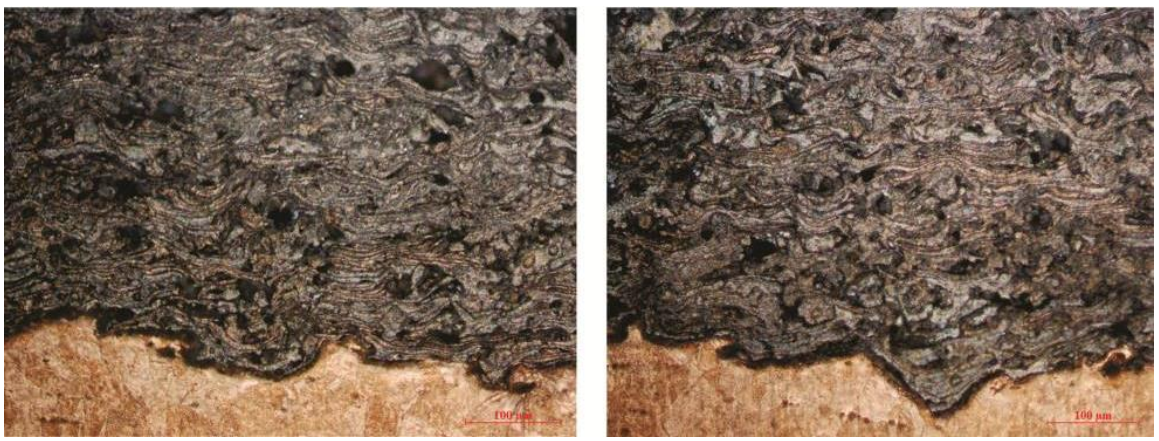

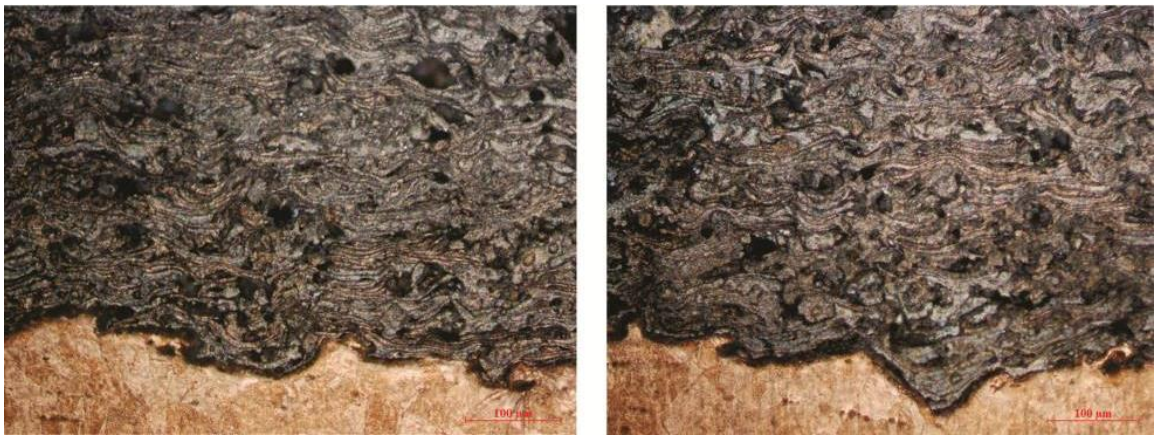

Figure 3.2.2 Structures in the specific deposition areas on the base metal Cu 10100 ($P_{Cu}7$) (Roata, 2017b).

The deposited layer has a lamellar structure and contains pores, oxides, and unmelted particles due to thermal spraying process. It features a solid solution α (Cu + Ni) as a result of phase transformations, and exhibits good adhesion to the substrate, though isolated areas with pores and oxides are present.

To achieve a significant reduction in porosity and oxidation rates, while simultaneously enhancing adhesive properties, it is imperative to implement a rigorously controlled experimental setup involving an electric field voltage of 70 volts. This voltage has been empirically demonstrated to facilitate improved material characteristics. Furthermore, it is essential to maintain a precise argon protective gas flow rate set at 35 liters per minute.

This specific flow rate serves to create an inert atmosphere, effectively mitigating the risk of detrimental reactions with ambient moisture and oxygen. Collectively, these parameters are expected to optimize physical and chemical interactions within the material system, ultimately leading to enhanced performance in applications requiring robust adhesion and structural integrity.

The implementation of these conditions should be conducted within a systematic framework to ensure replicability and reliability of results across various experimental iterations.

Microhardness tests

In order to provide a thorough characterization of the mechanical properties of coatings applied through flame spraying and powder deposition techniques, microhardness testing was systematically performed on the coatings along two distinct orientations. This approach enables a detailed analysis of the material's hardness response and directional dependence, contributing to a deeper understanding of mechanical performance of deposited layers.

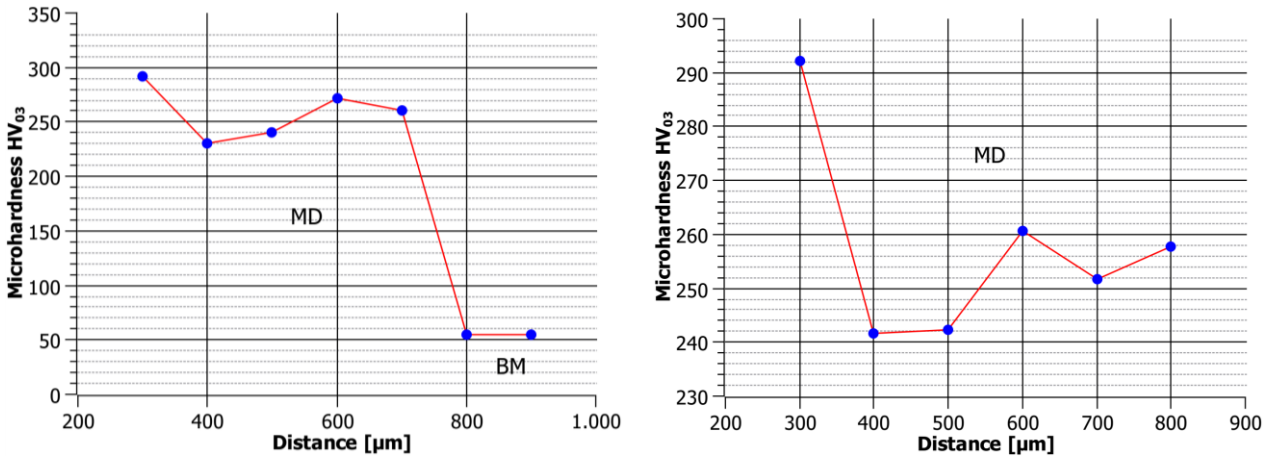

Figure 3.2.3 Graphic representation of distribution of values obtained on vertical (a) and horizontal (b) as a result of PCu2 sample hardness test (Roata, 2017b).

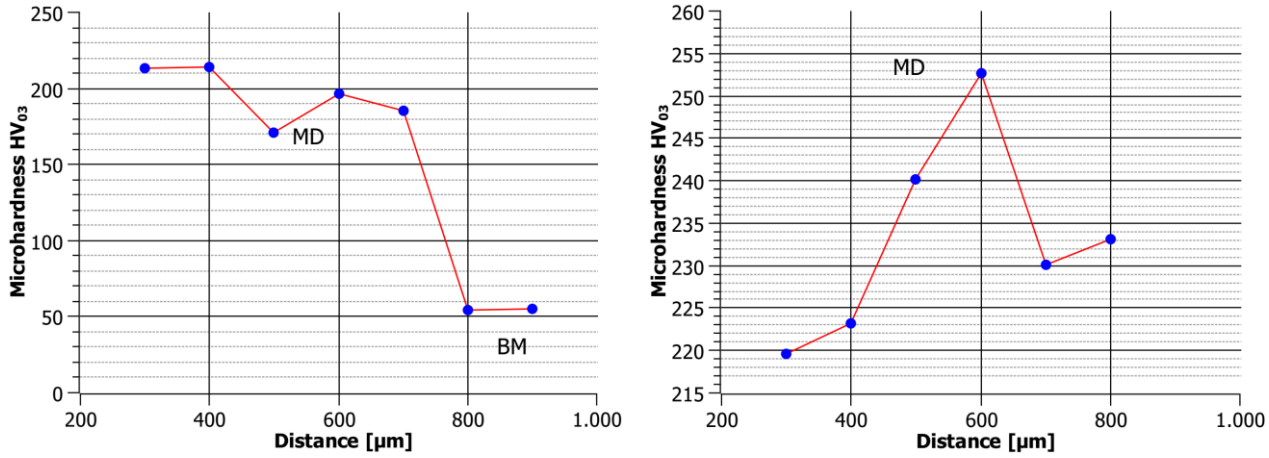

Figure 3.2.4 Graphic representation of distribution of values obtained on vertical (a) and horizontal (b) as a result of PCu7 sample hardness test (Roata, 2017b).

In order to facilitate a comprehensive interpretation and articulation of these results, it is imperative to employ statistical modeling of the process factors, thereby enabling the determination of coefficients associated with the linear model.

The analysis will commence with calculation of individual effects exerted by each factor. Following this, the interaction effects among these factors pertaining to the process will be evaluated. To effectively compute the effects of factors (denoted as a1, a2, and a3), it is necessary to calculate both minimum and maximum HV_{03} values for each specific factor. This methodological approach will provide a clearer understanding of the relationships and influences at play within the studied process.

$$HV_{03} = 223{,}26 + 7{,}63 * F1 - 13{,}64 * F2 - 9{,}80 * F3 - 1{,}48 * F1F2 - 1{,}78 * F1F3 + 0{,}88 * F2F3 + 0{,}36 * F1F2F3 \quad (3.2.1)$$

The information depicted in Figure 3.2.5 highlights the impact of primary variables, particularly the coefficients of linear terms in the mathematical model. An elevation in the hardness of deposited layers is noted with the adoption of increased spray distances, which promote the formation of oxides. In contrast, the use of electrical charges and protective gases reduces the occurrence of oxide formation, thereby preserving layer hardness; however, this approach also enhances the uniformity of the deposited layers.

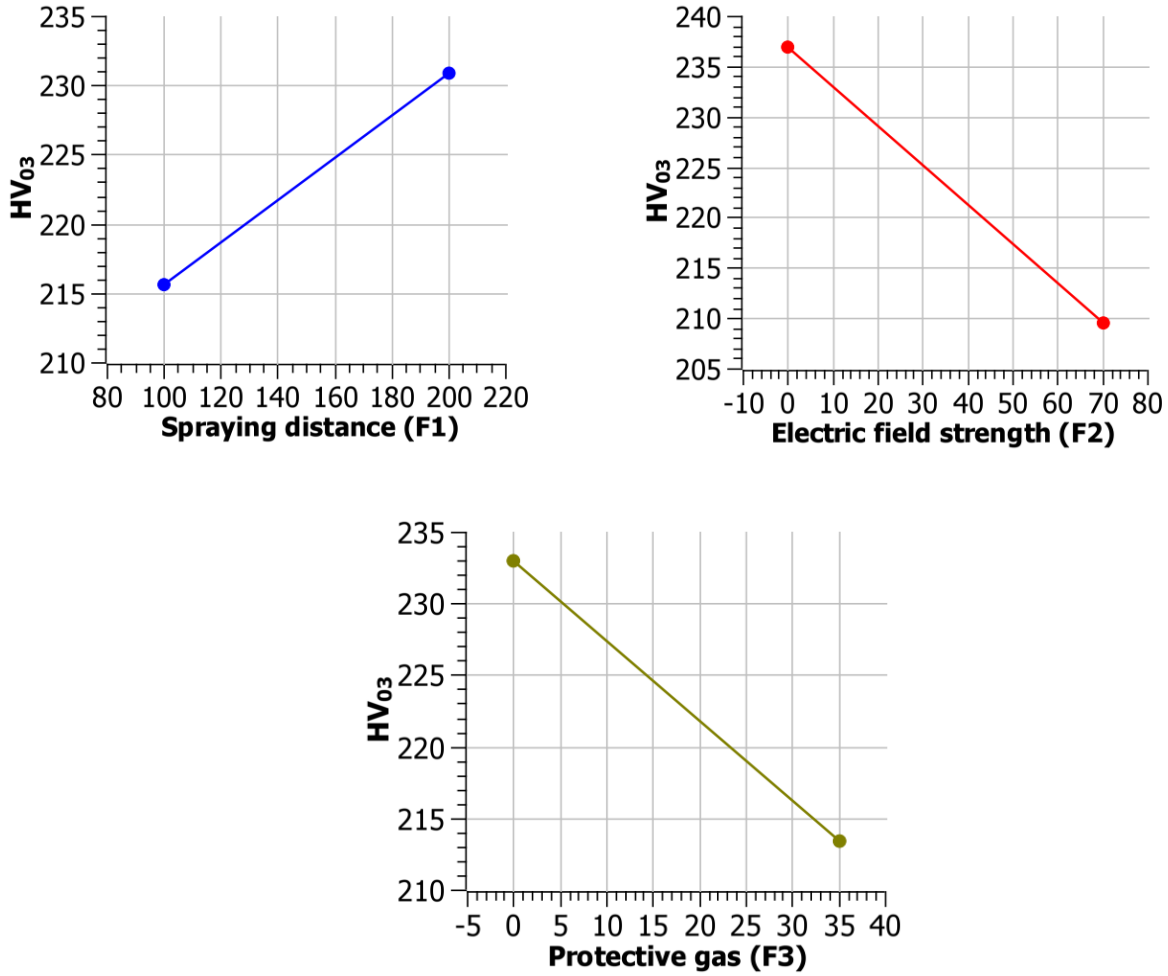

Figure 3.2.5 The effect of factors on the hardness of the deposited layers (Roata, 2017b).

To achieve a comprehensive interpretation of results, it is essential to consider the interactions among factors. The interaction graph illustrates the effects of one factor at its minimum and maximum levels on another factor. The response variable (hardness) is represented on y-axis, while the factor values are depicted on x-axis. Non-parallel lines indicate a significant interaction between the factors. This scenario arises when the slopes of effects differ for the two factors, leading to intersecting lines on the graph.

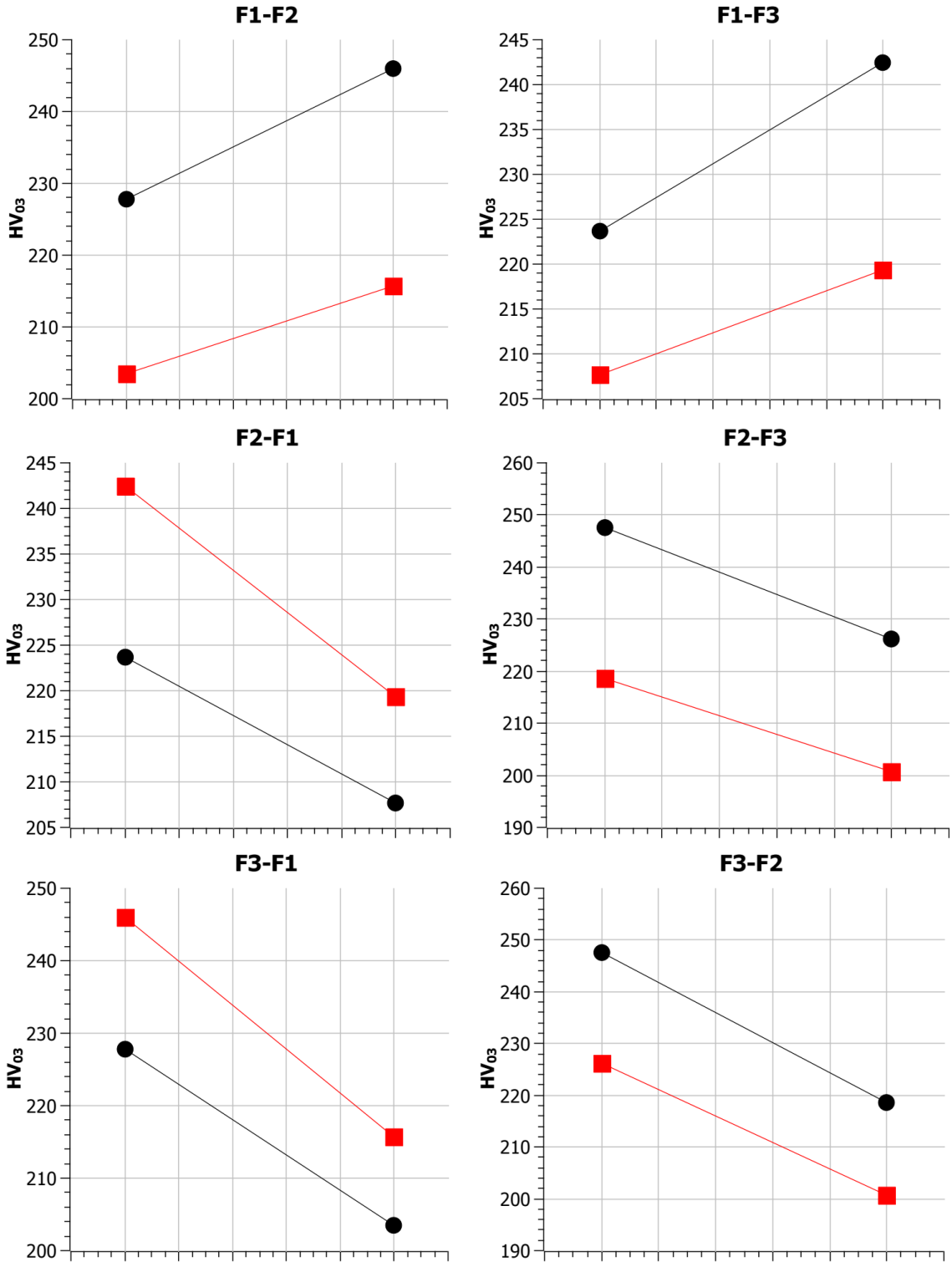

Figure 3.2.6 Interaction of factors (Roata, 2017b).

By applying an electric field with a voltage of 70 volts and maintaining an argon (Ar) protective gas flow rate of 35 liters per minute, the oxidation processes are effectively curtailed. This reduction in oxidation directly correlates with a decrease in the hardness of deposited layer, identified as Pcu7, thereby indicating a significant alteration in material properties consequent to employed parameters

Ohmic resistance

Based on Ohm's law, a setup has been developed for the measurement of ohmic resistance, as illustrated in Figure 3.2.7 This setup adheres to several key considerations:

- The current intensity is measured using an ammeter, which must be connected in series with the circuit elements under examination.
- The voltage (U) does not possess a precisely defined value; rather, it is influenced by the configuration of external circuit.
- The voltmeter, used for measuring voltage, is connected in parallel with the specific circuit element being analyzed.

As the voltage applied to the conductor is increased, there is a corresponding increase in current intensity flowing through the conductor. Provided that the temperature of the conductor remains constant, the ratio of voltage to current is effectively constant. For a metallic conductor held at a constant temperature, the ratio U/I remains consistent, thus serving as a characteristic property of the conductor. Furthermore, it is observed that an increase in the homogeneity of a material results in a decrease in its ohmic resistance.

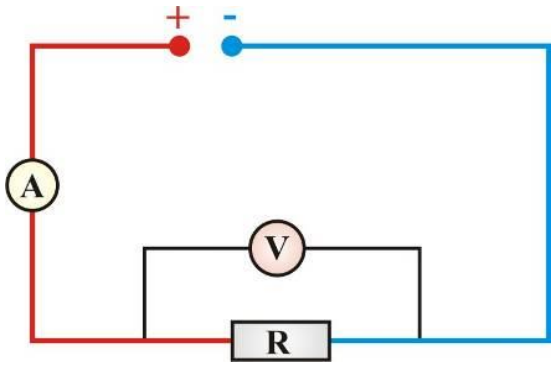

Figure 3.2.7 Schematic diagram of the setup for measuring ohmic resistance (Roata, 2017b).

Table 3.2.3 Electrical resistivities [Ω]

Measuring area	No. of measurements	U [V]	I [A]	R=U/I [Ω]	Average electrical resistivities [Ω]
Deposited layer $P_{Cu}2$	1	0,615	4,996	0,123	0,124
	2	0,620	4,996	0,124	
	3	0,630	4,997	0,126	
	4	0,620	4,996	0,124	
Deposited layer $P_{Cu}7$	1	0,460	4,996	0,092	0,095
	2	0,475	4,996	0,095	
	3	0,470	4,997	0,094	
	4	0,490	4,996	0,098	

$$R = 0{,}110 + 0{,}003 * F1 - 0{,}009 * F2 - 0{,}001 * F3 + 0 * F1F2 - 0{,}001 * F1F3 - 0{,}001 * F2F3 + 0{,}001 * F1F2F3 \quad (3.2.2)$$

The graphs (Figure 3.2.8) illustrate the effects of primary factors, specifically coefficients of first-degree terms in the mathematical model. The ohmic resistance of deposited layers decreases as sputtering distance decreases. The use of electrical charges and protective gas prevents the formation of oxides and, consequently, reduction in hardness; however, it enhances the homogeneity of deposited layers.

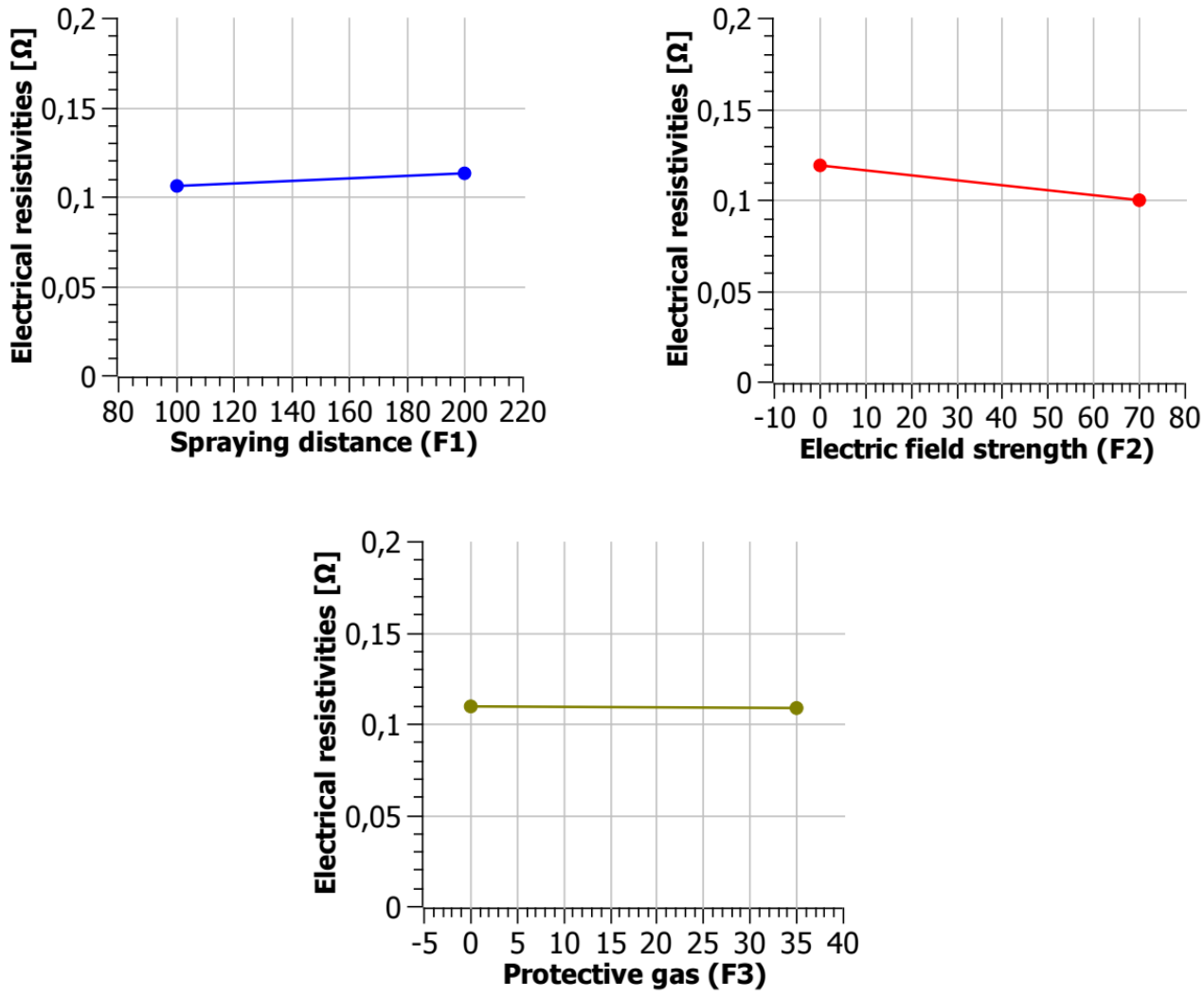

Figure 3.2.8 The effect of factors on the ohmic resistance of deposited layers (Roata, 2017).

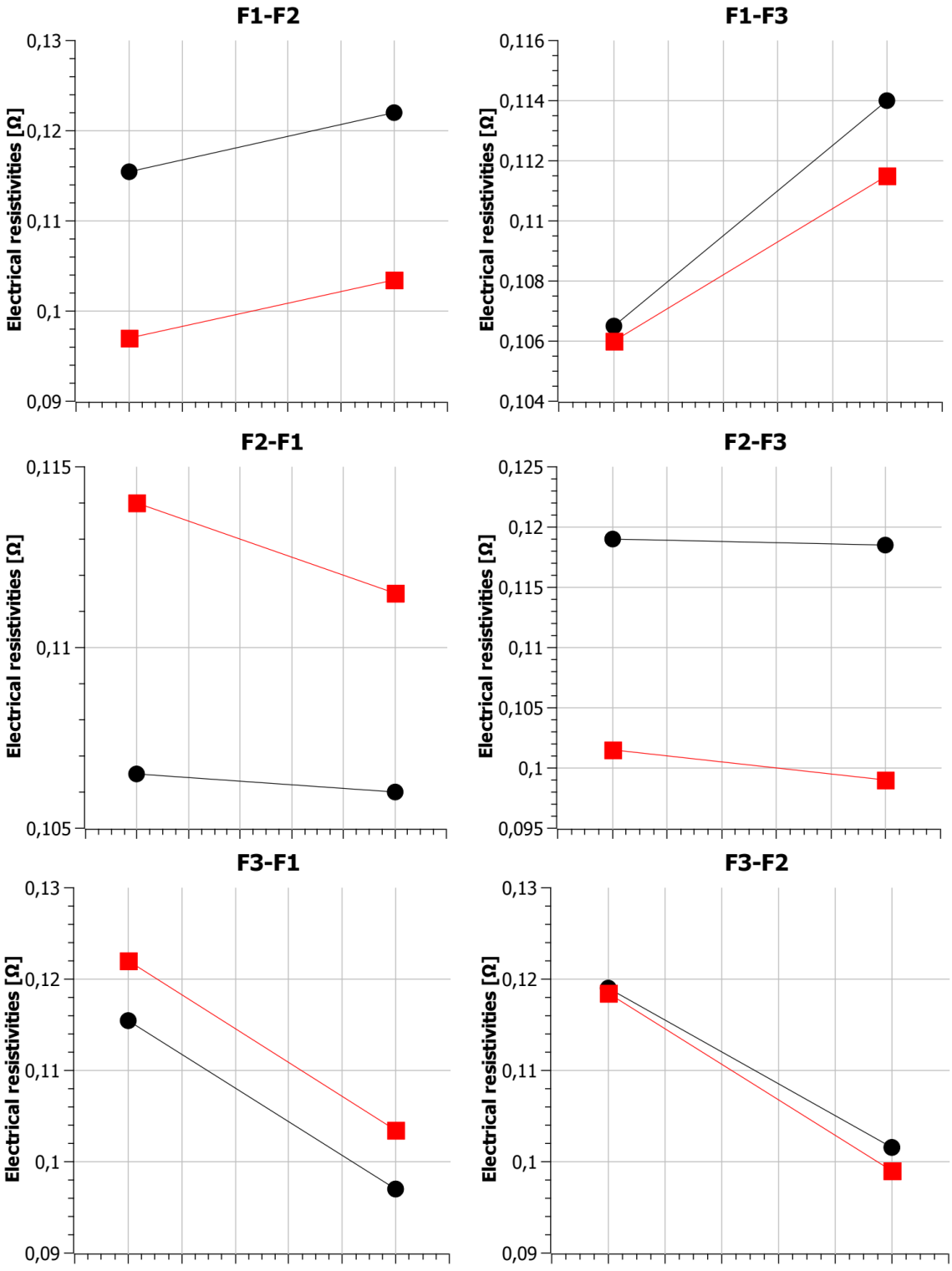

Figure 3.2.9 Interaction of factors (Roata, 2017b).

The interaction graph delineates the effects of a given factor at both its minimum and maximum levels on a second factor. The response variable, defined as ohmic resistance, is positioned along the y-axis, whereas the respective values of influencing factors are represented on x-axis. Notably, a substantial influence of factor F2 (electric field voltage) on the other two variables—namely,

sputtering distance and protective gas—is prominently observed, indicating that variations in electric field voltage significantly affect the interactions between these parameters (Roata, 2017).

The implementation of an electric field with a voltage of 70 V, alongside a protective argon gas flow rate of 35 L/min, significantly reduces the degree of oxidation occurring during the deposition process. This reduction in oxidation contributes to a marked decrease in electrical resistivity of the deposited layer (Pcu7), thereby enhancing its conductive properties.

The roughness of the deposited layers

Surface roughness is characterized by the presence of microscopic irregularities, which quantify the deviations from ideal surface profile along the normal vector to the surface (the direction of measurement). The assessment of surface roughness is performed through the computation of specific parameters outlined in the SR EN ISO 4287:2003 standard. This analysis encompasses two primary categories of parameters: physical, which pertain to measurable attributes of the surface, and statistical, which involve the analysis of surface height distributions and variations.

To ensure the highest level of accuracy in the obtained results, four parallel measurements were systematically performed in the direction of the spray application. The following section delineates the values for the parameters Ra, Rq, Rz, Rv, Rp, and Rt corresponding to the eight experimental samples investigated in this study.

Table 3.2.4 Roughness of deposited layers (Roata, 2017b).

Roughness [µm]	**Measurement area: deposited layer**				**Average roughness**
	Measurement number				
	1	**2**	**3**	**4**	
			$P_{Cu}2$		
Ra	10,410	10,010	10,505	10,443	**10,342**
Rq	12,731	12,670	13,199	13,075	**12,919**
Rz	55,510	55,097	54,156	53,495	**54,565**
Rv	24,955	29,339	27,790	24,967	**26,763**
Rp	30,556	25,758	26,366	28,528	**27,802**
Rt	55,511	55,097	54,156	53,495	**54,565**
			$P_{Cu}7$		
Ra	7,514	6,362	5,622	7,676	**6,794**
Rq	9,273	8,130	7,569	9,373	**8,586**
Rz	34,842	32,218	33,342	35,796	**34,050**
Rv	18,054	13,566	15,379	18,165	**16,291**
Rp	16,495	18,652	17,963	17,630	**17,685**
Rt	34,549	32,218	33,342	35,795	**33,976**

$$R = 45{,}120 + 1{,}777 * F1 - 4{,}782 * F2 - 3{,}073 * F3 - 0{,}247 * F1F2 - 0{,}04 * F1F3 - 1{,}131 * F2F3 + 2{,}553 * F1F2F3 \quad (3.2.3)$$

The graphs (Figure 3.2.10) illustrate the effects of primary factors, specifically the coefficients of first-degree terms of the mathematical model. Total roughness decreases as the sputtering distance decreases. By utilizing electric charges and protective gas, the formation of oxides is prevented, which in turn helps maintain hardness while improving the homogeneity of deposited layers.

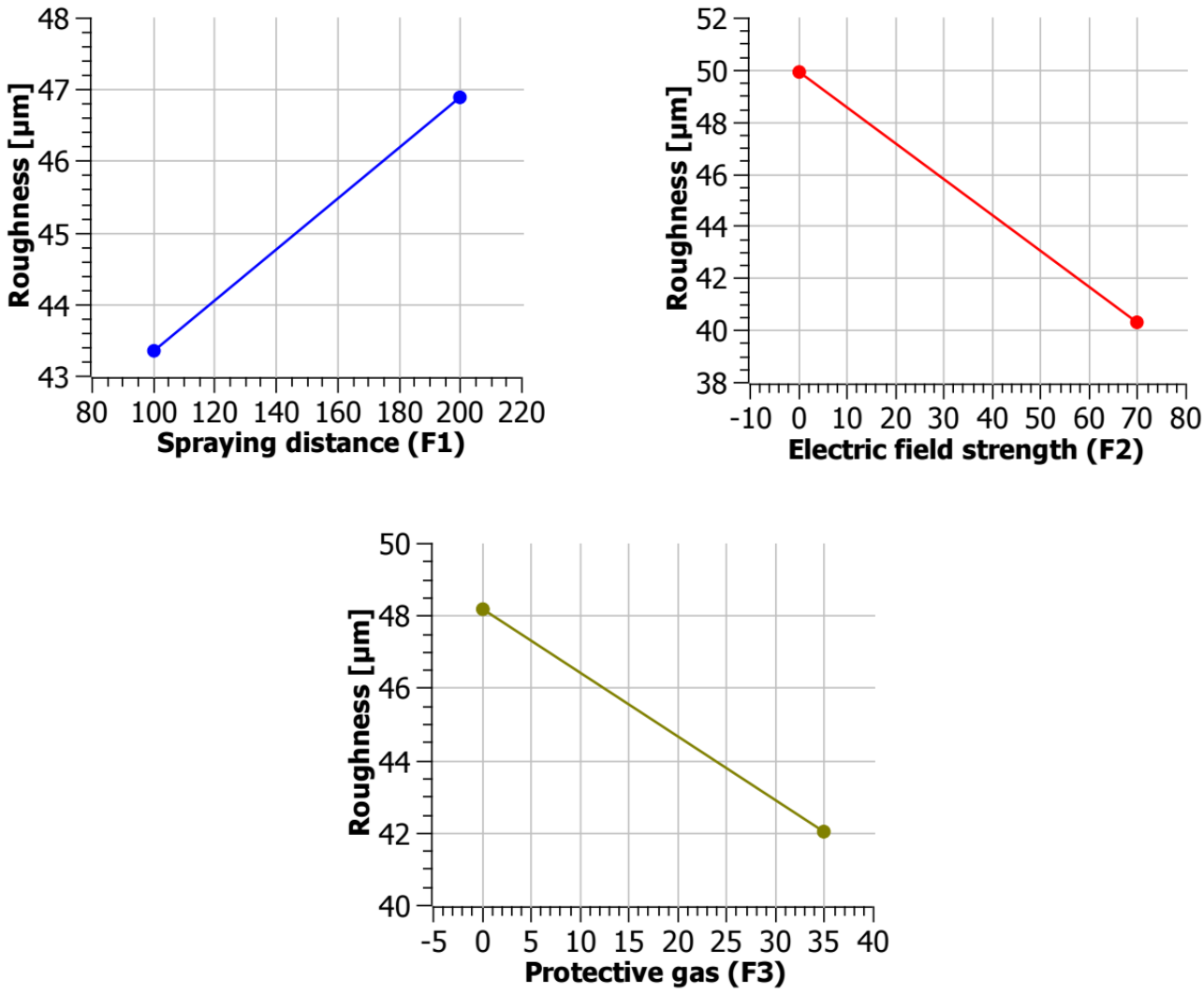

Figure 3.2.10 The effect of factors on the roughness of deposited layers (Roata, 2017b).

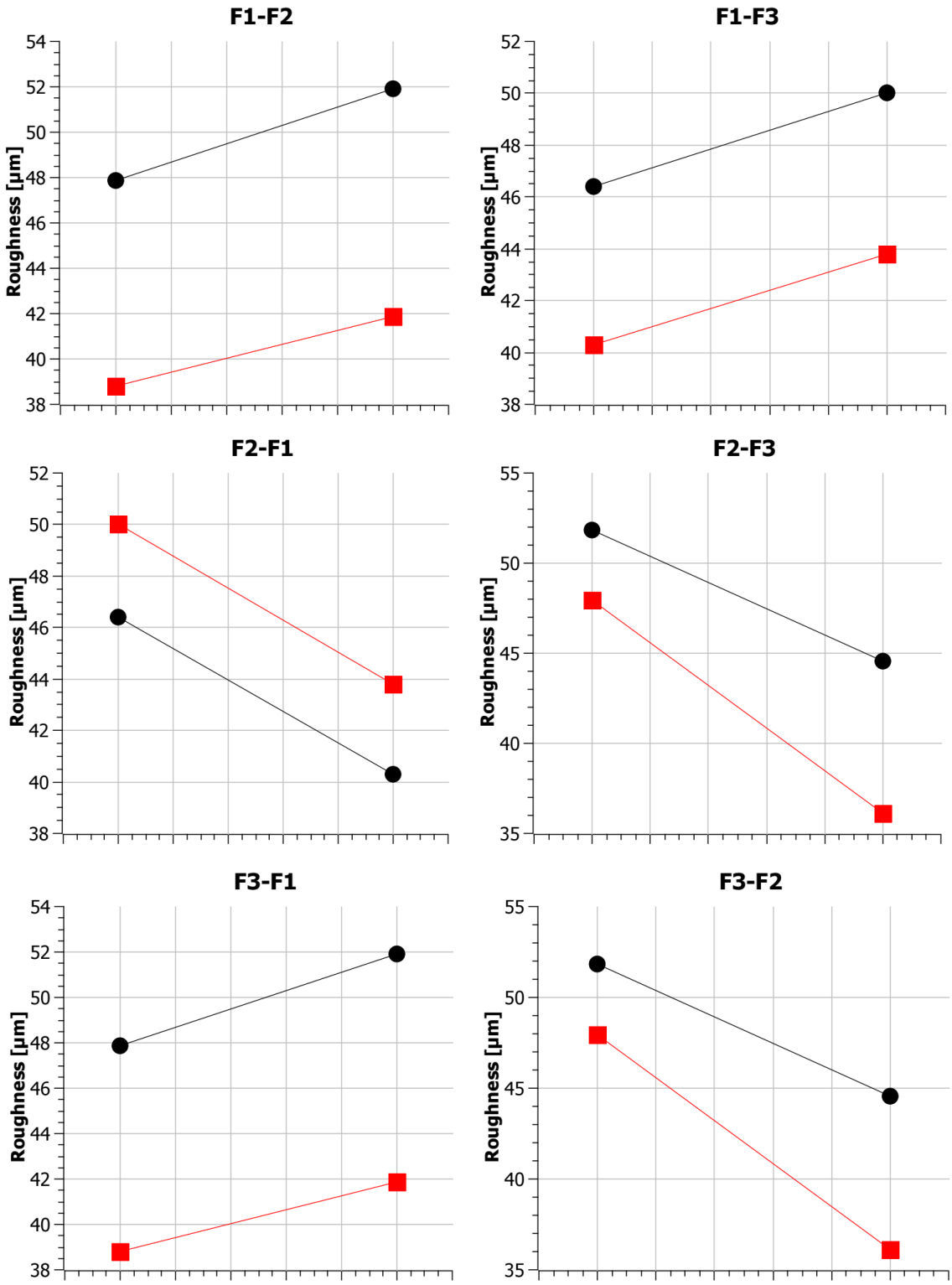

Figure 3.2.11 Interaction of factors (Roata, 2017b).

The response (total roughness) is represented on y-axis, while the values of factors are on x-axis. In this situation, a major influence of factor F2 (field voltage) on factor F3 (protective gas) is observed. In the other cases, the slopes are parallel, and the factors only influence the response (total roughness).

The application of an electric field voltage set at 70 V, in conjunction with a controlled argon gas flow rate of 35 liters per minute, facilitates a substantial reduction in the oxidation levels of deposited layer. This reduction is critical, as it leads to a corresponding decrease in several key surface roughness parameters, namely, Ra (average roughness), Rq (root mean square roughness), Rz (average maximum height), Rv (maximum depth), Rp (maximum profile peak height), and Rt (total height of the profile), for the layer identified as PCu7.

Determination of the contact angle

To determine the contact angle, one considers a droplet of liquid (such as water or oil) positioned on a horizontal surface. The droplet can exhibit two distinct configurations:

1. a contact angle of 0°, in which the liquid droplet is entirely spread across the surface;
2. a contact angle of 180°, where the droplet retains a spherical shape due to its higher density.

Between these two extreme configurations, the liquid droplet will display a measurable and variable contact angle, determined by the interaction with the denser phase. An interfacial tension arises between the droplet and the surface, exerting a tangential force at the surface of the droplet. This force includes a horizontal component represented by cos θ, which draws the perimeter of the droplet towards its center.

a) b)

Figure 3.2.12 Droplet of liquid on a solid surface: (a) The interfacial tension forces modify the liquid droplet into a spherical shape. (b) The forces acting on the liquid droplet and the contact angle (Erle & Waqi, 2008).

Table 3.2.5 The contact angle of the liquid droplet (water/oil) on the sample $P_{Cu}2$ (Roata, 2017b).

Angle [°]	**Measuring area: deposited layer Drop of liquid**					
	water		**Average of the angles**	**oil**		**Average of the angles**
	1	**2**		**1**	**2**	
$\boldsymbol{\theta_s}$	45,60	45,50	**45,55**	122,6	121,90	**122,25**
$\boldsymbol{\theta_d}$	42,60	42,00	**42,30**	121,8	122,30	**122,05**
$\boldsymbol{\theta_{circle}}$	38,80	40,00	**39,40**	120,1	120,40	**120,25**

$\boldsymbol{\theta_{ellipse}}$	40,70	41,20	**40,95**	121	119,80	**120,40**
$\boldsymbol{StDev_{circle}}$	0,57	0,48	**0,52**	0,165	0,158	**0,16**
$\boldsymbol{StDev_{ellipse}}$	1,05E-04	1,14E-04	**1,10E-04**	1,93E-04	1,82E-04	**1,88E-04**

Figure 3.2.13 Representation of contact angles for $P_{Cu}2$ (Roata, 2017b).

Table 3.2.6 The contact angle of the liquid droplet (water/oil) on the sample $P_{Cu}7$ (Roata, 2017b).

Angle [°]	**Measuring area: deposited layer Drop of liquid**					
	water		**Average of the angles**	**oil**		**Average of the angles**
	1	**2**		**1**	**2**	
$\boldsymbol{\theta_s}$	87,20	87,40	**87,30**	129,80	128,40	**129,10**
$\boldsymbol{\theta_d}$	79,60	80,00	**79,80**	131,50	130,80	**131,15**
$\boldsymbol{\theta_{circle}}$	87,20	85,40	**86,30**	131,20	131,40	**131,30**
$\boldsymbol{\theta_{ellipse}}$	83,40	87,20	**85,30**	131,40	131,70	**131,55**
$\boldsymbol{StDev_{circle}}$	0,98	0,94	**0,96**	0,08	0,12	**0,10**
$\boldsymbol{StDev_{ellipse}}$	5,73E-05	5,43E-05	**5,58E-05**	3,25E-04	3,75E-04	**3,50E-04**

Figure 3.2.14 Representation of contact angles for $P_{Cu}7$ (Roata, 2017b).

$$R = 59{,}69 - 4{,}59 * F1 + 10{,}44 * F2 + 5{,}49 * F3 - 0{,}89 * F1F2 + 1{,}64 * F1F3 + 3{,}91 * F2F3 + 2{,}55 * F1F2F3 \quad (3.2.4)$$

The graphs (Figure 3.2.15) illustrate the effects of main factors, namely coefficients of first-degree terms of the mathematical model. The contact angle of the water droplet increases as the

degree of homogeneity of deposited layer increases. The homogeneity of deposited layers is achieved by using electric charges and protective gas, which prevent the formation of oxides.

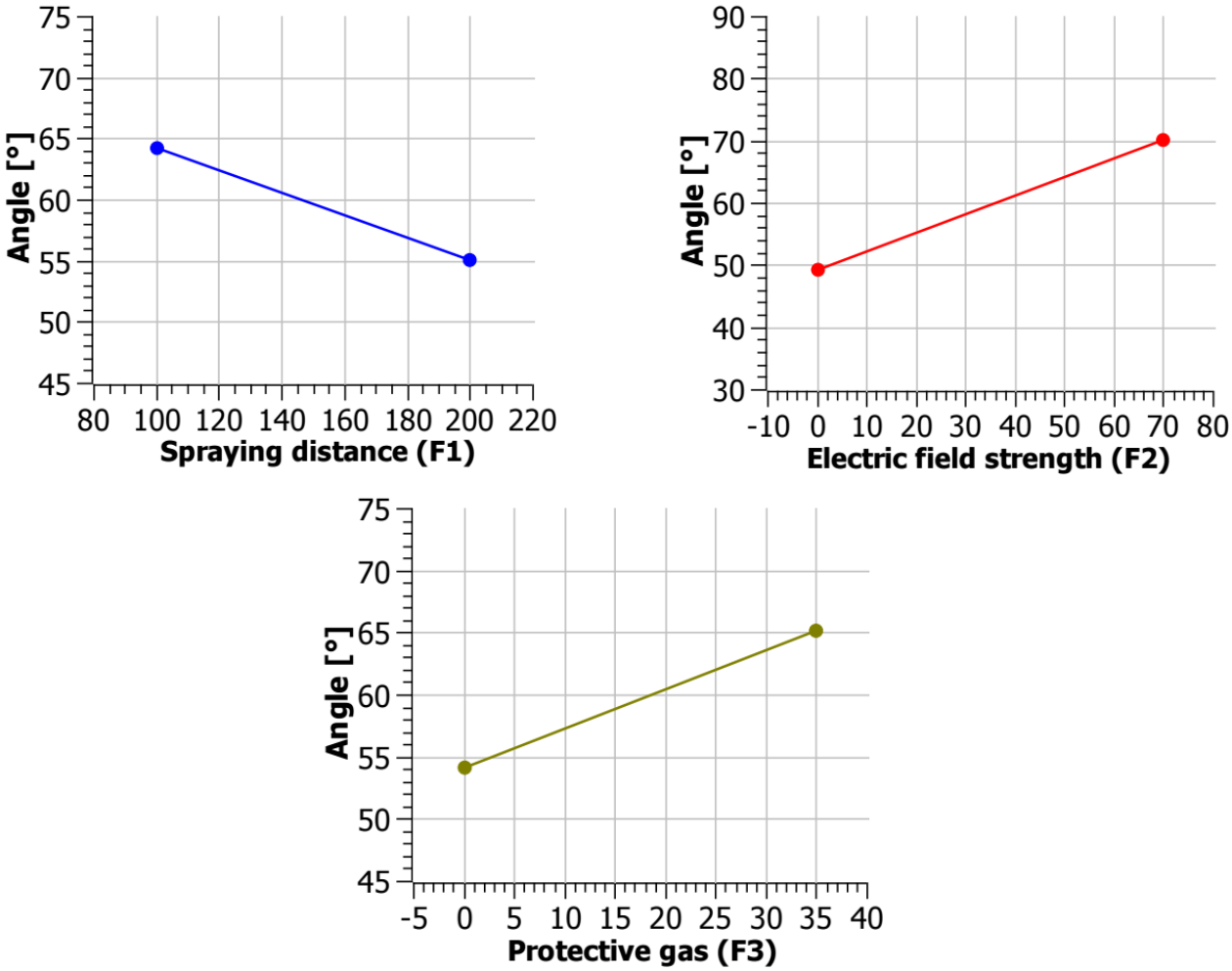

Figure 3.2.15 The effect of factors on the contact angles of deposited layers (Roata, 2017).

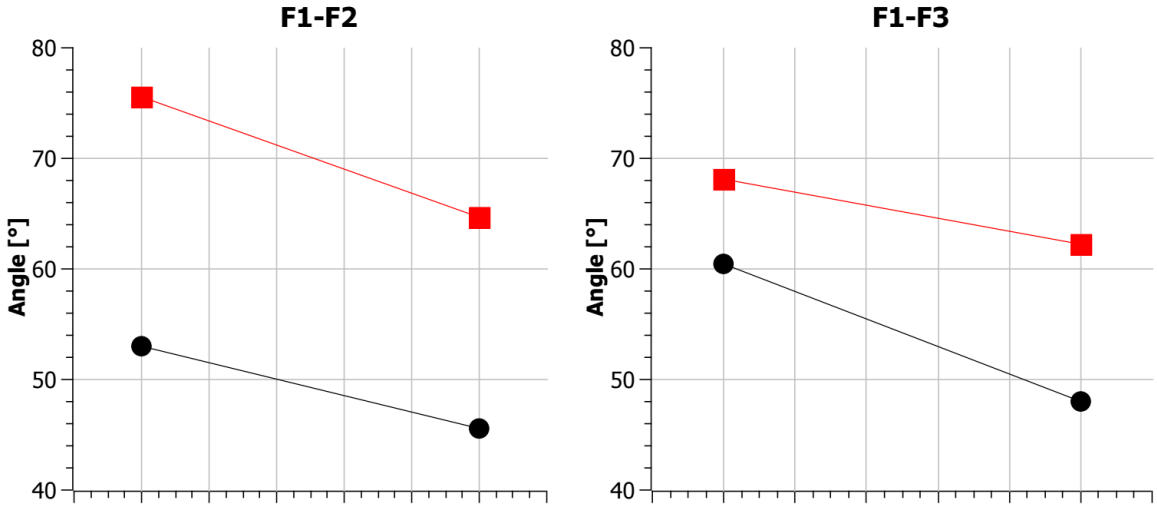

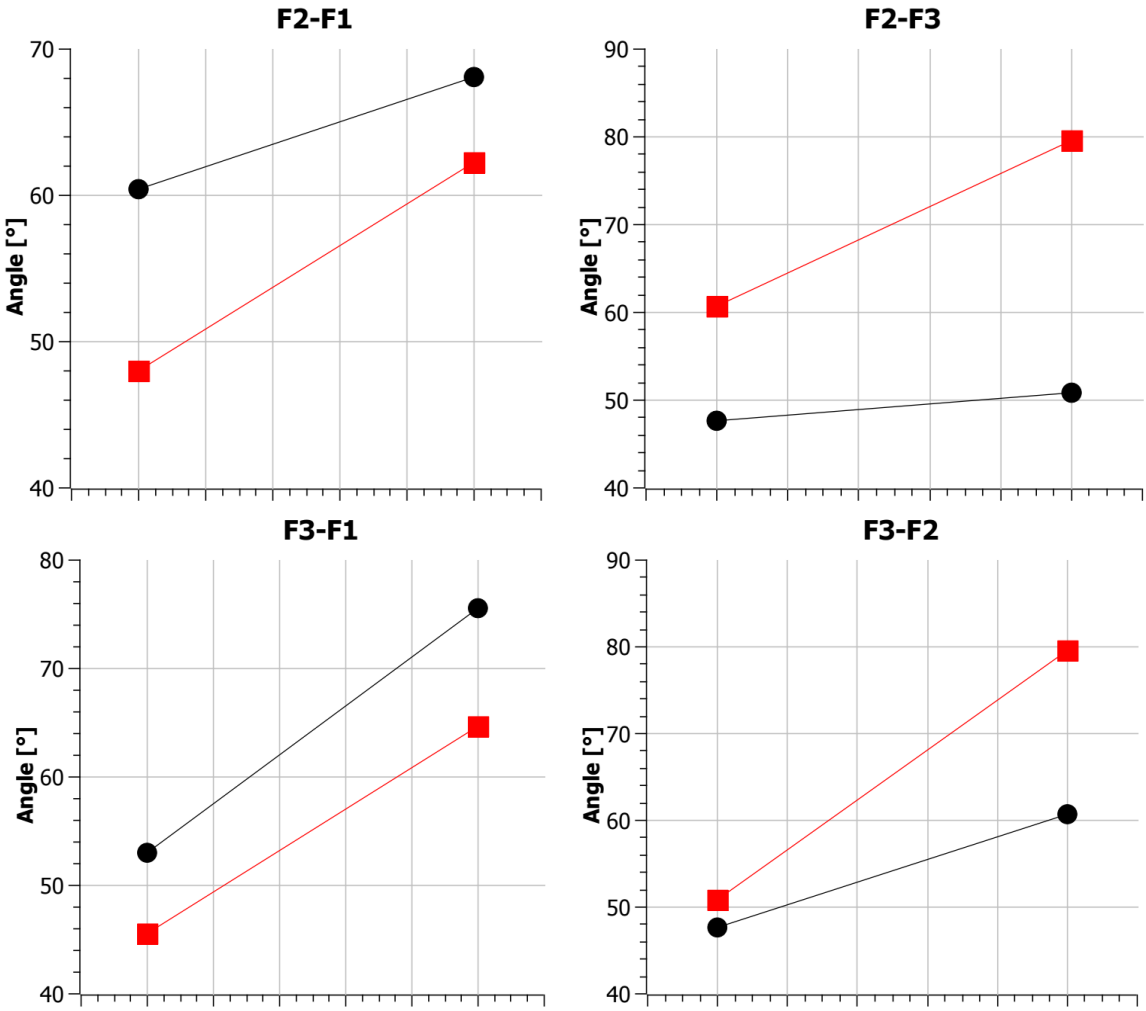

Figure 3.2.16 Interaction of factors (Roata, 2017b).

The response variable, represented by the contact angle of the water droplet, is depicted on the y-axis, whereas the corresponding values for the factors are displayed on the x-axis. In this context, a significant influence of factor F1 (spray distance) on factor F3 (protective gas) is evident. Additionally, factor F2 (electric field voltage) demonstrates a considerable impact on both factors F1 and F3. In other instances, the slopes of the graphs are parallel, indicating that the factors exert influence solely on the response variable, which is the contact angle of the water droplet (Roata, 2017).

The application of an electric field set at 70 volts and maintaining a consistent flow of argon gas at 35 liters per minute, the oxidation level during deposition is substantially decreased. This controlled environment not only minimizes the risk of unwanted oxidation but also facilitates the creation of a hydrophobic surface property in the PCu7 layer. The enhanced hydrophobic characteristics are pivotal for various applications, as they improve the material's resistance to moisture and enhance its overall durability and performance.

3.3 Influence of the protective gas on the properties of coatings NiCrBSiFe deposited by thermal spraying on S235JR

In this research initiative, we conducted a series of experimental investigations aimed at evaluating the properties and performance of samples fabricated through advanced flame and powder spray techniques. The CastoDyn DS 8000 system, notable for its incorporation of four distinct spray modules, provides a versatile platform that ensures high efficiency and adaptability in various industrial applications. This versatility is pivotal for manufacturing of components that require specific material characteristics, such as enhanced wear resistance or thermal protection. For sample preparation in this study, we opted for the standard spray mode known as SSM 10. This mode is designed to optimize the deposition parameters, thereby facilitating the attainment of a uniform and robust coating on the substrate materials. Utilizing this mode, we aimed to systematically assess the relationship between process parameters and the resulting microstructural and mechanical properties of the sprayed coatings. The selection of filler materials is critical in determining the performance outcomes of the deposition process. Therefore, we carefully chose a filler material with a specific chemical composition tailored to achieve desired characteristics in the final product. The detailed chemical makeup of the filler material, including its elemental percentages and any relevant phases, is comprehensively documented in Table 3.3.1 This table serves as a reference point for understanding how variations in composition may influence deposition behavior, adherence to substrates, and overall coating performance (Roata, 2018b).

Subsequent analyses will focus on evaluating key parameters such as adhesion strength, hardness, and microstructural integrity of the coatings produced. The insights gained from this investigation will contribute to the optimization of flame and powder spray processes, ultimately enhancing the quality and performance of coated components in demanding applications across various industries.

Table 3.3.1 The chemical composition of Cu38Ni filler material (Roata, 2018b).

Sample Mark	Type of powder	Chemical composition %				
		Ni	Cr	B	Si	Fe
P1 – P4	NiCrBSiFe	Balance	14 – 15	3 – 3.5	4 – 4.5	3.5 – 4

To determine the optimal number of experimental samples, the Design of Experiments (DOE) methodology was utilized. This systematic approach involves conducting repetitions of experiments while purposefully varying one or more input factors (F) to assess their effects on the outcome. In the context of this study, several critical parameters influencing the quality of layers deposited through the flame and powder thermal spraying process have been identified. Specifically, the following parameters were selected for further investigation:

- Parameter 1: Spraying distance (measured in millimeters), which is a crucial factor that affects the thermal profile and the kinetic energy of the particles during the deposition process.
- Parameter 2: Protection gas flow rate (measured in liters per minute), which plays a significant role in maintaining a controlled environment around the spray plume, thereby impacting the oxidation of particles and overall integrity of the coating.

By systematically varying these parameters within the experimental design, the study aims to elucidate their individual and collective effects on the deposition quality. The insights gained from this analysis will contribute significantly to enhancing the effectiveness and reliability of thermal spraying process, ultimately leading to improved coating performance across a range of industrial applications. Further optimization based on these results will help ensure that the resultant coatings meet the specified engineering standards and operational requirements (Roata, 2018b).

Table 3.3.2 The shape of experimental matrix and parameters of the thermal spraying process (Roata, 2018b).

Sample	Spraying distance [mm]	Protection gas Ar [l/min]
P1	-1 (100)	-1 (0)
P2	**1 (200)**	**-1 (0)**
P3	**-1 (100)**	**-1 (35)**
P4	1 (200)	-1 (35)

Microscopic analysis

The samples fabricated via flame and powder thermal spraying underwent comprehensive macroscopic and microscopic assessments to evaluate the quality of deposited layers, with a particular focus on adhesion properties, as well as the presence and volume of oxides and pores. To facilitate these analyses, multiple specimens were sectioned from flame-sprayed samples.

Subsequent to surface preparation, chemical etching was performed using a 3% Nital solution, applied for a brief duration of 4 to 6 seconds. This process was critical for revealing microstructural characteristics, such as grain boundaries and phases, thereby allowing for a thorough investigation of the quality metrics of coatings. The systematic approach to specimen preparation and analysis is intended to yield insights into the performance and durability of coatings produced through thermal spraying process, ultimately contributing to the enhancement of application-specific requirements in various industrial contexts.

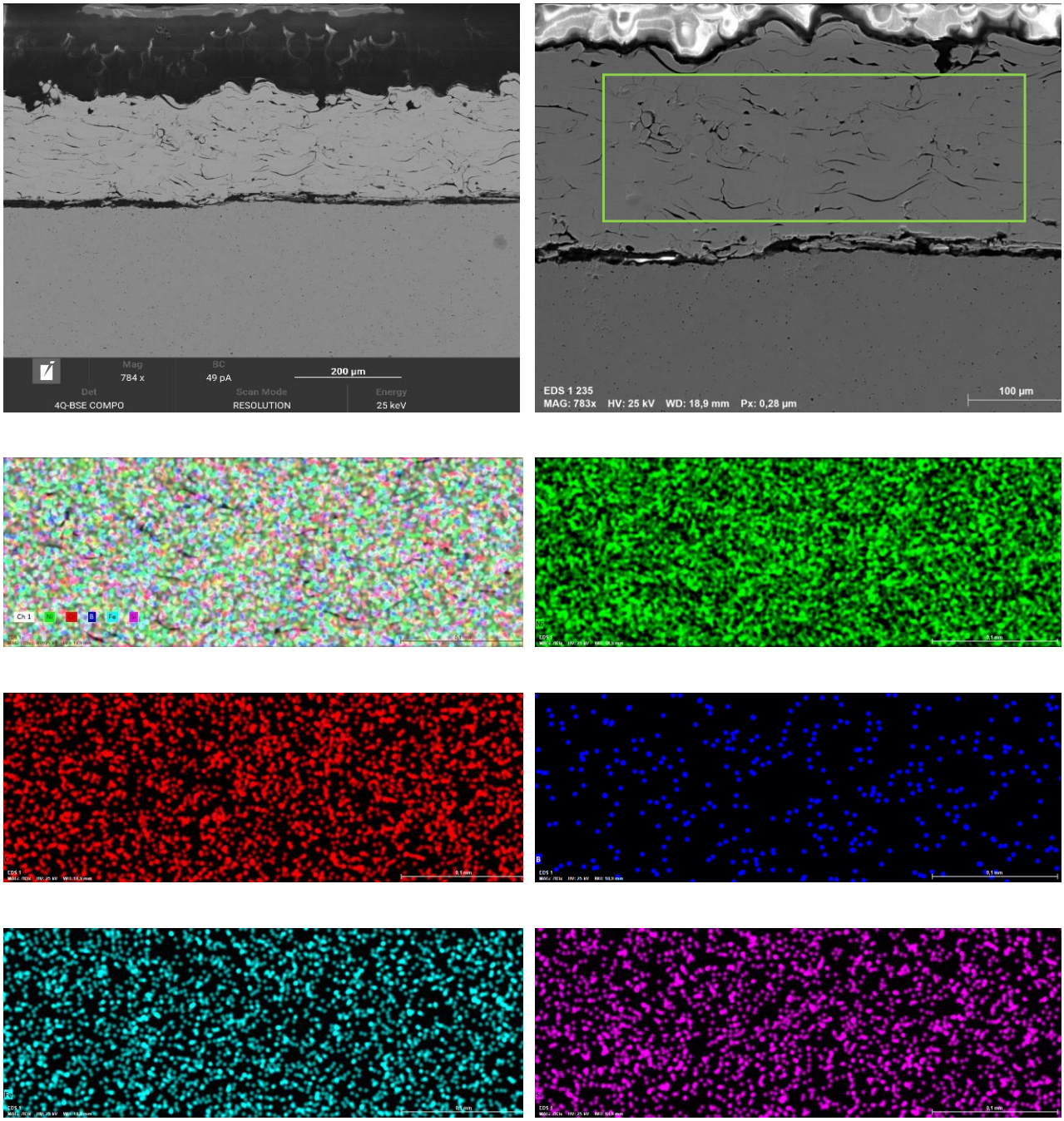

Figure 3.3.1 Structures in deposition areas on the base metal S235JR (P_2).

The deposited layer has a typical lamellar appearance (in several layers), and in some regions, pores, oxides and bent particles can be highlighted as a result of the thermal spraying process. The interface with the substrate has pores, partial melting and high density of oxides.

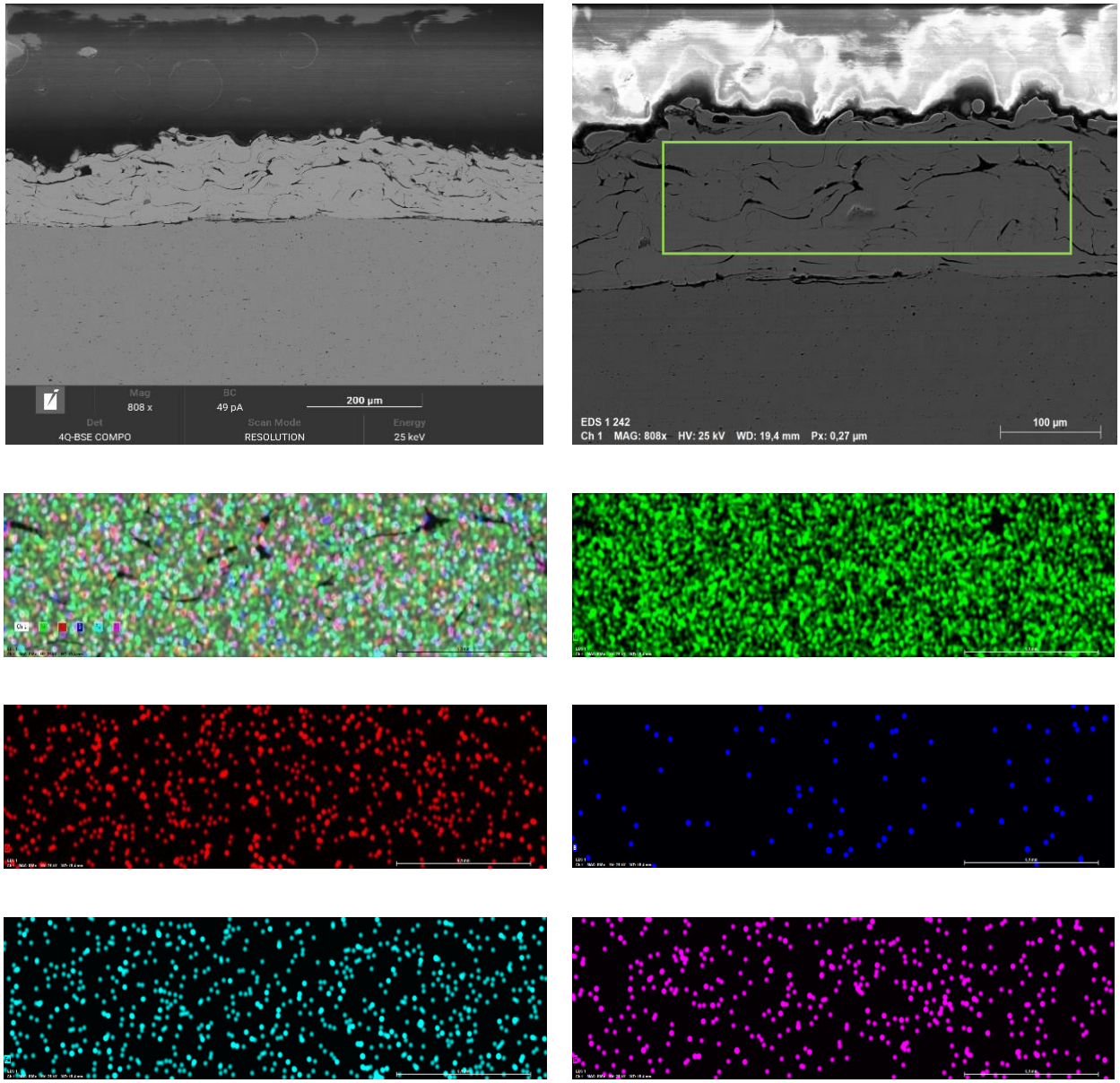

Figure 3.3.2 Structures in the deposition areas on the base metal S235JR (P3).

The deposited layer exhibits a characteristic lamellar structure, displaying distinct layers that are typical of the thermal spraying process. This layered morphology is indicative of the deposition technique employed, where molten or semi-molten particles adhere to form a cohesive coating. In several regions of the layer, imperfections such as pores, oxides, and bent particles become evident, reflecting variations in thermal energy and particle dynamics during application.

Particularly at the interface between the coating and substrate, several critical features are observed. The presence of pores can disrupt the integrity of the coating, potentially impacting adhesion and overall performance. Additionally, signs of partial melting at the interface suggest that some particles did not fully solidify before contact, which may influence the bonding characteristics between the layer and the substrate. The high density of oxides detected at this junction raises concerns regarding oxidation, which can compromise the mechanical properties and corrosion resistance of the coating (Roata, 2018b).

In summary, while the lamellar structure of deposited layer showcases the complex nature of thermal spray coatings, the observed defects—including pores, oxides, and bent particles—underscore the necessity of optimizing processing parameters to enhance adhesion and minimize flaws. Understanding these microstructural characteristics is crucial for improving the performance and durability of the coatings in their intended applications.

To achieve a substantial reduction in porosity and oxidation rates while simultaneously enhancing adhesive properties, it is essential to utilize a controlled experimental framework that incorporates an argon gas flow rate of 35 liters per minute. This specific flow rate is vital for establishing an inert atmosphere, which in turn mitigates interactions with moisture and oxygen. Such conditions are expected to optimize both physical and chemical interactions within the material system, thereby enhancing performance in applications that require robust adhesion and structural integrity. The implementation of these parameters within a systematic framework will facilitate the replicability and reliability of results across multiple experimental trials.

Microhardness tests

Microhardness testing, typically implemented through Vickers or Knoop methods, is particularly valuable for assessing localized hardness variations within the coating. By evaluating the coatings in two orientations, a more nuanced understanding of the hardness is obtained, taking into account the directional dependencies that may arise from the lamellar structure and the inherent characteristics of the deposited particles. The results of this microhardness evaluation provide critical insights into the performance of the coatings under operational stresses. Variations in hardness values along different orientations may indicate differing resistance to wear, deformation, and overall mechanical integrity. Such data are essential for predicting the coatings' behavior in applications where directional loading or specific surface interactions are expected (Roata, 2018b).

Table 3.3.3 The interaction of factors and results of microhardness tests (Roata, 2018b).

Sample number	**Metallization distance [mm]**	**Protective gas Ar [l/min]**	**HV_{03}**
P1(A)	-1	-1	542.44
P1(B)	+1	-1	736.78
P1(C)	-1	-1	501.20
P1(D)	+1	-1	632.96
		Arithmetic mean	**603.35**

Moreover, the correlation between hardness results and observed microstructural features, such as porosity, oxide content, and layer adherence, can inform further optimization of the deposition processes. Understanding these relationships helps in tailoring coatings to meet specific

performance requirements in various industrial applications, thereby enhancing their effectiveness and longevity.

To interpret the meaning of the intercept, denoted a_0, one should set both factors to a coded value of 0. This designated experimental point represents the center of the study domain, and the response at this point is designated as y_0.

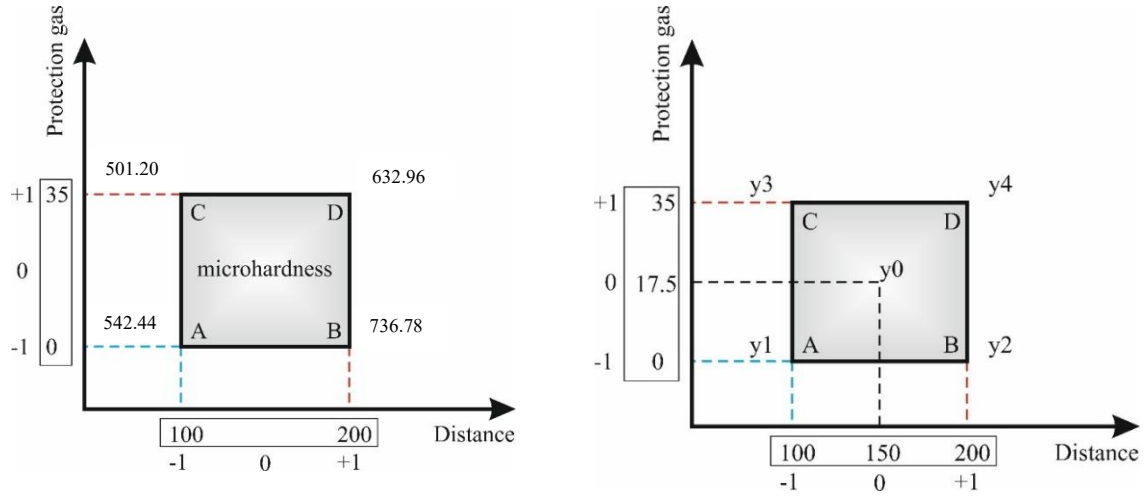

Figure 3.3.3 The response value at the intercept is at the center of the domain (Roata, 2018b).

Meaning of the coefficient of spraying distance (Factor 1)

Let us consider both points, B and D, which are positioned at the high level of factor 1 (spraying distance). The coordinates of these points, expressed in coded units, are as follows:

- Point B: (X1 = +1, X2 = -1)
- Point D: (X1 = +1, X2 = +1)

These coordinates are essential for analyzing the effects of spraying distance on the response variable. Investigating these points allows for a deeper understanding of how variations in this factor influence the outcomes within the context of the experimental study

The response at point B, denoted as y_2, can be derived by utilizing the respective factor levels represented in their coded units:

$$y_2 = a_0 + a_1 \cdot (+1) + a_2 \cdot (-1) + a_{12} \cdot (+1) \cdot (-1) = a_0 + a_1 - a_2 - a_{12} \quad (3.3.1)$$

Similarly, the response at point D, denoted as y_4, can be obtained by employing the corresponding factor levels expressed in coded units:

$$y_4 = a_0 + a_1 \cdot (+1) + a_2 \cdot (+1) + a_{12} \cdot (+1) \cdot (+1) = a_0 + a_1 + a_2 + a_{12} \quad (3.3.2)$$

$$y_2 + y_4 = 2 \cdot (a_0 + a_1)$$

Next, the same calculations for points A and C will be performed, which correspond to the

lower levels of the speed factor. The responses at these points are denoted as y_1 and y_3, respectively. The calculations will utilize the respective factor levels expressed in coded units for both points A and C.

$$y_1 + y_2 = 2 \cdot (a_0 - a_1)$$

$$\overline{y_+} = \frac{y_2 + y_4}{2} = \frac{736.78 + 632.96}{2} = 684.87 \quad (3.3.3)$$

$\overline{y_+} =$ *is the mean of the responses at the high level of the distance factor*

$$\overline{y_-} = \frac{y_1 + y_3}{2} = \frac{542.44 + 501.20}{2} = 521.82 \quad (3.3.4)$$

$\overline{y_-} =$ *is the mean of the responses at the low level of the distance factor*

$$a_1 = \frac{1}{2} \cdot \left(\frac{y_2 + y_4}{2} - \frac{y_1 + y_3}{2} \right) = 81.53 \quad (3.3.5)$$

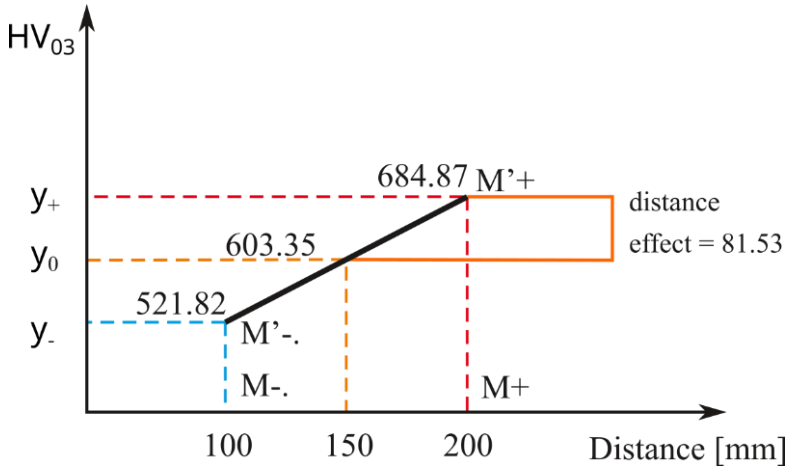

Figure 3.3.4 Illustration of the distance effect (Roata, 2018b).

Meaning of the coefficient of protection gas (Factor 2)

By applying the same rationale, the coefficient a_2 is defined as the average change in the response when factor 2 transitions from zero level to high level. This coefficient reflects the influence of factor 2 within the study domain and is referred to as "the effect of factor 2." In general, when the chosen model is a polynomial, the coefficients associated with first-degree terms represent the effects of respective factors.

$$\overline{y_+} = \frac{y_3 + y_4}{2} = \frac{501.20 + 632.96}{2} = 567.08 \quad (3.3.6)$$

$$\overline{y_+} = \text{is the mean of responses at the high level of distance factor}$$

$$\overline{y_-} = \frac{y_1 + y_2}{2} = \frac{542.44 + 736.78}{2} = 639.61 \tag{3.3.7}$$

$$\overline{y_-} = \text{is the mean of responses at the low level of distance factor}$$

$$a_2 = \frac{1}{4} \cdot (-y_1 - y_2 + y_3 + y_4)$$
$$a_2 = \frac{1}{4} \cdot (-542.44 - 736.78 + 501.20 + 632.96) = -36.27 \tag{3.3.8}$$

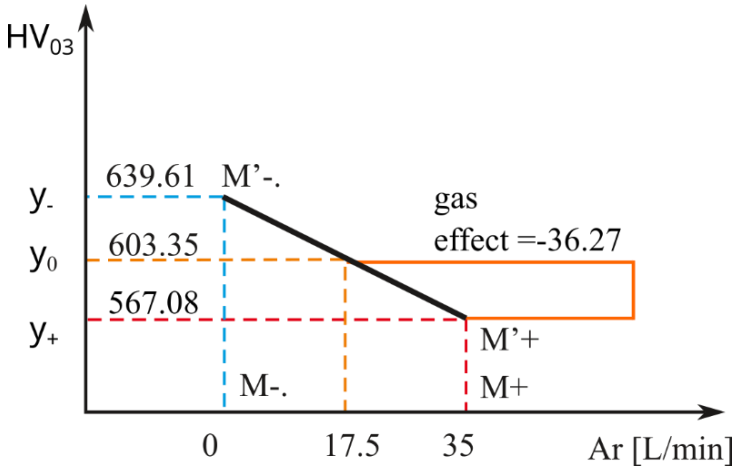

Figure 3.3.5 Illustration of the protection gas effect (Roata, 2018b).

Meaning of the coefficient a12

$$a_{12} = \frac{1}{2} \cdot \left(\frac{y_4 - y_3}{2} - \frac{y_2 - y_1}{2}\right)$$
$$a_{12} = \frac{1}{2} \cdot \left(\frac{632.96 - 501.20}{2} - \frac{736.78 - 542.44}{2}\right) = -7.82 \tag{3.3.9}$$

$$\frac{y_4 - y_3}{2} = \text{is the effect of factor 1 when factor 2 is at its high level}$$

$$\frac{y_2 - y_1}{2} = \text{is the effect of factor 1 when factor 2 is at its low level}$$

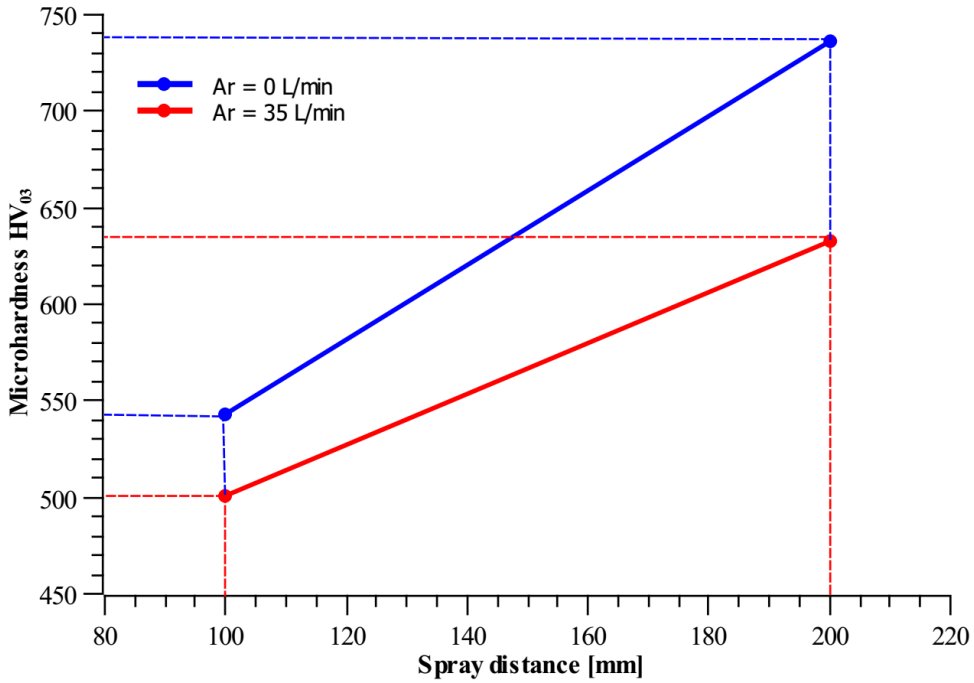

Figure 3.3.6 Illustration of the interaction effect (Roata, 2018b).

The coefficient a_{12} is defined as half of the difference between the two effects associated with the factors. Consequently, this coefficient quantifies the variation in factor 1 resulting from a change in the level of factor 2. Conversely, it can be demonstrated that a_{12} similarly measures the variation in the effect of factor 2 when the level of factor 1 is altered in an analogous manner. Thus, the coefficient a_{12} is referred to as the interaction between factors 1 and 2.

$$HV_{03} = a_0 + a_1 \cdot F1 + a_2 \cdot F2 + a_{12} \cdot F1 \cdot F2$$
$$HV_{03} = 603.35 + 81.53 \cdot F1 - 36.27 \cdot F2 - 7.82 \cdot F1 \cdot F2 \quad (3.3.10)$$

Ohmic resistance

Based on Ohm's law, a measurement setup has been established to determine the ohmic resistance. This setup incorporates several fundamental considerations for accurate measurements:

1. **Current measurement**: The current intensity (I) flowing through the circuit is measured using an ammeter, which is strategically connected in series with the components being analyzed. This configuration ensures that the current measured is representative of the total current flowing through the circuit.
2. **Voltage measurement**: The voltage (U) across the circuit elements does not have a fixed value; instead, it varies depending on the arrangement of the external circuit. This is an important consideration when interpreting the results, as external factors can influence the voltage readings.

3. **Connection of the voltmeter**: The voltmeter, used to measure the voltage across a specific circuit element, is connected in parallel with that element. This arrangement allows for an accurate measurement of the potential difference across the component without significantly altering the overall circuit.

As the applied voltage across the conductor is increased, there is a corresponding increase in the current flowing through it, provided that the conductor's temperature remains unchanged. According to Ohm's law, where V = I * R, the ratio of voltage (U) to current (I), denoted as U/I, remains constant for a particular metallic conductor at a constant temperature. This ratio is a defining characteristic of the conductor, indicating its resistance (R).

Additionally, it has been observed that enhancing the homogeneity of a material can led to a decrease in its ohmic resistance. This relationship suggests that materials with fewer defects, impurities, or inhomogeneities may allow for more efficient electron flow, resulting in lower resistance. Consequently, understanding the material properties and structural uniformity is crucial for optimizing the conductive performance of metals and developing effective applications in electrical and electronic systems (Roata, 2018b).

Table 3.3.4 The interaction of factors and results of ohmic resistance tests (Roata, 2018b).

Sample number	Metallization distance [mm]	Protective gas Ar [l/min]	Ohmic resistance [Ω]
P1(A)	-1	-1	0.318
P1(B)	+1	-1	0.355
P1(C)	-1	-1	0.265
P1(D)	+1	-1	0.334
		Arithmetic mean	**0.318**

Meaning of the coefficient of spraying distance (Factor 1)

$$\overline{y_+} = \frac{y_2 + y_4}{2} = \frac{0.355 + 0.334}{2} = 0.345 \tag{3.3.11}$$

$$\overline{y_+} = \textit{ is the mean of responses at the high level of distance factor}$$

$$\overline{y_-} = \frac{y_1 + y_3}{2} = \frac{542.44 + 501.20}{2} = 0.292 \tag{3.3.12}$$

$$\overline{y_-} = \textit{ is the mean of responses at the low level of distance factor}$$

$$a_1 = \frac{1}{2} \cdot \left(\frac{y_2 + y_4}{2} - \frac{y_1 + y_3}{2} \right) = 0.027 \tag{3.3.13}$$

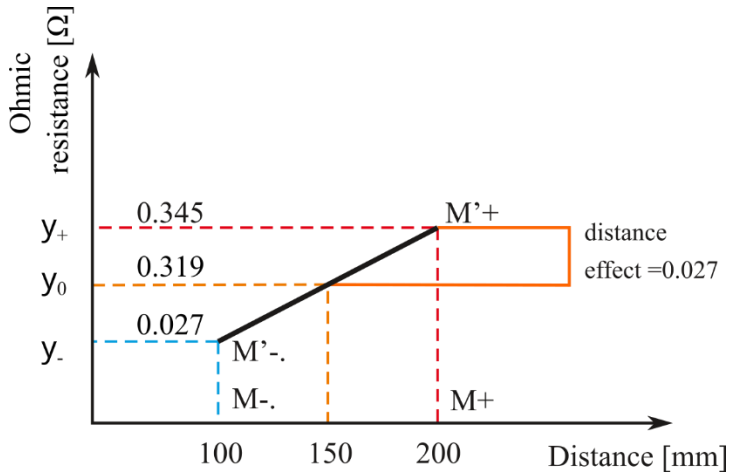

Figure 3.3.7 Illustration of the distance effect (Roata, 2018b).

Meaning of the coefficient of protection gas (Factor 2)

$$\overline{y_+} = \frac{y_3 + y_4}{2} = \frac{0.265 + 0.334}{2} = 0.3 \tag{3.3.14}$$

$\overline{y_+} =$ *is the mean of responses at the high level of distance factor*

$$\overline{y_-} = \frac{y_1 + y_2}{2} = \frac{0.318 + 0.355}{2} = 0.337 \tag{3.3.15}$$

$\overline{y_-} =$ *is the mean of responses at the low level of distance factor*

$$a_2 = \frac{1}{4} \cdot (-y_1 - y_2 + y_3 + y_4)$$
$$a_2 = \frac{1}{4} \cdot (-0.318 - 0.355 + 0.265 + 0.334) = -0.019 \tag{3.3.16}$$

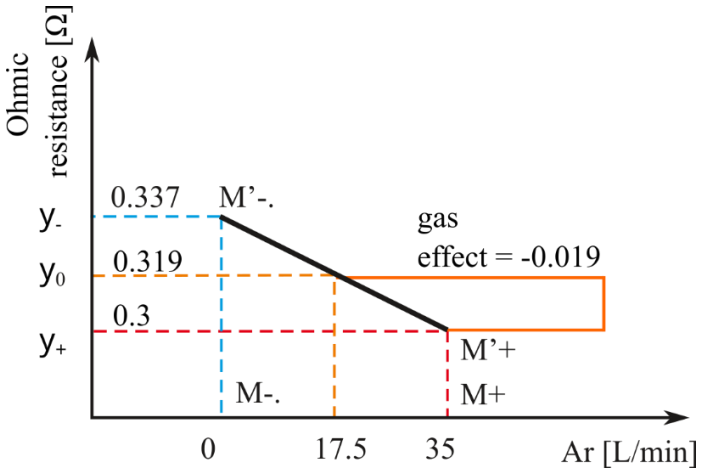

Figure 3.3.8 Illustration of the protection gas effect (Roata, 2018b).

Meaning of the coefficient a12

$$a_{12} = \frac{1}{2} \cdot \left(\frac{y_4 - y_3}{2} - \frac{y_2 - y_1}{2} \right)$$
$$a_{12} = \frac{1}{2} \cdot \left(\frac{0.334 - 0.265}{2} - \frac{0.355 - 0.318}{2} \right) = 0.008 \quad (3.3.17)$$

$$\frac{y_4 - y_3}{2} = is\ the\ effect\ of\ factor\ 1\ when\ factor\ 2\ is\ at\ its\ high\ level$$

$$\frac{y_2 - y_1}{2} = is\ the\ effect\ of\ factor\ 1\ when\ factor\ 2\ is\ at\ its\ low\ level$$

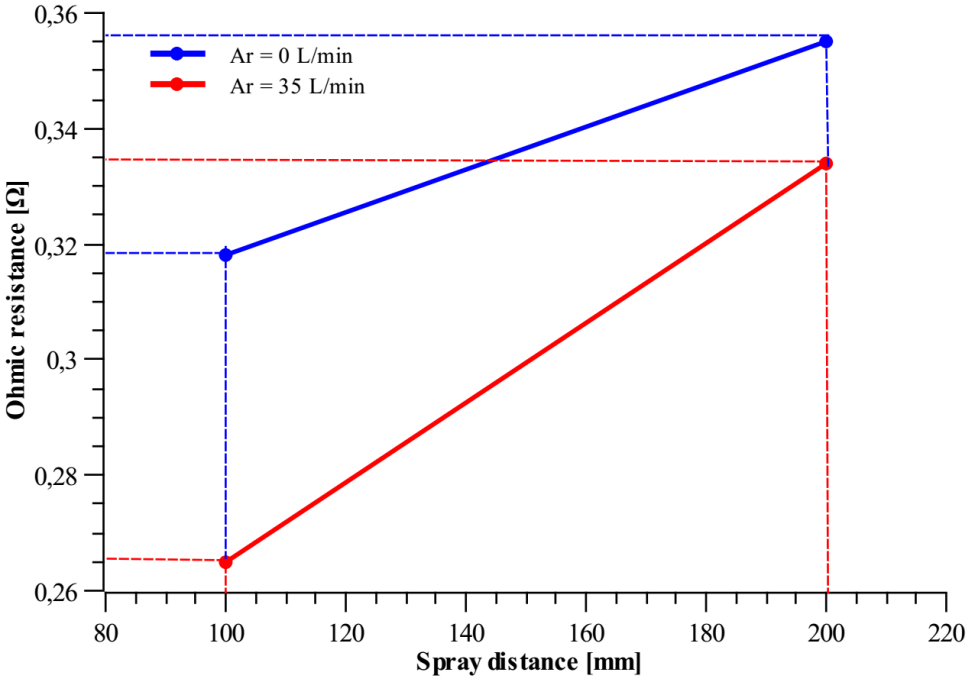

Figure 3.3.9 Illustration of the interaction effect (Roata, 2018b).

$$Ohmic\ resistance = a_0 + a_1 \cdot F1 + a_2 \cdot F2 + a_{12} \cdot F1 \cdot F2$$
$$Ohmic\ resistance = 0.3185 + 0.027 \cdot F1 - 0.019 \cdot F2 - 0.008 \cdot F1 \cdot F2 \quad (3.3.18)$$

The establishment of a protective argon gas flow rate of 35 liters per minute plays a crucial role in significantly mitigating the extent of oxidation that takes place during the deposition process. This reduction in oxidation is directly correlated with a substantial decrease in the electrical resistivity of deposited layer (P3). Consequently, this enhancement in electrical conductivity is likely to improve the overall performance and efficiency of the material in various applications requiring low-resistance conductive layers. The careful regulation of the argon gas environment, therefore, is essential not only for maintaining the integrity of deposited material but also for optimizing its functional properties.

3.4 Thermal spraying of CuAlFe powder on Cu5Sn alloy

This study focuses on depositing a copper-aluminum (Cu-Al) coating on a Cu_5Sn alloy substrate using flame spraying techniques. The coating is intended for applications in renewable energy as infrared (IR) absorbent coatings, electrical contacts, and photocatalysis substrates. To enhance the coating's composition and morphology, concentrated solar post-deposition thermal treatment is implemented, which is a cost-effective and environmentally friendly alternative compared to traditional heating methods.

The substrates utilized are Cu_5Sn alloy specimens measuring 20 mm × 20 mm × 25 mm, and the flame-sprayed coating is derived from Cu-Al-Fe powder sourced from Castolin Eutectic (Germany). The study highlights the benefits of using solar energy for thermal treatment, promoting sustainability while improving coating performance. Further exploration of the coating's properties and applications is suggested.

Table 3.4.1 The chemical composition of Cu-Al-Fe coating powder (Roata et al., 2017).

Element	Composition (wt. %)
Cu	Balance
Al	8.5 – 10.75
Fe	0.5 – 2

In figure 3.4.1, the solar thermal treatment plant scheme is explained. A thermocouple placed in the center of each sample's drilled hole has allowed for a comprehensive control of the solar thermal treatment. To establish the operational temperature domain (maximum of 970 °C), multiple samples were completely melted.

The samples underwent four separate steps of thermal treatment, as depicted in figure 3.4.2: I) Preheating the sample to 600 °C (T1); II) Holding the temperature at 600 °C for 5 min (T1-T2); III) Heating the sample to 950 °C at a rate of 50 °C per min (T3); and IV) Cooling the sample to room temperature (T4).

Table 3.4.2 Operational parameters of the thermal spraying process (Roata et al., 2017).

Parameters	Sample 1 S1 and Sample 2 S2
Thermal spraying distance Powder feed rate	150 mm
Thermal spraying distance Powder feed rate	38 g/min
Preheating	120 °C
Oxygen pressure	4 bar
Acetylene pressure	0.7 bar

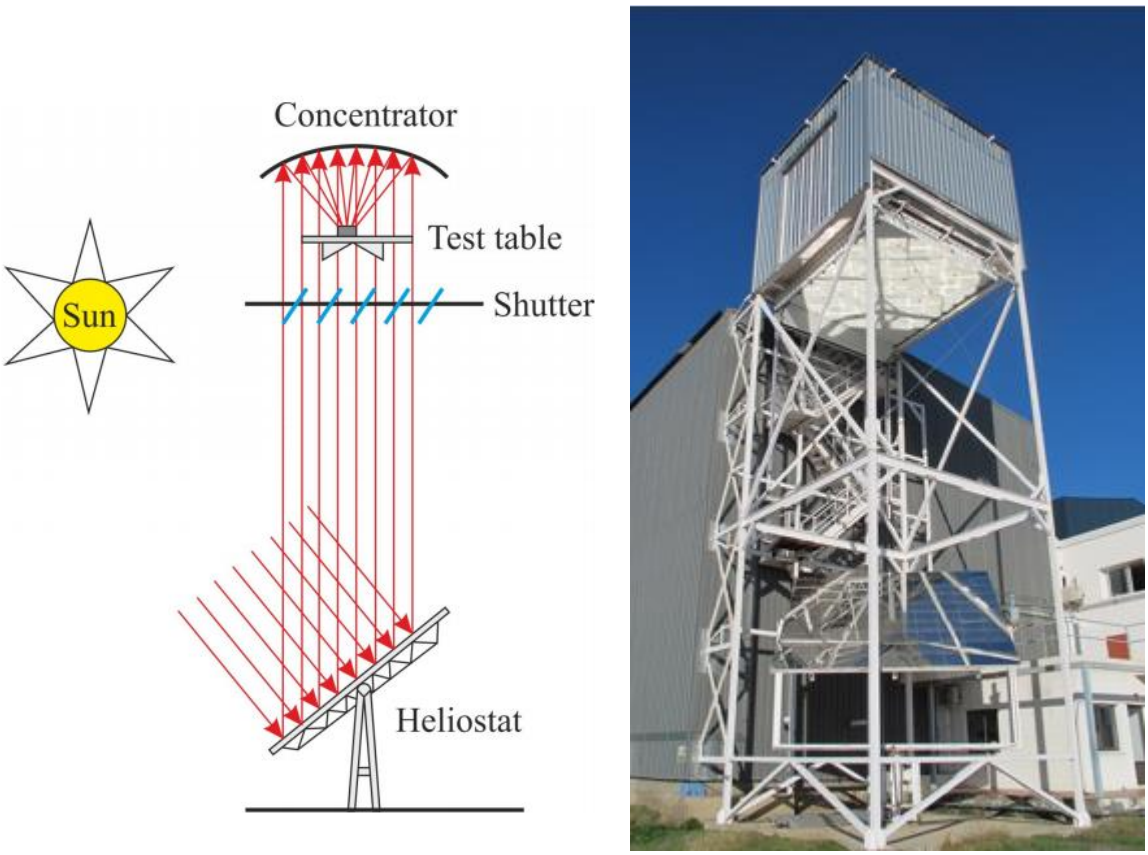

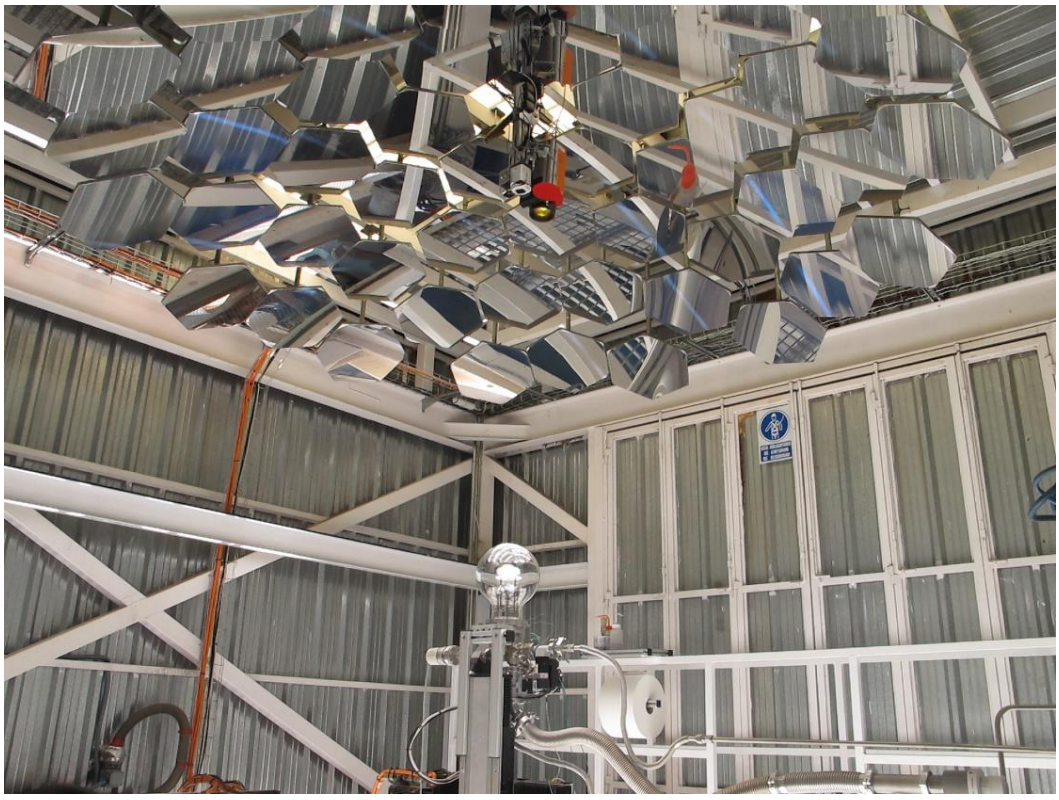

Figure 3.4.1 Functional diagram of the SF05 solar furnace(Roata et al., 2017; Rodríguez et al., 2014; ***SF05).

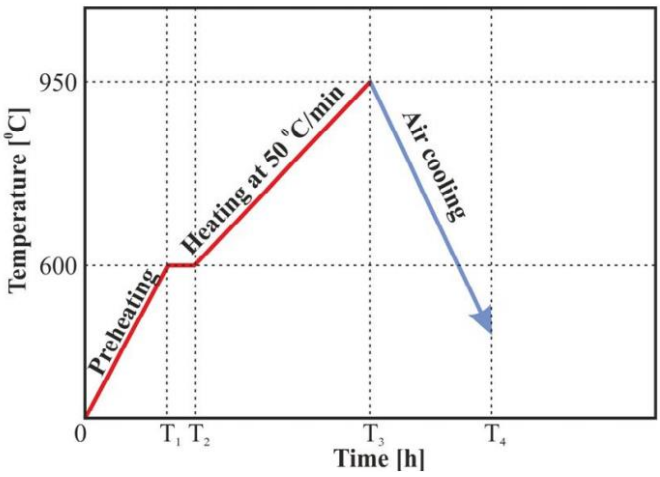

Figure 3.4.2 Solar heat treatment diagram (Roata et al., 2017).

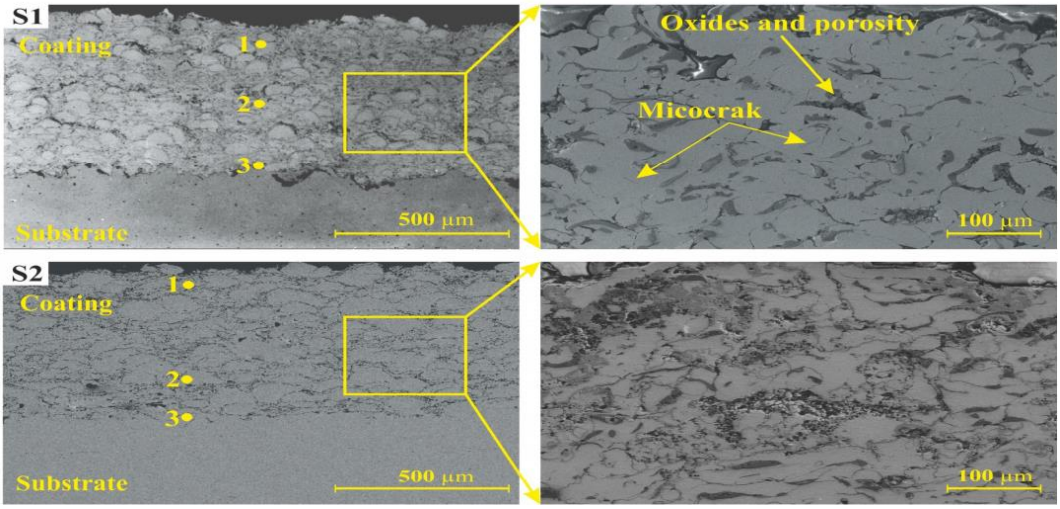

S1

Element	1 Wt%	2 Wt%	3 Wt%
CuK	86.50	88.32	96.27
AlK	9.81	10.21	6.97
FeK	1.35	1.47	0.98

S2

Element	1 Wt%	2 Wt%	3 Wt%
CuK	84.47	93.30	93.59
AlK	14.21	5.66	5.32
FeK	1.32	1.04	1.09

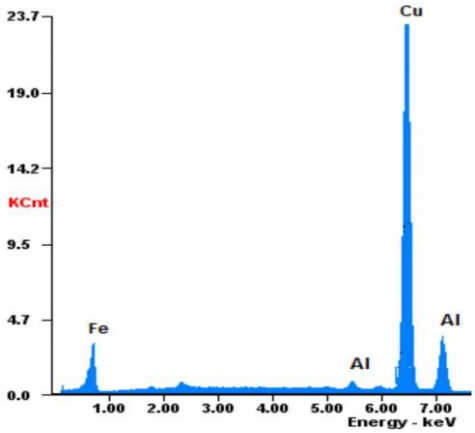

Figure 3.4.3 Cross-sectional SEM micrographs of S1 (initial sample) and S2 (heat treated at 950°C) (Roata et al., 2017).

Figures 3.4.3 (S1) and 4 (S2) display the cross-sectional morphology of Cu-Al-Fe intermetallic coatings before and after heat treatment at 950 °C, respectively. The untreated S1 sample exhibits a lamellar structure with partly unmelted splats and a complex microstructure observed through scanning electron microscopy (SEM), which includes dense splats and fine grains. The interface with

the substrate shows a heterogeneous morphology with pores and oxides. Post-thermal treatment improves the coating-substrate bonding, reducing crack and pore density, which enhances wear and corrosion resistance. Energy-dispersive spectroscopy (EDS) analysis reveals significant variations in elemental distribution, particularly a gradient in Cu and Al concentrations, likely due to the formation of hard phases like $CuAl_2$, contributing to the observed improvements in corrosion resistance (Roata et al., 2017).

The S2 sample demonstrates significant improvements in the microstructural characteristics of the Cu-Al-Fe coating, attributed to solar energy application. These enhancements likely stem from the formation of a dense, oxidation-resistant layer at the coating-substrate interface, which prevents corrosive species from diffusing. Future research should investigate the mechanisms behind the interaction of solar energy with thermal spray coatings to optimize their performance for industrial applications.

Micro-hardness testing reveals that the coating exhibits values ranging from 149.78 $HV_{0.1}$ to 158.09 $HV_{0.1}$, indicating high compositional homogeneity and minimal variation (±1%) in chemical composition. This consistency is crucial for the coating's wear resistance and corrosion protection capabilities. The uniform hardness is likely a result of controlled deposition and careful choice of precursor materials.

The application of solar heat treatment significantly increased the micro-hardness of the coating, with S1 measuring 158.09 $HV_{0.1}$ and S2 measuring 255.18 $HV_{0.1}$—an increase of about 97.09 $HV_{0.1}$ units. The longitudinal micro-hardness profile of S2 indicates a uniform value around 249 $HV_{0.1}$, significantly higher than S1's 155 $HV_{0.1}$. This increase in hardness is attributed to the formation of hard phases such as $CuAl_2$ or Al_2O_3, which enhance both wear resistance and corrosion performance.

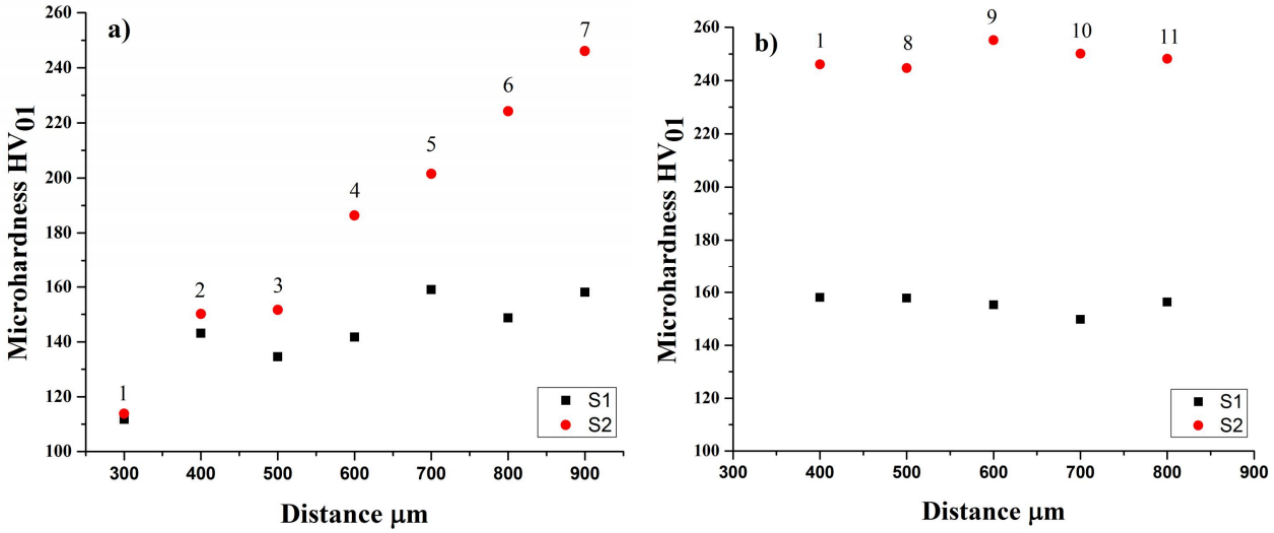

Figure 3.4.4 The influence of the temperature on the hardness values at different distances measured from the coating to the substrate (a) and the influence of temperature on the hardness along the coating (b) (Roata et al., 2017).

Overall, the thermal energy supplied by solar radiation facilitates atomic diffusion within the coating, leading to a uniform distribution of hard phases that sustain the coating's mechanical properties and corrosion resistance.

Future research should focus on exploring the relationship between micro-hardness and other mechanical properties like scratch resistance and fatigue life to better understand how compositional homogeneity affects the performance of coatings. Advanced analytical techniques, such as electron microscopy and spectroscopy, could help elucidate the microstructure and chemical composition, enhancing our understanding of their mechanical behavior. Corrosion experiments showed significant degradation in the non-annealed S1 sample, with a mass loss of 0.4996%, while the solar-annealed S2 sample showed a much lower loss of 0.1919%, indicating approximately threefold better corrosion resistance. This difference is attributed to the formation of hard phases and/or surface oxides during solar annealing, which likely create a protective barrier against corrosion.

A novel ternary copper-aluminum-iron composite coating, produced through flame spraying a core/shell powder, demonstrated reduced density of defects due to a subsequent concentrated solar energy treatment. This treatment fosters the formation of intermetallic hard phases, contributing to increased microhardness and enhanced corrosion resistance. The reduction in pore and crack density, combined with the hard-phase formation, likely improves the coating's mechanical properties and durability.

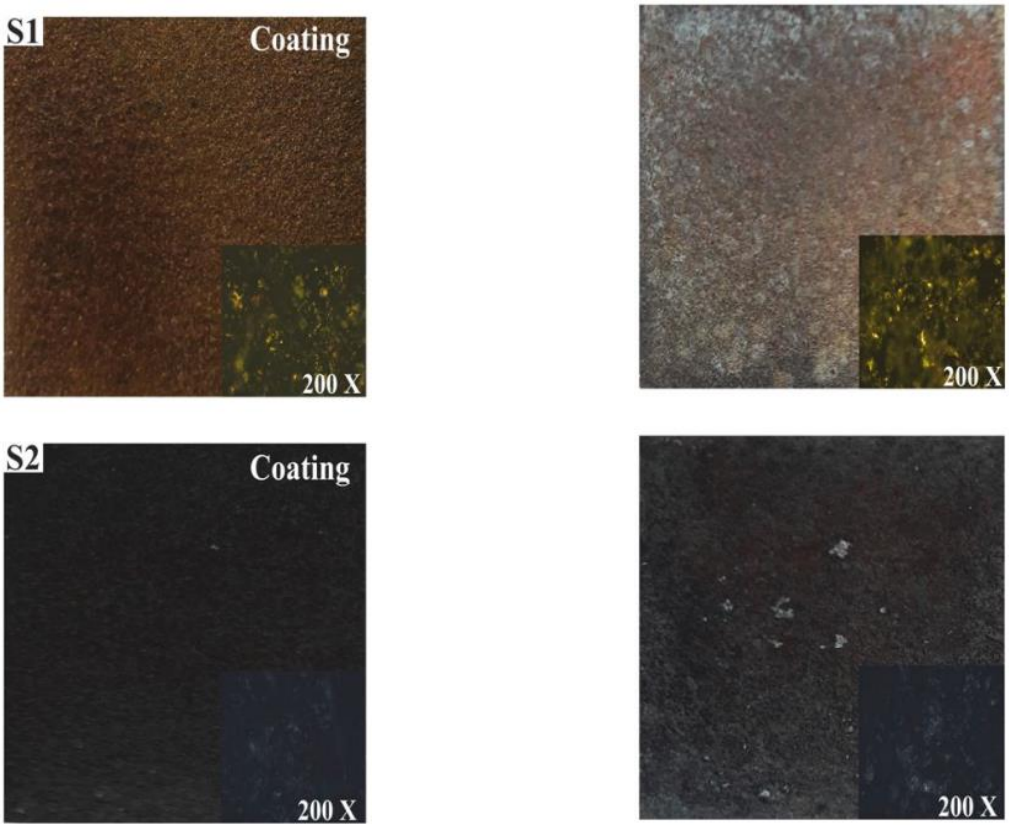

Initial surface morphology

Surface morphology after accelerated corrosion test

Figure 3.4.5 Corrosion testing of the flame-sprayed samples (Roata et al., 2017).

The use of concentrated solar energy for thermal treatment presents environmental and economic advantages over traditional methods, proving effective for producing high-performance coatings. Future studies should aim to determine optimal thermal treatment conditions and investigate how varying core/shell powder compositions affect coating properties. Utilizing advanced analytical techniques like scanning electron microscopy and energy-dispersive spectroscopy can also deepen our understanding of coating microstructure and behavior.

3.5 Photocatalytic performance of copper-based coatings

Thermal spraying was performed using a CastoDyn DS8000 unit to apply a Cu-Al-Fe alloy coating onto electrolytic copper plates (measuring 20 × 20 × 5 mm with 99.9% purity). The spraying process utilized Metco 51NS Cu-Al-Fe powder at a constant feed rate of 0.38 g/min, while the distance between the thermal spray gun nozzle and the sample was varied: 150 mm for sample S1 and 200 mm for sample S2.

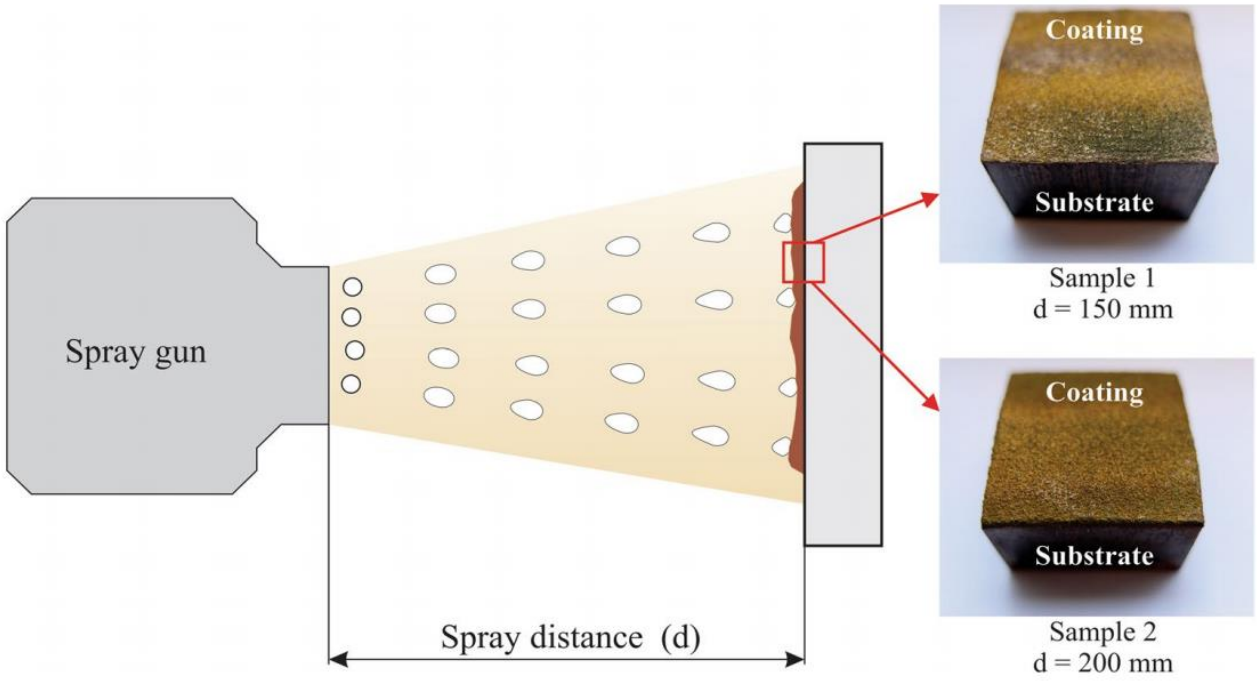

Figure 3.5.1 Schematic of the thermal spraying process for producing coatings (Roata et al., 2018).

Acetylene (at 7 × 10^4 N/m^2) served as the fuel gas, while oxygen was used as the oxidant gas (at 4 × 10^5 N/m^2). The chosen nozzle distances were critical; distances under 100 mm risked overheating the surface, leading to excessive oxidation and poor adherence of the coating. On the other hand, distances exceeding 200 mm could cause increased porosity due to the presence of unmelted metal particles in the deposited coating. The thermal spraying experiments aimed to examine how the varying nozzle distances impacted the microstructure and properties of the deposited Cu-Al-Fe alloy coating.

The crystalline structure of the thermally sprayed coatings was investigated using a Bruker D8 Discover X-ray diffractometer (XRD) equipped with CuKα1 radiation (λ = 0.154 nm) and a scanning speed of 5° min^{-1}.

The surface morphology of the coatings was characterized using a combination of techniques, including:

- reflected polarized light optical microscopy (Axio Scope.A1 Pol, Carl Zeiss) to examine the surface morphology;
- scanning electron microscopy (SEM, QUANTA 200) with energy-dispersive X-ray (EDX) spectroscopy to analyze the elemental composition and surface morphology;
- semicontact-mode atomic force microscopy (AFM, NT-MDT) with 2D imaging mode and phase imaging to investigate the surface topography and roughness (Roata et al., 2018).

In addition, the optical properties of the coatings were studied using a UV-Vis Perkin Elmer Lambda 950 spectrophotometer, which obtained reflectance spectra in the 200-900 nm range with a scan rate of 10 nm min^{-1} and integrating sphere. Attenuated total reflectance Fourier transform infrared (ATR-FTIR) spectroscopy was performed using a Bruker VERTEX 70 spectrometer at a resolution of 2 cm^{-1} and an integrating sphere.

Contact angle measurements were carried out by analyzing photographic images taken at predetermined time intervals using ImageJ software with the contact angle plugin. Due to the high surface roughness of the coatings, a corrected contact angle value was calculated using Equation 3.5.1 (Jardim et al., 2016).

$$cos\theta^{cor} = r * cos\theta_Y \tag{3.5.1}$$

where θ^{cor} is the roughness-corrected contact angle, θ_Y is the Young contact angle determined from image analysis, and r is the roughness ratio calculated using Eq. 3.5.2:

$$r = 1 + \frac{S_{dr}}{100} \tag{3.5.2}$$

In Equation 3.5.2, Sdr is the developed interfacial area ratio, which was calculated using image processing techniques with ImageJ software. The specific surface area of the thermally sprayed coatings was measured using a MicroMeritics TriStar 3000 instrument, employing the Brunauer-Emmett-Teller (BET) adsorption isotherm model after detaching the S1 and S2 coatings from their substrate.

For photodegradation experiments, a 400 W high-pressure mercury-vapor lamp (SYLVANIA 69450) was set 10 cm from a reaction flask, using filters to block UV light and wavelengths above 500 nm to prevent dye photobleaching. The average illuminance on the flask was 10 lux.

An aqueous solution of methylene blue (MB) dye at an initial concentration of 0.012 mM was used as a model for photocatalytic performance assessment. Samples were taken at set intervals

and analyzed for absorbance at λmax = 665 nm, and for total organic carbon (TOC) content according to EPA method 415.3, using potassium hydrogen o-phthalate and potassium persulfate as reagents. Prior to the experiments, samples were equilibrated in the dye solution for 2 hours in the dark.
The relative removal efficiency of MB was calculated with Eq. 3.5.3:

$$\eta(\%) = \left[1 - \frac{c(t)}{c_0}\right] * 100 \quad (3.5.3)$$

where c(t) is the concentration of the dye at time "t" and c_0 is the initial concentration (0.012 mM).

To ensure the reproducibility of the data, all photodegradation tests were performed in triplicate. Following the photodegradation experiments, the dissolved aluminum (Al), copper (Cu), and iron (Fe) concentrations in the solution were analyzed using an Agilent 280Z AA Zeeman graphite furnace atomic absorption spectrometer (GFAAS).
The morphological analysis of the thermally sprayed coatings (Figure 3.5.2) reveals an inhomogeneous distribution of phases, characterized by distinct metal and oxidic phases exhibiting different reflection modes under polarized light.

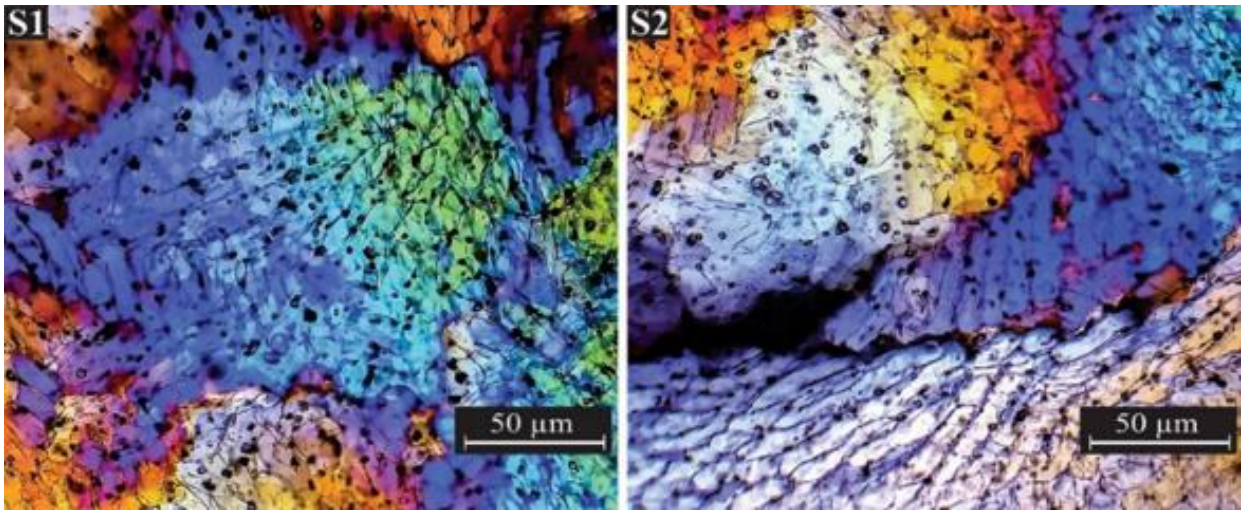

Figure 3.5.2 Polarized light microscopy of the thermal sprayed coatings (Roata et al., 2018).

Scanning electron microscopy (SEM) imaging reveals that sample S2 has a higher average surface roughness (Ra) of 175.71 nm compared to S1's 102.64 nm, likely due to a longer time-of-flight for molten metallic splats during the thermal spraying process, resulting in increased oxide content. Both samples consist of solidified and well-fused Cu-Al-Fe splats, but S2's splat aggregates are 15-20 % larger, with average diameters ranging from 60 to 110 nm. The oxide phases at the boundaries of the metallic phases display a nanopatterned appearance that is important for efficient photocatalysis, consistent with results from other plasma spraying studies on photocatalytic coatings.

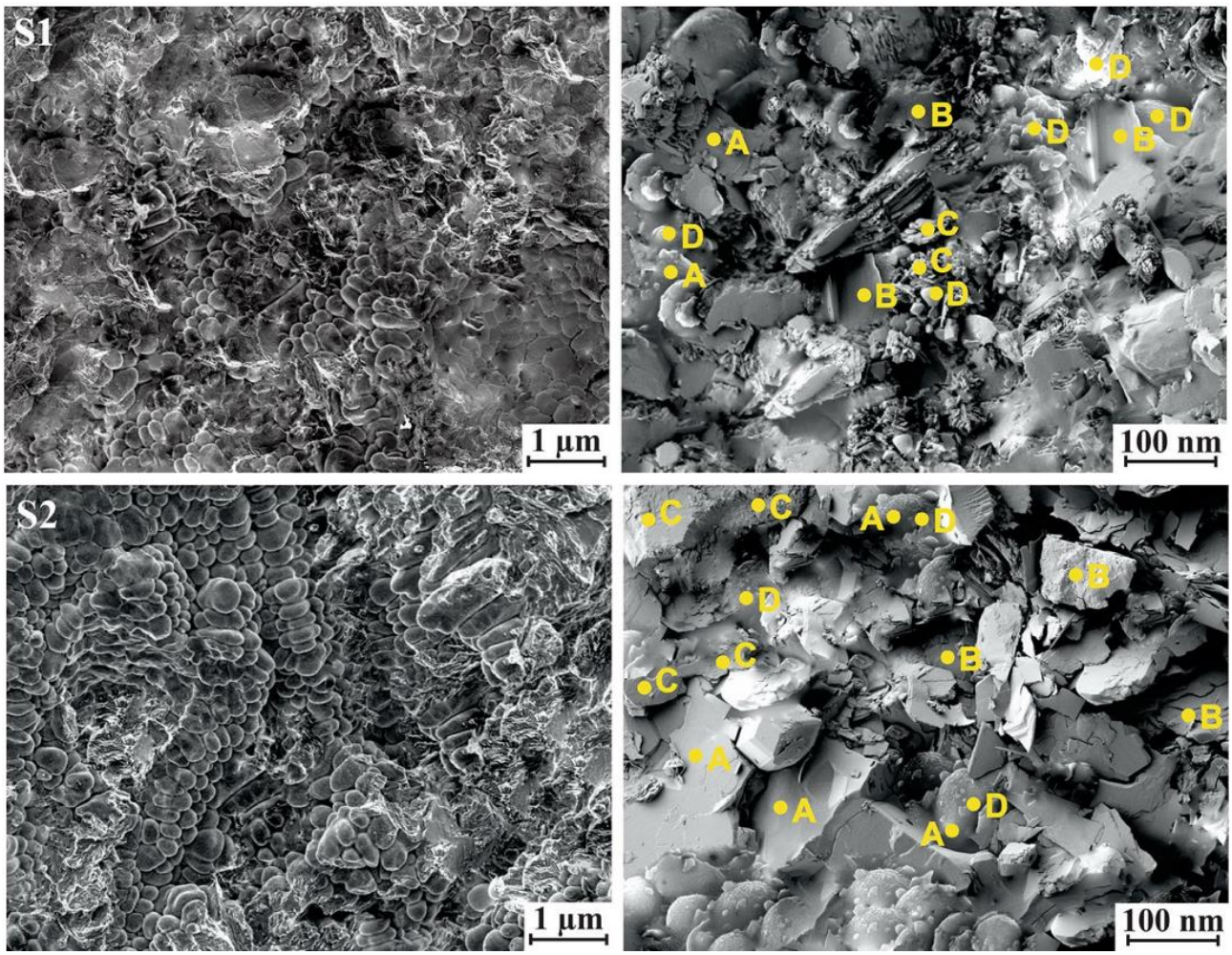

Figure 3.5.3 SEM micrographs of the thermally sprayed coatings surface before photocatalysis (Roata et al., 2018).

Through the application of energy-dispersive X-ray spectroscopy (EDX) to systematically analyze distinct surface regions in samples S1 and S2, four distinct zones have been identified (labeled A, B, C, and D). The average weight percentages of Cu, Al, Fe, and O, along with their corresponding standard deviations (σ), are presented in Table 3.5.1.

Table 3.5.1 Elemental composition (% wt.) of samples S1 and S2 surface (Roata et al., 2018).

Sample	**S1**				**S2**			
Zone	**Cu (%)**	**Al (%)**	**Fe (%)**	**O (%)**	**Cu (%)**	**Al (%)**	**Fe (%)**	**O (%)**
A	88.77 (σ = 1.75)	8.12 (σ = 0.85)	0.48 (σ = 0.08)	2.63 (σ = 0.12)	89.01 (σ = 1.75)	8.35 (σ = 1.05)	0.50 (σ = 1.25)	2.14 (σ = 1.72)
B	2.05 (σ = 0.25)	48.22 (σ = 0.98)	0.55 (σ = 0.07)	49.18 (σ = 1.15)	1.21 (σ = 0.09)	43.11 (σ = 1.55)	–	55.68 (σ = 2.01)
C	63.89 (σ = 1.33)	9.76 (σ = 0.28)	–	26.35 (σ = 1.25)	62.11 (σ = 1.35)	2.01 (σ = 0.83)	–	35.88 (σ = 1.14)

D	6.19 (σ = 1.25)	7.89 (σ = 0.17)	35.77 (σ = 1.83)	50.15 (σ = 1.72)	5.11 (σ = 1.28)	5.77 (σ = 1.35)	32.10 (σ = 1.32)	57.02 (σ = 1.36)

The bulk of the surface in S1 and S2 samples is comprised primarily of Cu and Al, potentially forming a solid solution as suggested by the X-ray diffraction (XRD) spectroscopy data. A minimal amount of Fe is also present. Zone B is characterized by a significant presence of Al and O, indicating the formation of Al2O3 as thin sheets. Zone C exhibits a high concentration of Cu and O, suggesting the presence of copper oxides with a bud-like appearance in S1 and plate-like appearance in S2. Zone D is rich in iron and oxygen, with the iron and oxygen-rich regions appearing as localized grooves and protuberances on Zone A.

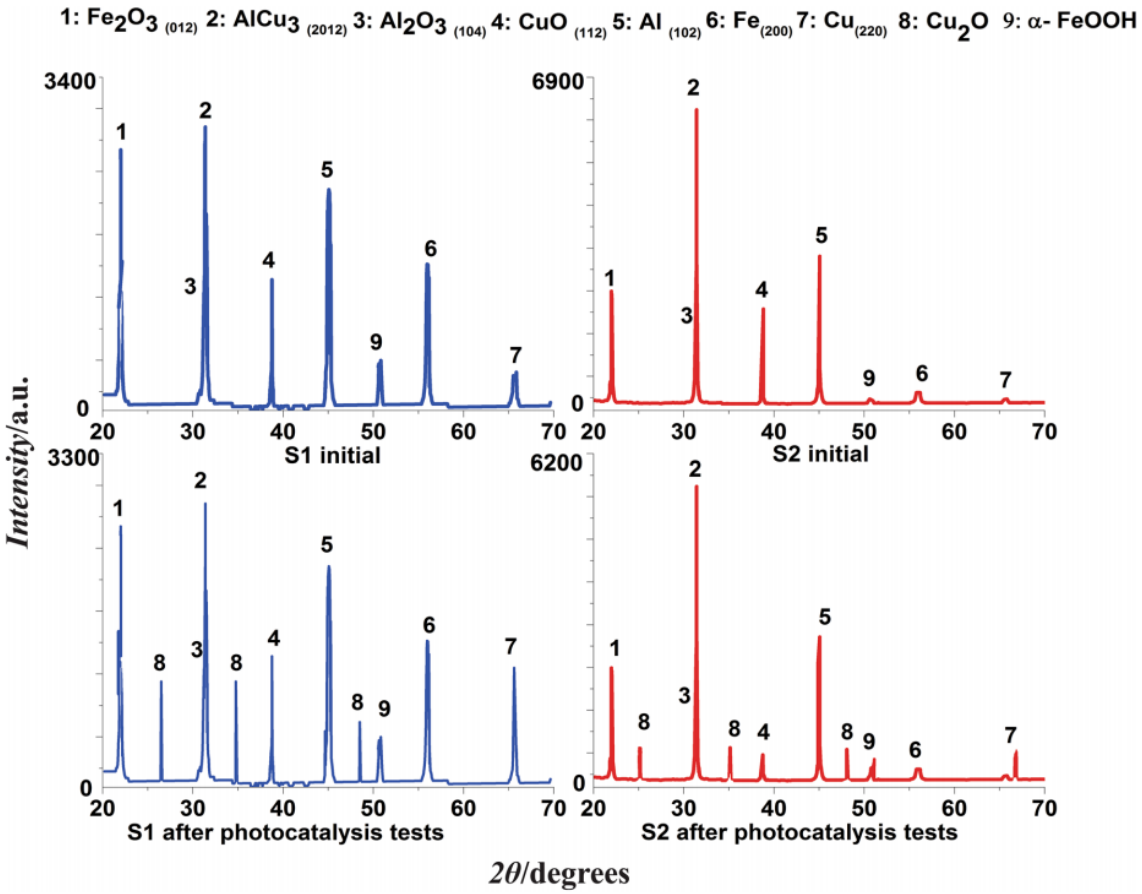

Figure 3.5.4 XRD patterns of the thermally sprayed coatings (Roata et al., 2018).

Sample S2 exhibits a higher surface oxygen content, likely contributing to its increased photocatalytic activity compared to S1, as oxygen is critical for forming oxides that facilitate photocatalysis. X-ray diffraction (XRD) patterns for both samples display sharp, intense peaks indicative of a well-organized polycrystalline structure, with crystallinity at 67.11% for S1 and 74.35% for S2.

The XRD analysis reveals a metallic matrix in both coatings consisting of face-centered cubic Al and Cu, as well as the intermetallic compound AlCu3. Additionally, several oxides from the oxidation

of the metallic phase during thermal spraying are present, including α-Fe2O3, CuO, and γ-Al2O3. The lower intensity of metal phase diffraction peaks relative to the oxides supports the presence of these oxides on the coating surfaces.

The absence of peaks corresponding to mixed oxides suggests that the coatings are relatively pure, though some limited diffusional interdoping may occur due to the high thermal process temperatures. The increased presence of crystalline oxide phases in S2 is attributed to prolonged exposure to atmospheric oxygen during the thermal spraying process. For example, the CuO to Fe2O3 intensity ratio increases from 0.44 in S1 to 0.92 in S2.

Al2O3, which forms on solidified splats, serves as an "anchor" for the photocatalytic oxides CuO and Fe2O3, enhancing their adhesion to the coating. This supportive role of Al2O3 has been observed in other systems, where it facilitates interaction between azo dyes and active photocatalysts through adsorption and slow release.

The apparent crystallite sizes perpendicular to the corresponding reflection plane (D) were estimated using the Stokes and Wilson approach (Table 3.5.2):

Table 3.5.2 Apparent crystallite sizes and specific surface areas of S1 and S2 (Roata et al., 2018).

Sample code	**BET specific surface area ($m^2\ g^{-1}$)**	**Crystallite sizes (Å)**			
		Fe_2O_3	**CuO**	**Al2O3**	**Cu_2O**
S1					
Initial	4.65 ± 0.03	94.47	43.78	128.11	–
After photocatalysis	n.a.	95.71	46.56	128.77	48.71
S2	4.87 ± 0.03	95.86	45.65	132.73	99.83
Initial	n.a.	97.21	47.03	133.46	
After photocatalysis					

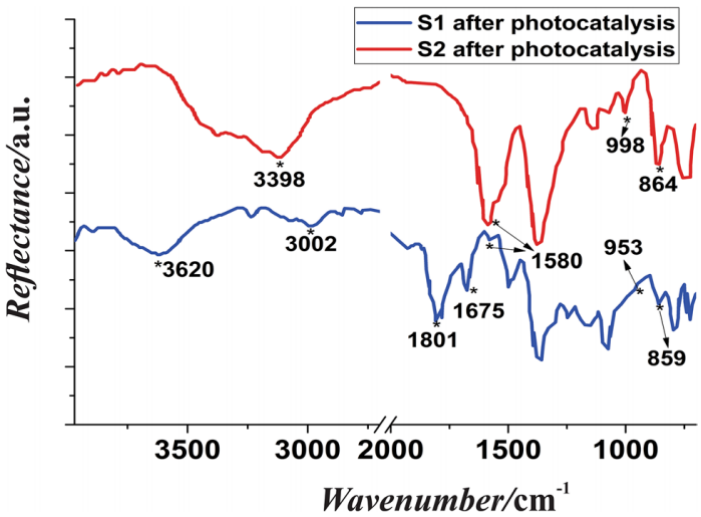

Figure 3.5.5 FTIR spectra of samples S1 and S2 after three photocatalytic cycles (Roata et al., 2018).

The X-ray diffraction (XRD) pattern of the sample surface after three photocatalytic cycles shows the emergence of cubic Cu2O (JCPDS No. 77-0199), potentially formed through the reduction of Cu2+ ions by Fe2+ ions during the photocatalytic process. The relative peak areas for Cu2O in the XRD patterns are 0.07 for S1 and 0.09 for S2, indicating a slight increase in Cu2O presence on the coatings. This gradual formation of Cu2O is beneficial as it has a broader band gap energy than CuO, which helps reduce the recombination of electron-hole pairs, thus enhancing photocatalytic efficiency during repeated cycles of methylene blue (MB) photodegradation.

Additionally, the increase in crystallite sizes observed after photodegradation suggests that restructuring occurs within the materials, leading to new interfaces that enhance photocatalytic activity.

The attenuated total reflectance Fourier transform infrared (ATR-FTIR) spectra provide further evidence of the formed phases, showing absorption bands associated with Cu2O and hydrated iron oxide. Specifically, absorption bands at 1580 and 998 cm−1 in sample S2, and at 1580 and 953 cm−1 in sample S1, correspond to Cu–O bending modes in Cu2O. The bands at 3398 and 998 cm−1 for S2, and at 3002 and 953 cm−1 for S1, are attributed to O–H stretching and Fe–O bending vibrations in hydrated iron oxide. Additional bands at 1350 and 1801 cm−1 are identified as Al–O out-of-plane vibrations.

The observed blue shift of the Cu2O-related absorption bands in sample S2 may be indicative of the presence of larger and more strained crystallites of Cu2O, which would result in a partial inhibition of vibrational modes due to increased lattice stress. This phenomenon is consistent with previous studies, which have demonstrated that the formation of Cu2O can lead to changes in the crystallite structure and morphology, resulting in altered vibrational properties.

The atomic force microscopy (AFM) topography images obtained on a 500×500 nm area of the surface of a splat (Figure 3.5.6 a, b) reveal the presence of multiple circular aggregates with average diameters ranging from 100-200 nm, exhibiting a morphology consistent with the SEM micrographs. The oxide phase exhibits a lighter coloration compared to the metal phase in both the topography and AFM phase images due to the differences in the elastic constants between these two phases (Nawi & Zain, 2012). The "softer" phase appears darker in color due to its increased compliance.

The AFM topography images from Figure 3.5.6 b confirm that the aggregates are significantly larger in the S2 sample, with a 15-20% increase in size compared to the S1 sample, indicating a higher degree of aggregate formation. Furthermore, the average surface roughness of the samples is higher for S2, which is in agreement with the observations derived from the SEM micrographs.

The specific surface area of the coating obtained using a spraying distance of 200 mm is 5% higher than that of the sample sprayed at a distance of 150 mm, suggesting a looser arrangement of crystalline oxidic species in the S2 coating. The results are comparable to those obtained for electrolytic plasma oxidation (EPO) coatings (Curran & Clyne, 2006).

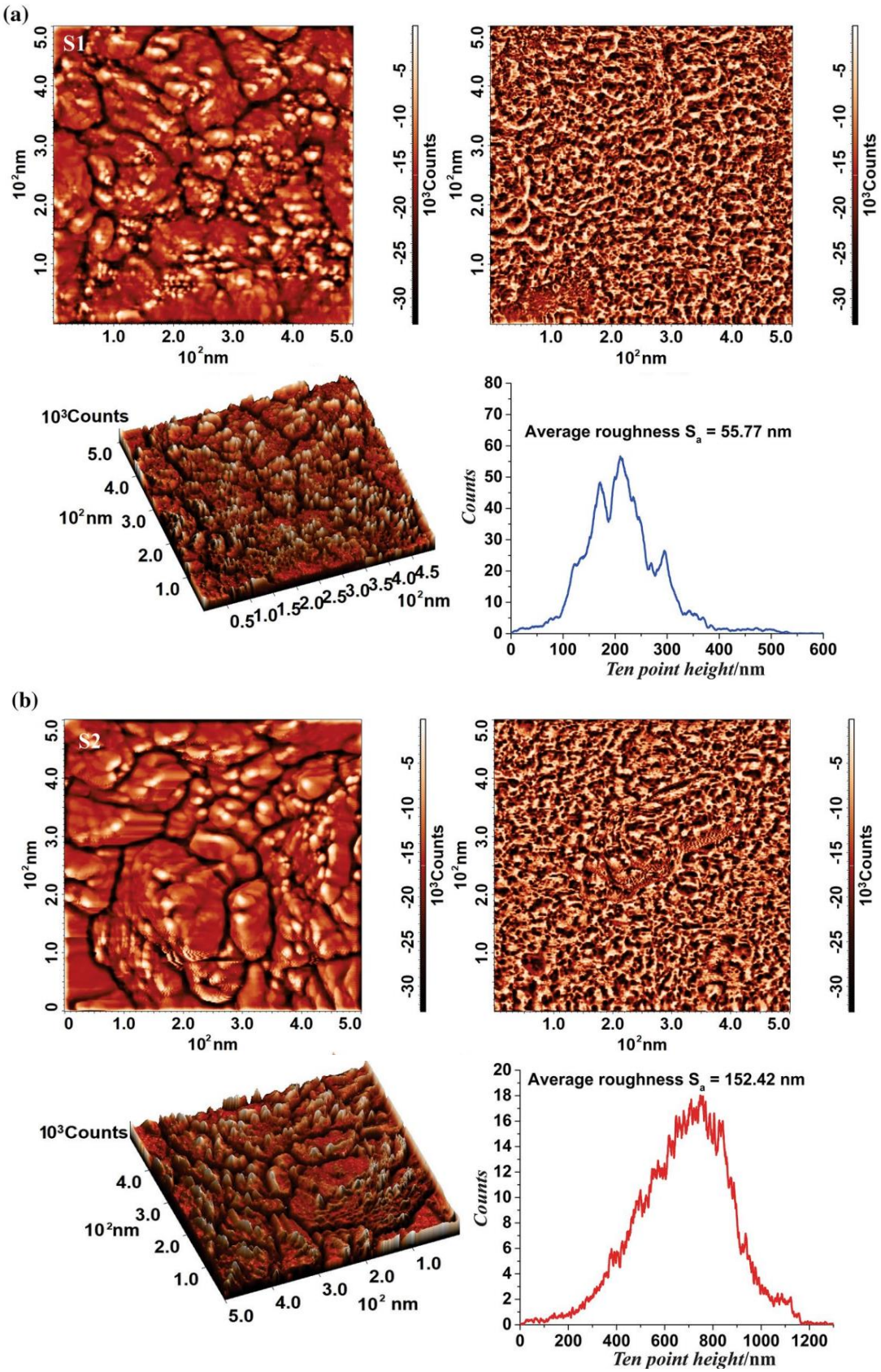

Figure 3.5.6 a AFM topography and phase imaging of a thermally sprayed aggregate in sample S1. b AFM topography and phase imaging of a thermally sprayed aggregate in sample S2 (Roata et al., 2018).

A high specific surface area is crucial for photocatalytic applications, as it maximizes the contact between the compound to be degraded and the photocatalytically active species (Toma et al., 2014). The specific surface area of the coatings is lower than that of nanoparticulate powders (~20-450 m2/g) (Siegmann et al., 2005), although the usage of powders creates additional issues related to their separation from the liquid state for recycling (Toma et al., 2014). Moreover, an increased specific surface area could lead to more rapid recombination of charge carriers, thereby impeding photocatalysis (Jafari et al., 2016). Furthermore, the surface area may also influence the adsorption behavior of pollutants and reactants, thereby affecting the photocatalytic activity.

While the thermally sprayed samples present the highest absorbance in the UV region, they also present significant absorption in the visible region (Figure 3.5.7a).

Furthermore, the overall absorbance is higher for sample S2 than sample S1 due to its higher surface oxide content. The shape of the spectrum corresponding to S2 resembles that of hematite (with ~307 and 410 nm maxima) due to the higher content of this type of oxide (determined from XRD and EDX) as well as of CuO, which exhibits a broad absorption band between 250 and 420 nm (particularly in sample S1).

Compared with the absorption maximum hematite, that of S2 at λmax=410 nm is shifted to a longer wavelength due to metal content in the crystalline lattice.

The optical absorption spectra of samples S1 and S2 in the UV–vis region was used to determine the nature of the transitions in the thermally sprayed oxide tandem and the optical band gap energy (Eg).

The absorption coefficient (α) is related to the photon energy (hv) by the following relation (in logarithmic form, Eq. 3.5.4) (Hassanien & Akl, 2015):

$$\ln(\alpha hv) = \ln\beta + n * \ln(hv - E_g) \quad (3.5.4)$$

where β is the band tailing parameter (a proportionality constant) and n is the power factor of the transition mode.

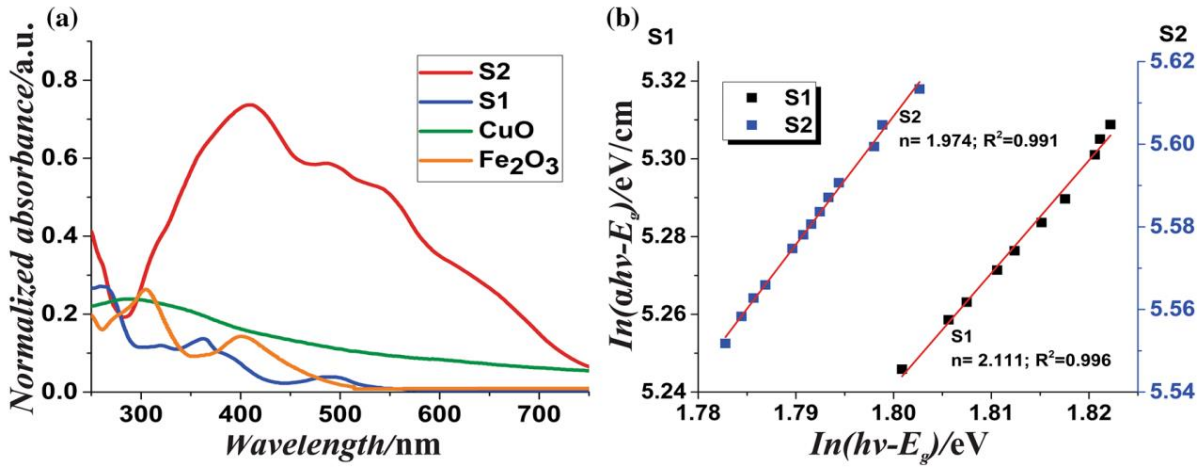

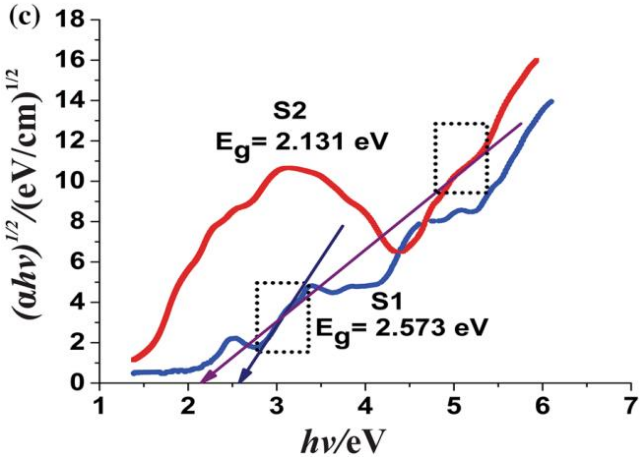

Figure 3.5.7 UV–vis spectra and energy plots for samples S1 and S2(Roata et al., 2018).

For the analysis of direct allowed transitions, the parameter n is theoretically equal to 1/2, whereas for indirect allowed transitions, n is theoretically equal to equation 3.5.2. The plot of ln(αhν) as a function of n·ln(hν-Eg) exhibits a linear correlation with a slope corresponding to the power factor n, thereby enabling the determination of the transition type (Figure 3.5.7b). The experimentally obtained values of n for the samples are 2.111 for S1 and 1.974 for S2, which are consistent with an indirect transition type (n ≈ 2), thereby corroborating the theoretical predictions.

The results indicate that the optical band gap energies (Eg) of two samples, S1 (2.573 eV) and S2 (2.131 eV), were determined using the linear relationship in the plot of $(\alpha h\nu)^{1/2}$ versus hν. The lower Eg of sample S2 is due to its higher content of CuO and Fe_2O_3, which absorb light more efficiently. Both samples have Eg values below 3 eV, highlighting their potential for use in photovoltaic applications.

Furthermore, a heterojunction forms between the n-type semiconductor α-Fe_2O_3 and the p-type semiconductor CuxO, enabling electron flow from CuxO's conduction band to that of α-Fe_2O_3, while holes move in the opposite direction. This p-n heterojunction promotes effective charge separation and reduces rapid recombination, enhancing photocatalytic efficiency. The charge transfer process may be further optimized by metallic phases or crystal lattice defects.

In the α-Fe_2O_3/CuxO heterojunction, photogenerated electrons and holes facilitate the degradation of organic dyes. Electrons react with adsorbed oxygen to produce superoxide radicals ($\cdot O_2^-$), while holes generate reactive hydroxyl radicals from water. These radicals degrade organic dyes through various mechanisms, including alterations to aromatic rings and hydrogen abstraction. A slower photo-Fenton-like mechanism may also contribute to this process due to the formation of FeOOH and Cu_2O, as well as trace iron ions in solution.

Additionally, effective photocatalysis is supported by improved surface wetting, demonstrated by a significant reduction in the contact angle of methylene blue (MB) solution to below 30° upon photoactivation under visible light. This indicates enhanced interaction between the photocatalyst surface and the aqueous phase.

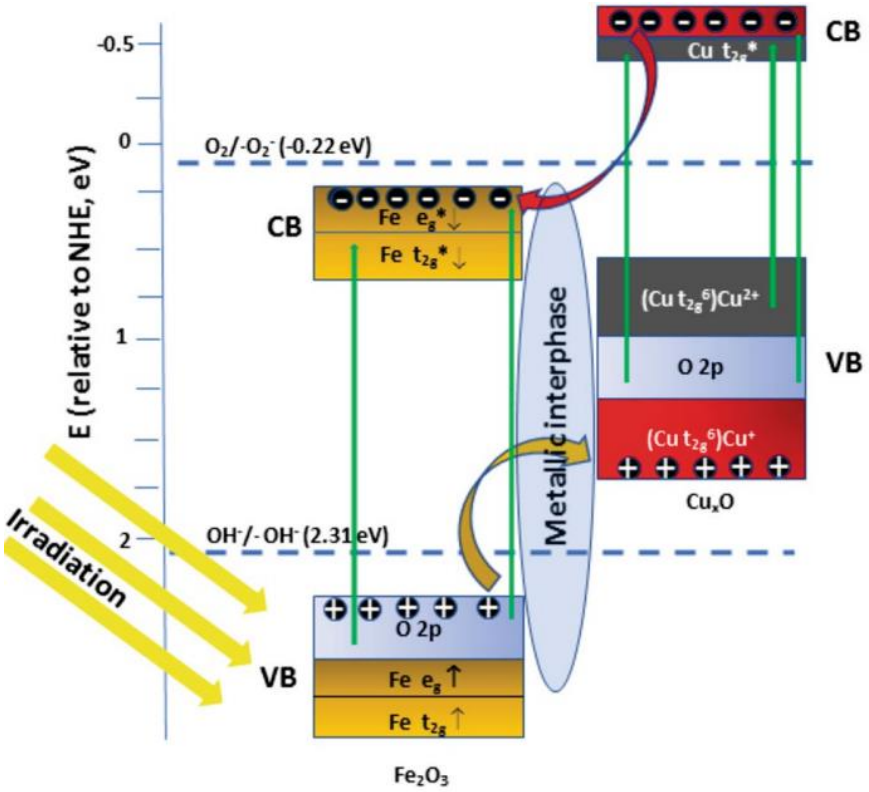

Figure 3.5.8 Mechanism for visible light-mediated photocatalysis of MB degradation by samples S1 and S2 (Roata et al., 2018).

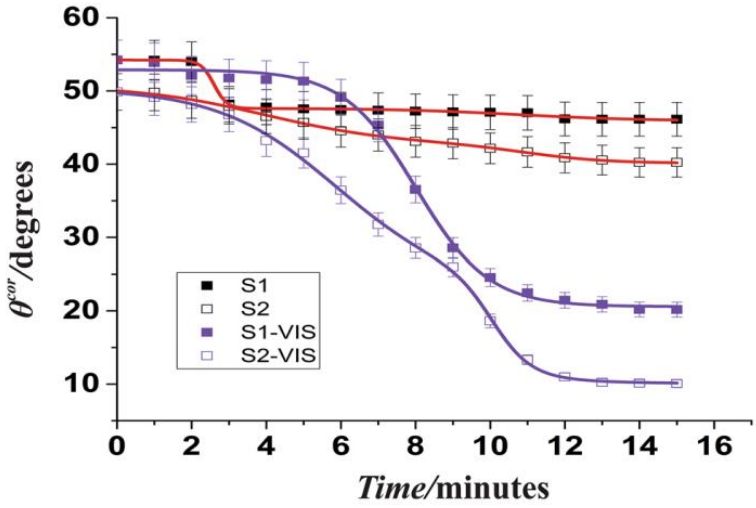

Figure 3.5.9 Contact angle kinetics for visible light-irradiated and non-irradiated samples(Roata et al., 2018).

Sample S2 displays a higher oxide content, leading to a more significant decrease in contact angle compared to sample S1, with equilibrium contact angles reached after about 12 minutes of irradiation, indicating rapid formation of hydrophilic oxidative species.

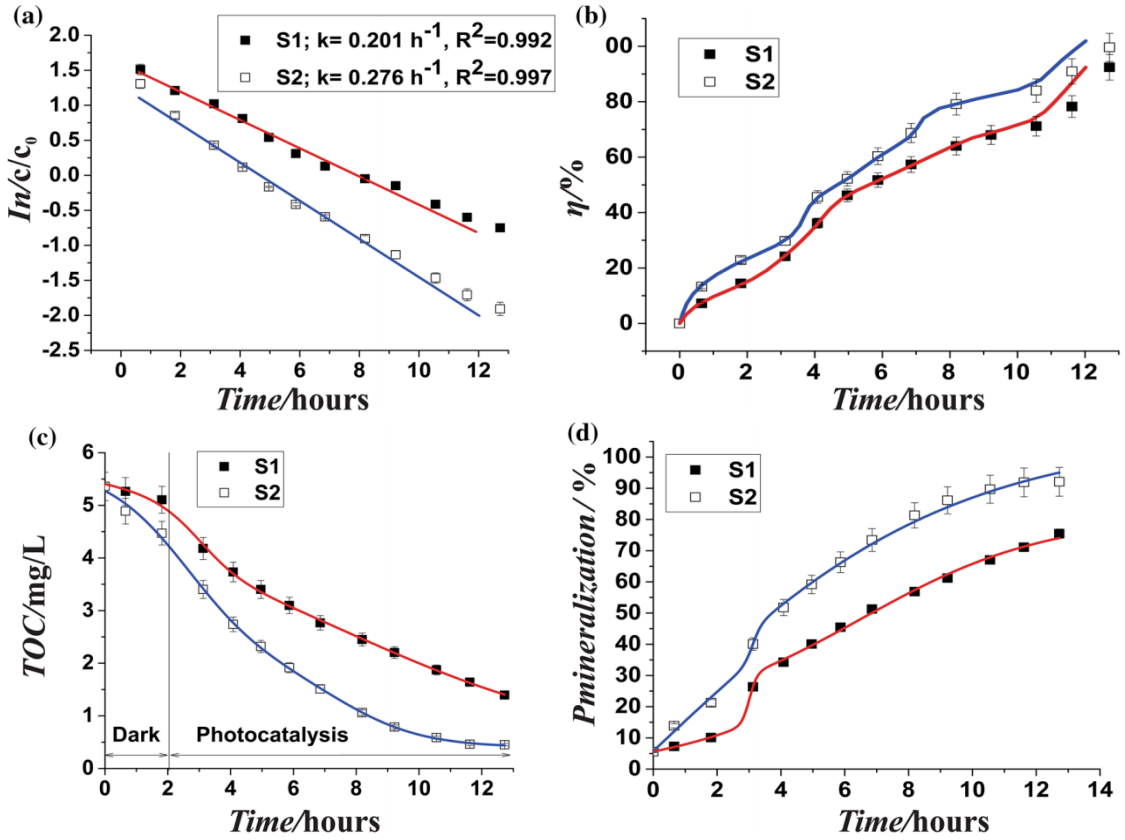

Figure 3.5.10 Photodegradation kinetics of MB with samples S1 and S2 (Roata et al., 2018).

The photodegradation of methylene blue (MB) follows pseudo-first-order kinetics, as shown in Figure 3.5.10a, and the kinetic constants for both samples are comparable to those reported for titanium dioxide (TiO_2) and zinc oxide (ZnO) films under similar conditions. Both coatings show exceptional removal efficiency for MB, with η values nearing 100%, which is noteworthy compared to typical heterogeneous photocatalysis studies that often report incomplete degradation. The initial rapid decomposition phase of the degradation process lasts 4-5 hours, breaking down C-C, C-H, and C-N bonds, leading to smaller compounds with carboxyl and carbonyl groups.

This is followed by a slower mineralization phase (Figure 3.5.10 c). The mineralization percentages calculated based on total organic carbon changes show 75.69% for S1 and 92.236% for S2 (Figure 3.5.10 d).

Additionally, the stability of the coatings against photocorrosion is essential for photocatalytic efficiency. The samples underwent three consecutive 12-hour cycles of UV irradiation and recovery periods to evaluate their catalytic activity and durability, ensuring their resilience in extended use.

The study evaluates the photocatalytic performance and stability of coatings composed of hematite and copper oxide synthesized via thermal spraying on copper substrates. Results indicate minimal performance differences between samples S1 and S2 after multiple photodegradation cycles, highlighting the stability of the oxide-metal phase assembly crucial for long-term efficacy.

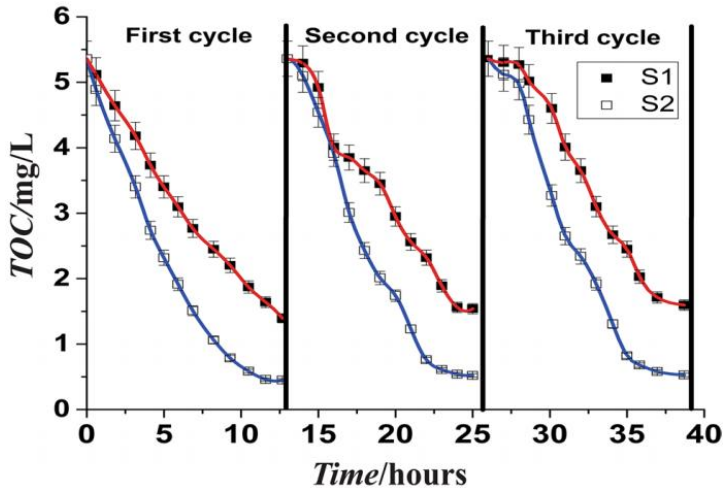

Figure 3.5.11 MB removal efficiencies of samples S1 and S2 during three successive photocatalytic cycles (Roata et al., 2018).

Metal ion leaching assessments showed safe levels of iron (Fe) in solution, while no aluminum (Al) or copper (Cu) was detected. The coatings demonstrated fast photocatalytic responses and high mineralization efficiency of methylene blue (MB), supported by UV-vis spectroscopy and GC-MS analysis.

Characterization techniques, including XRD and XPS, confirmed good compositional stability, with the formation of minor phases like α-FeOOH and Cu_2O that enhance photocatalytic activity. Ongoing research aims to investigate the coatings' performance across varying pH and ionic strengths and to evaluate their scalability for wastewater treatment through life cycle and techno-economic analyses.

The thermal spraying method proved effective in fostering stable nanopatterned coatings with superior photocatalytic characteristics, paving the way for the development of efficient systems for wastewater cleaning applications.

3.6 The impact of laser deposition speed on the mechanical properties and emission characteristics of metal alloys

The study examines the correlation between toxic emissions generated during a processing method and various factors, including deposition speed, laser power, and the material properties of the substrate, such as hardness and microstructure. By analyzing these relationships, the research determines optimal operating conditions intended to enhance both effectiveness and environmental sustainability. The substrate used in the investigation was a S235JR carbon steel plate with specific dimensions (50 mm x 20 mm x 3 mm) and a chemical composition that conforms to the EN ISO 10025-2:2004 standards.

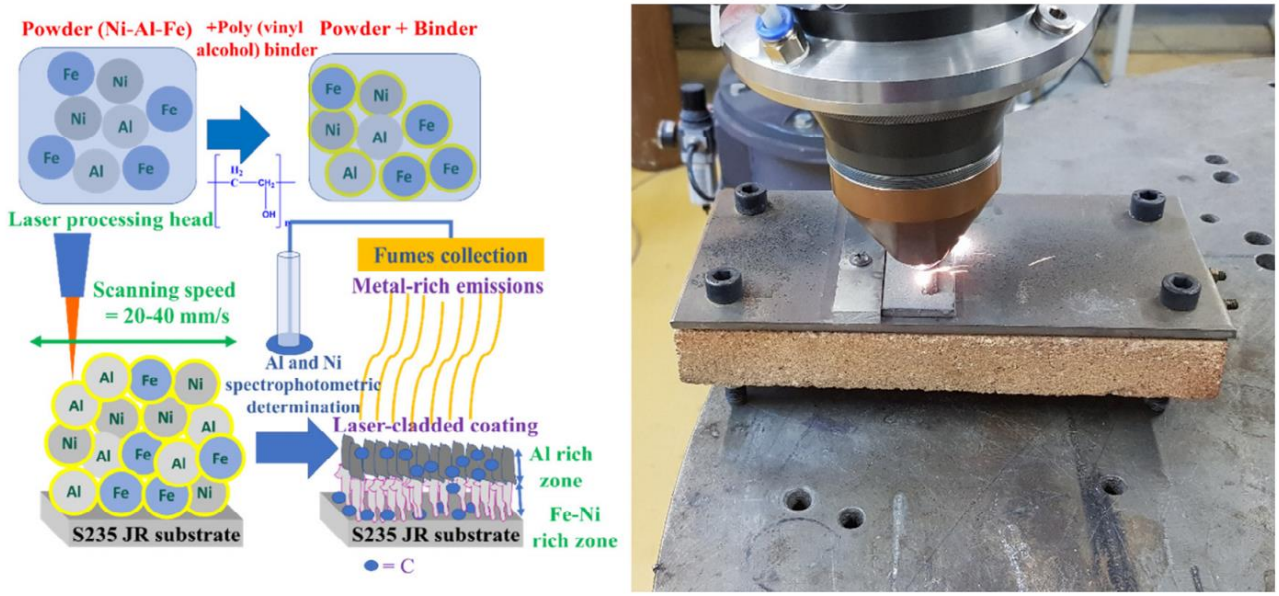

Figure 3.6.1 (a) Mechanism and (b) laser cladding equipment (Roata et al., 2019b).

A composite powder made from Metco 404NS (80 wt.% nickel and 20 wt.% aluminum) and Metco 99.9 wt.% zinc powder in a 4:1 weight ratio was prepared. This mixture was combined with a poly (vinyl alcohol) (PVA) binder in a 10 wt.% aqueous solution and applied to a S235JR carbon steel substrate using a brush-coating technique. The coated substrate was then allowed to dry for 1 hour at ambient conditions before undergoing laser cladding.

The gravimetric composition of the powder mixture in terms of metal species is presented in Table 3.6.1.

Table 3.6.1 Chemical composition of the powder mixture used for cladding (Roata et al., 2019b).

Element	**Ni**	**Al**	**Zn**
(Wt %)	60	15	25

During the laser cladding process, the poly (vinyl alcohol) (PVA) binder undergoes rapid thermal decomposition due to the high-temperature energy generated, converting its molecular structure into volatile compounds before the coating deposition is complete. As a result, the PVA binder does not contribute to the coating's chemical composition and acts as a non-reactive component.

The laser cladding was performed using a 530 W Nd:YAG laser (Trumpf TruPulse 556) in pulse mode (λ=1064 nm) and a PRECITEC YC50 processing head, mounted on a 6-axis Cloos QRC-E 315 industrial robot with 0.1 mm precision. A 600 µm optical fiber was used to create a defocused near-Gaussian laser spot of 1 mm at a distance of 12 mm from the substrate, while argon shielding gas was employed to prevent oxidation (Hulka et al., 2021).

To optimize the process, a Design of Experiments (DOE) methodology was used, focusing on two parameters: cladding speed (factor 1) and laser pulse frequency (factor 2). This approach allows for the assessment of individual effects and interactions between the factors, which are crucial for

understanding the cladding process. The experimental design is illustrated in Figure 3.6.2, showcasing the matrix of varying factor levels, and detailed in Table 3.6.2.

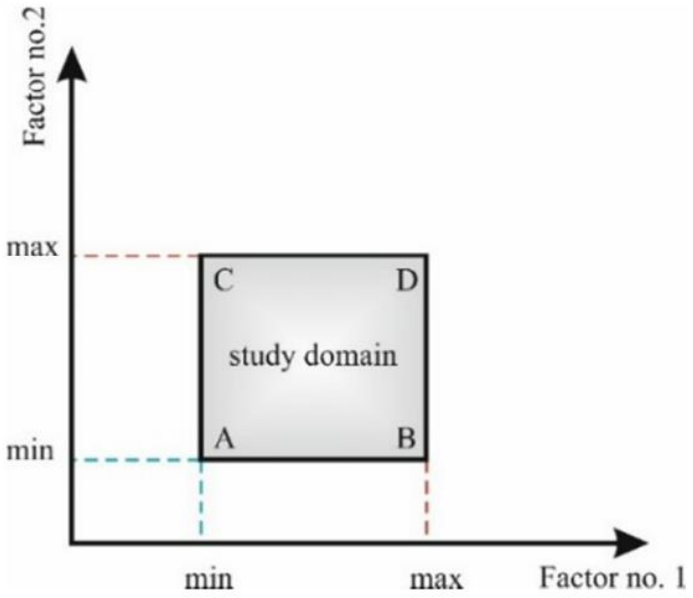

Figure 3.6.2 Experiment geometric model (Roata et al., 2019b).

Table 3.6.2 Experimental matrix of thermal spraying process (Roata et al., 2019 b).

Samples	Cladding speed [mm/s]	Pulse frequency [Hz]	Power [kW]	Pulse duration [ms]	Energy [J]	Shielding gas Ar [l/min]
P1 (A)	60	75	1.5	2	3.06	15
P2 (B)	90	75				
P3 (C)	60	100				
P4 (D)	90	100				

The coating was created by depositing parallel, overlapping laser beads with a partial overlap of 0.7 mm over a 50 mm length, resulting in a 40 mm width. This deposition method involved moving in the same direction while keeping the laser beam oriented front-fed, optimizing the coating width and ensuring uniform application.

Microhardness profiles of the coatings were measured from the top to the base material using a Vickers FM 700 tester. Metal emissions were collected by using a pre-moistened polyethylene terephthalate filter connected to a Kemppi Fume Extractor, which were treated with aqua regia (a mixture of 50 mL 37% HCl and 65% 1:3 HNO_3) and heated to 80 °C until nitrogen oxides ceased forming.

Figure 3.6.3 Typical sample of the laser cladding process (Roata et al., 2019b).

To analyze metal ions, the resulting solution was treated with 20 mL of 10M NaOH to precipitate Ni and Fe. The precipitate was then re-dissolved in 1M HNO_3 and diluted. Spectrophotometry was used to analyze 1 mL aliquots from both filtrates with specific color-developing reagents for each metal ion:

- Fe was determined at λmax = 512 nm after reduction and pH adjustment.
- Ni was measured at λmax = 445 nm after stabilizing and reacting with dimethylglyoxime and ammonia.
- Al content was assessed at λmax = 390 nm using a specific reagent.
- Zn content was measured at λmax = 661 nm with KSCN and other stabilizers.

The concentration of metal emissions, C_{em} expressed in mg/m^3 were determined based on the metallic ions' concentration in solution M (c_M, mg/L), the debit of the exhausting installation (D_{exh} =2m^3/h) and the duration of the cladding process, t_{clad} (1.08 minutes ≡ 0.018 h for a speed of 60 mm/s and 44 seconds ≡ 0.012 h for a speed of 90 mm/s).

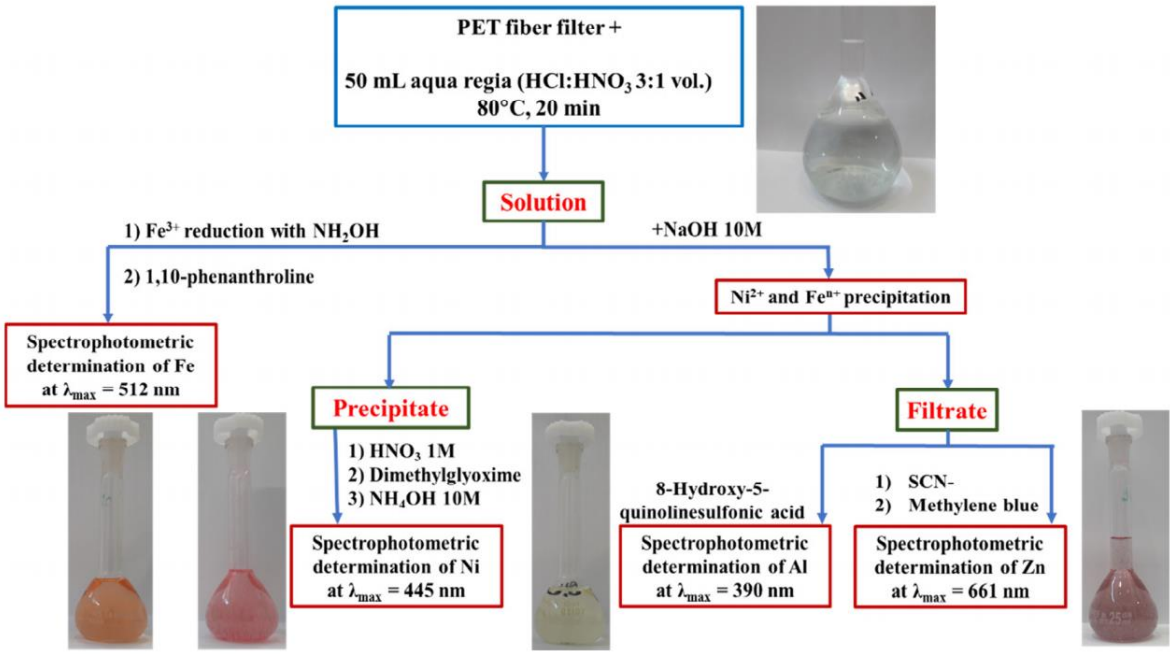

Figure 3.6.4 Separation and analysis scheme for the metal species collected on the filter (Roata et al., 2019b).

This concentration of metal emissions however is reported to the duration of the cladding process. To compare the obtained results with the occupational recommendations, the short-term exposure limit (STEL) for 15 minutes and the time-weighted average (TWA) for 8 hours.

Figure 3.6.5 presents optical and scanning electron micrographs for two representative samples, P1 and P4, which correspond to the (-1) × (-1) and (+1) × (+1) parameter combinations from the design of experiments (DOE) setup (Table 3.6.3).

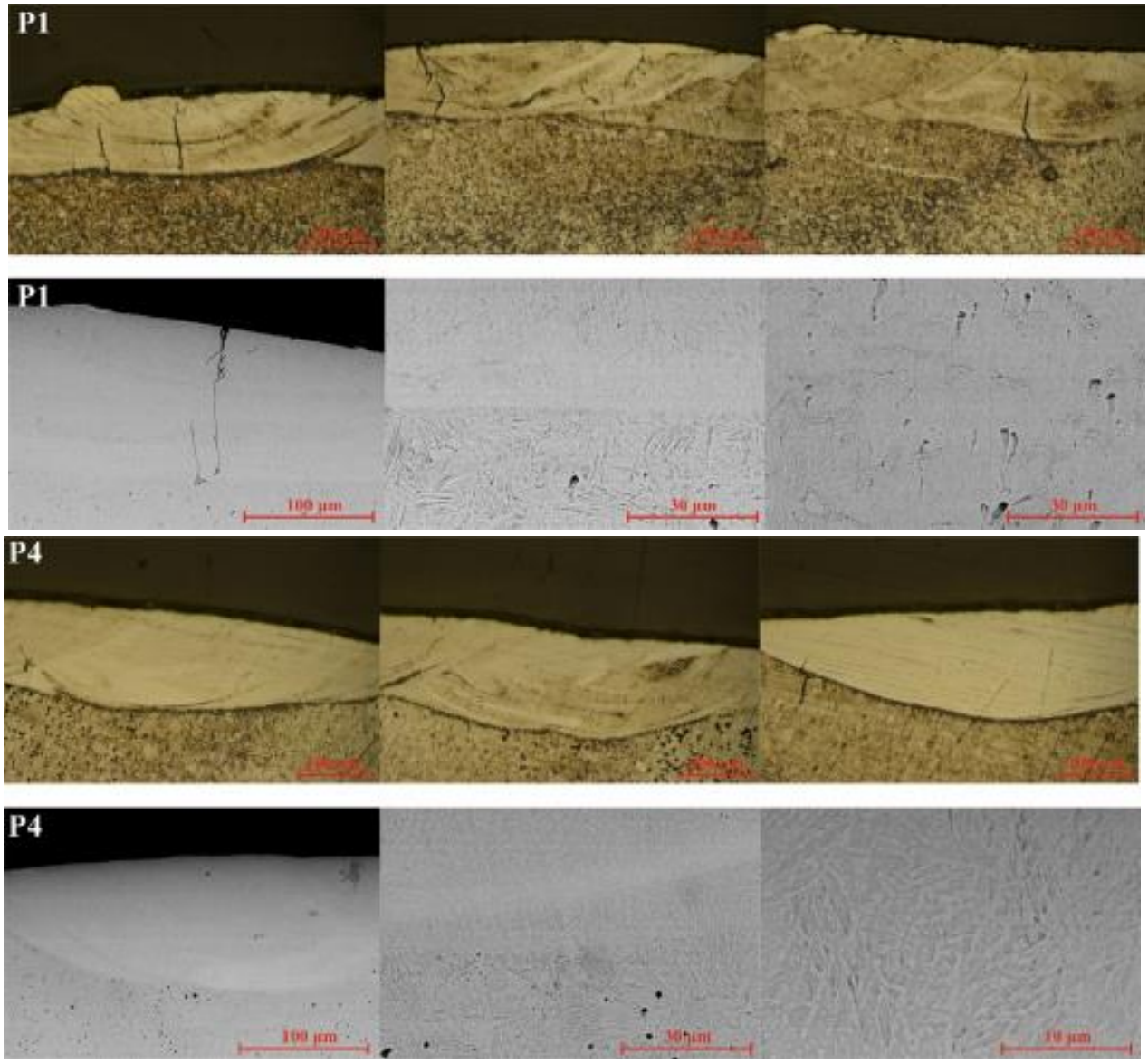

Figure 3.6.5 Optical and SEM micrographs for P1 and P4 samples (Roata et al., 2019b).

The study investigated the effects of laser cladding parameters on the microstructure and hardness of coatings. Using the lowest laser cladding speed (60 mm/s) and frequency (75 Hz) resulted in coatings with good fusion but some microdefects, such as cracks and pores, likely due to differences in the linear temperature coefficients of the metals. Conversely, the P4 sample, created using the highest speed (90 mm/s) and frequency (100 Hz), exhibited a defect-free microstructure

with strong bonding to the substrate and predominantly equiaxed crystals, attributed to higher nucleation and crystallization rates.

In contrast, the P1 sample exhibited a dendritic structure due to a slower nucleation and crystallization rate. To assess the influence of the cladding parameters on microstructure and mechanical properties, microhardness variations were measured across the base material (BM), heat affected zone (HAZ), and cladding layer (CL). This analysis aimed to understand how the processing conditions impact the coating's performance and durability.

Table 3.6.3 Microhardness HV_{01} values (Roata et al., 2019b).

Microhardness indent position		**P1(60 mm/s; 75Hz)**	**P2(90 mm/s; 75 Hz)**	**P3(60 mm/s; 100 Hz)**	**P4(90 mm/s; 100 Hz)**
CL	1	357.6	383.5	360.8	393.5
	2	362.3	391.2	367	404.4
	3	357	400.2	363.6	400.8
	4	368.1	395.6	382.2	398.2
HAZ	5	367	354.5	365.3	351.4
	6	387	355.2	361.9	348.5
BM	7	269.9	270.1	267.8	270.5
	8	267.7	267.8	272	271.8

The study examined how laser cladding parameters affect both the microhardness and metal emissions in coatings applied to S235JR carbon steel. The results showed that microhardness in the cladded layer and the heat-affected zone (HAZ) was notably influenced by the speed of cladding. A lower cladding speed (60 mm/s) resulted in a reduction of microhardness due to increased dilution from mixing with the base material, whereas a higher speed (90 mm/s) achieved a rise in microhardness because of a reduced dilution rate and a higher concentration of the cladded material. Specifically, the P4 sample, processed with faster parameters, exhibited the highest microhardness, while the P1 sample showed the lowest.

Table 3.6.4 Metal emissions concentrations (Roata et al., 2019b).

Sample	**C (µg/L)**				***C_{em}* mg/m^3)**				**STEL (mg/m^3)$_{15\ min}$**				**TWA (mg/m^3)$_{8h}$**			
	Fe	Ni	Al	Zn	Fe	Ni	Al	Zn	Fe	Ni	Al	Zn	Fe	Ni	Al	Zn
P1	35.40	4.10	0.37	2.32	0.25	0.02	0.002	0.01	3.41	0.39	0.03	0.22	109.25	12.65	1.14	7.16
P2	35.05	5.46	0.42	2.04	0.36	0.05	0.004	0.02	7.47	1.16	0.08	0.43	243.40	37.91	2.91	14.16
P3	34.90	6.32	0.51	2.33	0.24	0.04	0.003	0.02	3.36	0.60	0.04	0.22	107.71	19.50	1.57	7.19
P4	35.42	8.23	0.56	2.27	0.37	0.08	0.005	0.02	7.55	1.75	0.11	0.48	245.97	57.15	3.88	15.76

The analysis of metal emissions utilized Time-Weighted Average (TWA) and Short-Term Exposure Limit (STEL) values, revealing a significant correlation with laser frequency and an inverse relationship with cladding speed. The P4 sample recorded the highest metal emissions, likely due to greater exposure to laser radiation, aligning with thermodynamic principles that indicate increased vaporization with stronger laser exposure. The emissions of zinc were relatively stable, a result of its high thermal conductivity and low melting point, while a considerable amount of iron was emitted. This suggests that iron particles from the substrate steel were being vaporized during the cladding process, despite their absence in the cladded material.

A comparative analysis of TWA and STEL values for iron, nickel, aluminum, and zinc against established occupational exposure limits from OSHA and NIOSH revealed that TWA values for iron, nickel, and zinc exceeded the recommended limits, indicating potential health risks. In contrast, the TWA values for aluminum fell within acceptable ranges for samples P1 and P3, but surpassed the limit for sample P4.

Table 3.6.5 Maximal values for TWA and STEL (metal powders) (Roata et al., 2019b).

Metal	STEL (mg/m^3)	TWA (mg/m^3)
Fe	n.a.	1
Ni	n.a.	1
Al	n.a.	1
Zn	10	2

Overall, the study underscored how higher laser cladding speeds can enhance the hardness of coatings while also raising concerns about occupational exposure to metal emissions during the laser cladding process. Additional research is needed to fully understand these implications and to devise strategies for mitigating health risks in industries that employ laser cladding technology.

3.7 Solar heat treatment of Ni-Al coatings

A comprehensive study was conducted on the thermal spraying of a Ni-Al self-bonding powder onto C510 phosphor bronze substrates. The powder, consisting of 80.89% nickel and 19.11% aluminum, was characterized by optical emission spectroscopy, revealing a particle size of 150-200 µm via scanning electron microscopy (SEM).

Using a CastoDyn DS8000 powder flame spraying unit, a set of ten reference samples was created (labeled R), alongside another set thermally treated with concentrated solar energy (labeled SA) at varied temperatures, and a third set heated in an electric furnace (labeled EL). The solar treatment was conducted in the SF5 vertical axis solar furnace in Spain, employing a specific heating protocol that peaked at 970 °C.

The study found that the SA sample treated at 970 °C exhibited the best mechanical and corrosion resistance. Additional tests compared the CSE treatment with traditional electric furnace heating.

Characterization techniques included SEM for size distribution, surface roughness measurements, microhardness testing, nanoindentation for mechanical properties, friction and wear assessments using a pin-on-disk tribometer, and adhesion evaluations through scratch testing. Crystalline structure analysis was performed via X-ray diffraction, and contact angles were measured to evaluate surface energy using the Owens, Wendt, Rabel, and Kaelble method (Croitoru et al., 2019; Croitoru & Roata, 2023).

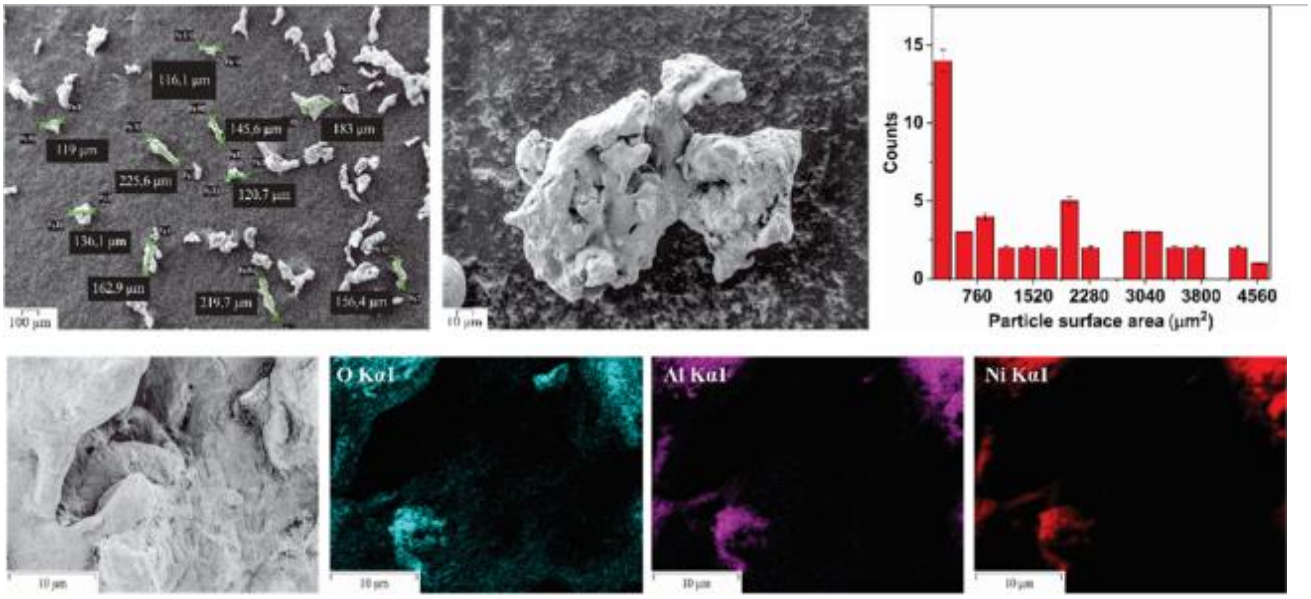

Figure 3.7.1 SEM micrographs, particle size distribution histogram and EDS mappings (O, Al, Ni) of feedstock powder (Roata et al., 2020).

The roughness of the surface influence on the contact angle value has been taken into consideration, by applying the Wenzel equation (3.7.1) (Jardim et al., 2016). The results obtained from this study provide valuable insights into the thermal spraying process and its effects on the properties of the coatings.

$$cos\theta_m = r * cos\theta \tag{3.7.1}$$

where r is the roughness ratio, θm is the measured contact angle, and θ is the Young contact angle, used to determine the surface energy:

$$r = 1 + \frac{S_{dr}}{100} \tag{3.7.2}$$

In equation 3.7.2, Sdr represents the developed interfacial area ratio, determined by image processing, with the help of the ImageJ software (Choe et al., 2014).

The corrosion rate of the coated samples was investigated using an Autolab 302 N potentiostat/galvanostat in a three-electrode setup with a working electrode (the coated material),

Ag/AgCl reference electrode, and graphite counter-electrode. Samples were equilibrated for 30 minutes in a 3.5 wt% NaCl electrolyte before testing. Corrosion rates (mm/year) were calculated from corrosion current density values (jcorr) obtained from Tafel polarization curves, using the Stern-Geary equation.

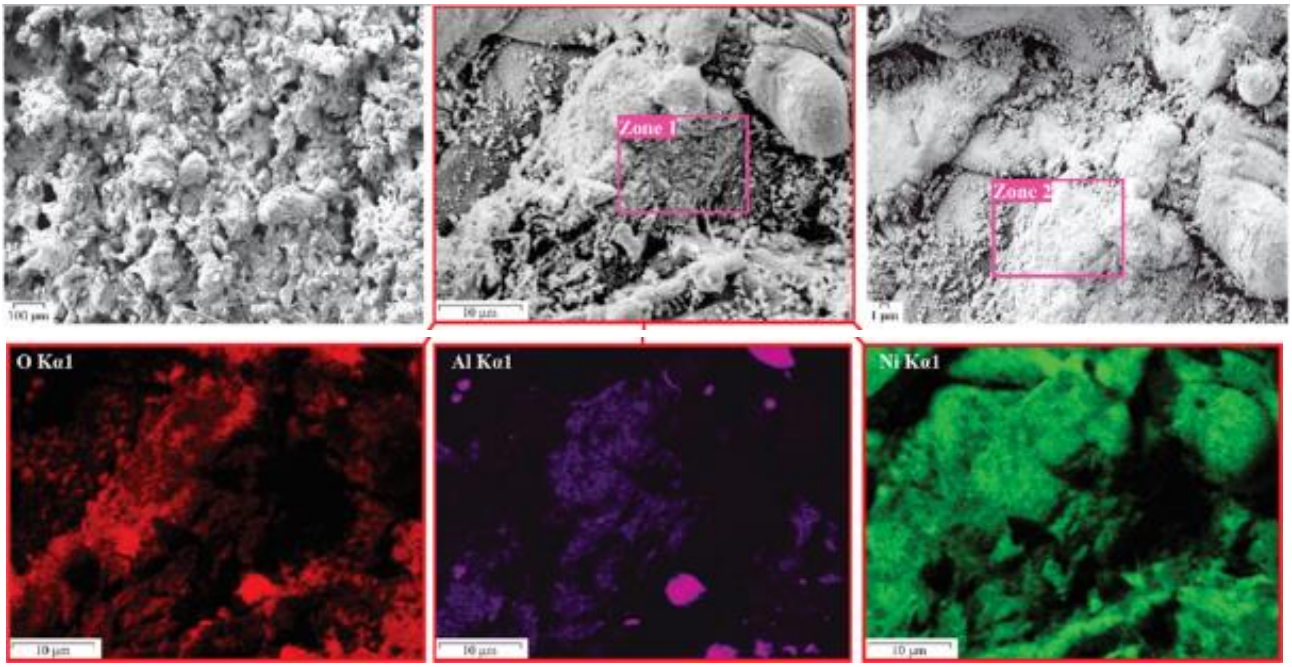

Figure 3.7.2 SEM micrographs and EDS elemental mapping on the surface of R sample (Roata et al., 2020).

The surface morphology of both reference and thermally treated coatings exhibited typical features of thermal spraying, including plastically-deformed feedstock particles and incompletely melted particles, contributing to high surface roughness, quantified by average roughness parameter (Ra) values ranging from 0.5 to 1.5 µm.

The reference sample surface was characterized by a high number of unmelted Ni-Al particles, as evident from Figure 3.7.2.

Elemental EDS mappings revealed the presence of Al in clusters, while Ni (the majoritarian phase) was more uniformly distributed on the surface. The presence of oxygen on the coating surface, detected by EDS, was attributed to the interaction with atmospheric oxygen during the time-of-flight of molten feedstock particles. The XRD patterns confirmed the formation of Ni or Al oxides on the surface.

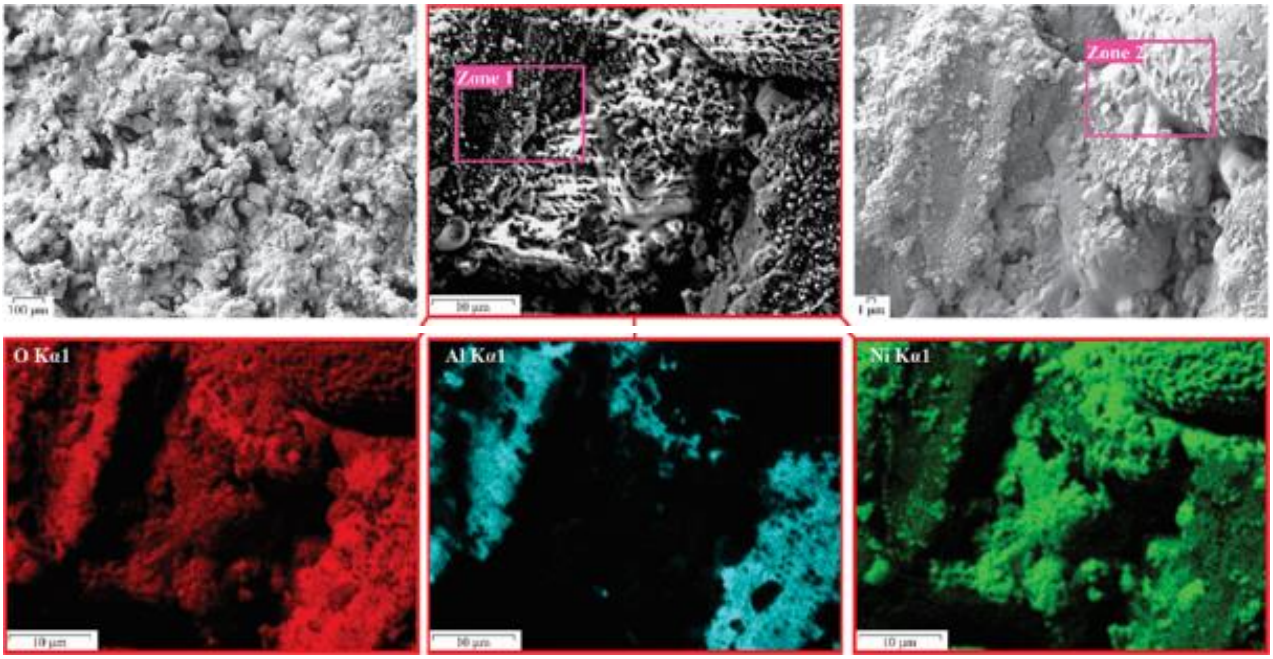

Figure 3.7.3 SEM micrographs and EDS elemental mapping on the surface of EL sample (Roata et al., 2020).

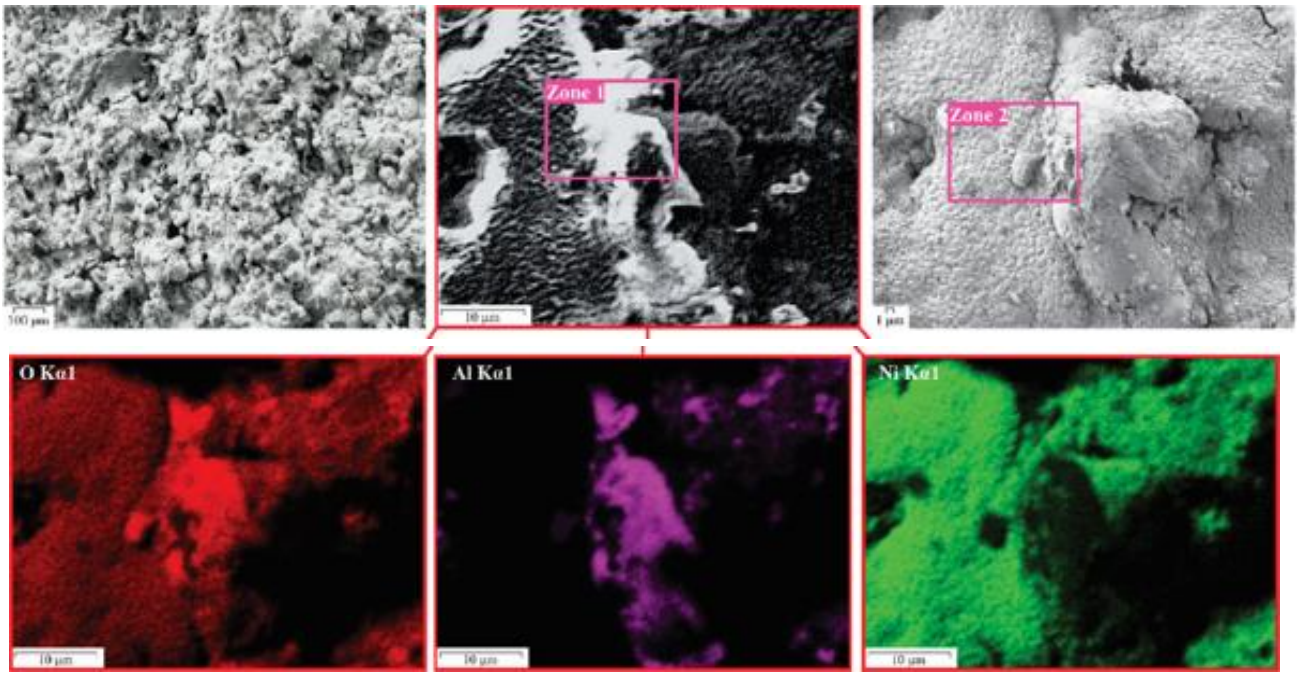

Figure 3.7.4 SEM micrographs and EDS elemental mapping on the surface of SA sample (Roata et al., 2020).

The thermally treated samples (EL and SA) exhibited a more uniform surface morphology, as visualized by scanning electron microscopy (SEM) in figures 3.7.3 and 3.7.4. The average surface roughness (Ra) values for EL and SA were 0.87 µm and 0.94 µm, respectively, indicating a significant reduction in surface roughness compared to the reference sample.

Table 3.7.1 EDS elemental content (Ni, Al, O) on the surface and the cross-sections of R, EL, SA (Roata et al., 2020).

Sample		Surface			Cross-section		
		Ni (% wt.)	Al (% wt.)	O (% wt.)	Ni (% wt.)	Al (% wt.)	O (% wt.)
R	Zone 1	82.3	12.1	5.6	83.9	11.8	4.3
	Zone 2	82.5	10.7	6.8	-	-	-
EL	Zone 1	77.0	15.3	7.7	76.8	16.3	6.9
	Zone 2	77.5	15.0	7.5	-	-	-
SA	Zone 1	77.5	14.7	7.8	77.7	16.1	6.2
	Zone 2	79.3	13.4	7.3	-	-	-

Heat treatment of the coatings enhanced elemental diffusion, possibly resulting in intermetallic compound formation. The EL and SA samples displayed a uniform aluminum distribution, with the EL sample showing higher aluminum content due to longer heat treatment. Both samples experienced increased surface oxidation, especially the EL sample, from prolonged high-temperature oxygen exposure. The resulting oxides had unusual lamellar crystal structures for metallic/intermetallic phases, and EDS mapping revealed elevated oxygen levels on both surfaces. The X-ray diffraction (XRD) patterns for the substrate, R, EL, and SA samples revealed important results regarding phase compositions. The reference sample displayed γ-Al_2O_3 and NiO, formed through interactions with atmospheric oxygen, along with minor quantities of nickel-aluminum intermetallic compounds like NiAl. A small amount of the intermetallic compound Cu_5Sn was detected, suggesting incomplete coating coverage. Additionally, Cu_3Al was observed at 34.36°. The EL sample's XRD analysis indicated the presence of various oxides, including NiO, and highlighted the formation of a novel intermetallic phase, Ni_3Al, likely due to enhanced elemental diffusion from thermal treatment.

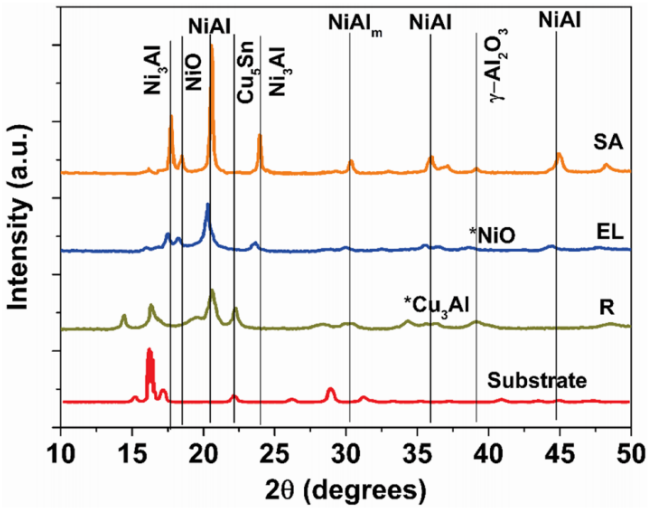

Figure 3.7.5 XRD pattern of the coatings surface and substrate (Roata et al., 2020).

The surface solar thermal treatment further promoted diffusion, leading to an increased presence of hard phases such as Ni_3Al and martensitic NiAl. The diffraction intensity for NiAl and Ni_3Al was notably high, indicating their potential contribution to the material's increased hardness and corrosion resistance, as supported by the data in Tables 3.7.2 and 3.7.3.

Table 3.7.2 Mechanical characteristics of the coatings (K: wear coefficient; Hit: indentation hardness; Eit: indentation modulus; Wp: plastic deformation work; Wt: total deformation work; hit: plastic work percent) (Roata et al., 2020).

Sample	$HV_{0.5}$ distance dependency		K (10^{-3} $mm^3/N{\cdot}m$)	Hit (GPa)	Eit (GPa)	Hit/Eit	Hit^2/Eit^2	Hit^3/Eit^2	W (nJ)		
	$a*10^{-3}$	b							Wp	Wt	H_{it} (%)
R	7.08	7.40	3.12	3.66	91.92	0.039	0.00158	0.0058	4.43	6.20	71.46
EL	9.05	5.84	2.78	3.78	212.74	0.017	0.00031	0.0011	4.66	6.48	71.85
SA	12.18	5.21	2.46	4.11	194.24	0.021	0.00044	0.0018	5.87	7.93	74.00

Table 3.7.3 Surface energy components of the coatings and corrosion rate.

Sample	$\theta_{m,water}$ (°)	r	γ (mN/m)	γd (mN/m)	γp (mN/m)	CR [10^{-3} mm/year]
R	87.52	1.081	39.25	17.34	21.91	97.78
EL	71.59	1.311	43.37	7.75	35.62	52.74
SA	62.88	1.562	41.05	8.12	32.93	12.90

The use of surface concentrated solar thermal treatment improves material properties by promoting oxidation primarily at the surface while keeping oxygen content lower in the bulk. This enhances intersplat cohesion and interfacial adhesion between the coating and bronze substrate, as shown in cross-sectional SEM micrographs.

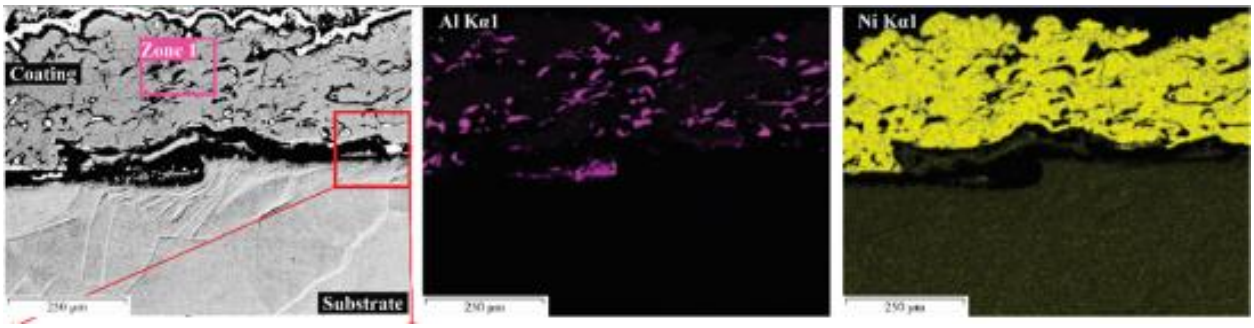

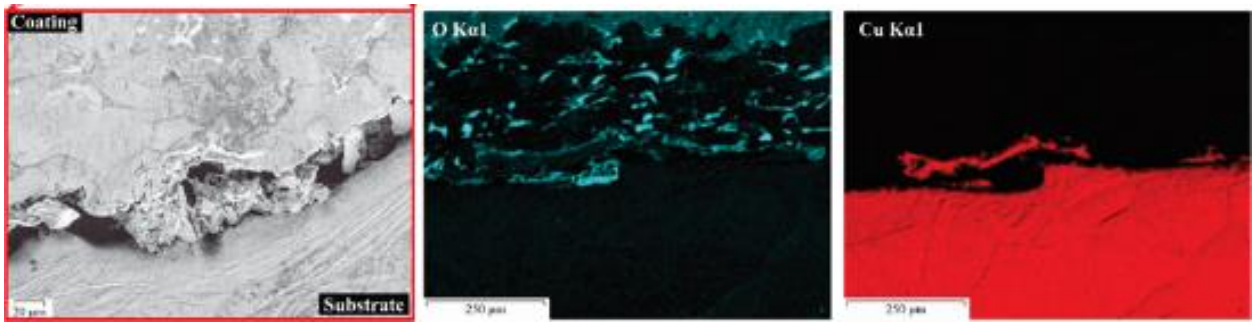

Figure 3.7.6 Cross-sectional SEM micrographs and EDS maps (Al, Ni, O, Cu) for the R sample (Roata et al., 2020).

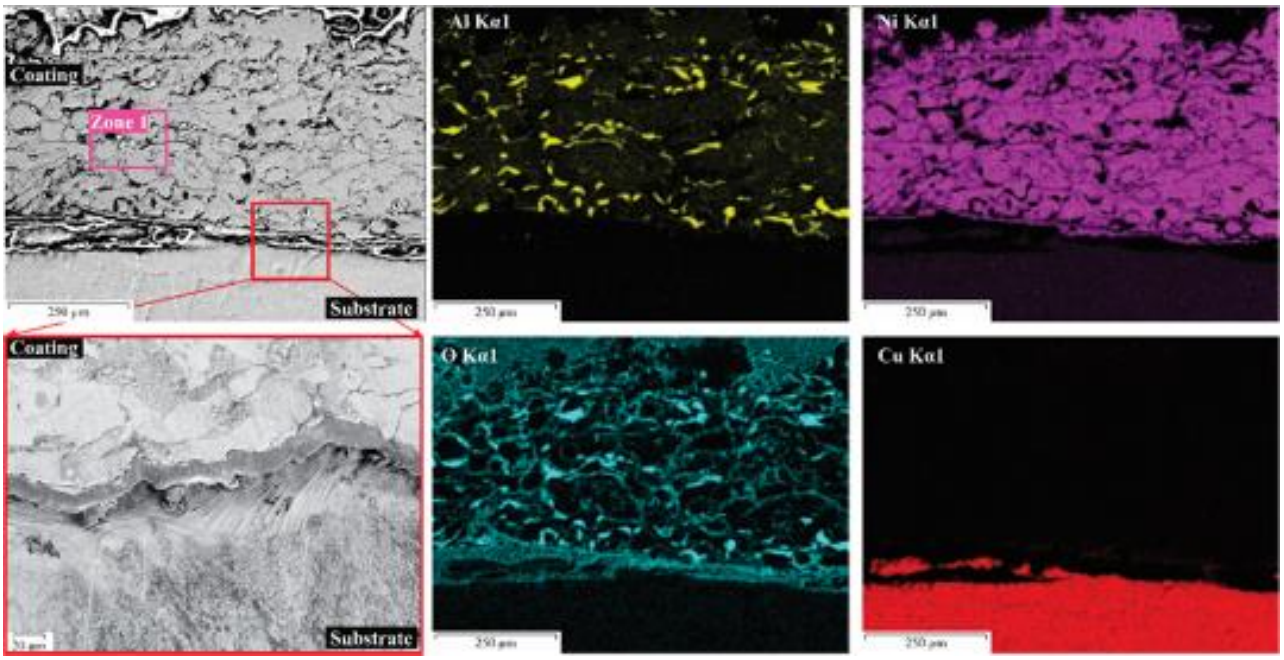

Figure 3.7.7 Cross-sectional SEM micrographs and EDS maps (Al, Ni, O, Cu) for the EL sample (Roata et al., 2020).

Figures 3.7.6-3.7.8 depict the elemental oxygen distribution in the coatings, with the reference sample (Figure 3.7.6) showing significant delamination likely due to insufficient melted particle fusion during thermal spraying. Post-deposition thermal treatment is suggested to improve coating-substrate integration, aligning with results from other studies.

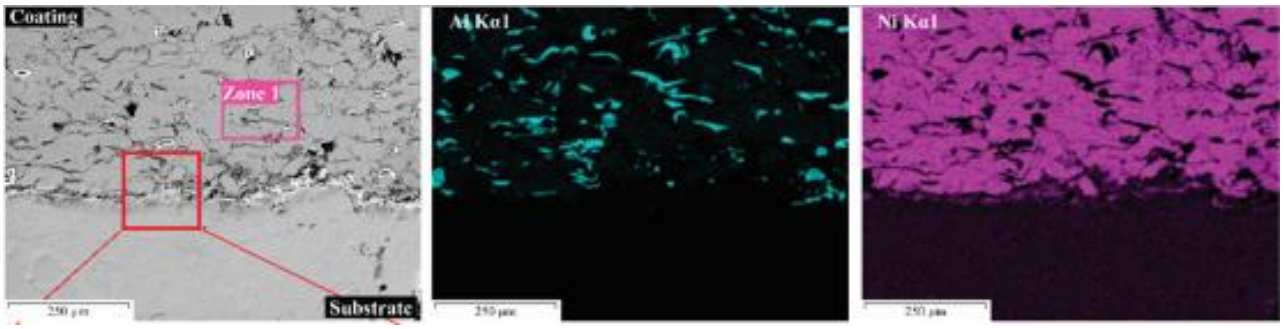

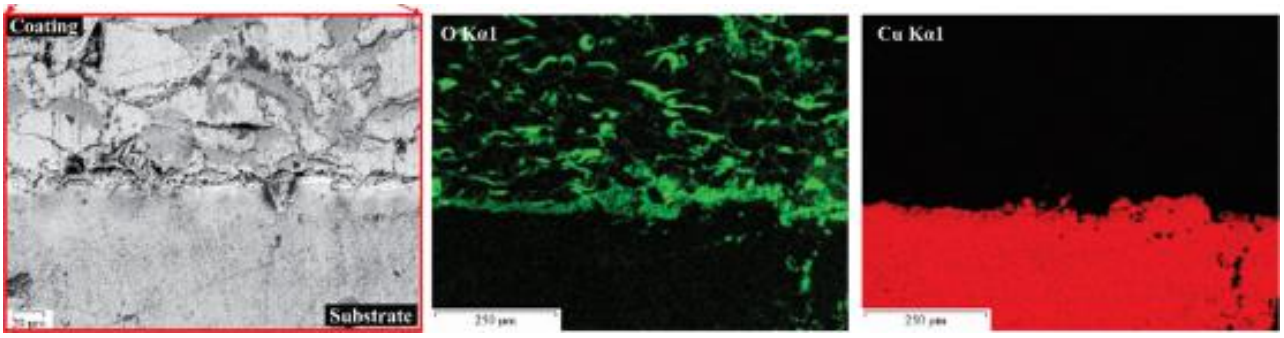

Figure 3.7.8 Cross-sectional SEM micrographs and EDS maps (Al, Ni, O, Cu) for the SA sample (Roata et al., 2020).

The study utilized energy-dispersive X-ray spectroscopy (EDS) to analyze the oxidation states of elements in coatings, finding higher oxidation in the EL sample compared to the reference sample. Thermal treatment increased the temperature significantly, enhancing elemental diffusion and intermetallic phase formation.

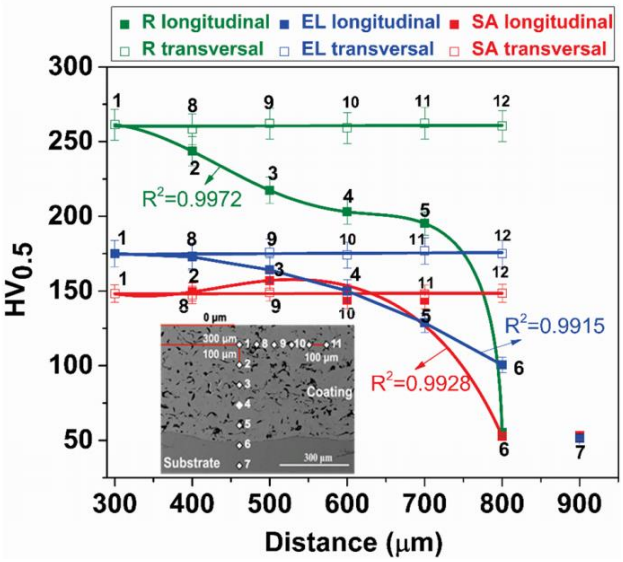

Figure 3.7.9 Cross-sectional and longitudinal hardness values at different distances from/along the coating (Roata et al., 2020).

The EL sample showed better lamellar fusion and a cohesive structure, but had a greater amount of oxide species at the coating-substrate interface, which could impact mechanical properties. In contrast, the SA sample had superior bonding with the substrate and revealed Al-rich zones, indicating γ-Al2O3 formation, aligning with X-ray diffraction (XRD) results. Additionally, the average roughness of the coatings decreased from the reference sample to the EL and SA samples, suggesting improved splat layer compaction, which could enhance tribological and corrosion resistance by limiting the movement of splat layers and penetration of corrosive agents.

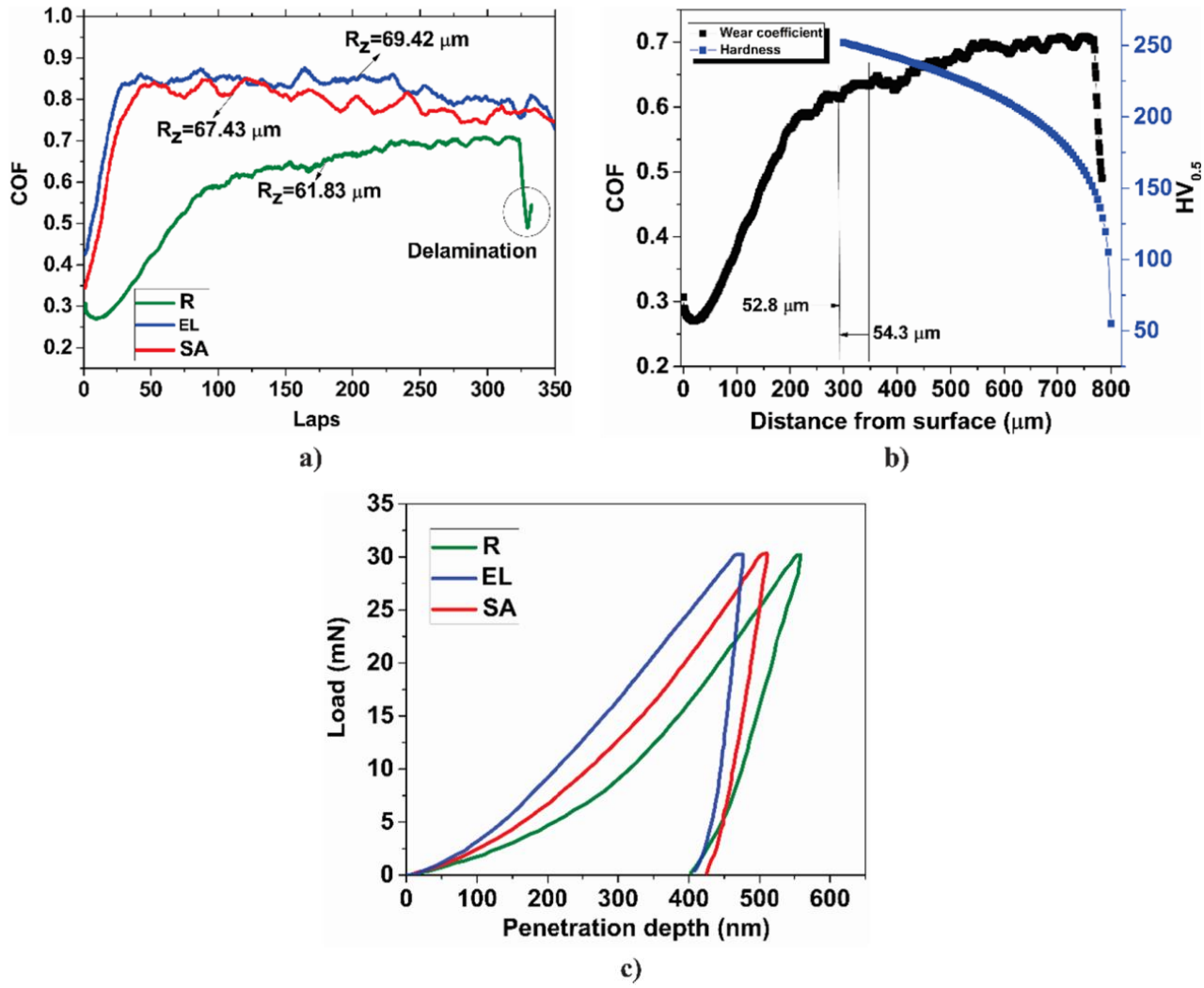

Figure 3.7.10 (a) Friction coefficient evolution on the samples surface; (b): friction coefficient variation with distance from the coating surface for the reference; (c): nanoindentation loading/unloading curves (Roata et al., 2020).

The study examined the hardness of coatings, revealing a hyperbolic decrease in hardness with distance from the surface, influenced by the mixing of Ni and Al and the formation of hard phases. Surface analysis using scanning electron microscopy (SEM) and atomic force microscopy (AFM) showed reduced roughness and increased surface area, which may enhance performance. Mechanical testing demonstrated significant improvements in hardness, scratch resistance, and wear resistance. Enhanced phase mixing was noted in the SA and EL samples, with the SA sample showing a 28 % increase in mixing and improved homogeneity, likely due to a reduced temperature gradient during cooling, supporting better diffusion and precipitation processes.

The study investigated the variation of the kinetic friction coefficient (COF) influenced by surface roughness and homogeneity. The initial low-friction phase relates inversely to surface roughness, with the reference sample lasting 50 cycles, EL for 40 cycles, and SA for 20 cycles. The steady-state regime displayed fluctuations due to the wear tip interacting with splat-derived layers, with the

reduced number of pseudo-variation plateaus in the SA sample suggesting better fusion between thicker layers.

The SA sample exhibited higher COF values, attributed to greater friction resistance and a more uniform dispersion of hard phases from solar annealing. COF values were similar to those reported in the literature, and they increased with decreasing hardness, likely due to new rough interfaces formed in less rigid materials during contact with the wear tip. The SA sample also showed a 20% lower wear coefficient (K value) compared to the reference, with delamination occurring in the reference.

Nanoindentation results indicated elastoplastic behavior in the coatings, with the SA sample demonstrating improved energy dissipation through plastic deformation. It also exhibited higher hardness (H) and elastic modulus (E) values due to more uniform hard-phase mixing. The H/E ratio, along with the H_2/E_2 and H_3/E_2 ratios, offered insights into the coatings' mechanical properties, showing that the reference coating had the highest values, followed by SA and EL samples. The results suggest that enhanced homogeneity and wear resistance from thermal treatments can slightly increase deformation and fracture susceptibility, with concentrated solar thermal treatment yielding better results than conventional furnace annealing.

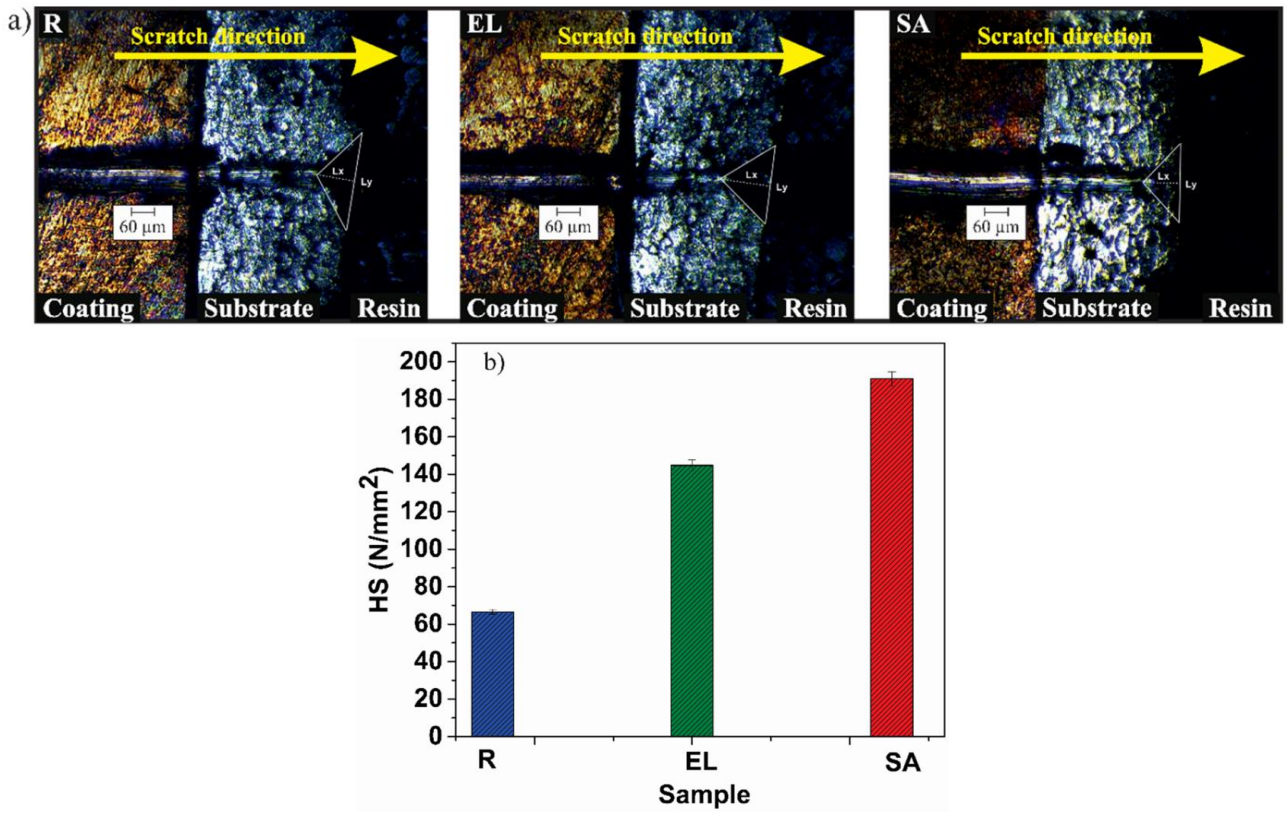

Figure 3.7.11 (a): Scratch test mark on cross-sectioned thermal sprayed samples; (b) scratch hardness values (Roata et al., 2020).

The scratch patterns for the thermal sprayed coatings are depicted in Figure 3.7.11 a, with the width of the indent cone (L_y) and cone height (L_x) measured and used to calculate the indent cone area (A_c) according to the mathematical formula described in Eq. (3.7.3).

$$A_c = \frac{1}{2} L_x * L_y \tag{3.7.2}$$

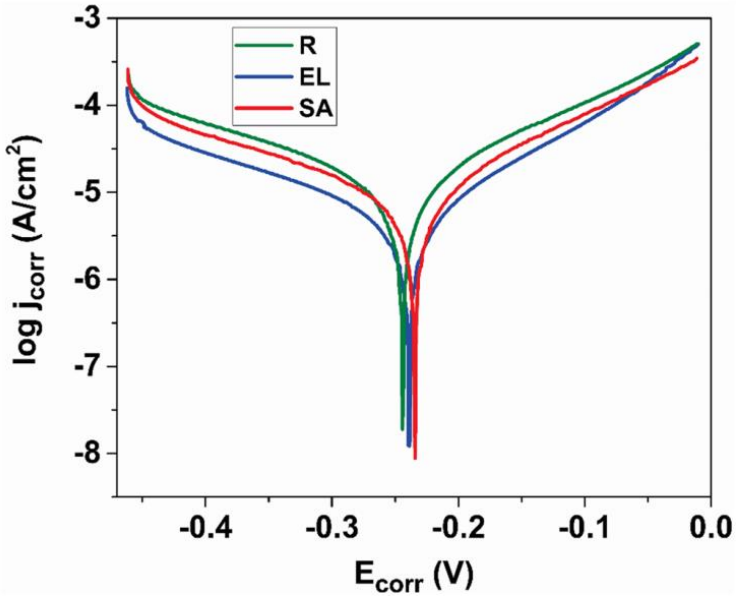

Figure 3.7.12 Tafel polarization curves for R, EL and SA samples (Roata et al., 2020).

The study revealed that the solar annealed (SA) sample demonstrated superior scratch resistance, with scratch hardness values approximately 65 % higher than the reference sample and 25 % higher than the electric furnace annealed (EL) sample. Solar annealing also increased the surface energy of the samples, attributed to polar oxidic compounds that enhanced hydrophilicity. Despite this, the presence of corrosion-resistant intermetallic NiAl compounds provided a barrier against corrosion-inducing agents. Corrosion resistance was significantly improved with solar annealing, showing an approximately 87 % reduction in corrosion current compared to the reference sample and a 46 % reduction compared to the EL sample. Overall, solar annealing positively affected both scratch and corrosion resistance of the coatings

Concentrated solar annealing significantly enhances the structural integrity of Ni-Al flame-sprayed coatings on phosphor bronze substrates. This process improves the uniformity and density of the microstructure by increasing intermetallic compounds, enhancing plasticity, and reducing defects and porosity. As a result, the coatings exhibit greater hardness, wear resistance, and a stronger interface with the substrate. These improvements suggest enhanced performance for applications like wear-resistant components and biomedical devices.

3.8 Photocatalytic surfaces obtained through one-step thermal spraying of Titanium

Titanium powder (99.5 wt.% Ti, Oerlikon-Metco, Metco 4010 A) was thermally sprayed without modification, exhibiting an average particle diameter of 80 µm (Figure 3.8.1). Rectangular aluminum plates (20 × 20 × 2 mm) with a chemical composition of 99.5 wt.% Al (confirmed via optical emission spectroscopy) served as substrates. Prior to deposition, the plates were polished using P360 grit abrasive paper and ultrasonicated in ethanol at 40 °C for 5 minutes to eliminate organic contaminants, given aluminum's favorable chemical stability and compatibility with titanium (Croitoru et al., 2020 b).

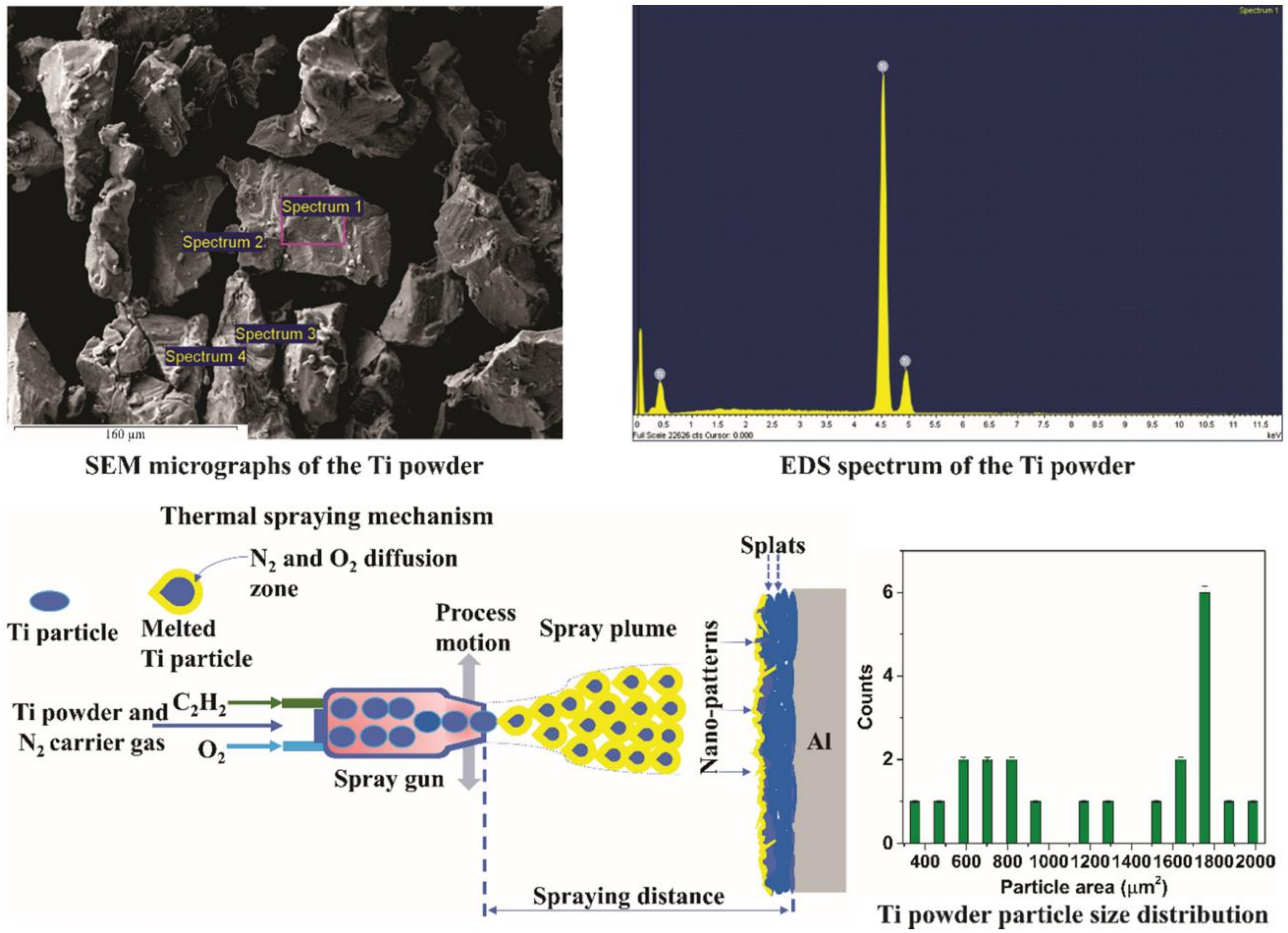

Figure 3.8.1 Titanium feedstock powder SEM micrograph (300×), EDS spectrum, size distribution and thermal spraying principle mechanism (Croitoru et al., 2020 b).

Methyl orange ($C_{14}H_{14}N_3SO_3Na$) was selected as the model dye due to its resistance to degradation and non-photobleaching under UV radiation, in contrast to other dyes used in photocatalysis. Additional chemicals sourced from Sigma-Aldrich included:

- Degussa P_{25} TiO_2 (>99.5% trace metals, primary particle size: 21 nm)
- Methyl isobutyl ketone (99.8% purity)
- Morin hydrate ($C_{15}H_{10}O_7 \cdot xH_2O$, ~95% purity)

- Coumarin (99% purity)
- Chromotropic acid disodium salt dehydrate ($(HO)_2C_{10}H_4(SO_3Na)_2 \cdot 2H_2O$, ~98% purity)
- Scavengers employed in this investigation were:
- Ethylenediaminetetraacetic acid disodium salt (EDTA2Na, 99% purity)
- Tert-butanol (TBuOH, 99.5% purity)
- Copper(II) nitrate trihydrate (99% purity)
- Ascorbic acid (HA, 99% purity)

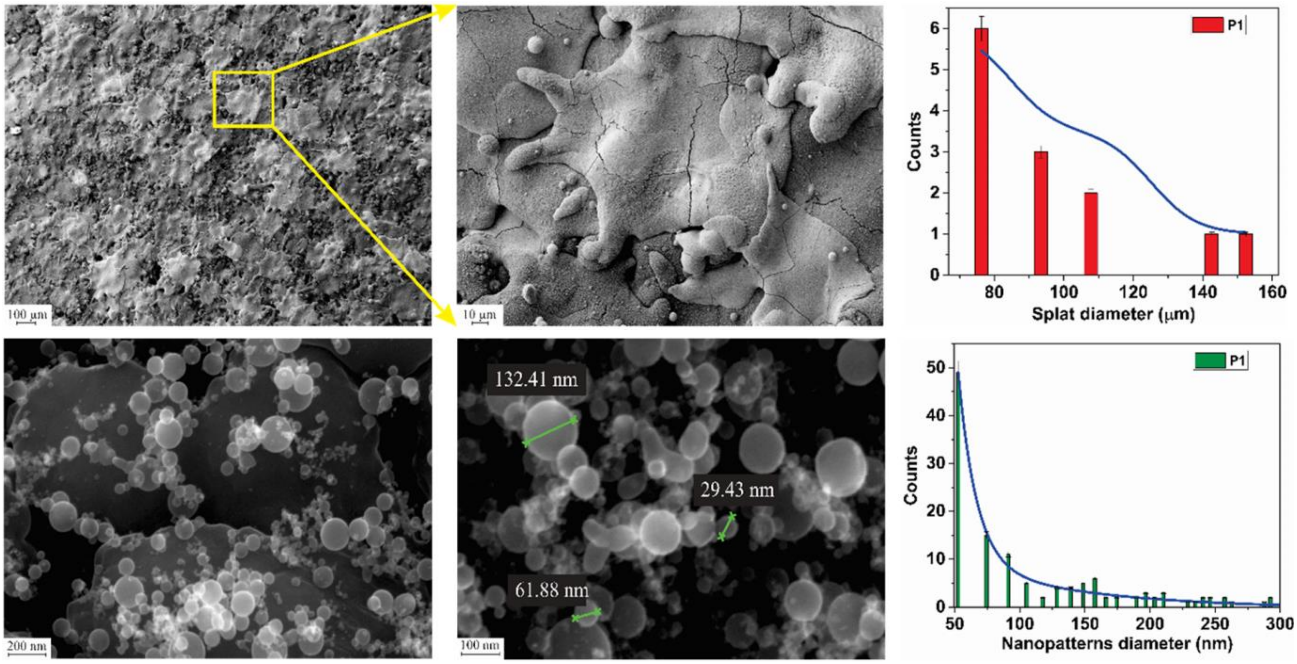

Figure 3.8.2 SEM micrographs and morphological features size distributions for P1 sample (Croitoru et al., 2020 b).

The morphology and surface chemistry of the coatings play a crucial role in their photocatalytic performance. Micrographs (Figure 3.8.2 and Figure 3.8.3) show that both coatings, formed by the deformation and agglomeration of titanium particles on aluminum substrates, reveal similar thermal spraying characteristics. The nanopatterned and porous surfaces, resulting from incomplete particle flattening, enhance the surface area and create regions rich in oxides and nitrogen, which are beneficial for photocatalysis.

Differences in chemical composition arise from the time-of-flight of molten particles during spraying. P2, having a longer time-of-flight, produces larger splats (90-170 µm) and exhibits lower roughness (Ra = 8.25 µm) compared to P1 (Ra = 11.74 µm), which has splats measuring 76-150 µm. The diameters of nanopatterned irregularities are maximally distributed at ~51 nm for P1 and ~18 nm for P2.

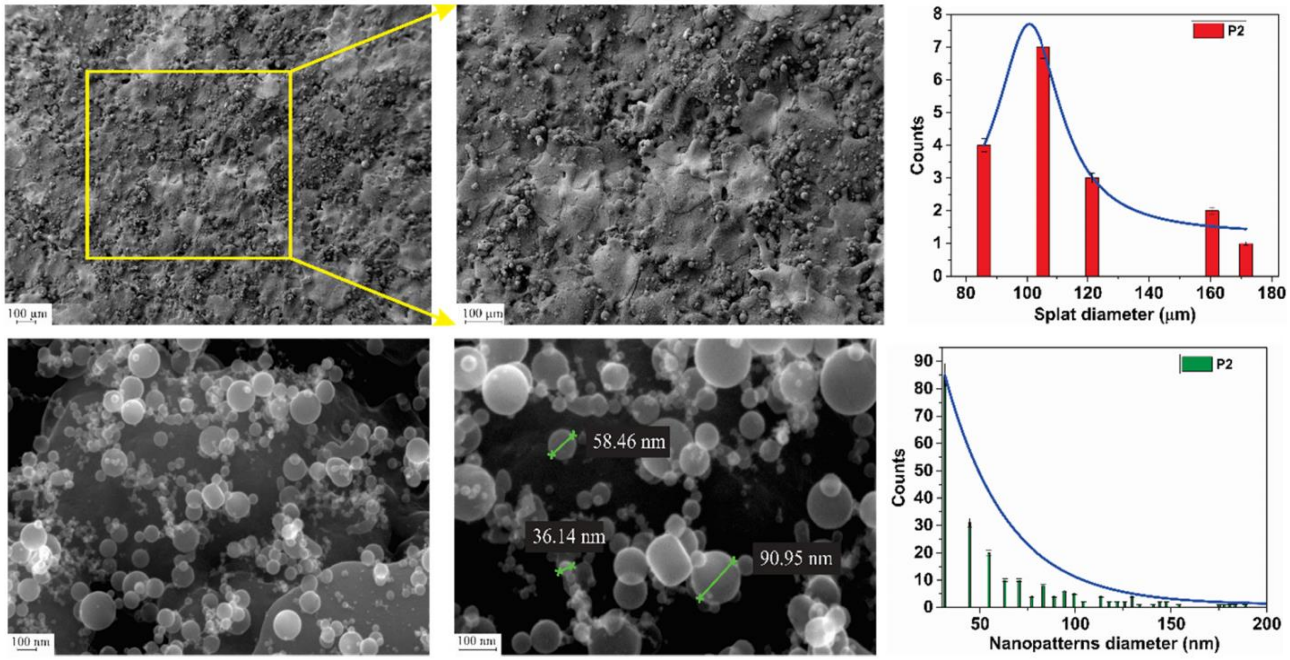

Figure 3.8.3 SEM micrographs and morphological features' size distributions for P2 sample (Croitoru et al., 2020 b).

The surface is rich in oxygen, as shown in Figures 3.8.4 and 3.8.5, due to the diffusion of atmospheric O_2 into the metal phase, forming various oxides. Nitrogen diffuses into the titanium phase, generating substitutional nitrides and interstitial oxynitrides, alongside N-doped TiO_2, which shifts the energy band gap to lower values than pure TiO_2 and enhances charge carrier separation under photoirradiation.

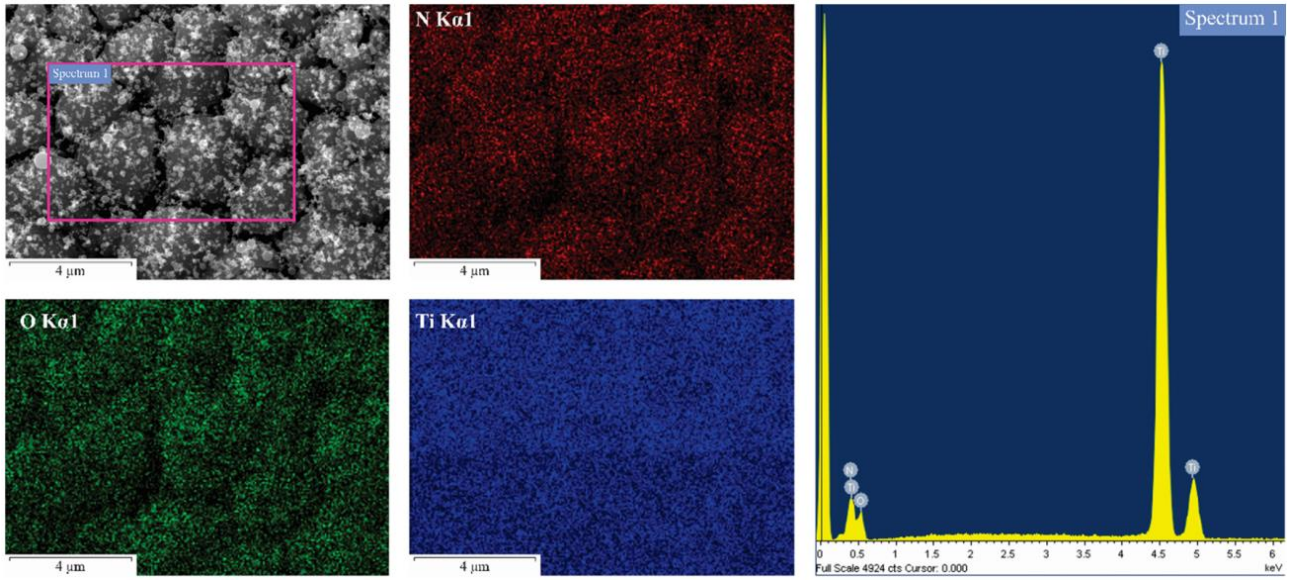

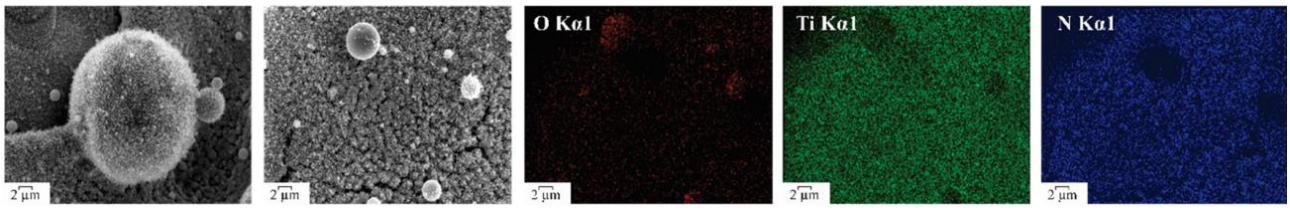

Figure 3.8.4 EDS elemental mapping and EDS spectrum (N, O, Ti) (top); EDS elemental mapping of incompletely molten spherical morphological features (bottom) for P1 sample (Croitoru et al., 2020 b).

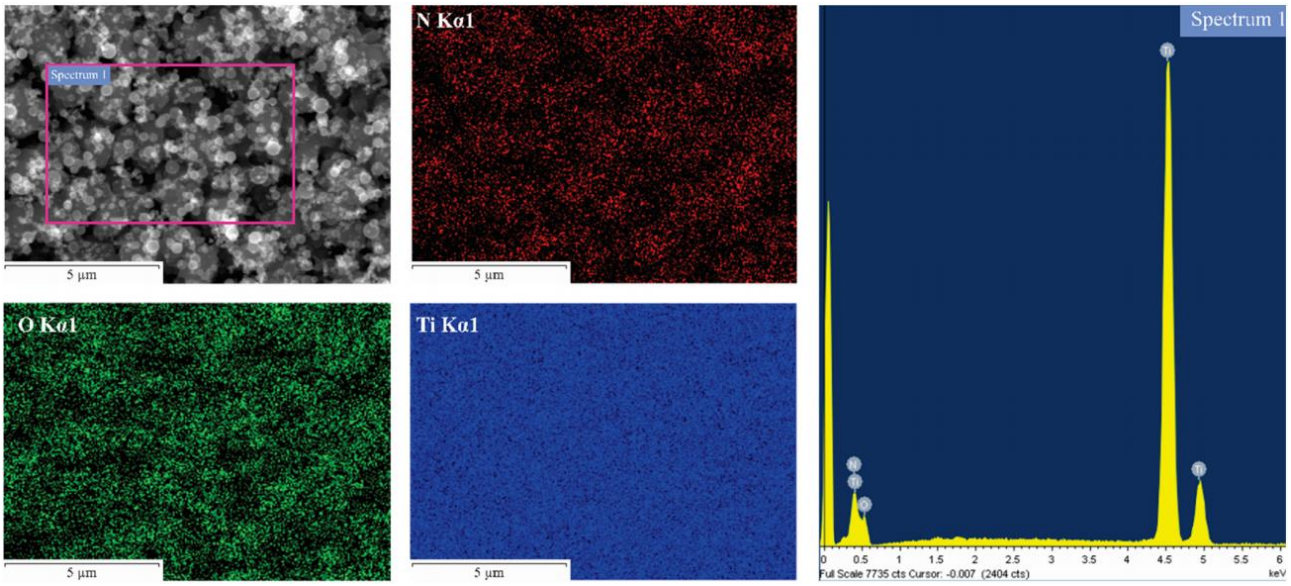

Figure 3.8.5 EDS elemental mapping and EDS spectrum (N, O, Ti) for P2 sample (Croitoru et al., 2020 b).

EDS mapping shows uniform Ti, N, and O distributions in both coatings, with P2 having higher oxygen content due to longer particle travel distance. Spherical features contribute to increased oxygen and photodegradation. Coating thickness: 115 ± 5 µm for P1 and 97.1 ± 5 µm for P2.
Both coatings have well-bonded interfaces with the aluminum substrate, with no delamination. EDS analysis confirms no intermixing between Ti and Al, indicating mechanical bonding.

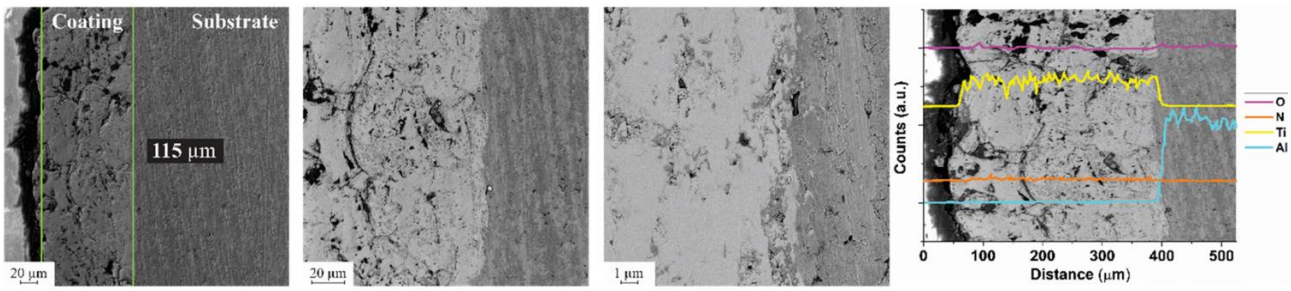

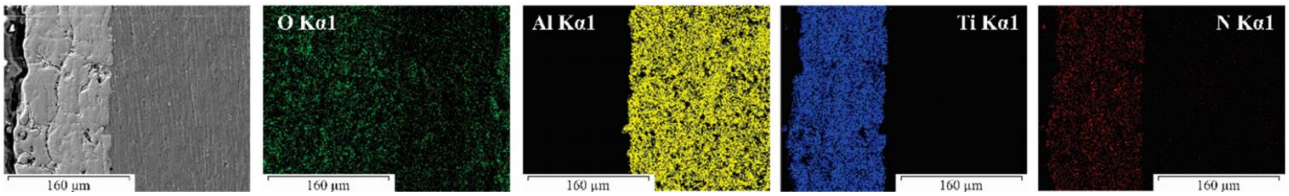

Figure 3.8.6 Cross-sectional SEM micrographs, EDS line scan and EDS elemental mapping (O, Al, Ti, N) for P1 sample (Croitoru et al., 2020 b).

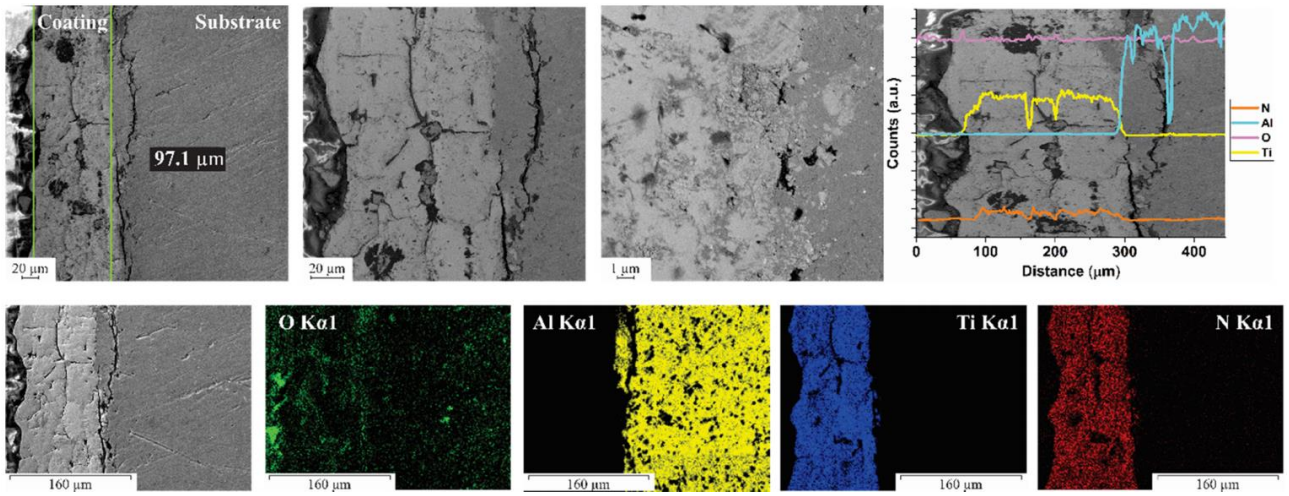

Figure 3.8.7 Cross-sectional SEM micrographs, EDS line scan and EDS elemental mapping (O, Al, Ti, N) for P2 sample (Croitoru et al., 2020 b).

XRD spectra reveal the presence of titanium and oxides (rutile and Ti3O5) on both samples. The Ti(1 0 2) peak is lower for P2, possibly due to increased oxidation. A weak diffraction peak at ~41.94° could be attributed to TiN.

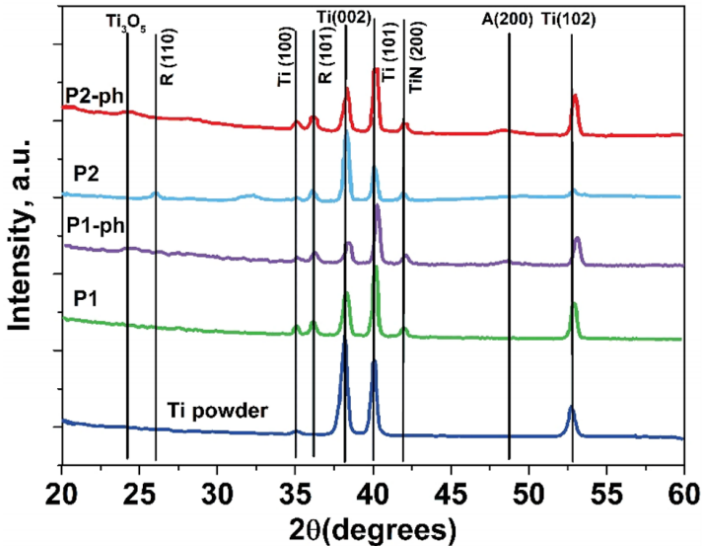

Figure 3.8.8 XRD diffractograms of Ti feedstock powder and achieved coatings before (P) and after photocatalysis (P-ph) (Croitoru et al., 2020 b).

After photocatalysis, XRD spectra reveal preserved crystalline phases along with an additional anatase peak at ~48.25° (JCPDS 73-1764) and a 0.2-0.4° shift in the Ti(1 0 2) peak, indicating local structural changes. Thermodynamic analysis suggests that Ti_3O_5 and rutile TiO_2 formation from Ti oxidation is favored, aligning with their surface presence. Elevated thermal spraying temperatures promote the TiO_2-Ti reaction, generating Ti3O5, which can convert to anatase under irradiation.
XPS analysis confirms the presence of TiO and Ti3O5, indicating photoinduced oxidation. The heightened diffraction peak intensities in P1-ph and P2-ph samples imply a photoinduced oxide generation mechanism. Anatase formation during irradiation in aqueous conditions may elucidate the two-step photodegradation kinetics of methyl orange dye, highlighting the importance of rutile-suboxide coupling for photocatalytic efficiency.

Crystallite sizes, estimated using the Stokes and Wilson method, show P1 and P2 sizes comparable to literature values, with P2 exhibiting larger dimensions likely due to lattice defects from longer particle flight times. XPS survey spectra indicate the presence of Ti, O, and N, consistent with EDS results. High-resolution Ti2p spectra reveal notable oxides (mainly rutile) and minimal metallic Ti, with a slight low-energy shift in the rutile peak suggesting stoichiometric deviations from oxygen vacancies or N ions, which are advantageous for photocatalysis by reducing charge carrier recombination and band gap energy.

O1s spectra present a primary feature at 530.7 eV for O-Ti bonding in undoped TiO_2, alongside a subfeature at 531.6 eV for O-Ti in titanium suboxides and interstitial N-doped TiO2. N1s scans show features at ~395.6 eV and ~396.7 eV attributed to N-Ti bonding in substitutional and interstitial forms, respectively, enhancing visible light photoactivity.
UV-VIS spectra of the coatings show absorption edges attributed to charge-transfer transitions, with a shift to the visible region in P1 and P2 coatings due to N doping. The shift is more pronounced in P2 coating, likely due to higher N doping (Croitoru et al., 2020 b).

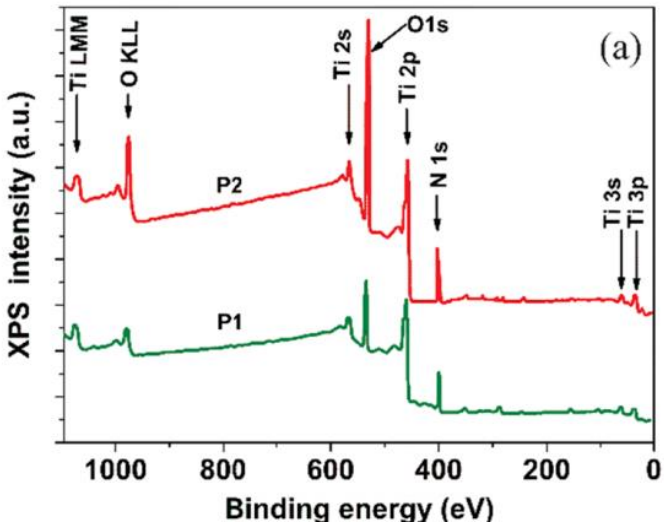

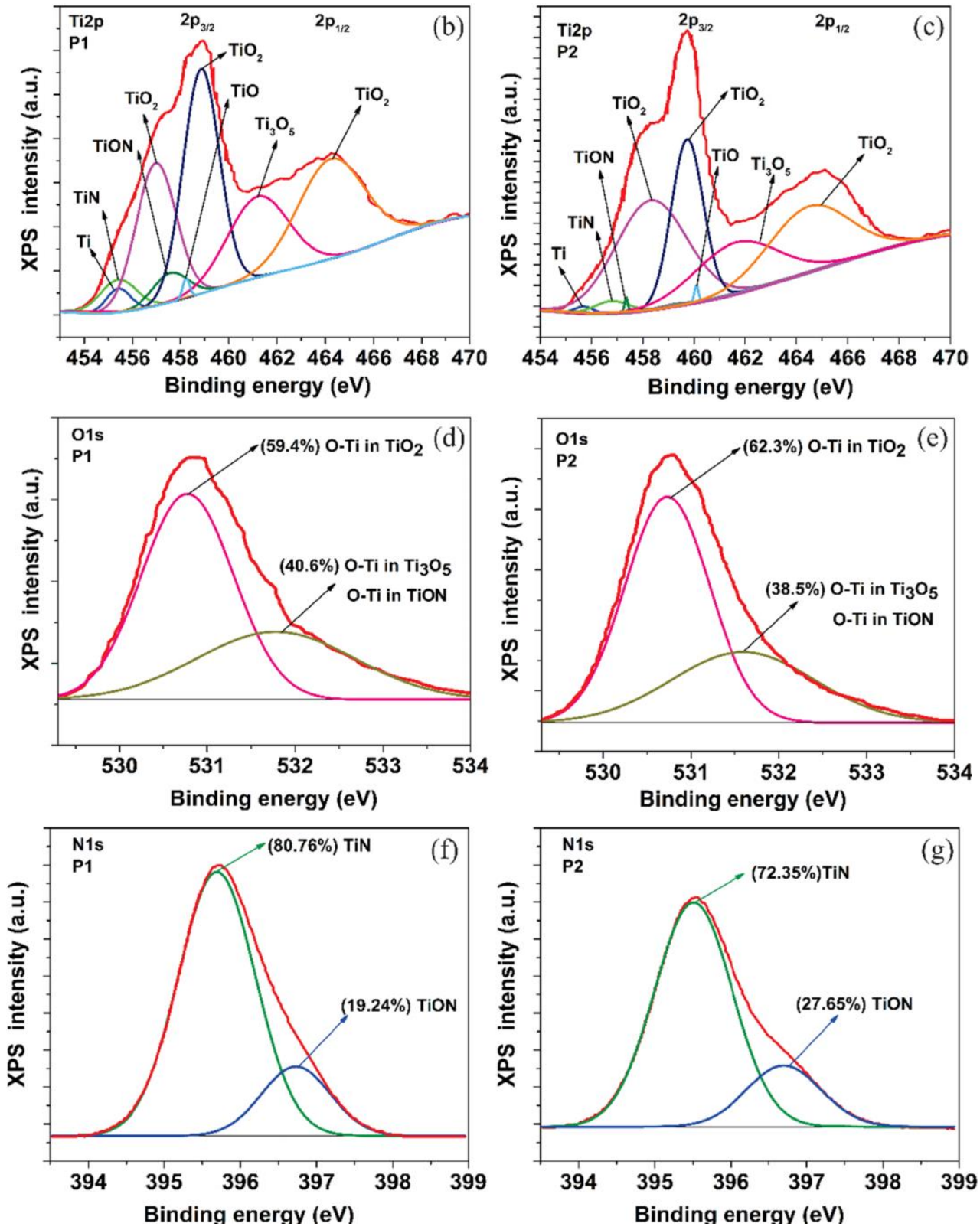

Figure 3.8.9 (a): XPS survey spectra for P1 and P2; (b) Ti 2p for P1, (c) Ti 2p for P2; (d) O1s for P1; (e) O1s for P2; (f) N1s for P1; (g) N1s for P2 core-level envelopes (Croitoru et al., 2020 b).

Figure 3.8.9 (b) displays Tauc plots for thermal sprayed coatings and Degussa P25 powder, from which optical band gap (Eg) values are derived. A significant decrease in Eg is observed, with values dropping from 2.90 eV for Degussa powder to 2.01 eV for P1 and 1.55 eV for P2, indicating increased photocatalytic activity in the visible region. The lower Eg in P2 is attributed to a greater concentration of doped TiO_2, enhancing energy conversion efficiency and yielding some of the lowest reported Eg values for TiO_2-N systems.

Moreover, UV-VIS spectra indicate an increase in band tail energy (Urbach energy), which is proportional to the width of localized states in the band gap. This energy rises with time-of-flight and is higher for the coatings compared to Degussa P25, likely due to localized states near the conduction band that can trap electrons, thereby mitigating recombination and improving photocatalytic efficacy.

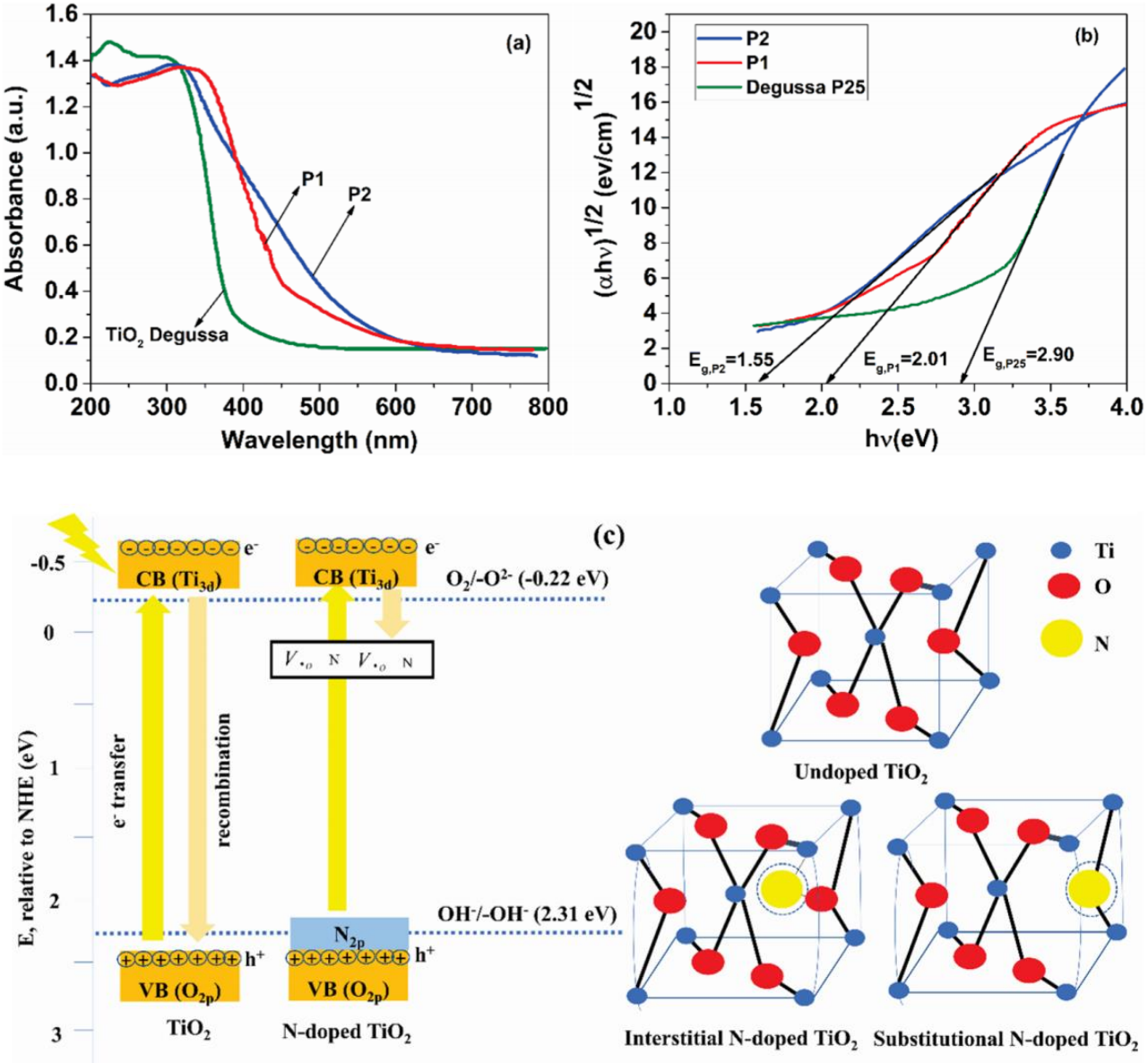

Figure 3.8.10 (a): UV–VIS spectra of P1, P2 and Degussa P25 powder; (b): Tauc plots; (c) schematic illustration of the photocatalysis mechanism (Croitoru et al., 2020 b).

Figure 3.8.11 displays surface energy values under dark and UV irradiation conditions, including their dispersive and polar components. Surface energies were calculated using corrected contact angles that account for roughness from coalesced splats and plastically-deformed feedstock particles, yielding values of 31.2 mN/m (P1) and 34.2 mN/m (P2), consistent with those reported for titanium biomaterials and thermal spray coatings.

While the dispersive component predominates, both samples show an approximately 20% increase in surface energy under UV irradiation (365 nm), with a significant rise in the polar component. This finding corroborates earlier research that identified surface energy increases of up to 50% under UVA exposure. The more pronounced increase in polar surface energy in P2 is attributed to the generation of reactive chemical species, such as hydroxyl and superoxide radicals, at the sample/liquid interface.

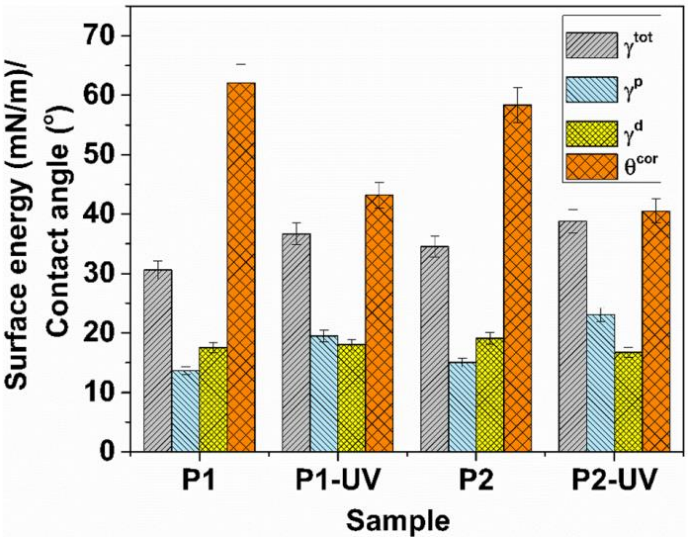

Figure 3.8.11 Corrected water contact angles and surface energy values for P1 and P2 sample (Croitoru et al., 2020 b).

A decrease in surface energy is often associated with increased wettability of polar liquids. In the context of photodegradation, this could imply improved and uniform wetting of the photocatalytic surface with the aqueous medium.

A comprehensive investigation of the photodegradation kinetics of MO was conducted utilizing P1, P2, and Degussa P25 powder under various irradiation conditions. The experimental data were subsequently fitted to the pseudo-first order kinetic model (Langmuir-Hinshelwood), with the results presented in Figure 3.8. 12. A pronounced disparity in the degradation patterns was observed between the thermally sprayed samples (P1 and P2) and the Degussa P25 powder. Specifically, the former exhibited a biphasic degradation profile, characterized by an initial slow decline in dye concentration followed by a more rapid decrease. In contrast, the Degussa P25 powder demonstrated a monophasic degradation pattern, in line with previously reported results in the literature.

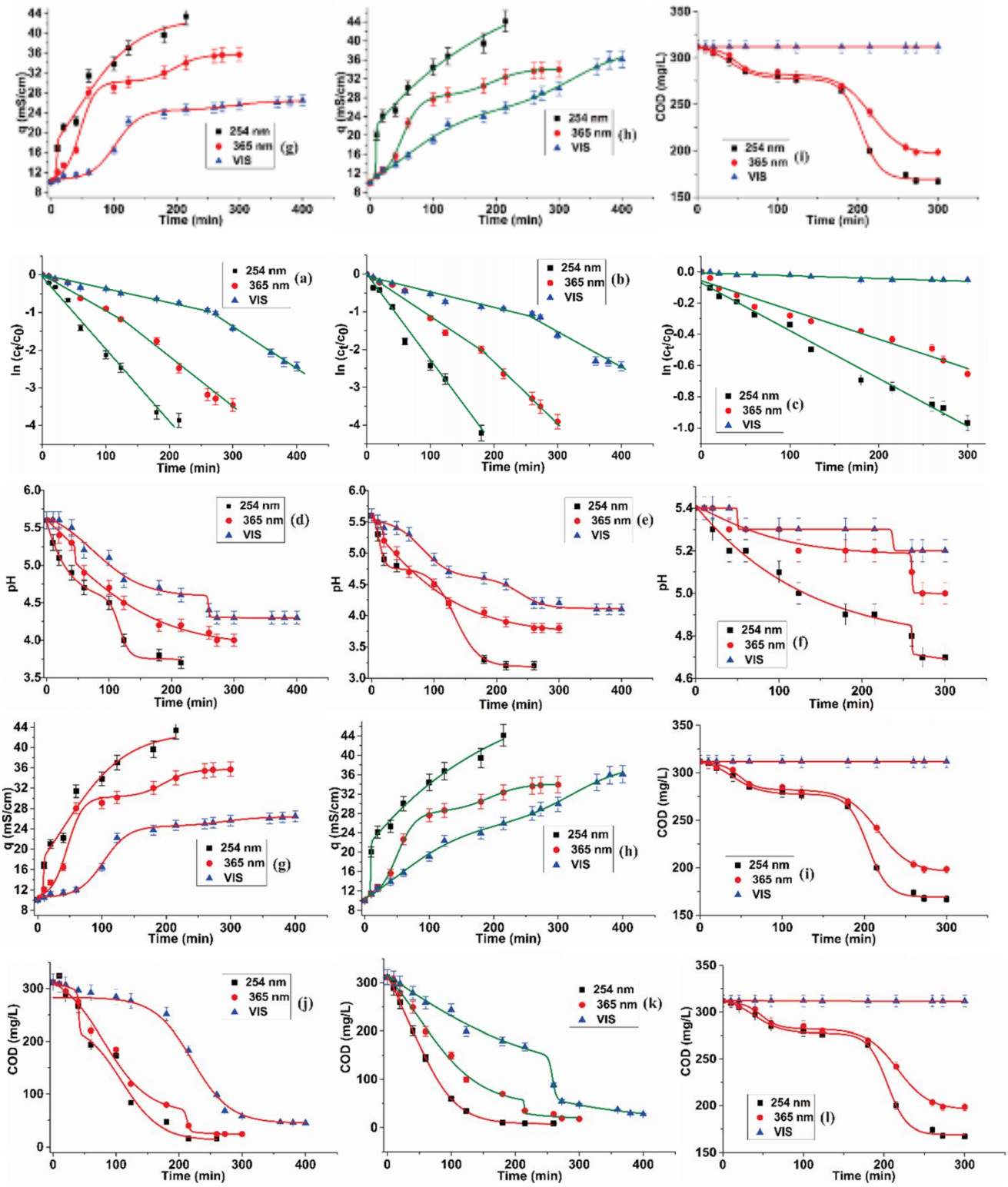

Figure 3.8.12 (a)–(c): linearized MO photodegradation kinetic for P1, P2 and Degussa P25; (d)–(f): pH kinetic for P1, P2 and Degussa P25; (g)–(i): conductance kinetic for P1, P2 and Degussa P25; (j)–(l): chemical oxygen demand values for P1, P2 and Degussa P25 of the MO solutions during photodegradation (Croitoru et al., 2020 b).

The investigation of active species in the photodegradation of methyl orange (MO) utilized hole/radical trapping experiments, revealing that holes (h+), hydroxyl (·OH) radicals, and superoxide (O_2−) radicals are the primary contributors, irrespective of UVC or VIS irradiation. The inhibition of photodegradation by the hole scavenger EDTA2Na underscores the critical role of holes in altering the chromophore structure of MO. Conversely, the electron trap Cu(NO3)2 had minimal impact, indicating limited direct electron interactions with adsorbed O2 or water.

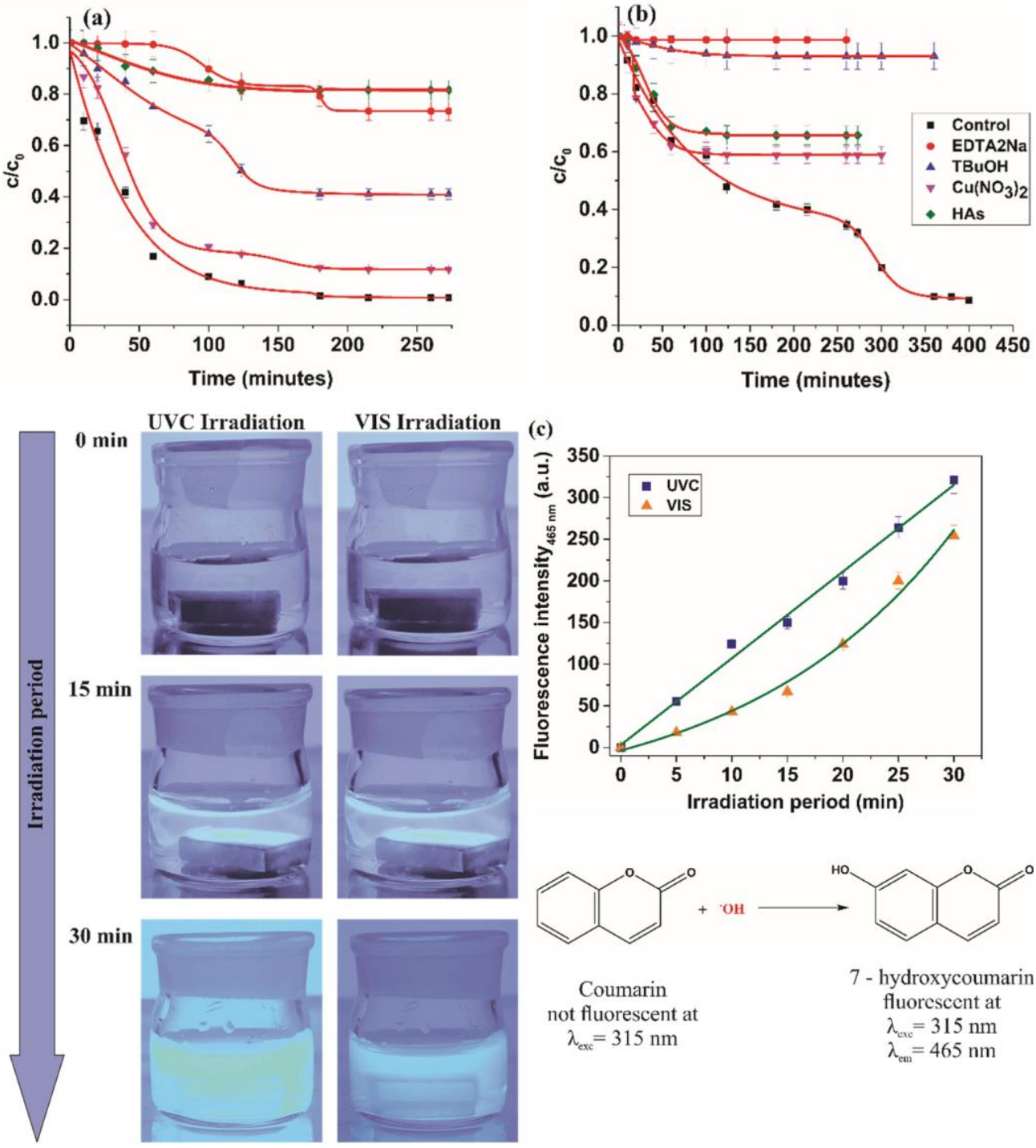

Figure 3.8.13 MO concentration decrease profiles for P2 under (a): UVC, (b): VIS irradiation with scavengers; (c): fluorescence intensity monitoring under UVC and VIS irradiation for P2 (Croitoru et al., 2020 b).

Superoxide radicals were prominent under UV irradiation, while hydroxyl radicals were essential in both UV and VIS contexts. The significant role of hydroxyl radical generation in achieving high mineralization yields aligns with existing literature. The production of hydroxyl radicals was further corroborated through the selective reaction of coumarin with ·OH radicals to yield 7-hydroxycoumarin, with fluorescence intensity proportional to hydroxyl radical generation. Notably, UVC irradiation produced a greater quantity of active species compared to VIS irradiation, consistent with enhanced photodegradation efficiencies. Early-stage photodegradation involved the generation of superoxide and hydroxyl radicals, with the former potentially enhancing hydroxyl radical production via interactions with SETOV-trapped electrons.

The photodegradation of methyl orange (MO) under 254 nm irradiation proceeds via a single kinetic step, attributed to the rapid formation of free radicals. Comprehensive studies reveal that hydroxyl radicals hydroxylate the aromatic ring and abstract H-atoms from (CH3)2N groups, while superoxide radicals cleave diazo and aromatic bonds, resulting in hydroxylated sulfonic acids and complex carboxylic acids at advanced degradation stages.

This photodegradation process is accompanied by increased conductance (Figure. 3.8.12 d-f) and decreased pH (Figure 3.8.12 g-i), particularly evident after 15-20 minutes of irradiation. The mineralization results, measured by chemical oxygen demand (COD) (Figure 3.8.12j-l), showed consistent trends for thermal-sprayed surfaces and P25 powder, with varying degradation rates likely due to the higher concentration of photodegrading species in the P2 sample.

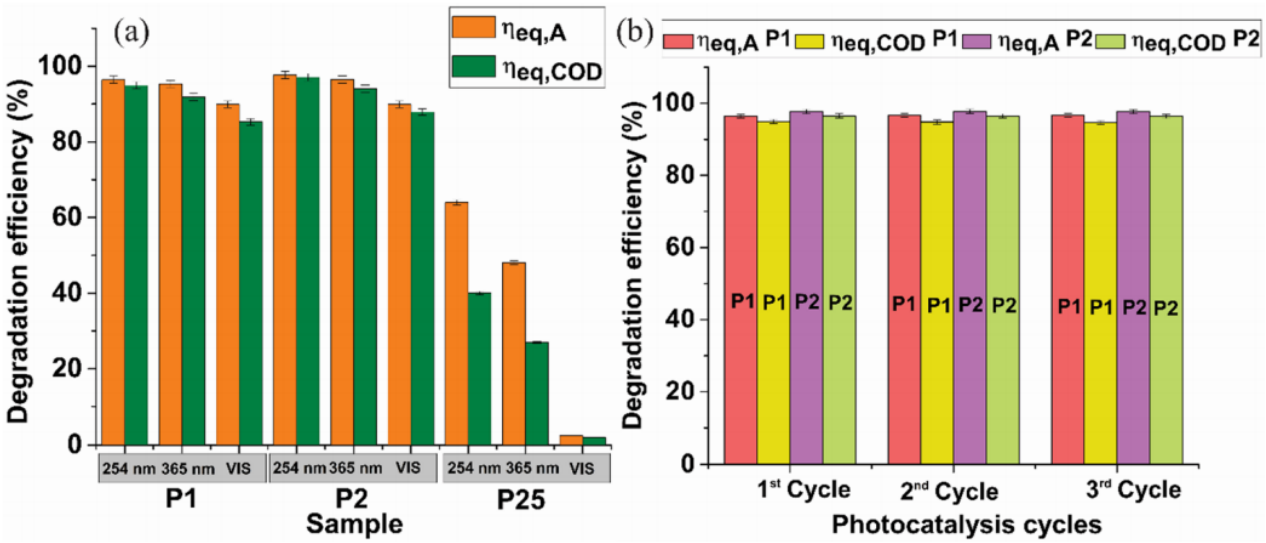

Figure 3.8.14 (a): the efficiency of methyl orange dye removal for P1, P2 and Degussa P25; (b): photodegradation efficiency variation during successive photocatalysis cycles.

Efficiency assessments based on COD and optical absorbance measurements (Figure 3.8.14 a) indicated substantial decreases in organic loading, signifying extensive mineralization over minimal chromophore disruption. The discoloration-based degradation efficiencies ranged from 91% to 99%, aligning with literature values for doped titania films, while COD-based efficiencies were lower, at

85% to 97%. The P2 sample consistently exhibited superior photocatalytic performance, with degradation efficiency directly proportional to the energy of the irradiation source.

Degussa powder demonstrated the lowest UVC photocatalytic performance, achieving only 40% mineralization efficiency and negligible activity in the visible light spectrum. Notably, aluminum was absent in solutions subjected to photoirradiation, indicating substrate stability, while titanium was detected at 26.8 ppb in solutions associated with P2 (irradiated at 254 nm), a significantly lower concentration than the 35-1230 ppb range reported for TiO_2 films or nano-TiO_2 suspensions. The coatings exhibited stability in aqueous media under UV-A and VIS irradiation. Although the 254 nm irradiation source raises economic and safety concerns for real-world applications, the coatings present a scalable and health-risk-free option. Efficiency measurements for P1 and P2 coatings regarding MO discoloration and mineralization remained consistent across three consecutive 8-hour UVC photocatalysis cycles, affirming their chemical stability (Figure 3.8.14 b).

Scanning Electron Microscopy (SEM) revealed that surface morphology, characterized by splats and nanopatterns, was largely unchanged after three UVC photocatalysis cycles (Figures 3.8.15 and 3.8.16), indicating minimal alteration during the photocatalytic process. Elemental distribution analyses for titanium, oxygen, and nitrogen displayed uniformity relative to neat samples (Figures 3.8.4 and 3.8.5). Energy-Dispersive Spectroscopy (EDS) showed a slight reduction in nitrogen content, likely due to leaching or abrasion of doped oxide species, while titanium content increased, suggesting exposure of underlying titanium phases. Fluorescence spectroscopy confirmed titanium leaching from the sample surfaces during photocatalysis.

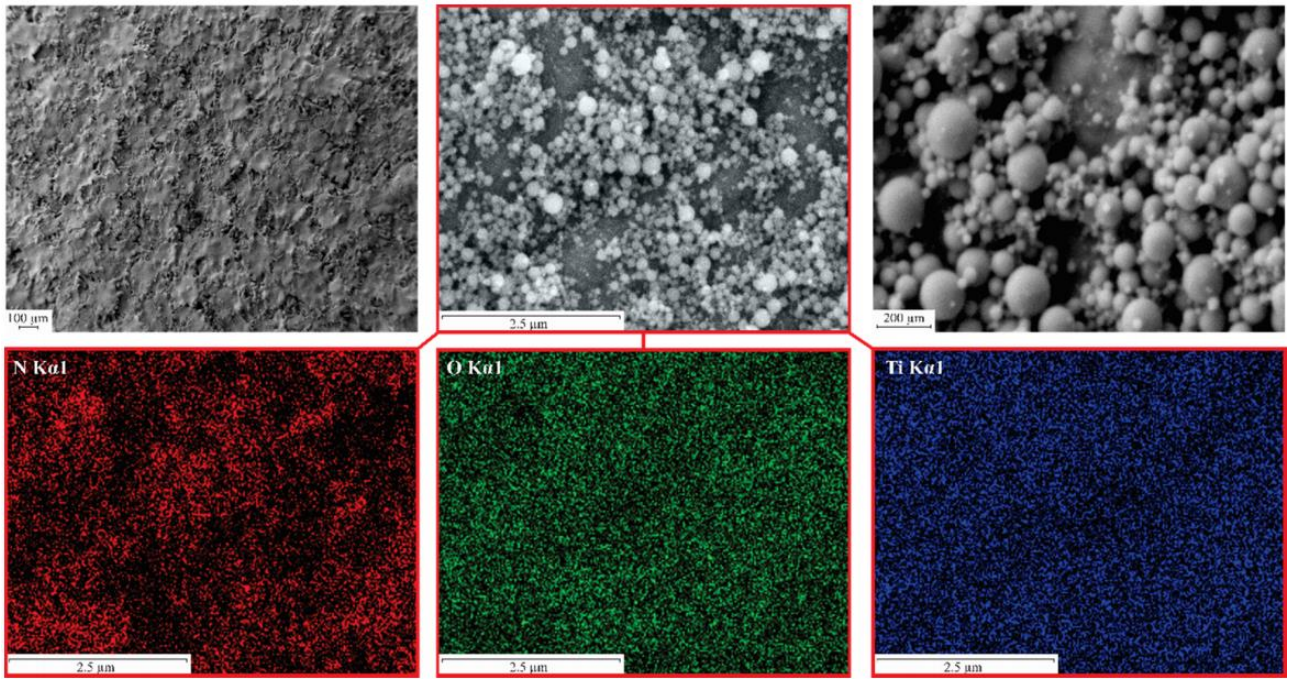

Figure 3.8.15 SEM micrographs of P1 sample surface after 3 consecutive UVC photocatalysis cycles and EDS elemental maps (N, O, Ti) (Croitoru et al., 2020 b).

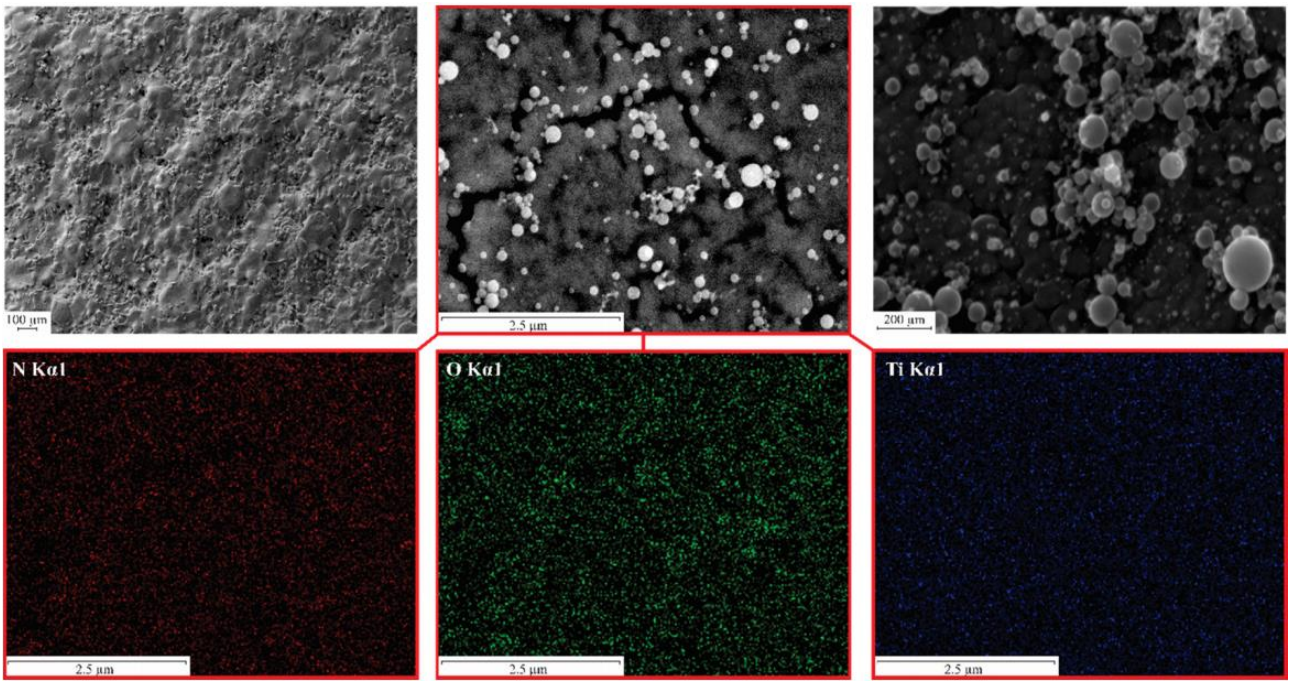

Figure 3.8.16 SEM micrographs of P2 sample surface after 3 consecutive UVC photocatalysis cycles and EDS elemental maps (N, O, Ti) (Croitoru et al., 2020 b).

Nitrogen-doped titanium dioxide coatings were successfully synthesized via thermal flame spraying technique using metallic titanium as the precursor. These coatings exhibited optical band gap energies as low as 1.55 eV, significantly narrower than commercial nanometric rutile-anatase powders (Degussa P25). Evaluations of photocatalytic activity indicated that the nitrogen-doped coatings achieved higher degradation efficiencies for methyl orange under both ultraviolet (UVC) and visible light irradiation compared to Degussa P25. Specifically, mineralization efficiencies reached 97 % under UVC after 350 minutes and 87 % under visible light.

Radical scavenger studies revealed that holes, hydroxyl radicals, and superoxide radicals were key reactive species in the degradation process, varying with irradiation conditions. The coatings demonstrated impressive stability, retaining their photocatalytic activity and surface chemistry across multiple cycles of photodegradation. Notably, higher nitrogen content and doping levels were achieved compared to prior studies employing titania as feedstock. Furthermore, the time-of-flight of the feedstock powder, defined as the distance from the spray nozzle to the substrate, was identified as a critical factor influencing the coatings' surface chemistry, enabling reproducible property modifications.

3.9 Visible domain photocatalysis performance of Ti-Si thermal-sprayed coatings

Titanium-silicon powder (10% wt. Si) with an average particle diameter of 115 µm was sourced from Oerlikon-Metco (Singapore), while substrate materials comprised electrolytic copper (99.5% Cu) and hipoeutectoid carbon steel (1.0044-S273JR, EN 10025-2:2004), both measuring 20 mm × 20

mm × 4 mm. For photocatalytic experiments, methylene blue (C16H18ClN3S, Mw = 319.85), isopropyl alcohol, and ascorbic acid, sourced from Sigma-Aldrich (Burlington, MA, USA), had a minimum purity of 99.5% wt.

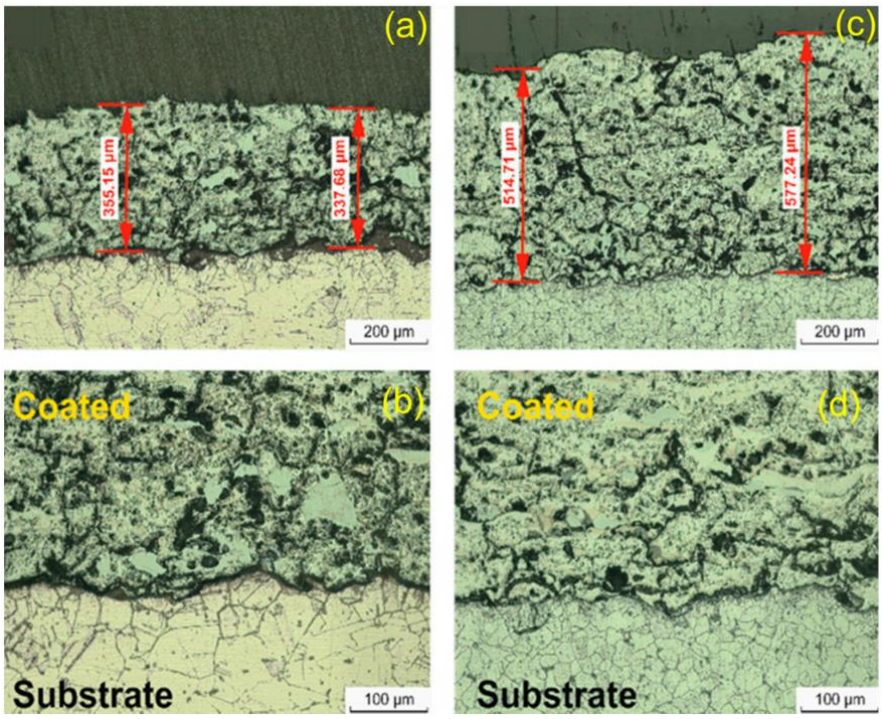

Figure 3.9.1 Cross-section optical microscopy of (a) Cu-TiSi (50×); (b) Cu-TiSi (100×); (c) St-TiSi (50×); and (d) St-TiSi (100×) samples (Uncu et al., 2021).

Morphological analysis (Figures 3.9.3 a-d) revealed that Ti-Si coatings exhibited a well-fused, thick structure characteristic of thermal spraying. The average thickness was measured at 336.41 µm for Cu-TiSi and 545.97 µm for St-TiSi. The reduced thickness on copper is attributed to its superior thermal conductivity, which enhanced the flattening of feedstock powders.

The coatings displayed lamellar overstacked layers, with the Cu-TiSi coating (Figure 3.9.3 a) being more compact than the St-TiSi coating (Figure 3.9.3 c). Dark areas on the splat margins were likely indicative of oxides or intermetallic phases formed during high-temperature processing. X-ray diffraction (XRD) and X-ray photoelectron spectroscopy (XPS) analyses (Figures 3.9.2 and 3.9.3) confirmed the presence of these phases. Additionally, localized incomplete melting of feedstock particles contributed to porosity in the coatings. Higher magnification images (Figures 3.9.3 b and 3.9.3 d) highlighted a higher density of non-metallic phases (oxides and silicides) in the copper-coated sample, corroborating spectroscopic data (Uncu et al., 2021).

The Ti-Si phase diagram indicates that the coating consists of α-Ti, silicon (Si), and titanium silicides, as confirmed by the X-ray diffraction (XRD) patterns shown in Figure 3.9.2. The feedstock powder is a mechanical mixture of hexagonal close-packed α-Ti (CIF card #00-151-2547) and Si (CIF card #00-901-1656), with the presence of Ti6O oxide (CIF card #00-152-9955) attributed to surface adsorption of atmospheric oxygen, and no other phases detected.

The flame spraying process facilitates high-temperature reactions between α-Ti and Si, resulting in the formation of the silicides $TiSi_2$ (orthorhombic, CIF card #00-100-9012) and Ti_5Si_3 (hexagonal, CIF card #00-154-1130). The similarity in diffraction patterns for both coatings arises from identical deposition parameters. Additionally, oxidation of Ti and Si in contact with atmospheric oxygen leads to the formation of Ti_2O_3 (CIF card #00-900-8082) and SiO_2 (α-cristobalite, CIF card #00-101-0954).

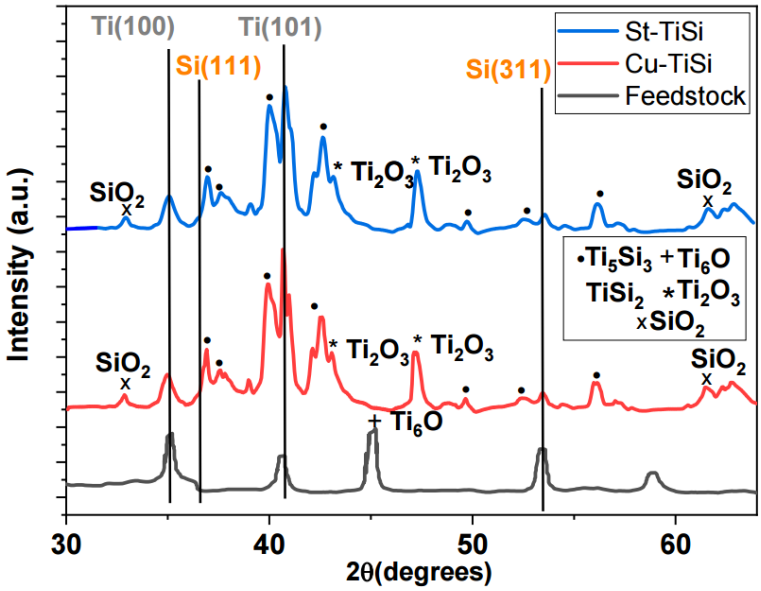

Figure 3.9.2 XRD spectra of Cu-TiSi and St-TiSi samples (Uncu et al., 2021).

The presence of Ti_2O_3 (Ti_3+) could be attributed to thermal reduction in TiO_2 in the presence of Si and metallic Ti, as no TiO_2 was detected in the XRD diffraction data. This could be due to either low crystallinity or a high ratio of Ti_2O_3 to TiO_2 with Ti_2O_3 formed on the surface of TiO2. The presence of Ti_4+ detected by XPS (Figure 3.9.3 a-c) confirms this mechanism of formation.

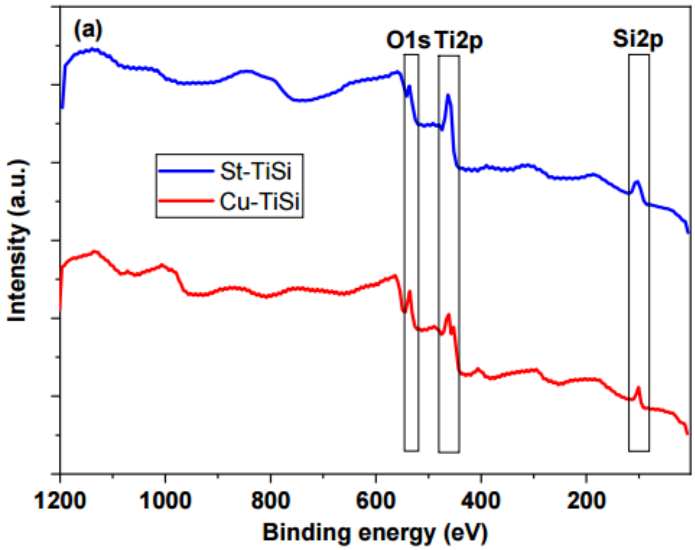

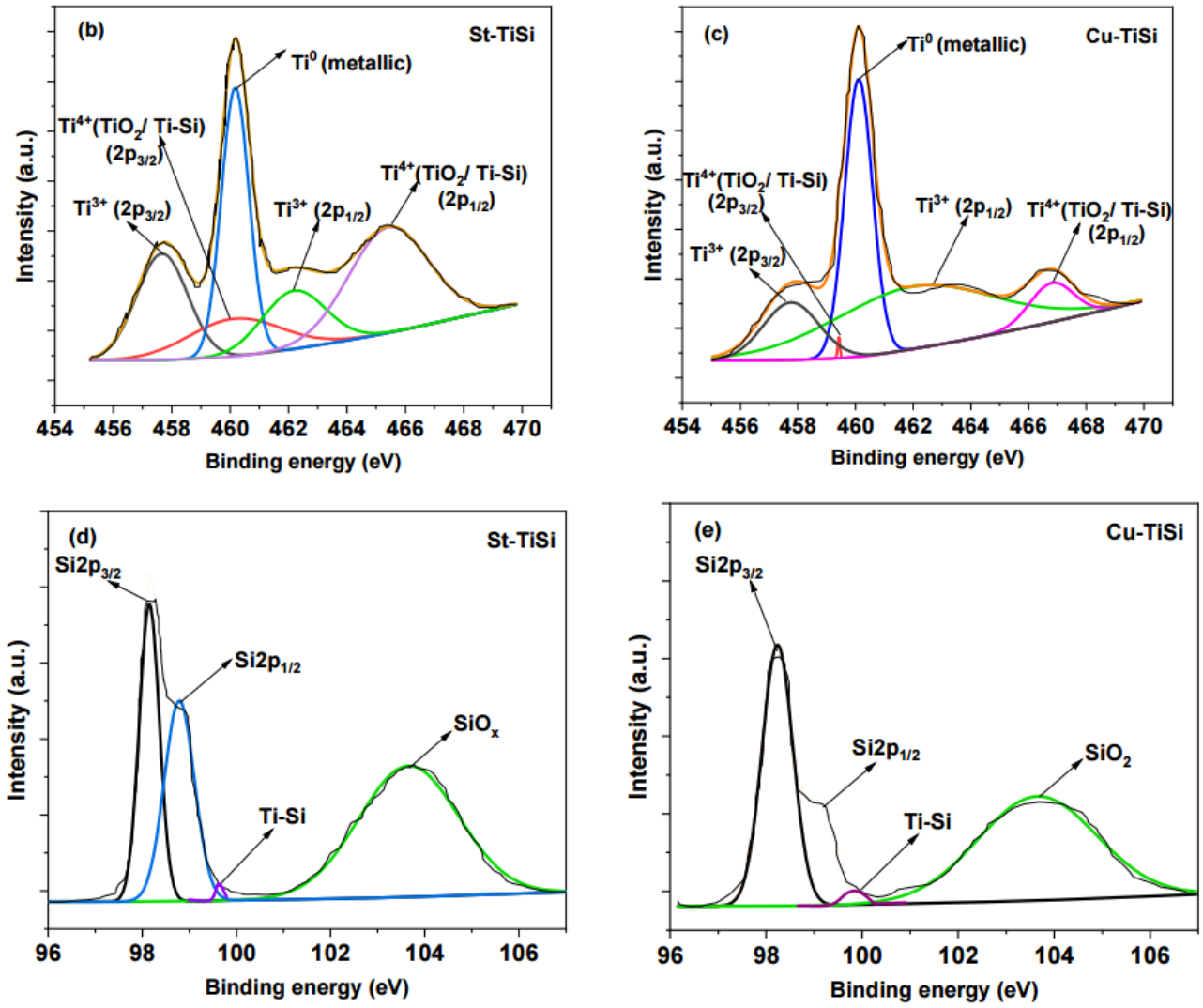

Figure 3.9.3 XPS spectra: (a) survey; (b,c) Ti2p envelopes; (d,e) Si2p envelopes of Cu-TiSi and St-TiSi samples (Uncu et al., 2021).

The energy level of titanium(III) oxide, a narrow band-gap semiconductor, is located between the conduction and valence bands of titanium dioxide (TiO2), facilitating electron transitions upon visible light excitation. Although X-ray diffraction (XRD) and X-ray photoelectron spectroscopy (XPS) did not detect titanium(III) oxide (Ti_2O_3), the formation of mixed titanium-silicon oxides below detection limits could significantly lower the energy band gap, thereby enhancing photocatalytic performance.

Figure 3.9.3 a shows that the surface composition of the thermal spray-deposited samples includes titanium, oxygen, and silicon. Analysis indicates the presence of metallic titanium, silicon, and oxygen, contributing to the formation of Ti_4+, Ti_3+ oxides, and silicon dioxide. XPS data reveal Ti_2p3/2 binding energies of 460.3 eV for Ti_4+ and 457.6 eV for Ti_3+, as well as a Si_2p binding energy at 103.7 eV for Si_4+ (Figure 3.9.3 b-e), confirming these species. Additionally, Ti-Si bonds were identified in the Si2p core-level envelopes of Cu-TiSi and St-TiSi at 1.8% and 3.7%, respectively, with peaks centered at 99.6 eV.

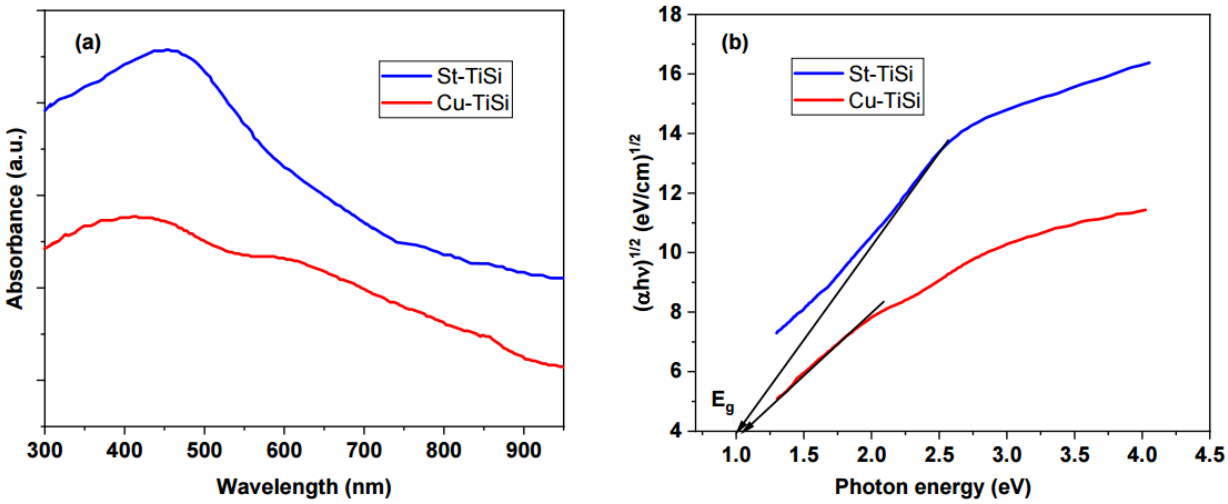

Figure 3.9.4 (a): UV–VIS spectra of St-TiSi and Cu-TiSi; (b): Tauc plots for determining Eg .(Uncu et al., 2021)

The visible-light photocatalytic activity of the coatings is demonstrated by UV-visible absorption spectra in Figure 3.9.4 a, showing maximum absorption at 451 nm (2.74 eV) for St-TiSi and at 423 nm (2.93 eV) for Cu-TiSi. Figure 3.9.5 a illustrates the photocatalytic kinetic efficiency, revealing equilibrium values of 89.50% for Cu-TiSi and 99.26% for St-TiSi. Notably, the coating deposited on steel exhibits a concurrent photo-Fenton process, likely resulting from the oxidation of the metallic substrate, which forms Fe2+ ions.

The introduction of isopropyl alcohol, a scavenger for hydroxyl radicals (•OH), substantially diminishes photocatalytic efficiency, highlighting the importance of these radicals in the degradation of methylene blue (MB) to smaller molecular compounds (MB•) as described in Mechanism (4). In contrast, ascorbic acid, which scavenges superoxide radicals, exerts little effect on photocatalytic efficiency, suggesting a minor role for superoxide radicals in visible-light-mediated MB degradation. The photocatalytic process aligns with the pseudo-first-order kinetic model proposed by Langmuir and Hinshelwood (Figure 3.9.5b).

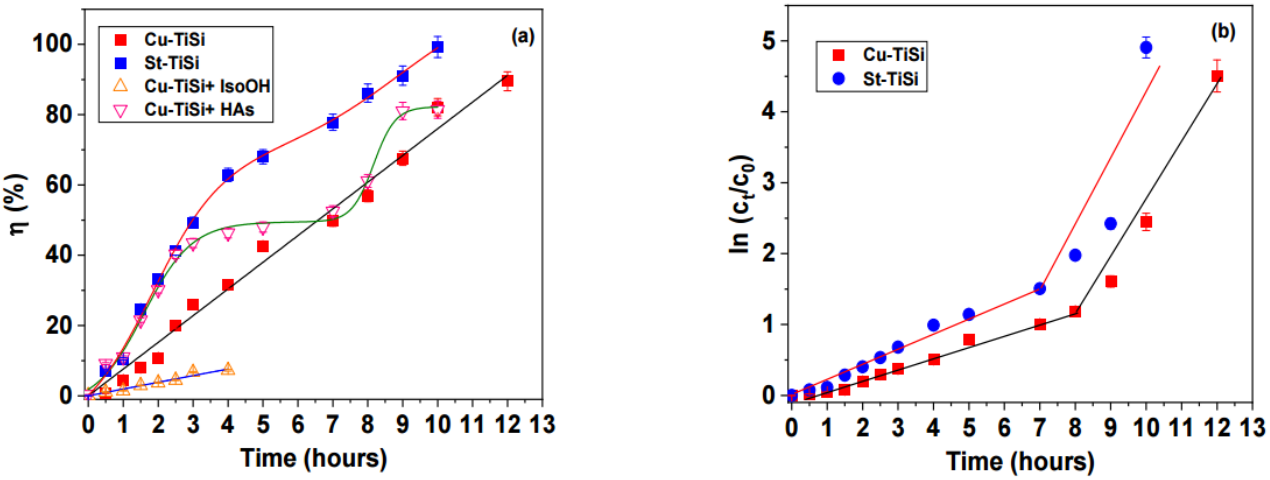

Figure 3.9.5 (a) Photocatalysis efficiency; (b) photo-Fenton degradation efficiency (Uncu et al., 2021)

The photodegradation of MB with Ti-Si coatings occurs in two phases: an initial slower phase (lower k1 values) related to the generation of hydroxyl radicals, followed by a subsequent, faster phase (constant rate k2) involving the degradation of MB to smaller molecular entities.
This research aims to enhance the international database of sustainable coatings that efficiently utilize visible light for pollutant degradation in wastewater. Employing thermal flame spraying of mixed titanium-silicon feedstock powders, durable coatings were applied to copper and carbon steel substrates, commonly utilized in wastewater treatment facilities. These coatings demonstrated high photodecoloration and mineralization efficiencies, as well as degradation rates comparable to those of doped titania.

The surface chemistry revealed the presence of titanium (III) oxide and non-stoichiometric silicides (Ti_5Si_3 and $TiSi_2$), resulting in a reduced optical bandgap of approximately 1.000 eV, functioning as an indirect semiconductor. Notably, the coatings preserved their surface roughness post-photocatalysis, indicating strong corrosion and erosion resistance. Future investigations will assess the lifecycle of these coatings and their efficacy in real-world wastewater conditions, considering the impact of interfering anions and cations.

3.10 Multifunctional Ni-Cr-Al-Y coatings via thermal spraying

The thermal spraying powder utilized in this study was obtained from Oerlikon-Metco (catalog code Amdry 962) in its as-received form, with an average particle diameter of approximately 120 µm. This powder is classified within the MCrAlY coating family, where "M" typically represents cobalt (Co), nickel (Ni), iron (Fe), or their combinations. Upon exposure to high temperatures, it develops a durable oxide layer that provides protection against oxidation and corrosion.

Table 3.10.1 Chemical composition of the powder feedstock used in thermal spraying (Roata et al., 2023).

Powder	Chemical composition [%]						
	Ni	Cr	Al	Y	Ta	Nb	Fe
NiCrAlY	45	24	8	0.5	1	0.5	Balance

Rectangular S273JR plates (40 mm × 40 mm × 5 mm) served as the substrate for thermal spraying. Prior to deposition, the plates were polished with P360 grit abrasive paper and cleaned in an ultrasonic bath with ethanol at 40 °C for 5 minutes to eliminate organic contaminants.
The electrochemical behavior of the coatings was evaluated in a 3.5% w/w sodium chloride solution using a PalmSens EmStat 4LR potentiostat-galvanostat linked to a Faraday-isolated three-electrode cell. This setup included an Ag/AgCl reference electrode, a platinum counter electrode, and the sample as the working electrode. Linear polarization (LP) and electrochemical impedance spectroscopy (EIS) were conducted to assess corrosion resistance, with LP measurements taken over a potential range of ±150 mV relative to the open circuit potential (OCP) at a scan rate of 10 mV/s.

EIS involved an alternating current of 10 mV amplitude across a frequency range of 100 mHz to 100 kHz. Prior to measurements, samples were equilibrated in the sodium chloride electrolyte for 600 seconds.

Wetting characteristics, indicating hydrophilicity or hydrophobicity, were examined using an L2004A1 contact angle goniometer (Ossila Inc., UK). Contact angles for distilled water and glycerol (5 µL sessile drops) were measured, and surface energy was determined using the Owens-Wendt-Rabel & Kaelble (OWRK) model.

Electrochemical analyses were performed on both substrate plates and thermally sprayed samples to provide a comprehensive understanding of their corrosion behavior, with results presented in Figures 3.10.1 a and 3.10.1 b for LP analysis.

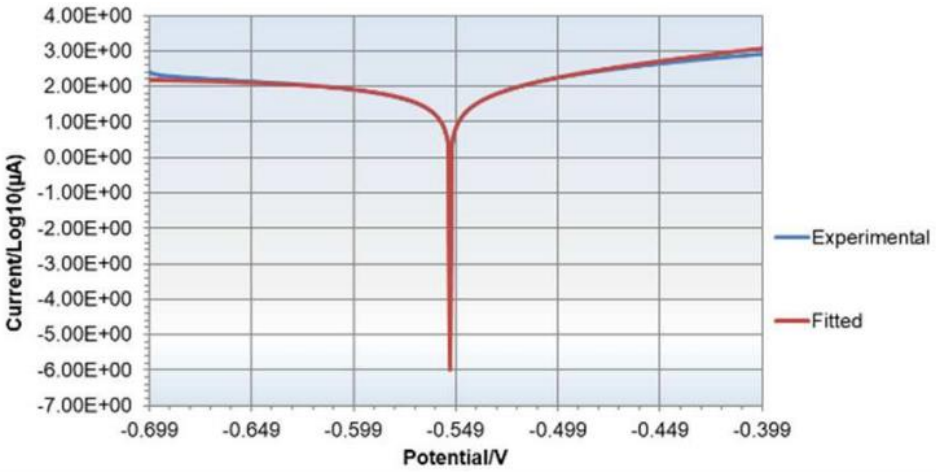

a)

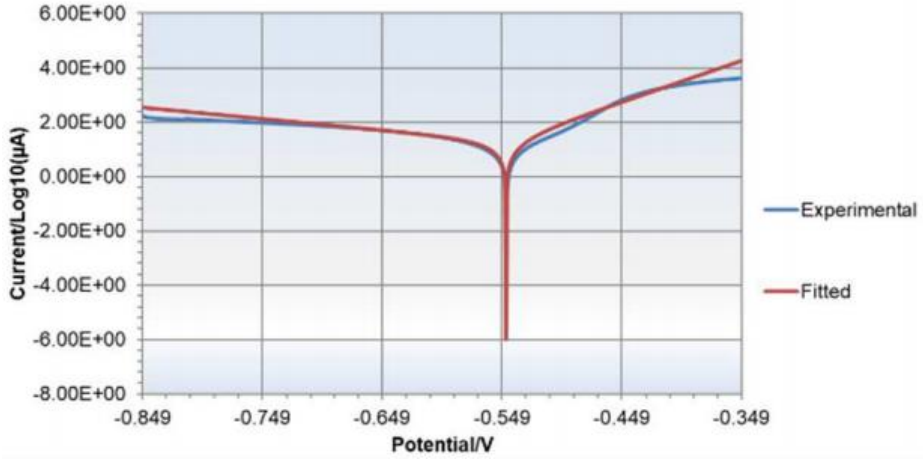

b)

Figure 3.10.1 Linear polarization curves with fitted Butler-Volmer model for the samples: (a): steel substrate, (b): NiCrAlY (Roata et al., 2023).

OCP measurements (Figures 3.10.1 a and 3.10.1 b) reveal that both the substrate and NiCrAlY thermal spray (TS) exhibit similar values of -56 mV and -54 mV, respectively, indicating comparable electrochemical behavior reflective of their iron-based composition. Corrosion current density

(Icorr) was calculated by fitting linear polarization curves to the Butler-Volmer equation, demonstrating that the TS samples possess significantly lower corrosion rates than the steel substrates, as confirmed by electrochemical impedance spectroscopy (EIS) and potentiodynamic polarization measurements.

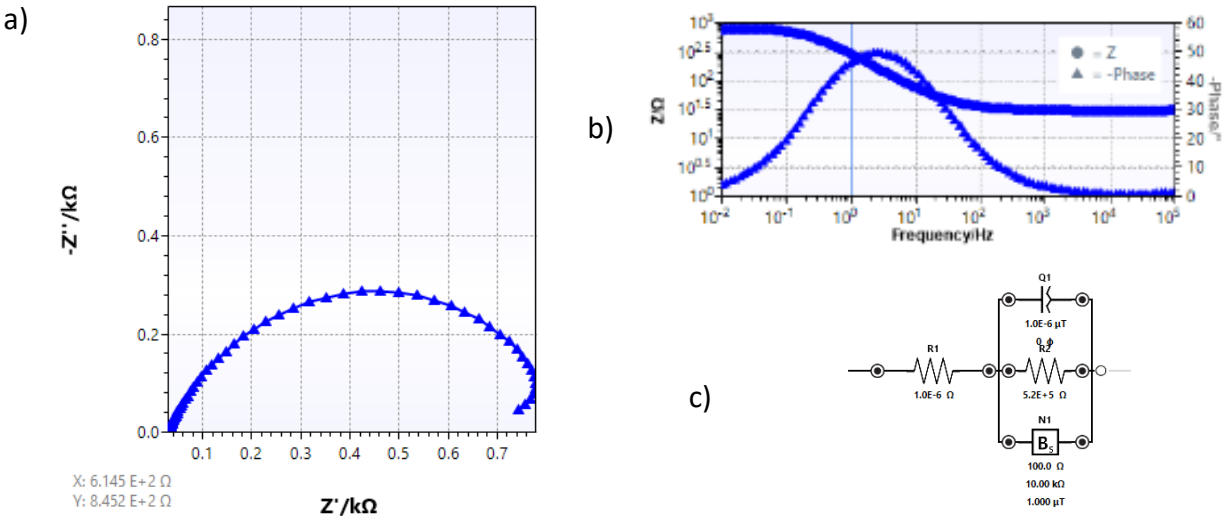

Figure 3.10.2 EIS data as Nyquist plots (a), Bode plots (b) and model equivalent electrical circuit for the steel substrate (c) (Roata et al., 2023).

EIS results (Figures 3.10.2 a and 3.10.3 a) present Nyquist plots, characterized by semicircular arcs that signify capacitance and resistance components. Bode plots (Figures 3.10.2b and 3.10.3b) further delineate frequency-dependent impedance magnitude (Z) and phase angle characteristics, elucidating the corrosion mechanisms in both materials. Analysis of the EIS data utilized equivalent electrical circuits comprising resistors (R), capacitors (C), and constant phase elements (CPE) to model the corrosion processes, yielding insights into electrochemical kinetics, including Icorr, corrosion rate (CR), and double-layer capacitance (Cdl).

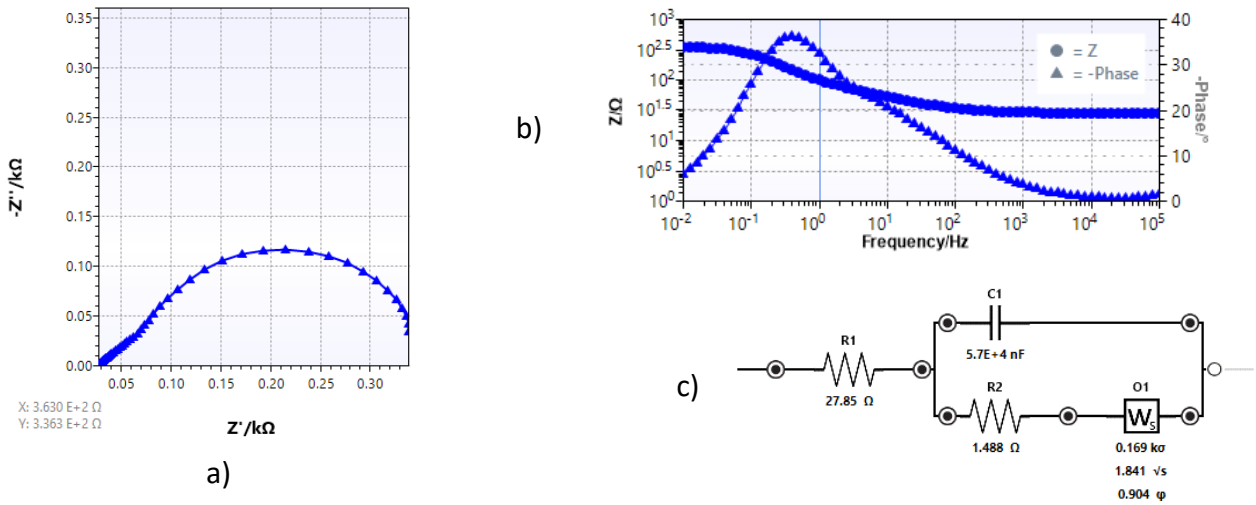

Figure 3.10.3 EIS data as Nyquist plots (a), Bode plots (b) and model equivalent electrical circuit for the NiCrAlY sample (c) (Roata et al., 2023).

Electrochemical impedance spectroscopy (EIS) analysis of both substrate and sintered (TS) samples revealed a dissipative-capacitive behavior indicative of pitting corrosion, characterized by localized surface deterioration. The EIS data suggest a complex interaction of resistive and capacitive elements in the corrosive environment. Notably, the TS sample exhibited a substantially lower corrosion rate than the substrate, highlighting the efficacy of sintering in enhancing material properties and protective characteristics.

The results underscore sintering as a strategy to optimize surface morphology, composition, and structural integrity, improving corrosion resistance and broadening the applicability of the materials, including in corrosion-resistant coatings, biomedical implants, and advanced composites.

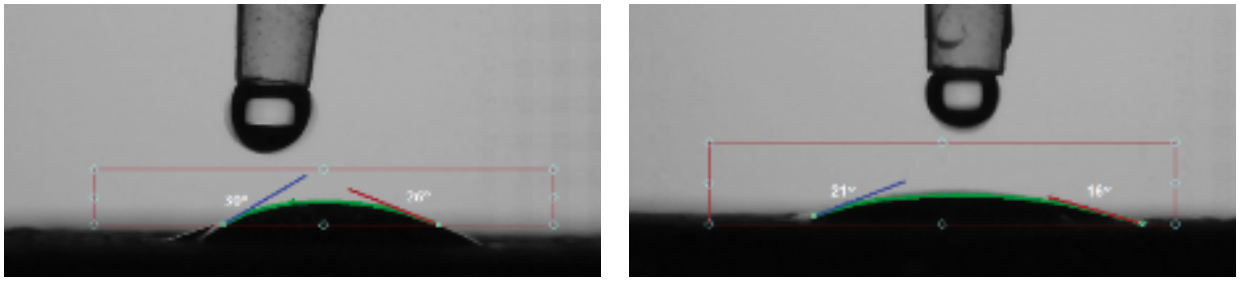

Figure 3.10.4 Water contact angles for the samples: (a): S273JR, (b): NiCrAlY (Roata et al., 2023).

Figures 3.10.4 a and 3.10.4 b illustrate the initial contact angles for both substrate and TS samples during wetting with distilled water, revealing hydrophilic behavior with angles under 90 degrees. The TS sample, exhibiting greater hydrophilicity due to its favorable surface chemistry and the presence of surface oxides, demonstrates enhanced wettability.

These results have important implications for practical applications, particularly in sectors where surface properties are critical, such as biomedical devices, oil-water separation technologies, and environmental remediation systems.

This study on thermal spraying of NiCrAlY coatings presents several key findings:

- Microstructure control: The thermal spraying process enables precise manipulation of the coatings' microstructure, evidenced by the formation of surface oxides during deposition, which alters phase composition, grain size, and defect characteristics.
- Corrosion resistance: Corrosion testing in a 3.5% wt. NaCl solution shows that the thermally sprayed coatings demonstrate superior corrosion resistance compared to the substrate, reflected in lower mass loss and higher polarization resistance, indicating their efficacy in harsh environments.
- Hydrophilic properties: The coatings exhibit hydrophilicity, which is beneficial for applications in humid conditions (e.g., biomaterials, coatings, paints, photocatalysis) by improving wettability, adhesion, and reaction rates.

In summary, thermal spraying presents significant potential for producing coatings with optimized microstructures and properties. Ongoing research is vital for advancing materials science and developing high-performance materials with tailored attributes for diverse applications requiring corrosion resistance and hydrophilicity.

(B3) Evolution and development plans for career development

My career objectives encompass both academic development and research activities, which I intend to pursue within the University of Transilvania in Brașov, at the Faculty of Science and Engineering of Materials. Upon obtaining the position of doctoral supervisor, I plan to continue my professional growth by making significant contributions to the university's academic and research endeavors.

An important goal in my career development is the promotion of student-centered teaching activities adapted to their needs and interests, aiming to provide a meaningful and effective educational experience. Furthermore, I regard mentorship as an essential component, involving not only the transmission of knowledge but also guiding and inspiring students to develop solid principles and critical thinking skills. Additionally, I believe it is fundamental to maintain a close connection with the challenges and opportunities presented by the ongoing evolution of the industrial environment, in order to integrate the latest technologies and practices into both teaching and research processes.

Another key objective is active participation in research projects within priority domains, as I consider that innovation and scientific discoveries contribute to the advancement of knowledge and strengthen the university’s reputation.

B.3.1. Plans and development on the didactical level

I am a strong advocate of the principle of lifelong learning and continuous professional development, considering that enhancing pedagogical and didactic competencies is an essential component for career advancement and for ensuring a high-quality educational process. From this perspective, I aim to optimize and diversify teaching methods through regular participation in specialized professional development programs, as well as active involvement in Erasmus academic mobility projects for teaching, with the goal of acquiring and implementing the most recent and effective educational methodologies adapted to the contemporary context.

In terms of professional growth, I plan to continue expanding my skills in communication and public presentation, fostering an exchange of experiences and knowledge with students and colleagues, as well as participating in international faculty exchange programs. Throughout my teaching career, I have approached the process of curriculum development and updating as a continuous and adaptive activity, grounded in the analysis of rapid developments within my field of expertise and in constant, constructive feedback from students, colleagues, and representatives from the private sector involved in collaborations, research projects, or professional practice. This approach has enabled me to adjust curricular content to reflect the latest trends, technologies, and teaching methodologies, as well as to respond to emerging needs of the labor market and society at large.

To maintain the relevance and currency of the study programs, I intend to implement a systematic update policy for all courses, planning major revisions at least once every two academic

years. These revisions will include the integration of the latest research and innovative practices, as well as adaptation to legislative changes and the evolving demands of the economic and social environment. In addition to periodic updates, I plan to collaborate with private sector specialists and domain experts to ensure a practical and applied perspective on the delivered content.

This strategy of continuous curriculum updating and improvement aims not only to strengthen the quality of the educational process but also to adequately prepare students for the real challenges of the professional environment, thereby contributing to the formation of competent, adaptable, and innovative specialists.

In the context of developing my educational and research strategy, I intend to actively involve undergraduate and master's students in teaching and research activities from the early stages of their studies. This involvement will include participation in research project teams, thus preparing them for future doctoral studies. Subsequently, once I obtain the position of doctoral supervisor within the Doctoral School of the University of Transilvania in Brașov, I will conduct activities related to the recruitment and selection of candidates for doctoral programs in the field of industrial engineering. In collaboration with specialists from various related domains, I will promote the formation of a multidisciplinary group with a long-term vision capable of sustaining itself in research activities. Furthermore, I will encourage doctoral candidates to submit research projects to national and international competitions, thereby increasing the visibility of the research activities of the group.

As the coordinator of the master's program in Welding Engineering, I plan to ensure ongoing adaptation of the curriculum and educational activities to technological developments and industry trends. To this end, I will strengthen collaboration with experts from the industrial sector, including engineers, researchers, and representatives of relevant companies, to facilitate knowledge transfer and practical experience.

To support this strategy, I will organize and coordinate students' participation in specialized technical workshops, seminars, training sessions, and site visits to economic and research partners, ensuring an integrated and applied learning experience. These activities will contribute to developing technical skills, understanding industrial processes, and familiarizing students with the latest technologies in the field.

Additionally, I intend to promote networking and collaboration initiatives among students, faculty members, and the business environment to stimulate joint projects, internships, and applied research opportunities. Through these efforts, the program will serve as an effective bridge between academia and industry, preparing graduates for the current challenges of the labor market and for active participation in innovative projects, emerging technologies, and sustainable development within the field of welding and related technologies.

B.3.2. Plans for research development and evolution

Following the completion of my doctoral program, I have accumulated extensive experience in the field of research and am committed to further developing and deepening this activity. In this regard, I aim to highlight and valorize the results obtained thus far, as well as to explore new, innovative directions within the field of industrial engineering research. To achieve these objectives, I plan to consolidate and expand existing collaborations with colleagues and research institutes both within Romania and internationally, with the goal of increasing the impact and visibility of our scientific activities.

B.3.2.1 Optimization of technological parameters for flame spraying and powder coatings based on NiCrAlX to achieve corrosion-resistant layers

This research aims to develop and optimize a process for depositing protective coatings onto metallic substrates using flame spraying techniques, with particular emphasis on powders composed of NiCrAlX alloys, where X represents alloying elements aimed at enhancing corrosion and oxidation resistance. The spraying process will undergo a rigorous analysis of operational parameters, including flame temperature, spraying velocity, nozzle-to-substrate distance, and application speed, in order to determine the optimal conditions that produce homogeneous, adherent layers with a controlled microstructure.

Advanced characterization techniques such as Scanning Electron Microscopy with Energy Dispersive X-ray Spectroscopy (SEM-EDX), X-ray Diffraction (XRD), as well as adhesion, hardness, and corrosion resistance tests in acidic and saline environments, will be employed to evaluate these coatings. The microstructure of the layers will be analyzed to assess crystal formation, porosity, and elemental distribution, facilitating the correlation of these microstructural features with the mechanical properties and corrosion resistance.

Ultimately, durability studies will include prolonged exposure tests in saline and acidic media, along with high-temperature performance assessments, to ensure the long-term stability and effectiveness of the coatings. The outcomes of this research will underpin the development of innovative technological strategies for protecting critical components in industries subjected to harsh environmental conditions, thereby contributing to extended service life and improved reliability of industrial equipment.

B.3.2.2 Optimization of technological parameters for flame spraying of biocompatible powders (zirconium dioxide, aluminum oxide, calcium oxide)

The process of optimizing technological parameters for flame spraying of biocompatible powders, such as zirconium dioxide (ZrO_2), aluminum oxide (Al_2O_3), and calcium oxide (CaO), constitutes a critical step in the development of functional coatings for medical applications. Through precise adjustment of variables including flame temperature, spraying velocity, nozzle-to-

substrate distance, and application rate, the goal is to achieve uniform, adherent coatings with a homogeneous microstructure that ensure superior mechanical strength and biocompatibility.

Controlling these parameters allows adaptation of the process to various substrate types and specific requirements of each implant or medical device, thereby minimizing the risk of defects or coating delamination. Furthermore, this optimization enhances the durability of the deposited layer, improves tissue compatibility, and reduces the risk of rejection or infection.

Ultimately, this advanced technological approach facilitates the development of high-quality biocompatible coatings essential for the success and safety of implanted medical devices, holding the potential to revolutionize coating technologies within the biomedical field.

B.3.2.3 Utilization of laser beam for fusion of layers deposited via flame and powder spraying

The deployment of laser beam technology for the fusion of layers deposited through flame spraying and powder application represents an innovative and highly effective approach within the field of material processing. This technique offers precise control over the consolidation process of the coated layers. By directing a laser beam onto the surface of the deposited layer, rapid and localized melting of the powders is achieved, resulting in the formation of a strong and durable bond between the coating and the substrate. This process also reduces porosity and internal defects that could compromise the structural integrity of the final product.

The method allows fine-tuning of process parameters, including laser power, fusion speed, exposure time, and environmental conditions, to produce uniform and resilient microstructures. Additionally, laser fusion contributes to the management of internal stresses, mitigates cracking, and prevents deformation. Beyond enhancing the mechanical and chemical properties of the coating, this technique enables the fabrication of stratified structures with tailored functionalities—such as increased wear resistance or biocompatibility.

In conclusion, laser fusion constitutes a versatile and precise method that complements coating deposition techniques, fostering the development of innovative and durable solutions in the realm of industrial engineering.

B.3.2.4 Expansion of deposited layers in protective gas environments for weight reduction, corrosion resistance enhancement, and thermal performance improvement

The expansion of applications involving deposited layers in protective gas environments represents a critical direction of research and development aimed at advancing high-performance manufacturing technologies across various industries, including aerospace, automotive, biomedical, energy, and electronics. Utilizing a protective gas atmosphere during the deposition processes enables precise control of the environment in which the layer formation occurs, thereby preventing oxidation and other undesirable reactions that could compromise the quality and uniformity of the coatings. This technology facilitates the creation of homogeneous layers with superior mechanical and chemical properties adapted to the specific requirements of different applications. Through the

application of protective gas environments, it is possible to produce densely packed layers devoid of porosity or internal defects, significantly contributing to the reduction of the overall weight of structural components. This aspect is particularly impactful in sectors where weight is a critical factor, such as aerospace and space industries, where mass reduction leads to fuel savings and enhanced operational efficiency. Furthermore, these layers, deposited under controlled conditions, provide increased resistance to corrosion, safeguarding components against aggressive environmental factors such as humidity, salinity, and chemical agents, thereby extending service life and reducing maintenance costs. Additionally, depositions performed in protective gas atmospheres enable improvements in the thermal performance of materials by producing layers with controlled thermal conductivity, high-temperature resistance, and efficient heat dissipation capabilities. These properties are essential for components used in turbines, internal combustion engines, electronic devices, power generation systems, and advanced cooling systems. Moreover, such layers can be engineered to possess special functionalities, including wear resistance, non-stick properties, or biocompatibility, making them suitable for medical applications such as implants, prostheses, and diagnostic devices.

(B4) Bibliography

1	(Ando et al., 2009)	Ando, Y., Tobe, S., & Tahara, H. (2009). High-Rate Diamond Deposition by Combustion Flame Method Using Twin Acetylene/Oxygen Gas Welding Torch. *J. Therm. Spray Technol.*, *18*(4), 483–489. https://doi.org/10.1007/s11666-009-9400-8
2	(Arabgol et al., 2017)	Arabgol, Z., Vidaller, M. V., Assadi, H., Gaertner, F., & Klassen, T. (2017). Influence of thermal properties and temperature of substrate on the quality of cold-sprayed deposits. *Acta Mater.*, *127*, 287–301. https://doi.org/10.1016/j.actamat.2017.01.040
3	(Arboleda et al., 2018)	Arboleda, J. A., Serna, C. M., Cadavid, E., Barrios, A. C., Vargas, F., & Toro, A. (2018). Effect of Flame Spray Deposition Parameters on The Microstructure of Al2 O3 - 13 %TiO2 Coatings Applied Onto 7075 Aluminum Alloy. *Materials Research*, *21*(5), e20180038. https://doi.org/10.1590/1980-5373-MR-2018-0038
4	(Baumann et al., 2021)	Baumann, I., Hagen, L., Tillmann, W., Hollingsworth, P., Stangier, D., Schmidtmann, G., Tolan, M., Paulus, M., & Sternemann, C. (2021). Process characteristics, particle behavior and coating properties during HVOF spraying of conventional, fine and nanostructured WC-12Co powders. *Surface and Coatings Technology*, *405*, 126716. https://doi.org/10.1016/J.SURFCOAT.2020.126716
5	(Berger, 2014)	Berger, L. M. (2014). Coatings by Thermal Spray. *Comprehensive Hard Materials*, *1*, 471–506. https://doi.org/10.1016/B978-0-08-096527-7.00017-9
6	(Bolelli et al., 2009)	Bolelli, G., Cannillo, V., Gadow, R., Killinger, A., Lusvarghi, L., & Rauch, J. (2009). Properties of High Velocity Suspension Flame Sprayed (HVSFS) TiO2 coatings. *Surface and Coatings Technology*, *203*(12), 1722–1732. https://doi.org/10.1016/J.SURFCOAT.2009.01.006
7	(Brupbacher et al., 2018)	Brupbacher, M. C., Zhang, D., Buchta, W. M., Montalbano, T. J., Caruso, K. S., Airola, M. B., Brown, D. M., Thomas, M. E., & Spicer, J. B. (2018). Experimental characterization and physics-based modeling of the temperature-dependent diffuse reflectance of plasma-sprayed Nd 2 Zr 2 O 7 in the near to short-wave infrared. *Applied Optics*, *57*(27), 7782. https://doi.org/10.1364/AO.57.007782
8	(Chandra et al., 2020)	Chandra, N. P. S., Otsuka, Y., Mutoh, Y., & Yamamoto, K. (2020). Effect of coating thickness on fatigue behavior of TiAlN coated Ti-alloys. *Int. J. Fatigue*, *140*, 105767. https://doi.org/10.1016/j.ijfatigue.2020.105767

9	(Chen et al., 2020)	Chen, H., Fan, M., Zhu, W., & Norton, A. D. (2020). High temperature oxidation behaviour of combustion flame sprayed CoNiCrAlY coatings. *Surf. Coat. Technol.*, *385*, 125431. https://doi.org/10.1016/j.surfcoat.2020.125431
10	(Choe et al., 2014)	Choe, H.-B., Lee, H.-S., & Shin, J.-H. (2014). Experimental Study on the Electrochemical Anti-Corrosion Properties of Steel Structures Applying the Arc Thermal Metal Spraying Method. *Materials*, *7*(12), 7722–7736. https://doi.org/10.3390/ma7127722
11	(Croitoru et al., 2019)	Croitoru, C., Pascu, A., Stanciu, E. M., & **Roata, I. C.** (2019). Solar synthesis of carbon microparticles from polymer waste. *MATERIALS TODAY-PROCEEDINGS*, *19*, 996–1002. https://doi.org/10.1016/j.matpr.2019.08.012
12	(Croitoru et al., 2020)	Croitoru, C., **Roata, I. C.**, Pascu, A., & Stanciu, E. M. (2020). Diffusion and Controlled Release in Physically Crosslinked Poly (Vinyl Alcohol)/Iota-Carrageenan Hydrogel Blends. *Polymers*, *12*(7), 1544. https://doi.org/10.3390/polym12071544
13	(Croitoru et al., 2020b)	Croitoru, C., **Roata, I. C.**, Pascu, A., Stanciu, E. M., Hulka, I., Stoian, G., & Lupu, N. (2020). Photocatalytic surfaces obtained through one-step thermal spraying of titanium. *Applied Surface Science*, *504*, 144173. https://doi.org/10.1016/j.apsusc.2019.144173
14	(Croitoru & Roata, 2023)	Croitoru, C., & **Roata, I. C.** (2023). Ni-Ti MULTIFUNCTIONAL MATERIALS SINTERED VIA CONCENTRATED SOLAR ENERGY. *Acta Tech. Napoc. Ser.-Appl. Math. Mech. Eng.*, *66*(5), 511–518.
15	(Curran & Clyne, 2006)	Curran, J. A., & Clyne, T. W. (2006). Porosity in plasma electrolytic oxide coatings. *Acta Materialia*, *54*(7), 1985–1993. https://doi.org/10.1016/j.actamat.2005.12.029
16	(Delbos et al., 2004)	Delbos, C., Rat, V., Bonhomme, C., Fazilleau, J., Coudert, J. F., & Fauchais, P. (2004). Influence of powder size distributions on microstrutural features of finely structured plasma sprayed coatings. *High Temp. Mater. Process*, *8*(3), 397–406. https://doi.org/10.1615/HighTempMatProc.v8.i3.50
17	(Erle & Waqi, 2008)	Erle, D., & Waqi, A. (2008). *Wettability*. Gulf Publishing Company Houston, Texas.
18	(Faisal et al., 2025)	Faisal, N. H., Rajendran, V., Kaniapan, S., Ramalingam, V., Prathuru, A., Ahmed, R., Katiyar, N. K., Bansal, A., Whittaker, T., Isherwood, P., Whittow, W., Egiza, M., & Goel, S. (2025). Air plasma sprayed multi-material composite coatings for enhanced light absorption and thermal emission. *Surface and Coatings Technology*, *498*, 131854. https://doi.org/10.1016/J.SURFCOAT.2025.131854

19	(Fauchais et al., 2010)	Fauchais, P., Montavon, G., & Bertrand, G. (2010). From Powders to Thermally Sprayed Coatings. *Journal of Thermal Spray Technology*, *19*(1–2), 56–80. https://doi.org/10.1007/s11666-009-9435-x
20	(Feitosa et al., 2018)	Feitosa, F. R. P., Gomes, R. M., Silva, M. M. R., De Lima, S. J. G., & Dubois, J. M. (2018). Effect of oxygen/fuel ratio on the microstructure and properties of HVOF-sprayed Al59Cu25.5Fe12.5B3 quasicrystalline coatings. *Surface and Coatings Technology*, *353*, 171–178. https://doi.org/10.1016/j.surfcoat.2018.08.081
21	(Gardon & Guilemany, 2014)	Gardon, M., & Guilemany, J. M. (2014). Milestones in Functional Titanium Dioxide Thermal Spray Coatings: A Review. *Journal of Thermal Spray Technology*, *23*(4), 577–595. https://doi.org/10.1007/s11666-014-0066-5
22	(Hao et al., 2024)	Hao, X., Chen, J., Zou, X., Guo, Y., Li, Z., & Wang, C. (2024). INFLUENCE OF SUBSTRATE TEMPERATURE ON THE MICROSTRUCTURE AND PROPERTIES OF CoCrFeNiNb_ x HIGH ENTROPY ALLOY COATINGS. *Surf. Rev. Lett.*, 2450125. https://doi.org/10.1142/S0218625X24501257
23	(Hassanien & Akl, 2015)	Hassanien, A. S., & Akl, A. A. (2015). Influence of composition on optical and dispersion parameters of thermally evaporated non-crystalline Cd50S50−xSex thin films. *Journal of Alloys and Compounds*, *648*, 280–290. https://doi.org/10.1016/j.jallcom.2015.06.231
24	(Hebbale et al., 2025)	Hebbale, A. M., Ramesh, M. R., Petru, J., Chandramouli, T. V., Srinath, M. S., & Shetty, R. K. (2025). A microstructural study and high-temperature oxidation behaviour of plasma sprayed NiCrAlY based composite coatings. *Results in Engineering*, *25*, 103926. https://doi.org/10.1016/J.RINENG.2025.103926
25	(Heimann, 2006)	Heimann, R. B. (2006). Thermal spraying of biomaterials. *Surface and Coatings Technology*, *201*(5), 2012–2019. https://doi.org/10.1016/j.surfcoat.2006.04.052
26	(Hulka et al., 2021)	Hulka, I., Uțu, I. D., Avram, D., Dan, M. L., Pascu, A., Stanciu, E. M., & Roată, I. C. (2021). Influence of the Laser Cladding Parameters on the Morphology, Wear and Corrosion Resistance of WC-Co/NiCrBSi Composite Coatings. *Materials*, *14*(19), 5583. https://doi.org/10.3390/ma14195583
27	(Jafari et al., 2016)	Jafari, T., Moharreri, E., Amin, A., Miao, R., Song, W., & Suib, S. (2016). Photocatalytic Water Splitting—The Untamed Dream: A Review of Recent Advances. *Molecules*, *21*(7), 900. https://doi.org/10.3390/molecules21070900
28	(Jagadeeswar et al., 2020)	Jagadeeswar, A. S., Kumar, S., Venkataraman, B., Babu, P. S., & Jyothirmayi, A. (2020). Effect of thermal energy on the deposition behaviour, wear and corrosion resistance of cold sprayed Ni-WC cermet coatings. *Surface and Coatings Technology*, *399*, 126138.

https://doi.org/10.1016/J.SURFCOAT.2020.126138

29 (Jardim et al., 2016) Jardim, P. L. G., Horowitz, F., Felde, N., Schröder, S., Coriand, L., & Duparré, A. (2016). Determination of the Wenzel roughness parameter by the Power Spectral Density of functional Alumina surfaces. *Thin Solid Films*, *606*, 57–62. https://doi.org/10.1016/j.tsf.2016.03.027

30 (Jariya et al., 2021) Jariya, S. A. I., Ravichandran, K., & Narayanan, T. S. N. S. (2021). Development of novel multi-functional composite coatings on titanium: Evaluation of structural characteristics, bioactivity and corrosion behaviour. *Journal of Alloys and Compounds*, *855*, 157290. https://doi.org/10.1016/j.jallcom.2020.157290

31 (Jing et al., 2018) Jing, M., Li, J., & Liu, K. (2018). Research progress in photolectric materials of CuFeS 2. *IOP Conference Series: Earth and Environmental Science*, *128*, 012087. https://doi.org/10.1088/1755-1315/128/1/012087

32 (Jonda et al., 2024) Jonda, E., Latka, L., Lont, A., Golombek, K., & Szala, M. (2024). The Effect of HVOF Spray Distance on Solid Particle Erosion Resistance of WC-Based Cermets Bonded by Co, Co-Cr and Ni Deposited on Mg-Alloy Substrate. *Adv. Sci. Technol.-Res. J.*, *18*(2), 115–128. https://doi.org/10.12913/22998624/184025

33 (Karthikayan et al., 2017) Karthikayan, S., Ganesan, S., Vasanthakumar, P., Sankaranarayanan, G., & Dinakar, M. (2017). Innovative Research Trends in the Application of Thermal Barrier Metal Coating in Internal Combustion Engines. *Materials Today: Proceedings*, *4*(8), 9004–9012. https://doi.org/10.1016/j.matpr.2017.07.253

34 (Karthikeyan et al., 1997) Karthikeyan, J., Berndt, C. C., Tikkanen, J., Reddy, S., & Herman, H. (1997). Plasma spray synthesis of nanomaterial powders and deposits. *Mater Sci Eng A*, *238*(2), 275. https://doi.org/10.1016/s0921-5093(96)10568-2

35 (Khandanjou et al., 2018) Khandanjou, S., Ghoranneviss, M., Saviz, S., & Afshar, M. R. (2018). Influences of substrate temperature on microstructure and corrosion behavior of APS Ni50Ti25Al25 inter-metallic coating. *Chin. Phys. B*, *27*(2), 28104. https://doi.org/10.1088/1674-1056/27/2/028104

36 (Košević et al., 2019) Košević, M., Stopic, S., Cvetković, V., Schroeder, M., Stevanović, J., Panić, V., & Friedrich, B. (2019). Mixed RuO2/TiO2 uniform microspheres synthesized by low-temperature ultrasonic spray pyrolysis and their advanced electrochemical performances. *Applied Surface Science*, *464*, 1–9. https://doi.org/10.1016/j.apsusc.2018.09.066

37 (Kovarik et al., 2015) Kovarik, O., Hausild, P., Siegl, J., Chraska, T., Matejicek, J., Pala, Z., & Boulos, M. (2015). The influence of substrate temperature on properties of APS and VPS W coatings. *Surf. Coat. Technol.*, *268*, 7–14. https://doi.org/10.1016/j.surfcoat.2014.07.041

38	(Krieg et al., 2017)	Krieg, P., Killinger, A., Gadow, R., Burtscher, S., & Bernstein, A. (2017). High velocity suspension flame spraying (HVSFS) of metal doped bioceramic coatings. *Bioactive Materials*, *2*(3), 162–169. https://doi.org/10.1016/J.BIOACTMAT.2017.04.006
39	(Kuchumova et al., 2020)	Kuchumova, I. D., Batraev, I. S., Cherkasova, N. Y., Rybin, D. K., Ukhina, A. V., José Botta, W., Yuuki Koga, G., & Moreira Jorge, A. (2020). The influence of the O2/C2H2 ratio on the structure and properties of Fe66Cr10Nb5B19 detonation coatings. *Materials Today: Proceedings*, *25*, 384–386. https://doi.org/10.1016/J.MATPR.2019.12.098
40	(Kumar et al., 2025)	Kumar, K., Kumar, S., & Singh Gill, H. (2025). HIGH-TEMPERATURE OXIDATION PERFORMANCE OF HVOF AND PLASMA-SPRAYED Ni-20Cr, Ni-20Cr + TiC, AND Ni-20Cr + TiN COATINGS ON T22 BOILER STEELS. *Surf. Rev. Lett.*, 2550130. https://doi.org/10.1142/S0218625X25501306
41	(Lara & de Mello, 2012)	Lara, L. O. C., & de Mello, J. D. B. (2012). Influence of layer thickness on hardness and scratch resistance of Si-DLC/CrN coatings. *Tribol.-Mater. Surf. Interfaces*, *6*(4), 168–173. https://doi.org/10.1179/1751584X12Y.0000000019
42	(Lazar et al., 2010)	Lazar, M. A., Tadvani, J. K., Tung, W. S., Lopez, L., & Daoud, W. A. (2010). Nanostructured thin films as functional coatings. *IOP Conference Series: Materials Science and Engineering*, *12*(1), 012017. https://doi.org/10.1088/1757-899X/12/1/012017
43	(Lei et al., 2007)	Lei, S., Kuang, T., Cheng, X., Yin, S., & Zhu, H. (2007). Deposition of carbon nanofibers on a low carbon steel substrate using an oxy-acetylene reducing flame. *New Carbon Mater.*, *22*(1), 70–74. https://doi.org/10.1016/S1872-5805(07)60008-0
44	(C. J. Li et al., 1999)	Li, C. J., Yang, H., & Li, H. (1999). Effect of gas conditions on HVOF flame and properties of WC-Co coatings. *Mater. Manuf. Process.*, *14*(3), 383–395. https://doi.org/10.1080/10426919908914834
45	(S. Li et al., 2025)	Li, S., Li, C., Wang, X., Liu, P., & Han, X. (2025). Evaluation and Analysis of Particle Oxidation of HVOF Thermal Spraying Based on GA-BP Neural Network Algorithm. *J Therm Spray Tech*, *34*(1), 267–290. https://doi.org/10.1007/s11666-024-01906-0
46	(Y. Li et al., 2024)	Li, Y., Cai, D., Wang, J., Zhou, K., Peng, C., Li, Y., Li, N., Yang, S., & E, T. (2024). Precisely regulated crystalline phase of TiO2@composite G doped with Al3+: For the preparation of highly conductive, corrosion resistant conductive coatings. *Journal of Alloys and Compounds*, *1008*, 176387. https://doi.org/10.1016/j.jallcom.2024.176387
47	(Long et al., 2020)	Long, H., Liang, L. H., & Wei, Y. (2020). Influences of interface properties and coating thickness on fracture behaviors of coating/substrate systems.

Strength Fract. Complex., *12*(2–4), 113–117. https://doi.org/10.3233/SFC-190239

48 (Mahrukh et al., 2025) Mahrukh, M., Liu, S.-H., Zhang, L., Husnain, S., Yang, C.-C., Luo, X.-T., & Li, C.-J. (2025). A Study of Particle Heating and Oxidation Protection in a Modified Internally Injected Ar-H2 Atmospheric Plasma Spraying Torch. *Plasma-Basel*, *8*(1), 5. https://doi.org/10.3390/plasma8010005

49 (Marcano et al., 2017) Marcano, D., Mauer, G., Vaßen, R., & Weber, A. (2017). Manufacturing of high performance solid oxide fuel cells (SOFCs) with atmospheric plasma spraying (APS) and plasma spray-physical vapor deposition (PS-PVD). *Surface and Coatings Technology*, *318*, 170–177. https://doi.org/10.1016/j.surfcoat.2016.10.088

50 (Marinou et al., 2015) Marinou, A., Xanthopoulou, G., Vekinis, G., Lekatou, A., & Vardavoulias, M. (2015). Synthesis and Heat Treatment of Sprayed High-Temperature NiAl-Ni3Al Coatings by In-Flight Combustion Synthesis (CAFSY). *Int. J. Self-Propag. High-Temp. Synth.*, *24*(4), 192–202. https://doi.org/10.3103/S106138621504007X

51 (Martínez-García et al., 2024) Martínez-García, J., Martínez-García, V., & Killinger, A. (2024). Modelling and Experimental Validation of the Flame Temperature Profile in Atmospheric Plasma Coating Processes on the Substrate. *Coatings 2024, Vol. 14, Page 1248*, *14*(10), 1248. https://doi.org/10.3390/COATINGS14101248

52 (Meghwal et al., 2020) Meghwal, A., Anupam, A., Murty, B. S., Berndt, C. C., Kottada, R. S., & Ang, A. S. M. (2020). Thermal Spray High-Entropy Alloy Coatings: A Review. *J. Therm. Spray Technol.*, *29*(5), 857–893. https://doi.org/10.1007/s11666-020-01047-0

53 (Melentiev et al., 2022) Melentiev, R., Yudhanto, A., Tao, R., Vuchkov, T., & Lubineau, G. (2022). Metallization of polymers and composites: State-of-the-art approaches. *Materials and Design*, *221*. https://doi.org/10.1016/j.matdes.2022.110958

54 (Meng et al., 2009) Meng, X., Zhang, H., & Zhu, J. (2009). Characterization of particle size evolution of the deposited layer during electrostatic powder coating processes. *Powder Technol.*, *195*(3), 264–270. https://doi.org/10.1016/j.powtec.2009.06.010

55 (Mohanty & Roy, 2012) Mohanty, R. M., & Roy, M. (2012). Thermal sprayed WC-Co coatings for tribological application. *Materials and Surface Engineering*, 121–162. https://doi.org/10.1533/9780857096036.121

56 (Morks & Kobayashi, 2006) Morks, M. F., & Kobayashi, A. (2006). Influence of gas flow rate on the microstructure and mechanical properties of hydroxyapatite coatings fabricated by gas tunnel type plasma spraying. *Surf. Coat. Technol.*, *201*(6), 2560–2566. https://doi.org/10.1016/j.surfcoat.2006.04.030

57	(Nawi & Zain, 2012)	Nawi, M. A., & Zain, S. Md. (2012). Enhancing the surface properties of the immobilized Degussa P-25 TiO2 for the efficient photocatalytic removal of methylene blue from aqueous solution. *Applied Surface Science*, *258*(16), 6148–6157. https://doi.org/10.1016/j.apsusc.2012.03.024
58	(Nikkanen et al., 2015)	Nikkanen, J. P., Huttunen-Saarivirta, E., Salminen, T., Hyvärinen, L., Honkanen, M., Isotahdon, E., Heinonen, S., & Levänen, E. (2015). Enhanced photoactive and photoelectrochemical properties of TiO2 sol–gel coated steel by the application of SiO2 intermediate layer. *Applied Catalysis B: Environment and Energy*, *174–175*, 533–543. https://doi.org/10.1016/J.APCATB.2015.03.014
59	(Niu et al., 2012)	Niu, Y., Zheng, X., Liu, X., Ji, H., & Ding, C. (2012). Influence of powder size on characteristics of air plasma sprayed silicon coatings. *Ceram. Int.*, *38*(7), 5897–5905. https://doi.org/10.1016/j.ceramint.2012.03.080
60	(Nowotny et al., 2014)	Nowotny, S., Berger, L. M., & Spatzier, J. (2014). Coatings by Laser Cladding. *Comprehensive Hard Materials*, *1*, 507–525. https://doi.org/10.1016/B978-0-08-096527-7.00018-0
61	(Pala et al., 2017)	Pala, Z., Shaw, E., Murray, J. W., Senin, N., & Hussain, T. (2017). Suspension high velocity oxy-fuel spraying of TiO2: A quantitative approach to phase composition. *Journal of the European Ceramic Society*, *37*(2), 801–810. https://doi.org/10.1016/j.jeurceramsoc.2016.08.030
62	(Pshyk et al., 2016)	Pshyk, A. V., Coy, L. E., Nowaczyk, G., Kempiński, M., Peplińska, B., Pogrebnjak, A. D., Beresnev, V. M., & Jurga, S. (2016). High temperature behavior of functional TiAlBSiN nanocomposite coatings. *Surface and Coatings Technology*, *305*, 49–61. https://doi.org/10.1016/j.surfcoat.2016.07.075
63	(Rakhadilov et al., 2024)	Rakhadilov, B., Magazov, N., Kakimzhanov, D., Apsezhanova, A., Molbossynov, Y., & Kengesbekov, A. (2024). Influence of Spraying Process Parameters on the Characteristics of Steel Coatings Produced by Arc Spraying Method. *Coatings 2024, Vol. 14, Page 1145*, *14*(9), 1145. https://doi.org/10.3390/COATINGS14091145
64	(Riastuti et al., n.d.)	Riastuti, R., Bancin, B. A. H., & Rahmat, Z. (n.d.). *Thermal Arc Spray Overview The Influence of Spray Distance of Thermal Sprayed Aluminum (TSA) on its Corrosion Resistance and Bond Strength*. https://doi.org/10.1088/1757-899X/46/1/012028
65	**(Roata et al., 2009)**	**Roata, I. C.**, Iovanas, R., Andreescu, F., Andreescu, B., & Dozescu, S. I. (2009). Studies About the Electric Loading of the Powders Used in the Recondtioning Process Through Spraying. *Metal. Int.*, *14*, 199–202.

66 **(Roata & Iovanas, 2011)** **Roata, I. C.**, & Iovanas, R. (2011). Experimental Researches Regarding the Microhardness Evolution in the Case of Layers That Are Deposited by Metallization. *Metal. Int.*, *16*(3), 85–88.

67 **(Roata et al., 2011)** **Roata, I. C.**, Iovanas, R., & Iovanas, D. M. (2011). The Influence of Powders Cladded with Electric Charges Upon the Adherence of the Layers That Are Deposited by Metallization. *Metal. Int.*, *16*(5), 161–165.

68 **(Roata et al., 2014)** **Roata, I.C.**, Pascu, A., & Stanciu, E.-M. (2014). Influence of the electric field voltage on the microhardness of the layers coated by thermal spraying. In M. Nicoara & C. Opris (Eds.), *ADVANCED MATERIALS AND STRUCTURES V* (Vol. 216, pp. 316–321). Trans Tech Publications Ltd. https://doi.org/10.4028/www.scientific.net/SSP.216.316

69 **(Roata et al., 2017)** **Roata, I. C**., Pascu, A., Croitoru, C., Stanciu, E. M., & Pop, M. A. (2017). Thermal Spraying of CuAlFe Powder on Cu5Sn Alloy. In A. V Sandu, M. M. A. Abdullah, P. Vizureanu, C. M. R. Ghazali, & I. Sandu (Eds.), *INTERNATIONAL CONFERENCE ON INNOVATIVE RESEARCH - ICIR EUROINVENT 2017* (Vol. 209, p. 12042). IoP Publishing Ltd. https://doi.org/10.1088/1757-899X/209/1/012042

70 **(Roata, 2017b)** **Roata, I. C.** (2017). *Acoperiri prin pulverizare termică:* Lux Libris, ISBN:978-973-131-000-8.

71 **(Roata et al., 2018)** **Roata, I. C.**, Croitoru, C., Pascu, A., & Stanciu, E. M. (2018). Photocatalytic performance of copper-based coatings deposited by thermal spraying. *J Mater Sci: Mater Electron*, *29*(13), 11345–11357. https://doi.org/10.1007/s10854-018-9222-x

72 **(Roata, 2018b)** **Roata, I. C.** (2018). *Applications of thermal spray technologies;* Lux Libris, ISBN:978-973-131-410-5.

73 **(Roata, et al., 2019)** **Roata, I. C.**, Croitoru, C., Pascu, A., Manuela Stanciu, E., Department of Materials Engineering, & Welding Transilvania University of Brasov, 500036 Eroilor 29 Brasov Romania. (2019). Photocatalytic coatings via thermal spraying: a mini-review. *AIMS Materials Science*, *6*(3), 335–353. https://doi.org/10.3934/matersci.2019.3.335

74 **(Roata et al., 2019b)** **Roata, I. C.**, Croitoru, C., Stanciu, E. M., & Pascu, A. (2019). Cladding under the spotlight: between performance materials and occupational health hazards. *MATERIALS TODAY-PROCEEDINGS*, *19*, 1051–1058.

75 **(Roata et al., 2020)** **Roata, I. C**., Croitoru, C., Pascu, A., Stanciu, E. M., Hulka, I., Petre, I., Gabor, C., Patroi, D., & Sbarcea, B.-G. (2020). Surface engineering of Ni-Al coatings through concentrated solar heat treatment. *Applied Surface Science*, *506*, 144185. https://doi.org/10.1016/j.apsusc.2019.144185

76	**(Roata et al., 2023)**	**Roata, I. C.**, Plamadiala, I., & Uncu, I. (2023). MULTIFUNCTIONAL Ni-Cr-Al-Y COATINGS VIA THERMAL SPRAYING. *Acta Tech. Napoc. Ser.-Appl. Math. Mech. Eng.*, *66*(5), 519–528.
77	(Rodríguez et al., 2014)	Rodríguez, J., Cañadas, I., & Zarza, E. (2014). PSA Vertical Axis Solar Furnace SF5. *Energy Procedia*, *49*, 1511–1522. https://doi.org/10.1016/J.EGYPRO.2014.03.160
78	(Semikolenov et al., 2024)	Semikolenov, A., Mamaev, N., Larionova, T., Shalnova, S., & Tolochko, O. (2024). Effect of Powder Preparation of FeNiCoCrMo0.5Al1.3 High-Entropy Alloy on the Phase Composition and Properties of High-Velocity Oxy-Fuel-Sprayed Coatings. *JMMP*, *8*(6), 280. https://doi.org/10.3390/jmmp8060280
79	(Shahbazi et al., 2025)	Shahbazi, H., Lima, R. S., Stoyanov, P., & Moreau, C. (2025). Effect of Microstructure on Oxidation Resistance and TGO Formation in FeCoNiCrAl HEA Coatings Deposited by Low-Temperature HVAF Spraying. *Materials*, *18*(7), 1569. https://doi.org/10.3390/ma18071569
80	(Siegmann et al., 2005)	Siegmann, S., Leparoux, M., & Rohr, L. (2005). *The role of nano-particles in the field of thermal spray coating technology* (W. J. Blau, D. Kennedy, & J. Colreavy, Eds.; p. 224). https://doi.org/10.1117/12.605225
81	(Sirjani et al., 2025)	Sirjani, F. K., Shabani, A., Raeissi, K., Nahvi, S. M., & Molavian, A. M. (2025). Effect of heat treatment on microstructure and high-temperature oxidation behavior of flame-sprayed Ni-5 wt.% Al coating on low carbon steel. *Results in Surfaces and Interfaces*, *19*, 100515. https://doi.org/10.1016/j.rsurfi.2025.100515
82	(Sivakumar et al., 2018)	Sivakumar, G., Banerjee, S., Raja, V. S., & Joshi, S. V. (2018). Hot corrosion behavior of plasma sprayed powder-solution precursor hybrid thermal barrier coatings. *Surface and Coatings Technology*, *349*, 452–461. https://doi.org/10.1016/j.surfcoat.2018.06.021
83	(Szymański et al., 2015)	Szymański, K., Hernas, A., Moskal, G., & Myalska, H. (2015). Thermally sprayed coatings resistant to erosion and corrosion for power plant boilers - A review. *Surface and Coatings Technology*, *268*, 153–164. https://doi.org/10.1016/j.surfcoat.2014.10.046
84	(Toma et al., 2008)	Toma, F.-L., Bertrand, G., Klein, D., Meunier, C., & Begin, S. (2008). Development of Photocatalytic Active TiO 2 Surfaces by Thermal Spraying of Nanopowders. *Journal of Nanomaterials*, *2008*(1). https://doi.org/10.1155/2008/384171
85	(Toma et al., 2014)	Toma, F.-L., Berger, L.-M., Shakhverdova, I., Leupolt, B., Potthoff, A., Oelschlägel, K., Meissner, T., Gomez, J. A. I., & de Miguel, Y. (2014). Parameters Influencing the Photocatalytic Activity of Suspension-Sprayed

TiO2 Coatings. *Journal of Thermal Spray Technology*, *23*(7), 1037–1053. https://doi.org/10.1007/s11666-014-0090-5

86 (Tomaszek et al., 2006) Tomaszek, R., Pawlowski, L., Gengembre, L., Laureyns, J., Znamirowski, Z., & Zdanowski, J. (2006). Microstructural characterization of plasma sprayed TiO2 functional coating with gradient of crystal grain size. *Surface and Coatings Technology*, *201*(1–2), 45–56. https://doi.org/10.1016/J.SURFCOAT.2005.10.033

87 (Uncu et al., 2021) Uncu, I., **Roata, I. C.,** Croitoru, C., & Machedon-Pisu, T. (2021). Visible Domain Photocatalysis Performance of Ti-Si Thermal-Sprayed Coatings. *Sustainability*, *14*(1), 85. https://doi.org/10.3390/su14010085

88 (Vardelle et al., 2015b) Vardelle, A., Moreau, C., Themelis, N. J., & Chazelas, C. (2015a). A Perspective on Plasma Spray Technology. *Plasma Chemistry and Plasma Processing*, *35*(3), 491–509. https://doi.org/10.1007/S11090-014-9600-Y/FIGURES/7

89 (Vaßen et al., 2010) Vaßen, R., Jarligo, M. O., Steinke, T., Mack, D. E., & Stöver, D. (2010). Overview on advanced thermal barrier coatings. *Surface and Coatings Technology*, *205*(4), 938–942. https://doi.org/10.1016/j.surfcoat.2010.08.151

90 (Vuoristo, 2014) Vuoristo, P. (2014). Thermal Spray Coating Processes. *Comprehensive Materials Processing: Thirteen Volume Set*, *4*, V4-229-V4-276. https://doi.org/10.1016/B978-0-08-096532-1.00407-6

91 (Wang et al., 2023) Wang, S., Guo, T., Xu, G., & Ding, F. (2023). Corrosion behavior and mechanism of electric arc-sprayed Al-Mg coating and Zn-Al-Mg pseudo-alloy coatings. *Surface and Coatings Technology*, *475*, 130126. https://doi.org/10.1016/J.SURFCOAT.2023.130126

92 (Wu et al., 2009) Wu, D., Long, M., Zhou, J., Cai, W., Zhu, X., Chen, C., & Wu, Y. (2009). Synthesis and characterization of self-cleaning cotton fabrics modified by TiO2 through a facile approach. *Surface and Coatings Technology*, *203*(24), 3728–3733. https://doi.org/10.1016/j.surfcoat.2009.06.008

93 (Xanthopoulou et al., 2014) Xanthopoulou, G., Marinou, A., Vekinis, G., Lekatou, A., & Vardavoulias, M. (2014). Ni-Al and NiO-Al Composite Coatings by Combustion-Assisted Flame Spraying. *Coatings*, *4*(2), 231–252. https://doi.org/10.3390/coatings4020231

94 (Yamada et al., 2010) Yamada, M., Isago, H., Nakano, H., & Fukumoto, M. (2010). Cold spraying of TiO 2 photocatalyst coating with nitrogen process gas. *Journal of Thermal Spray Technology*, *19*(6), 1218–1223. https://doi.org/10.1007/S11666-010-9520-1/FIGURES/8

95 (G. J. Yang et al., 2008) Yang, G. J., Li, C. J., Han, F., Li, W. Y., & Ohmori, A. (2008). Low temperature deposition and characterization of TiO2 photocatalytic film through cold

spray. *Applied Surface Science*, *254*(13), 3979–3982. https://doi.org/10.1016/J.APSUSC.2007.12.016

96 (G. J. Yang et al., 2005) Yang, G. J., Li, C. J., & Wang, Y. Y. (2005). Phase formation of nano-TiO2 particles during flame spraying with liquid feedstock. *Journal of Thermal Spray Technology*, *14*(4), 480–486. https://doi.org/10.1361/105996305X76487/METRICS

97 (Y. Yang et al., 2015) Yang, Y., Wang, Y., Tian, W., Yan, D., Zhang, J.-X., & Wang, L. (2015). Influence of composite powders' microstructure on the microstructure and properties of Al2O3-TiO2 coatings fabricated by plasma spraying. *Mater. Des.*, *65*, 814–822. https://doi.org/10.1016/j.matdes.2014.09.078

98 (Z. Y. Yang, 2004) Yang, Z. Y. (2004). Influences of gas flow rates on melting of particles of HVOF sprayed CoCrW coating and coating properties. *Rare Metals*, *23*(1), 53–58.

99 (Zha et al., 2017) Zha, B., Gao, S., Yuan, X., Luo, L., Li, Z., Ji, S., & Zhang, B. (2017). Effect of Thickness on Microstructure of HVOF Sprayed WC-12Co Coatings. *Rare Metal Mat. Eng.*, *46*(2), 509–514.

100 (Zhang et al., 2002) Zhang, R., Gao, L., Yu, L., & Guo, J. K. (2002). Influence of particle size-distribution on the phase homogeneity between SiC particles and Cu coating. *J. Inorg. Mater.*, *17*(6), 1311–1314.

101 (Zhao et al., 2018) Zhao, Y., Yu, Z., Planche, M.-P., Lasalle, A., Allimant, A., Montavon, G., & Liao, H. (2018). Influence of Substrate Properties on the Formation of Suspension Plasma Sprayed Coatings. *J. Therm. Spray Technol.*, *27*(1–2), 73–83. https://doi.org/10.1007/s11666-017-0671-1

102 (Zhu et al., 2024) Zhu, X., Xie, J., Zhang, H., Liu, W., Zhang, H., & Zhu, J. (2024). Insights into powder coating excellence: Unveiling the effects of particle-size distribution. *Progress in Organic Coatings*, *197*, 108815. https://doi.org/10.1016/j.porgcoat.2024.108815

103 (Zurecki et al., 1997) Zurecki, Z., Garg, D., & Bowe, D. (1997). Electric arc deposition of carbon steel coatings with improved mechanical properties. *Journal of Thermal Spray Technology*, *6*(4), 417–421. https://doi.org/10.1007/S11666-997-0023-7/METRICS

104 (***SF05) https://www.psa.es/en/facilities/solar_furnaces/sf5.php